UNIVERSITY OF IOANNINA
SCHOOL OF SCIENCES
DEPARTMENT OF PHYSICS

Structure and Dynamics of Biomacromolecules in the bulk and under Confinement

Maria-Ioanna Spyridakou

PHD THESIS

IOANNINA 2025

ΠΑΝΕΠΙΣΤΗΜΙΟ ΙΩΑΝΝΙΝΩΝ
ΣΧΟΛΗ ΘΕΤΙΚΩΝ ΕΠΙΣΤΗΜΩΝ
ΤΜΗΜΑ ΦΥΣΙΚΗΣ

Δομή και Δυναμική Βιο-μακρομορίων στην καθαρή τους κατάσταση και υπό Περιορισμό

Μαρία-Ιωάννα Σπυριδάκου

ΔΙΔΑΚΤΟΡΙΚΗ ΔΙΑΤΡΙΒΗ

ΙΩΑΝΝΙΝΑ 2025

Three-member committee

- *Georgios Floudas* (Supervisor), Professor, Department of Physics, University of Ioannina
- *Georgios Papageorgiou*, Professor, Department of Chemistry, University of Ioannina
- *Periklis Papadopoulos*, Associate Professor, Department of Physics, University of Ioannina

Seven-member committee

- *Georgios Floudas*, Professor, Department of Physics, University of Ioannina
- *Georgios Papageorgiou*, Professor, Department of Chemistry, University of Ioannina
- *Periklis Papadopoulos*, Associate Professor, Department of Physics, University of Ioannina
- *Georgios Evangelakis*, Emeritus Professor, Department of Physics, University of Ioannina
- *Ermolaos Iatrou*, Professor, Department of Physics, National and Kapodistrian University of Athens
- *Kostas Daoulas*, Associate Professor, Department of Physics, University of Ioannina
- *Anastasia Rissanou*, Associate Researcher, Theoretical and Physical Chemistry Institute, National Hellenic Research Foundation

Acknowledgements

This doctoral dissertation was conducted at the Soft Matter Physics Lab in the Department of Physics at the University of Ioannina. I would like to express my sincere gratitude to everyone who contributed to the realization of this research.

First and foremost, I would like to thank my supervisor, Professor Georgios Floudas, for his continuous guidance, encouragement, and unwavering support throughout the years. I deeply appreciate the trust he placed in me, as well as his foresight in assigning a project that challenged me to explore new frontiers in our field. His insightful feedback, scientific rigor, and belief in my work have shaped both this Thesis and my growth as a researcher.

I am also grateful to the members of the three-member committee, Prof. G. Papageorgiou and Associate Prof. P. Papadopoulos, for their constructive feedback and advice. In addition, I would like to thank Emeritus Professor G. Evangelakis, Prof. E. Iatrou, Associate Prof. K. Daoulas, and Associate Researcher A. Rissanou, for serving in the seven-member committee.

Thanks are also in order to Prof. E. Iatrou and his group, I. G. Stavrakaki, E. Tsagkaraki, and C. Varfi, from the Department of Chemistry at the National and Kapodistrian University of Athens for synthesizing the poly(γ-benzyl-L-glutamate) (PBLG) homopolypeptides. I am equally grateful to Prof. S. Lecommandoux and his group, Dr. C. Bonduelle, and H. Beauseroy, at the University of Bordeaux for synthesizing the diblock copolymers PEG-*b*-PBLG and PEG-*b*-PLeu. I am also thankful to Dr. R. Graf for the advanced NMR measurements at the Max-Planck Institute for Polymer Research (MPI-P).

Special thanks go to my colleagues and collaborators in the lab, for the stimulating scientific conversations, and for being such great companions. They made the work environment dynamic and supportive. I would also like to acknowledge Mr. George Tsoumanis for his consistent technical assistance.

On a personal note, I would like to thank my partner, my family, and my friends for their unconditional love, endless patience, and unwavering encouragement throughout this journey.

Finally, this Thesis was supported by the Hellenic Foundation for Research and Innovation (H.F.R.I.) under the “First Call for H.F.R.I. Research Projects to support Faculty members and Researchers and the procurement of high-cost research equipment grant” (Project Number: 183),

and by the program ″PERIFEREIAKI ARISTEIA″ (Regional Excellence) cofinanced by the European Union and the Hellenic Republic Ministry of development and investments under NSRF 2014-2020 (Region of Epirus, call 111). Their financial support was essential for the completion of this work.

Abstract

Proteins achieve their functional diversity through precisely controlled hierarchical organization. Secondary structural motifs – particularly α-helices and β-sheets – dictate both topology and dynamics. However, the inherent complexity of natural systems often obscures clear structure-dynamics relationships. Synthetic polypeptides provide a platform for investigating these relationships while mimicking nature's design strategies. This thesis demonstrates how secondary structures govern protein behavior across different length- and timescales, through two complementary investigations: the inherent dynamics of the different secondary structures in non-hydrated environments, and their controlled hierarchical organization in block copolymers.

The first part investigates poly(γ-benzyl-L-glutamate) (PBLG) homopolypeptides, which adopt either α-helical or/and β-sheet motifs depending on molar mass and chain end-group chemistry. We demonstrate that the two secondary structures exhibit distinct *local* and *global* dynamics. Two glass temperatures (T_gs) are evident in polypeptides that stabilize both secondary structures, each associated with the segmental dynamics of the amorphous α-helical and β-sheet segments. β-sheets exhibit slower local dynamics, lower fragility, and reduced pressure sensitivity compared to α-helices. We discuss these differences in terms of the different structural environments imposed by the type of hydrogen bonding (intra vs inter). The relaxation of the α-helical and β-sheet macrodipoles was also evident at longer timescales. We report that β-sheet forming oligopeptides exhibit a dipolar relaxation perpendicular to the chain. In addition, the different secondary structures have distinct viscoelastic signatures at the segmental level and at the domain level. The latter reflects the emergence of a tertiary structure, i.e., a "mesh", that decreases in size with increasing molar mass. β-sheet oligopeptides form rigid networks, ideal for bone scaffolds or load-bearing tissue (10^7 Pa), while low-molar-mass α-helical peptides form soft matrices, suited for tissue interfaces or membranes (1-20 kPa). Due to this self-organization, an elastic response was observed across all polypeptides at all frequencies.

The second part explores amphiphilic diblock copolymers composed of PBLG and poly(ethylene glycol) (PEG), synthesized via ring-opening polymerization-induced self-assembly (ROPISA) in aqueous buffer. Using a combination of static (^{13}C NMR, X-ray scattering, polarizing optical microscopy), thermodynamic (differential scanning calorimetry), and dynamic (dielectric spectroscopy) probes, we demonstrate an unprecedented six-level hierarchical organization – a

phenomenon previously observed only in natural systems, such as tendons. Starting from smaller lengthscales, these levels include: the peptide secondary structures (α-helices and β-sheets), the PEG monoclinic unit cell, the lamellar nanodomain morphology of unlike blocks, an intermediate rod-like structure and the anisotropic superstructures of PEG crystals. These levels of organization could not be obtained in earlier morphology investigations of copolymers based on PEG and PBLG prepared by different methods. Furthermore, the type of NCA monomer (BLG-NCA vs Leu-NCA) and the solvent treatment method had an influence on the degree of segregation, the α-helical content, and the order-to-disorder transition temperature in the PEG-*b*-PBLG and PEG-*b*-PLeu (PLeu: poly(L-leucine)) copolymers.

This work establishes that secondary structure, dictated by hydrogen-bonding patterns, governs polypeptide organization and dynamics across seven length- and time-scales. In homopolypeptides, β-sheets form rigid, pressure-resistant networks with low fragility, exhibiting mechanical properties suitable for stiff biomedical implants. Conversely, α-helices yield softer, more compliant matrices ideal for use as drug delivery carriers. In block copolymers, ROPISA leverages these same interactions to build six-level hierarchical architectures that mimic native protein organizations. Together, these findings may provide a framework for designing biomaterials with precisely controllable structural, dynamic, and mechanical properties, achieving multiscale, protein-like precision.

Περίληψη

Οι πρωτεΐνες επιτυγχάνουν τη λειτουργική τους ποικιλομορφία μέσω μιας ελεγχόμενης ιεραρχικής οργάνωσης. Οι δευτεροταγείς δομές – α-έλικες και β-φύλλα – καθορίσουν τόσο την αρχιτεκτονική όσο και τη δυναμική των πρωτεϊνών. Αυτές οι δομές διέπουν τη συμπεριφορά των πρωτεϊνών σε διάφορες χρονικές κλίμακες, επηρεάζοντας την αναδίπλωση, τη λειτουργία και τη συναρμολόγηση τους. Ωστόσο, η εγγενής πολυπλοκότητα των φυσικών συστημάτων συχνά δυσκολεύει τη μελέτη των σχέσεων μεταξύ δομής-δυναμικής. Τα συνθετικά πολυπεπτίδια αποτελούν ένα ισχυρό εργαλείο για τη διερεύνηση αυτών των σχέσεων, εξαιτίας της δομικής και λειτουργικής τους ομοιότητα με τις πρωτεΐνες. Η παρούσα Διατριβή εξετάζει πώς τα συνθετικά πολυπεπτίδια μπορούν να μιμηθούν την ιεραρχική οργάνωση των πρωτεϊνών, απαντώντας σε δύο αλληλένδετα ερωτήματα: πρώτον, πώς οι δευτεροταγείς δομές καθορίζουν τη δυναμική και μηχανική συμπεριφορά των πολυπεπτιδίων σε μη ενυδατωμένα συστήματα και δεύτερον, πώς μπορούμε να ελέγξουμε την ανώτερη οργάνωση αυτών των δομικών μονάδων σε κλίμακες μήκους από νανόμετρα έως μικρόμετρα.

Το πρώτο μέρος εστιάζει σε ομοπολυπεπτίδια πολυ(γ-βενζυλο-L-γλουταμινικού οξέος) (PBLG), τα οποία μπορούν να υιοθετήσουν α-έλικες ή/και β-φύλλα, ανάλογα με τη μοριακή μάζα και τη μακρομοριακή διασπορά του πεπτιδίου. Τα αποτελέσματα έδειξαν δύο διακριτές θερμοκρασίες "μετάβασης υάλου" (T_gs) σε πολυπεπτίδια που σταθεροποιούν και τις δύο δευτεροταγείς δομές, καθεμία συσχετιζόμενη με τη δυναμική των άμορφων τμημάτων των α-ελίκων και β-φύλλων. Η μοριακή δυναμική αποκαλύπτει διακριτά χαρακτηριστικά για τα β-φύλλα, σε σύγκριση με τις α-έλικες: (i) πιο αργή δυναμική που σχετίζεται με το T_g, (ii) συστηματικά χαμηλότερες τιμές ευθραυστότητας και (iii) σημαντικά μειωμένη απόκριση σε πίεση. Οι διαφορές αυτές αποδίδονται στα διαφορετικά δομικά περιβάλλοντα που δημιουργούνται από τις δύο δομές εξαιτίας του διαφορετικού τύπου δεσμών υδρογόνου (διαμοριακοί δ.υ. για τα β-φύλλα έναντι ενδομοριακών δ.υ. για τις α-έλικες). Ακόμη, η χαλάρωση των μακροδιπόλων των α-ελίκων και β-φύλλων ήταν εμφανής σε μεγαλύτερες χρονικές κλίμακες. Είναι η πρώτη φορά που παρατηρείται μηχανισμός χαλάρωσης δίπολου των β-φύλλων κάθετα προς την αλυσίδα. Επιπλέον, οι δύο δευτεροταγείς δομές παρουσιάζουν διακριτή ιξωδοελαστική συμπεριφορά σε μοριακό επίπεδο, τόσο σε μοριακό όσο και σε μεσοσκοπικό επίπεδο, γεγονός που σχετίζεται με την εμφάνιση μιας τριτοταγούς δομής, τύπου "δικτύου", το οποίο μειώνεται σε μέγεθος με την αύξηση της μοριακής μάζας. Τα πεπτίδια που σταθεροποιούν β-φύλλα σχηματίζουν άκαμπτα δίκτυα,

κατάλληλα για εφαρμογές ως οστικά ικριώματα (~10^7 Pa), ενώ τα μικρής μοριακή μάζας πεπτίδια που σταθεροποιούν α-έλικες σχηματίζουν πιο μαλακές μήτρες (1–20 kPa), κατάλληλες για βιοϊατρικές μεμβράνες ή διεπιφάνειες ιστών. Εξαιτίας αυτής της αυτοοργάνωσης, παρατηρήθηκε ελαστική απόκριση σε όλα τα δείγματα.

Το δεύτερο μέρος εξετάζει αμφίφιλα δισυσταδικά συμπολυμερή πολυ(αιθυλενογλυκόλης)-*b*-πολυ(*γ*-βενζυλο-L-γλουταμινικού οξέος) (PEG-*b*-PBLG), που συντέθηκαν μέσω πολυμερισμού διάνοιξης δακτυλίου των N-καρβοξυανυδριτών των α-αμινοξέων με ταυτόχρονη αυτο-οργάνωση (ROPISA) σε υδατικό διάλυμα. Μέσω ενός συνδυασμού στατικών (^{13}C NMR, σκέδαση ακτίνων Χ, πολωτική οπτική μικροσκοπία), θερμοδυναμικών (διαφορική θερμιδομετρία) και δυναμικών (διηλεκτρική φασματοσκοπία) τεχνικών, αποδεικνύουμε μια ιεραρχική οργάνωση έξι επιπέδων – φαινόμενο που έχει παρατηρηθεί μόνο σε φυσικά συστήματα, όπως οι τένοντες. Ξεκινώντας από μικρότερες κλίμακες, τα επίπεδα αυτά περιλαμβάνουν: τις δευτερογενείς δομές (α-έλικες και β-φύλλα), τη μονοκλινή κυψελίδα του κρυσταλλικού PEG, τη φυλλοειδή μορφολογία των διαφορετικών συστάδων, μια ενδιάμεση ραβδοειδή δομή και τις ανισότροπες υπερδομές των κρυστάλλων του PEG. Αυτά τα επίπεδα οργάνωσης δεν είχαν παρατηρηθεί σε προηγούμενες μελέτες συμπολυμερών PEG-PBLG που παρασκευάστηκαν με άλλες μεθόδους. Επιπλέον, ο τύπος του μονομερούς NCA (BLG-NCA έναντι Leu-NCA) και η μέθοδος προετοιμασίας του διαλύματος επηρέασαν το βαθμό διαχωρισμού, το ποσοστό των α-ελίκων και τη θερμοκρασία μετάβασης τάξης-αταξίας στα συμπολυμερή PEG-*b*-PBLG και PEG-*b*-PLeu (PLeu: πολυ(L-λευκίνη)).

Συνολικά, η Διατριβή αποδεικνύει ότι η δευτεροταγής δομή διέπει την οργάνωση των πολυπεπτιδίων σε όλες τις κλίμακες μήκους. Στα ομοπολυπεπτίδια, τα β-φύλλα σχηματίζουν άκαμπτα, ανθεκτικά στην πίεση δίκτυα με χαμηλή ευθραυστότητα, παρουσιάζοντας μηχανικές ιδιότητες, κατάλληλα ως άκαμπτα βιοϊατρικά εμφυτεύματα. Αντίθετα, οι α-έλικες σχηματίζουν πιο εύκαμπτες μήτρες, ιδανικές για χρήση ως φορείς χορήγησης φαρμάκων. Στα συμπολυμερή, ο νέος τρόπος σύνθεσης (ROPISA) αξιοποιεί τις ίδιες δομές για τη δημιουργία ιεραρχικών επιπέδων, που μιμούνται την οργάνωση φυσικών πρωτεϊνών. Τα αποτελέσματα συμβάλλουν στο σχεδιασμό βιοϋλικών με ελεγχόμενες δομικές, δυναμικές και μηχανικές ιδιότητες, επιτυγχάνοντας ακρίβεια συγκρίσιμη με αυτή των πρωτεϊνών.

Table of contents

Chapter 1. Introduction

1.1 Proteins

Proteins are complex biological macromolecules that are essential for nearly every biological function of living organisms. They are composed of smaller units, called amino acids, that are linked together in long linear chains which fold into specific three-dimensional structures. Proteins perform a wide variety of diverse key functions, acting as building blocks, structural supports, enzymes, hormones, antibodies, receptors and transporters.[1,2] The sequence of amino acids, known as the *primary structure*, determines the physical and chemical properties of a protein. There are 20 amino acids that contain a central carbon atom (the α-carbon) that is attached to an amino group ($–NH_2$), a carboxyl group (–COOH), a hydrogen atom and a distinctive R group (side chain).[3,4] To form a protein, the carbon of the carboxyl groups and the nitrogen of the amino groups of each amino acid are linked by a covalent bond, forming a "peptide bond". Depending on the number of amino acids, molecules can be classified as oligopeptides (fewer than 20 amino acids), polypeptides, (up to 150 amino acid residues), or proteins (hundreds to thousands of amino acids).

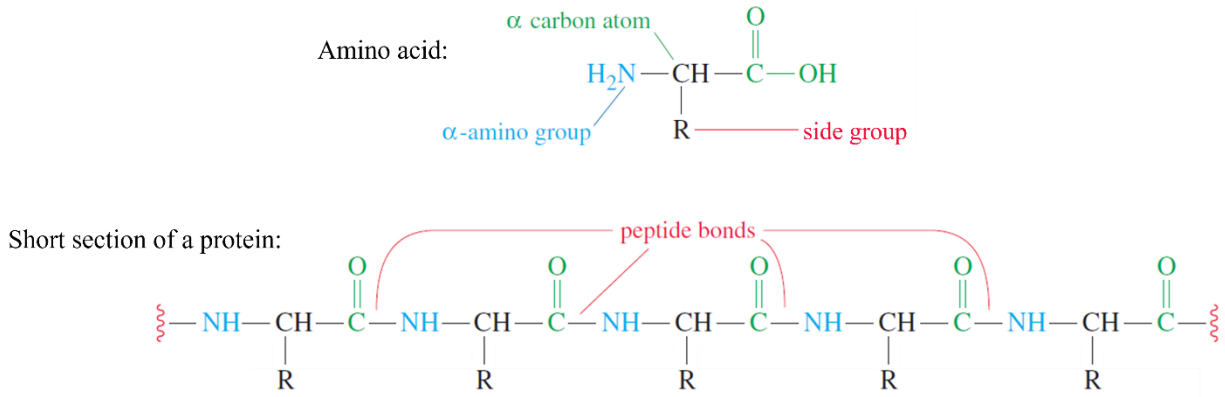

Figure 1.1. (above) Chemical structure of amino acids. (below) The sequence of a short section of a protein. [3]

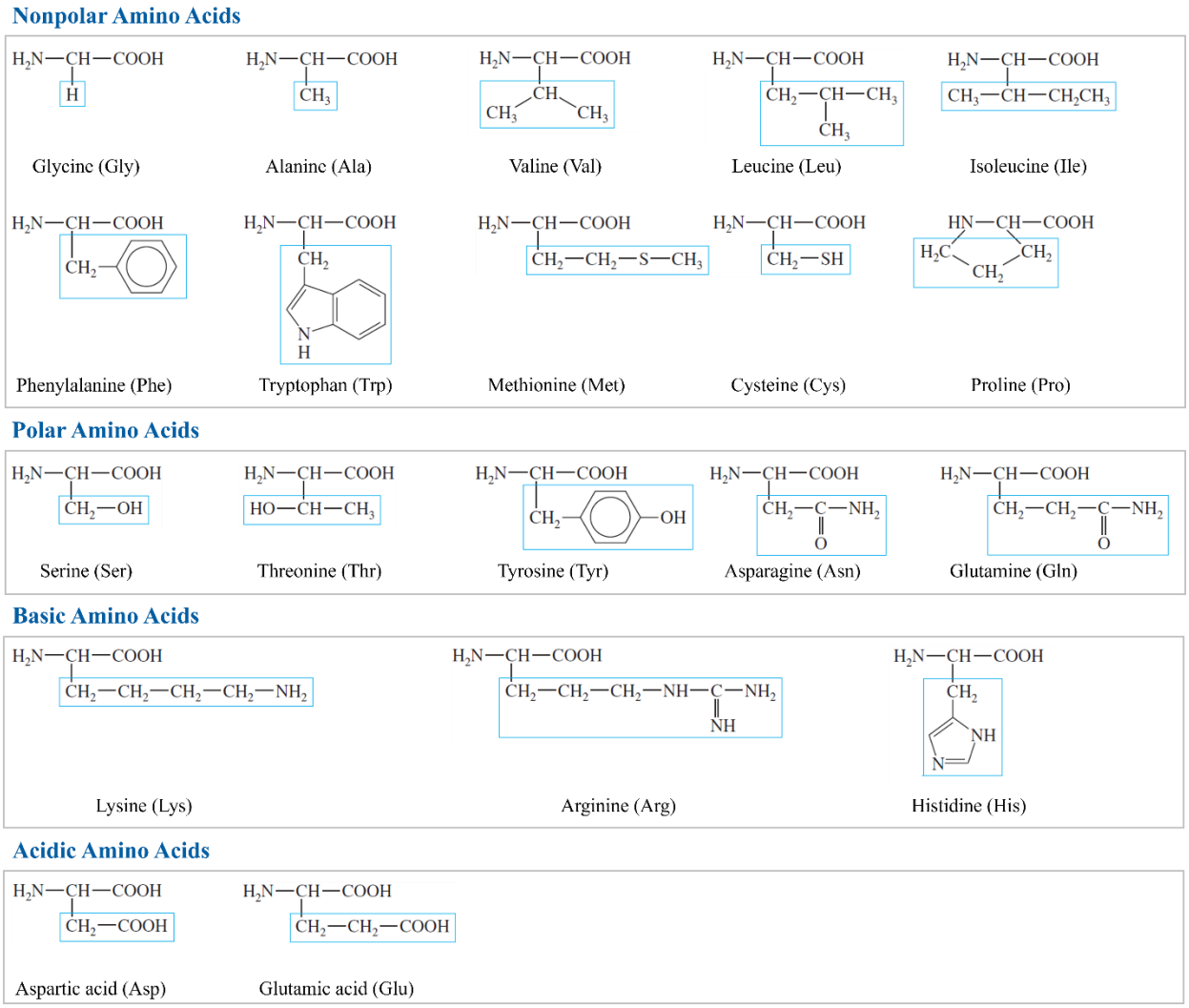

Figure 1.2. The 20 amino acids. Based on the properties of the side groups (polarity and charge), they are divided into four classes: nonpolar, polar, basic (positively charged) and acidic (negatively charged). Adapted from ref. [3].

As the chains fold, they tend to form localized spatial conformations through hydrogen bonding. This gives rise to a second level of structural organization, the *secondary structure*. These structures are stabilized by hydrogen bonds between the carboxyl oxygens of one amino acid and the amide hydrogens of another. The two most common secondary structures are the α-helix and the β-(pleated) sheet. An α-helix is usually a right-handed helical coil, stabilized by intramolecular hydrogen bonds, resulting in a rigid rodlike structure. In this configuration, the side groups are positioned on the outside of the helix. However, its precise geometry can vary depending on factors such as amino acid sequence, local interactions, and environmental conditions.[5,6] These variations result in the different types of α-helices observed in nature, each of which is tailored to the specific

structural and functional needs of the protein. The flexibility of the polypeptide backbone, combined with the unique properties of the side groups, allows for subtle adjustments in helical dimensions and hydrogen bonding patterns. This demonstrates the versatility of this fundamental structure. Conversely, β-sheets are formed by intermolecular hydrogen bonds, when polypeptide chain segments line up side by side. Each segment is fully extended and called a strand. β-sheets can be parallel (hydrogen bonds are aligned in the same direction), antiparallel (hydrogen bonds are aligned in opposite directions), or occasionally mixed. In addition to these structures, there are parts of the chains that have no ordered structure, called random coils. A protein can contain all different configurations along its entire length.

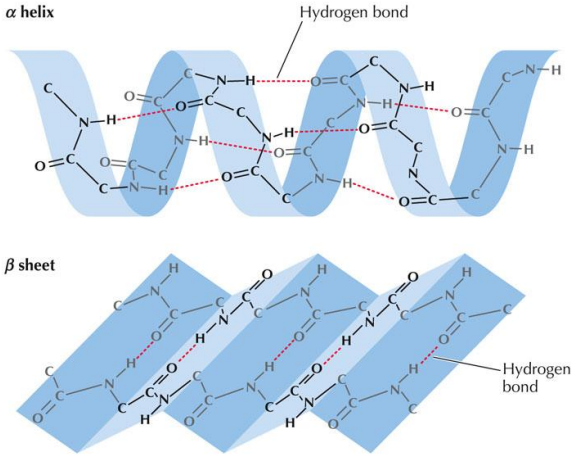

Figure 1.3. The α-helical (above) and β-sheet (below) conformations. The α-helix is stabilized by intramolecular hydrogen bonds, while the β-sheet is stabilized by intermolecular hydrogen bonds. (from *THE CELL, Fourth Edition*)

The dynamic nature of secondary structures, i.e., their ability to switch between different conformations in response to environmental stimuli, directly affects protein function. Often, α-helices and β-sheets form the core of globular proteins, providing the stability necessary to maintain their overall three-dimensional structure. Additionally, the specific arrangement of these structural elements can create binding sites for other molecules, catalytic sites for enzymes or ion transport channels. For example, α-helices in membrane proteins are usually found in the lipid bilayer, where they form pores or transport channels, a critical function in maintaining cellular homeostasis (Figure 1.4).[7,8] Furthermore, interactions with ligands, substrates, or other proteins often depend on the specific protein conformation. In this case, subtle changes in structure can significantly affect its specificity.

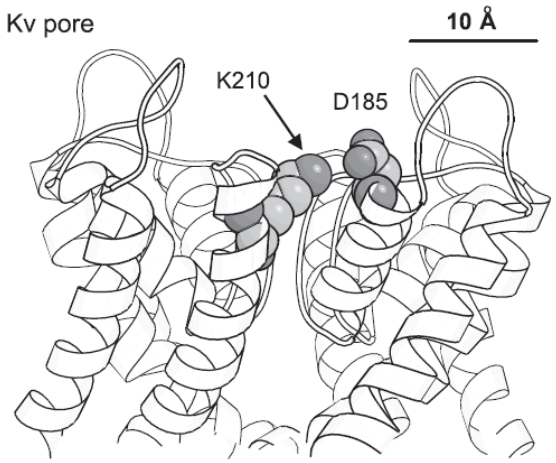

Figure 1.4. Helical structural model of the voltage-gated potassium (Kv) channel, a type of membrane protein that allows potassium ions (K^+) to pass through the cell membrane in response to changes in membrane voltage. K210 and D185 are amino acid residues (lysine and aspartic acid, respectively) within the protein structure. Their close positioning suggests an important stabilizing electrostatic interaction for the gating mechanism, which controls the flow of K^+ ions across the membrane and is essential for maintaining overall cellular homeostasis. [7]

The third level of protein organization is the *tertiary structure*. It refers to the unique three-dimensional conformation that a single globular protein can assume when it spontaneously folds into a more compact arrangement. The tertiary structure contains all the secondary structures, including the random coils, the kinks and folds. It is stabilized by the side-chain interactions, such as hydrophobic and hydrophilic interactions, electrostatic interactions, hydrogen bonds and covalent bonds.[9,10] A characteristic protein known for its well-defined tertiary structure is hemoglobin, which transports oxygen in the blood.[11] This precise folding allows hemoglobin to form pockets that bind heme groups, which are critical for oxygen binding and release. The tertiary structure, or the final protein conformation, is often referred to as the protein's physical state, as it regulates its biological function. Disruption or misfolding of this structure can lead to dysfunction and disease.[12-14]

Prion diseases are a compelling example of how protein misfolding can lead to pathological consequences.[15-18] The mechanisms of protein misfolding in prion diseases are deeply rooted in the structural transformation of the cellular prion protein (PrP). Under normal conditions, PrP exists in a conformation known as PrP^C, which is predominantly composed of α-helices. These helical structures provide stability and solubility, allowing PrP to perform its physiological functions, including cellular signaling and protection against oxidative stress. However, under certain pathological conditions, PrP^C undergoes a misfolding, shifting its tertiary structure from a configuration rich in α-helices (~ 40 % helical content and only 3% β-sheet content) to one dominated by β-sheets (~ 30 % α-helical content and ~ 45 % β-sheet content), known as PrP^{Sc} (Figure 1.5).[16] This new β-sheet-rich conformation alters the protein's physical and biochemical

properties, making it resistant to the cell's normal protein degradation mechanisms and prone to aggregation. These aggregates often adopt an amyloid structure, in which β-sheets are stacked in a highly organized, fibrillar arrangement. The latter is associated with the pathological features of prion diseases, as it disrupts normal cellular processes and causes neuronal toxicity.

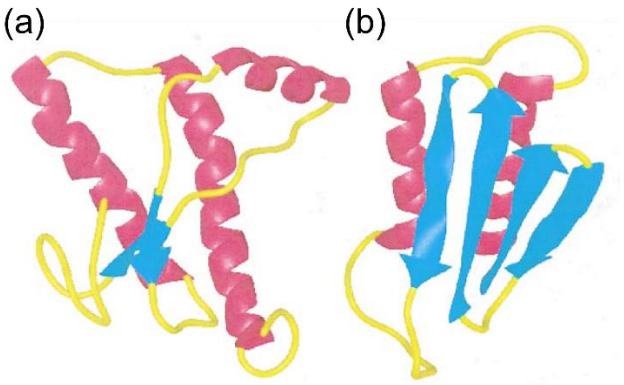

Figure 1.5. Schematic representation of (a) the structure of the normal prion protein (PrP^{C}), which is predominantly composed of α-helices, and (b) its pathogenic counterpart (PrP^{Sc}), in which β-sheets dominate. [16]

Prion diseases are unique in their infectious nature. Once formed, PrP^{Sc} acts as a template for misfolding. This process enables the pathogenic protein to propagate without the need for genetic material, such as DNA or RNA. Over time, misfolded PrP accumulates in the brain and forms amyloid fibrils, which are highly ordered aggregates that lead to widespread neuronal damage. Both Creutzfeldt-Jakob Disease (CJD) in humans and Bovine Spongiform Encephalopathy (BSE), or "mad cow disease" in cattle, are caused by misfolded prion proteins.[15,17] Such structural changes reflect a broader biological principle underlying many neurodegenerative disorders, including Alzheimer's and Parkinson's diseases, in which misfolded proteins, such as β-amyloid or α-synuclein, form toxic aggregates.

Proteins composed of two or more polypeptide chains can exhibit an additional level of organization known as *quaternary structure*. A quaternary structure is the three-dimensional arrangement of multiple polypeptides in a protein, each of which folds independently. Quaternary structure refers to how these multi-subunits cooperate and interact to form protein complexes that are stabilized by interactions similar to those in the tertiary structure. A classic example is hemoglobin, which consists of four polypeptide subunits that work together to transport oxygen in the blood (Figure 1.6).

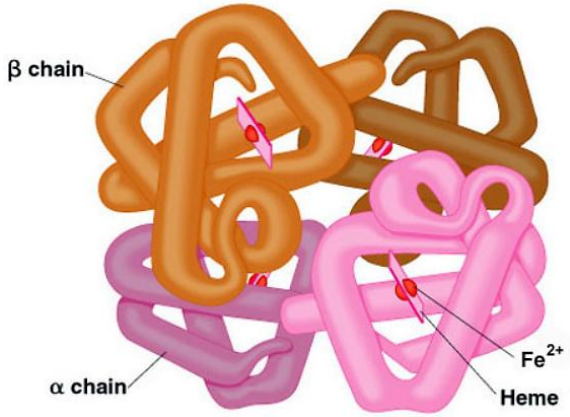

Figure 1.6. Schematic representation of the quaternary structure of hemoglobin, illustrating its four globin subunits (two α chains and two β chains) and their associated heme groups. Each heme group contains an Fe^{2+} ion, that binds oxygen reversibly in the heme group, enabling oxygen transport in blood. [From *The Medical Biochemistry Page*]

In addition to proteins with well-defined, stable three-dimensional structures, many proteins are partially or completely disordered. Intrinsically disordered proteins (IDPs) have recently gained attention due to their functional importance.[19] Unlike conventionally structured proteins, IDPs lack a stable three-dimensional structure and exist as dynamic conformational ensembles. IDPs exhibit remarkable flexibility and adaptability; they can bind to multiple partners and change their conformation to fit different targets.[20,21] Therefore, their structure and dynamics are both linked to their function. In this context, IDPs can form secondary structures, such as α-helices and β-sheets, upon interaction. These transitions, from disorder to order and vice versa, are essential for a wide range of cellular functions. For example, the p53 tumor suppressor protein adopts specific conformations when binding to DNA or regulatory proteins, thereby enabling its role in cell cycle control and apoptosis.[22] Another example is α-synuclein, a protein involved in synaptic vesicle regulation, that transitions from a disordered state to an ordered α-helical structure when binding to membranes.[23] Similarly, the transcriptional activator CREB (Cyclic AMP-Responsive Element-Binding Protein) forms structured regions upon interacting with cofactors, thereby facilitating its role in gene regulation.[22]

1.2 Folding dynamics

The diverse structural motifs of proteins – α-helices and β-sheets – achieve their functional roles through precisely orchestrated folding pathways. The previous section explained how these secondary structures organize into stable three-dimensional architectures. However, distinct kinetic principles govern their formation: the timescales, cooperativity, and energy landscapes that dictate how unstructured polypeptide chains fold into ordered conformations.

α-helices were among the first secondary structures studied in folding studies, largely due to their structural regularity and experimental accessibility. Their relatively simple topology, which is governed by local (i, i+4) hydrogen-bonding patterns, allows them to fold rapidly and cooperatively. This behavior contrasts with the more complex dynamics of β-sheets. Early theoretical work by Zimm and Bragg[24] formalized this behavior through the nucleation-propagation model, which remains fundamental to helix-coil transition theory (see Chapter 2 for details). These fast kinetics reflect the one-dimensional nature of helix formation. Nucleation, the rate-limiting step, involves stabilizing a critical cluster of three to four residues (~ 100 ns), followed by near-diffusion-limited elongation (~ 1 ns per residue) along the backbone.[25] As equilibrium studies of model peptides have demonstrated, the high cooperativity (nucleation parameter, $\sigma \approx 10^{-3}$-10^{-4}) arises from cumulative hydrogen-bond stabilization.[26]

Key experimental studies using laser-induced temperature-jump (*T*-jump) spectroscopy revealed that α-helix formation occurs on the timescale of nanosecond to microsecond. For example, Ballew et al.[27] and Gilmanshin et al.[28] found that helices in apomyoglobin form within 100-500 ns and fully propagate within ~ 1 μs. These findings have been complemented by computational studies: early simulations highlighted the importance of local conformational sampling and solvent conditions in modulating helix stability and kinetics.[29,30] These theoretical, experimental, and computational approaches have established α-helices as model systems for investigating the fundamental principles of protein folding.

Unlike the well-characterized dynamics of α-helices, the study of β-sheet folding dynamics presents considerable challenges, due to their inherent instability, low solubility, and strong propensity for aggregation. β-sheets require long-range interactions between residues that are far apart in the primary sequence. These interactions bring disparate chain segments into close spatial proximity. This process exhibits two-dimensional cooperativity – perpendicular and parallel to the strand direction (Figure 1.7).

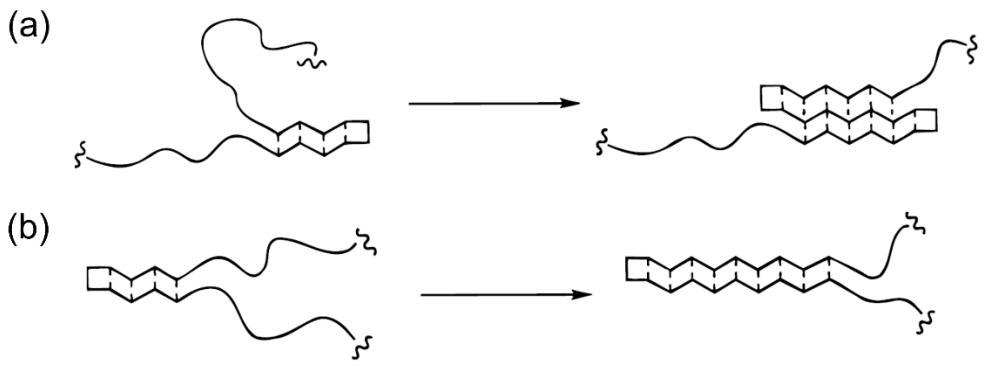

Figure 1.7. Schematic representation of the two propagation modes for a single-chain antiparallel β-sheet conformation: (a) perpendicular to the strand direction and (b) along the strand direction. [31]

Early theoretical explorations provided fundamental insights into β-sheet dynamics. Yapa et al.[32] used a simplified, coarse-grained polypeptide model, in which each amino acid residue was considered as a single quasiparticle, to study the β-sheet-coil transition via Brownian dynamics simulations in an implicit solvent. They found that relaxation times in β-sheet dynamics are significantly slower than atomic-scale fluctuations, with sheet-coil rate constants in the range of tens of ns^{-1}. This is attributed to the collective motions and extensive hydrogen bond rearrangements required. Notably, the sheet-coil transition rates were nearly uniform across all residues, suggesting minimal kinetic cooperativity ($\sigma \approx 1$). This contrast sharply with the highly cooperative kinetics ($\sigma \ll 1$) of α-helix nucleation.

Soon, experimental studies demonstrated that very short peptides (approximately 16 residues) could fold into stable β-hairpins (i.e., the minimal unit of a β-sheet consisting of two antiparallel β-strands connected by a short turn) in aqueous solution. This folding was driven solely by local sequence motifs and solvent conditions.[33,34] The findings revealed that minimal turns and hydrophobic interactions are sufficient to nucleate β-sheet formation, even without tertiary context. Subsequent work on designed β-sheet systems further elucidated the balance of forces governing stability. Turns or loops act as nucleation sites in hairpins. Larger sheets, however, depend on edge-protecting residues (e.g., charged residues) or tertiary contacts to prevent aggregation.[35]

Studies with double- and triple-stranded assemblies provided direct evidence for positive cooperativity in β-sheet propagation. Schenck and Gellman[31] found that a third strand bound more favorably to a preformed sheet, indicating that interstrand hydrogen bonding networks and

hydrophobic packing become increasingly favorable as the sheet expands. This cooperative behavior is similar to the nucleation-propagation mechanisms seen in amyloid fibril formation. It also highlights the dual nature of β-sheet cooperativity, natural protein folding versus pathological aggregation. Advances in *T*-jump spectroscopy provided sub-microsecond resolution of β-hairpin folding pathways. Muñoz et al.[36] observed that the 16-residue C-terminal hairpin of protein G folds via a highly cooperative, two-state mechanism in approximately 6 μs, which is among the fastest times recorded for a cooperative structural motif. Alba and co-workers[37] extended these kinetic measurements to a designed 20-residue, three-stranded β-sheet and reported similar folding timescales on the order of microseconds.

Complementary computational studies have reconciled these rapid, motif-level folding events with the broader energy landscape of protein folding. Lazaridis and Karplus[38] used unfolding simulations to demonstrate that folding proceeds along multiple, heterogeneous pathways funneling toward the native state, which is consistent with the energy landscape theory. They showed that β-hairpin folding involves early turn formation, hydrogen-bond zipping, and hydrophobic collapse.[39] This process passed through short-lived intermediates on a rugged but shallow landscape. These findings suggested that, although small β-motifs fold quickly and cooperatively, larger systems may experience kinetic traps driven by non-native interactions, which tend to become more significant as the folding complexity increases. Finally, comparative timescale analyses indicated that α-helix formation, such as four-turn helices, takes place in ~ 500 ns, much faster than β-sheet assembly, which takes ~ 10 μs. This difference reflects fundamental variations in topology and cooperativity.[40] These solutions studies converge on a unified picture: β-sheet formation is governed by the interplay of long-range hydrogen bonds, local turn propensity, hydrophobic packing, and rugged folding landscapes, yielding mechanically robust yet kinetically complex structures. Invariably, β-sheet formation is a slower process than α-helix formation.

The distinct folding behaviors of α-helices and β-sheets, which are rooted in their different topologies and timescales, demonstrate how secondary structure governs protein energy landscapes. The studies discussed here not only established core principles, but also paved the way for subsequent research into more complex dynamical regimes. These include coupled folding-binding processes and aggregation pathways, which further highlight the functional consequences of these structural motifs. For instance, the kinetic efficiency of α-helix formation supports roles

in dynamic processes such as signal transduction and ligand binding, where speed and reversibility are crucial. Conversely, the rugged energy landscape of β-sheets and their propensity for long-range interactions underpin their roles in structural scaffolds and amyloid fibrils, where stability and mechanical resistance are key features. Understanding how these folding dynamics emerged helps us appreciate their functional specialization in native and pathological contexts, a theme explored in the next section.

1.3 Functional roles of α-helices and β-sheets in proteins

The three-dimensional architecture of proteins is fundamentally governed by the interplay between α-helices and β-sheets, the two dominant secondary structures that dictate both the structural integrity and functional versatility of these biomacromolecules. These structural motifs are rarely found in isolation, but often work together to regulate protein stability, function, and dynamics. The complementary nature of these structures is evident in their distinct but synergistic roles: α-helices often provide mechanical flexibility and mediate dynamic processes such as allosteric regulation and membrane spanning, while β-sheets contribute to structural rigidity and facilitate the formation of extended binding surfaces.

This interplay of α-helices and β-sheets is demonstrated in α/β domains, where these elements alternate to form stable scaffolds. A classic example is the Rossmann fold (Figure 1.8),[41] a ubiquitous structural motif in NAD^+-binding proteins such as lactate dehydrogenase (an enzyme of the anaerobic metabolic pathway). In this fold, a central six-stranded parallel β-sheet is flanked by α-helices, creating a rigid yet dynamic core. The β-sheet provides a stable platform for cofactor binding, while the surrounding helices shield hydrophobic residues from solvent exposure, thereby enhancing thermodynamic stability.[42] This arrangement is not static; the hinge regions connecting helices and sheets exhibit conformational flexibility, allowing the structural adjustments required for substrate binding and catalysis.[43]

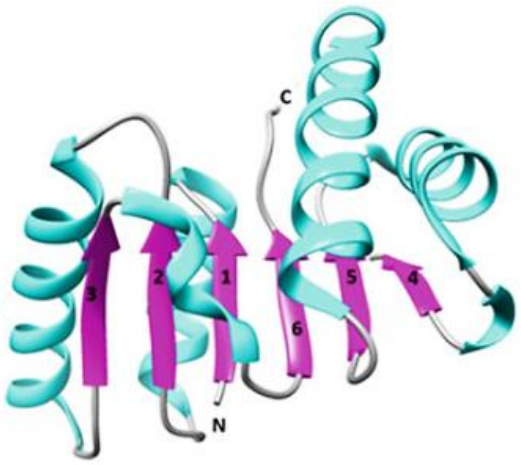

Figure 1.8. The characteristic Rossmann fold, composed of a six-stranded parallel β-sheet (magenta, numbered 1-6) and intervening α-helices (cyan). The six β-strands form a sheet in the order of 321456 counted, from the N-terminus to the C-terminus. [41]

To further illustrate this synergy, serine proteases (enzymes that cleave peptide bonds in proteins) rely on a β-barrel core (often two β-barrel domains) to provide structural stability, while adjacent helices precisely position (i.e., stabilize and orient) catalytic residues for efficient hydrolysis.[44] Upon substrate binding, subtle shifts in these helices optimize the active site geometry, demonstrating how helices fine-tune function within a β-sheet scaffold. Thus, most proteins combine α-helices and β-sheets to achieve optimal stability and more complex functions. However, some notable exceptions adopt structures composed entirely of one secondary structure.

Proteins composed entirely of β-sheets represent an important class of proteins that emphasize rigidity and the formation of extended interaction surfaces. The immunoglobulin superfamily is a prime example, where β-sheets arranged in a characteristic β-sandwich fold (Ig-fold) form the structural basis of antibody recognition (Figure 1.9a).[45] Each Ig domain consists of two antiparallel β-sheets packed against each other, with the hypervariable loops of antibody complementarity-determining regions (CDRs) emerging from the sheet termini to mediate antigen recognition.[46] The absence of α-helices in these domains is functionally critical: the all-β architecture provides exceptional mechanical stability, enabling antibodies to withstand the conformational stresses of immune complex formation while maintaining precise binding specificity. However, exceptions exist at domain boundaries. While individual immunoglobulin domains are all-β, multi-domain antibodies may contain helical linkers, illustrating how nature combines these motifs at higher levels of organizational.

Another example of all-β proteins are the transmembrane β-barrel proteins.[47] These proteins form cylindrical structures composed entirely of antiparallel β-strands, with each strand

connected by loops of varying lengths. A well-known example is bacterial porins, which form water-filled channels composed of 16 antiparallel β-strands arranged in a cylindrical barrel (Figure 1.9b). This β-barrel architecture is ideally suited for membrane environments, because the alternating hydrophobic and hydrophilic residues of the β-strands allow for stable integration into lipid bilayers while creating a hydrophilic pore for the transport of small solutes, including nutrients, ions, metabolites, and even certain antibiotics. This architecture is particularly advantageous for outer membrane proteins, as the extensive hydrogen bonding network provides exceptional stability in harsh extracellular environments, while maintaining conformational flexibility for solute transport.

While all-β architectures are characteristic of many membrane proteins (e.g., β-barrels), they also occur in soluble enzymes. A prominent example is neuraminidase from the influenza virus, a membrane-anchored enzyme, whose functional domain adopts a β-propeller fold. This distinct topology consists of six blade-like β-sheets arranged symmetrically around a central axis, with each blade consisting of four antiparallel β-strands.[48] The curved β-sheets of the propeller create well-defined catalytic sites for glycan cleavage, specifically targeting terminal sialic acid residues on the host cell glycans. This cleavage allows newly formed viral particles to detach after budding and spread to infect new cells.

At the extreme end of β-sheet organization are amyloid fibrils; highly ordered, unbranched filaments in which stacked β-sheets form rigid structures with mechanical strength comparable to steel.[49] In Alzheimer's disease, amyloid-β (Aβ) peptides transition from soluble, natively disordered monomers to insoluble cross-β assemblies, in which β-strands align perpendicular to the fibril axis (Figure 1.9c).[50] This structural arrangement forms a steric zipper motif, with interdigitated side chains forming dry, tightly packed interfaces, that provide exceptional stability.[51] The transition underscores the dual nature of β-sheet architectures: while their precise organization enables critical biological functions (e.g., mechanical strength of silk fibroin or antibody recognition), their dysregulated assembly into amyloid fibrils drives neurodegenerative pathologies.

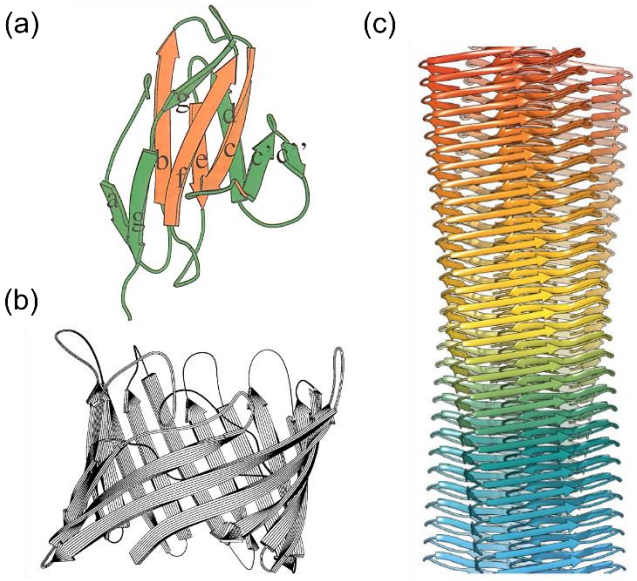

Figure 1.9. (a) The characteristic β-sandwich fold (Ig-fold) of immunoglobulin, with two antiparallel β-sheets packed against each other. [45] (b) The β-barrel structure of a bacterial porin, composed of 16 antiparallel β-strands. [47] (c) An atomic model of the cross-β structure, typical of amyloid fibrils, showing a highly ordered and repetitive stacking of β-strands along the fibril axis. [50]

In contrast to all-β proteins, all-α proteins specialize in flexibility and dynamic responses to cellular signals. The globin family, including myoglobin and hemoglobin, represents a classic example. The globin fold consists of eight α-helices arranged to form a hydrophobic pocket for heme binding (Figure1.10a).[52,53] The absence of β-sheets in these proteins is functionally critical; subtle helical motions upon oxygen binding mediate cooperative interactions between subunits,[54] a function that would be mechanically constrained by the rigid β-sheet structures.

Coiled-coil proteins, such as the leucine zipper family transcription factors, represent a major class of α-helical structures. These proteins assemble via two or more α-helices that supercoil around each other, with hydrophobic residues (often leucines) forming the interhelical interface (Figure 1.10b).[55,56] The all-α structure allows for remarkable conformational adaptability: helices can unwind under mechanical deformation, dissociate for DNA binding, or reassemble in response to post-translational modifications. This structural behavior is central to their roles in gene regulation and cytoskeletal organization. On the contrary, G protein-coupled receptors (GPCRs) demonstrate how all-α architectures excel at signal transduction across lipid bilayers. The seven-transmembrane α-helix bundle undergoes precise rearrangements upon ligand binding, with the helix 6 (H6) playing a critical role in G protein activation (Figure 1.10c).[57,58] The ability of α-helices to undergo torsional motions makes them uniquely suited for this mechanical signaling role.

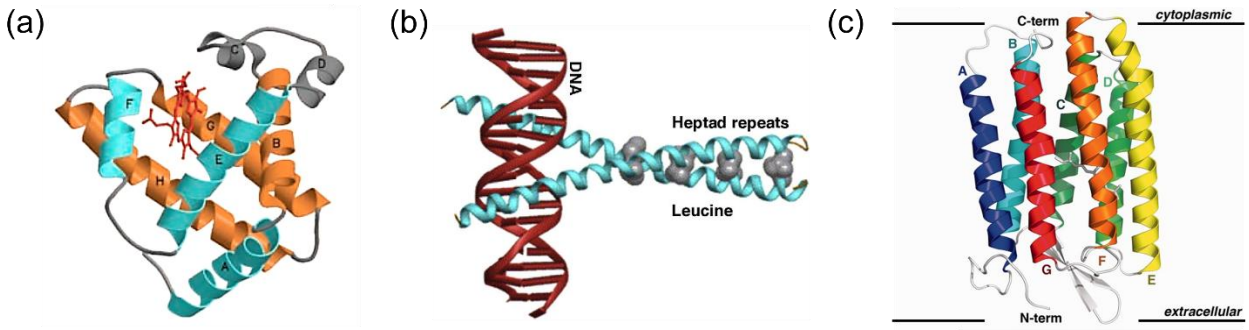

Figure 1.10. (a) The α-helical structure of myoglobin, the classical globin fold, with the heme group (in red) bound within the hydrophobic pocket. [52] (b) The leucine zipper, a coiled-coil protein, in a protein-DNA complex, illustrating its characteristic heptad repeats (blue) with leucine residues (grey) which facilitate protein dimerization and DNA binding. [56] (c) The seven-transmembrane α-helix bundle of bovine rhodopsin (seven α-helices labeled A-G) spanning the cellular membrane, typical of G protein-coupled receptors (GPCRs). The extracellular and cytoplasmic sides are indicated, showing the positions of the N-terminus and C-terminus. [58]

The distribution of all-α and all-β proteins in biological systems reflects important evolutionary adaptations. β-sheet-rich proteins dominate in extracellular environments (e.g., antibodies) or harsh conditions (e.g., bacterial outer membranes), where extreme stability is required. Conversely, α-helical proteins dominate where conformational flexibility and rapid dynamic responses are required, such as in intracellular signaling or oxygen transport. Advances in protein design have exploited these principles to create novel structures. Computational design has produced all-β "ideal proteins" with exceptional stability,[59] while de novo α-helical coiled coils serve as modular scaffolds for synthetic biology.[60] These achievements demonstrate how understanding nature's structural principles enables protein engineering.

Although rational design has yielded stable artificial proteins, a deeper understanding of folding principles has emerged from computational approaches leveraging artificial intelligence (AI). Recent breakthroughs in machine learning (ML), particularly deep neural network-based models like AlphaFold,[61] now allow for prediction of 3D protein structures with near-experimental accuracy directly from amino acid sequences. By integrating evolutionary constraints (i.e., which residues interact) with physical interactions (i.e., how residues interact), AlphaFold's attention mechanisms resolve long-range contacts critical for β-sheet arrangements and helix-helix packing, mirroring nature's solutions for stability and flexibility.[62] Similar tools, such as RoseTTAFold,[63] extend these capabilities to proteins lacking homologs, with broad implications for drug discovery and amyloid research. Yet, major challenges remain, including accurate modeling of

conformational dynamics, reliable prediction of multidomain proteins and protein-protein complexes, and elucidating protein folding pathways.[64] Future efforts combining neural-network-based predictions with physics-based simulations promise to provide functional annotations,[65] from catalytic residues to binding pockets, thereby further bridging the sequence-structure-function gap.

The intricate biological functions of proteins inherently rely on their dynamic flexibility. Even subtle interactions necessitate atomic-scale rearrangements. This functional plasticity stems from the unique capacity of proteins, as biological polymers, to exhibit hierarchical motions spanning vast time and length scales. These essential motions are thermally activated, making them temperature-dependent. This profound *T*-dependence becomes explicit at the glass temperature (T_g), where the protein's energy landscape shifts between two regimes: a low-temperature glassy state with restricted motions and a high-temperature functionally active state with enhanced conformational flexibility. The origin of this "transition" is the focus of the next section.

1.4 Origin of the protein liquid-to-glass "transition"

The discovery of the functional diversity of proteins made scientists realize that analyzing their dynamic conformational changes required more than just studying their static structures. This realization was underlined by early studies of myoglobin, one of the first proteins to have its three-dimensional structure determined by X-ray crystallography (Kendrew, 1958).[52] With a detailed structural model already available, myoglobin became an ideal candidate for studying protein dynamics.[66,67] In the years that followed, researchers identified significant changes in the dynamic behavior of proteins, such as a characteristic liquid-to-glass "transition". Most studies of protein dynamics have focused on α-helical proteins due to the structural simplicity and well-defined folding patterns of α-helices. However, studies have shown that dynamic transitions are evident despite the protein architecture, i.e., in mixed α/β proteins such as lysozyme or the ε-polylysine (ε-PLL) peptide, which will be discussed in this chapter.

One of the first studies of protein dynamics was carried out by Doster et al.,[68,69] who explored the behavior of hydrated myoglobin at temperatures ranging from 4 K to 350 K using inelastic neutron scattering. The results showed that the protein underwent a "transition" at 180 K (Figure 1.11a). An increase in the average mean-square displacement of hydrogen atoms was observed; from the vibrational motions characterized by a linear mean-square temperature

dependence, to a diffusive-like behavior (collective motions), more typical of dynamical systems. Therefore, two distinct conformational states were identified, a β-process and a α-process, distinguished by the shape of the data and their temperature dependence. The results were further supported by molecular dynamics simulations.[70] The so-called α-process resembled the glass "transition" observed in polymeric glasses. The authors also found that this "excited state" was hydration-dependent.

The same research was extended years later to Nitrophorin 4 (NP4), an almost pure β-sheet heme protein.[71] The goal was to determine if NP4 exhibited similar dynamic properties despite its different structural motif. Mössbauer spectroscopy measurements revealed mean square displacements in NP4 that were comparable to those observed in myoglobin. NP4 exhibited a similar "transition" around ~ 200 K. X-ray crystallography confirmed these findings. However, the slopes of the mean square displacements as a function of temperature were approximately 60 % larger for NP4 than for myoglobin. This discrepancy was attributed to the inherent differences in the time sensitivity between the two experimental techniques. Mössbauer spectroscopy captures rapid fluctuations by self-correlation on timescales faster than 140 ns. In contrast, X-ray crystallography, is sensitive to pair correlations and reflects both static disorder and slower structural rearrangements (integration over all frequencies). Regarding the similarity of protein motions above the characteristic temperature in both NP4 and myoglobin, the authors attributed this behavior to the strong coupling between protein-specific motions and the mobility of the hydration shell. It was proposed that the fluctuation of surface water enables NP4, despite its β-sheet architecture, to exhibit dynamic properties similar to those of the α-helical myoglobin.

In a follow-up study, Iben et al. used infrared (IR) spectroscopy to monitor carbonmonoxymyoglobin (MbCO) in a solvent environment as a function of temperature and pressure.[72] They observed the same "transition", now termed the "slaved glass transition" (T_{sg}) (Figure 1.11b) and supported their argument with DSC results (data not shown in the paper), claiming to detect two distinct glass temperatures, one for the solvent and one for the protein. The proximity of the two T_gs (i.e., $T_g^{solvent}$ = 175 K and $T_{sg}^{protein}$ = 178 K), and the same non-Arrhenius temperature dependence of the main relaxations, suggested that the protein dynamics was "slaved" to that of the solvent. This study was one of the first to introduce the term "slaving" to describe the coupling of the protein motions to the dynamic properties of the surrounding solvent. Subsequent

studies of various proteins, such as ribonuclease A, showed that, below this "transition", the protein loses its ability to bind to substrates, rendering it functionally inactive. At the same time, a similar dynamic behavior was observed in DNA.[73-76]

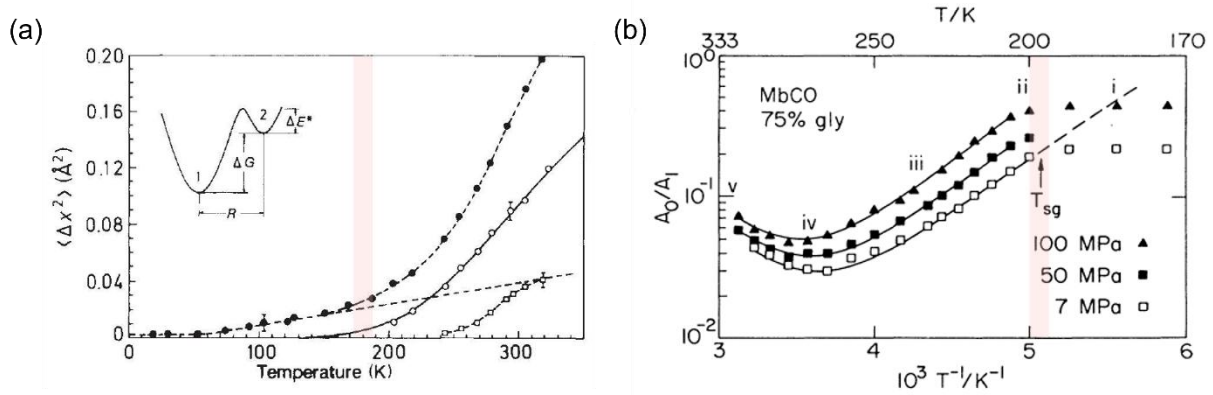

Figure 1.11. (a) Average mean-square hydrogen displacements of hydrated myoglobin as a function of temperature. Two contributions were identified. At low and intermediate *T*, vibrational contributions dominate, indicated by the dashed straight line (Debye-Waller factor). With increasing *T* (> 200 K), a deviation from the Debye-Waller behavior was observed, signaling a possible dynamic transition in the system. [68] (b) Ratio of the relative area of the infrared CO stretch band A_0 (A_0/A_1) in hydrated carbonmonoxymyoglobin (MbCO) as a function of temperature for three different pressures. The transition temperature, T_{sg}, indicates the onset of metastable behavior. [72]

Ongoing research into the protein "glass transition" led specific scientific groups to investigate the role of water at various hydration levels. Several studies,[77-80] using differential scanning calorimetry, have shown that proteins with low hydration exhibit a "glass transition" at temperatures between 300 – 400 K, whereas fully hydrated proteins at 180 – 220 K (Figure 1.12a). These results indicated that the "transition" was dependent on water content, a behavior expected if water acted as a plasticizer enhancing protein flexibility and conformational transitions to much lower temperatures (Figure 1.12b). The authors did not discuss the case of zero hydration, probably due to the view that bulk proteins were non-functional. However, a later study by Kurkal et al. demonstrated diffusive dynamics in enzymes in the absence of water.[81]

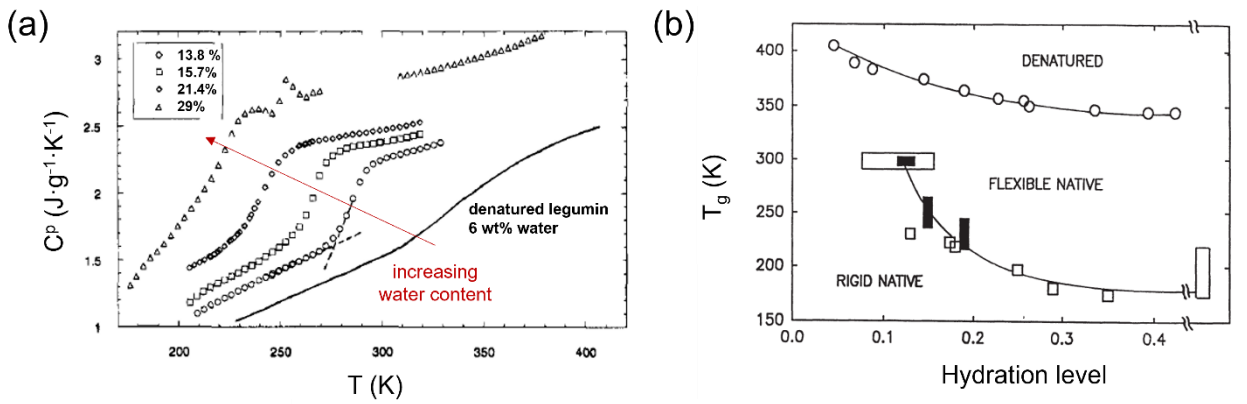

Figure 1.12. (a) Temperature dependence of the heat capacity of poly-L-asparagine/water solutions for four different water contents and denatured legumin in water. Note the protein "glass transition" temperature is decreasing with increasing water content. [78] (b) Hydration dependence of the "glass transition" temperature of lysozyme. The data show a decrease in T_g with increasing hydration. Note that the case of zero hydration is not included. [80]

To understand the origin of the "glass transition" and the role of the solvent environment on biological macromolecules, Karplus et al. conducted a molecular dynamic simulation study on myoglobin.[82] The authors investigated the protein "glass transition" by monitoring the protein fluctuations as a function of the protein and the solvent temperature. Their results showed that the global protein fluctuations were primarily governed by the solvent, as they were independent of the protein temperature (Figure 1.13). Additionally, the electrostatic and hydrogen bonding interactions between the water molecules and the protein were found to be responsible for their "freezing out" at low *T*. On the other hand, the local protein fluctuations were mainly determined by the intrinsic protein potential and atomic energy. Based on this result they suggested that proteins are analogous to glasses only at low temperatures; at high temperatures, the increase in protein fluctuations is caused by the increasing motions of the solvent rather than their increasing thermal energy.

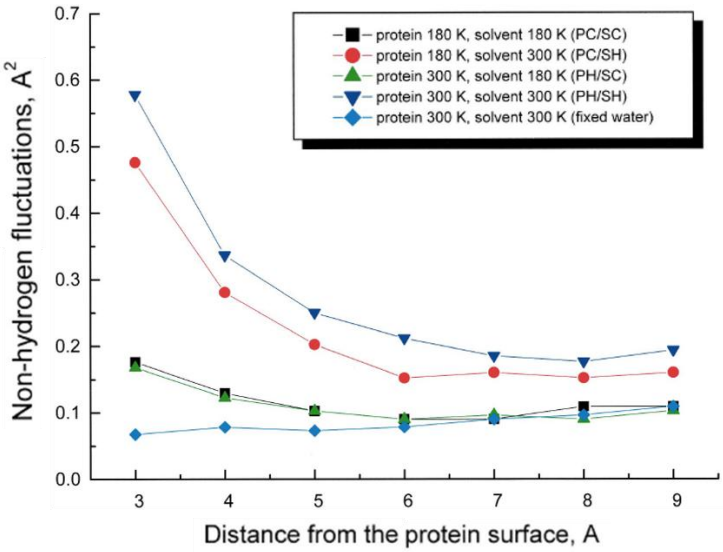

Figure 1.13. Mean-square fluctuations of the non-hydrogen myoglobin atoms as a function of the distance from the protein surface for different protein and solvent temperatures. An increase in the fluctuations was only observed when the solvent temperature was increased. [82]

Further pioneering work by Martin Karplus in molecular dynamics (MD) simulations revealed that proteins exist as dynamic ensembles of conformations rather than static structures. This fundamentally reshaped the understanding of biomolecular flexibility and function. In their 1977 *Nature* study,[83] Karplus, McCammon, and Gelin performed the first MD simulation of a folded protein, the bovine pancreatic trypsin inhibitor (BPTI), and showed that even well-structured proteins undergo structural atomic-level fluctuations at ordinary temperatures. The subsequent creation of the CHARMM (Chemistry at HARvard Molecular Mechanics) force field by Karplus's group provided a robust framework for simulating protein-solvent interactions and conformational dynamics.[84] For these and related contributions linking theoretical chemistry to biological applications, Karplus was awarded the 2013 Nobel Prize in Chemistry. He later expanded on these concepts in his reviews,[85,86] highlighting how MD simulations can capture biologically relevant timescales (e.g., motions and conformational changes in adenylate kinase), and emphasizing that functional mechanisms (e.g., enzyme catalysis) require an understanding of energy landscapes and solvent-coupled motions.

From then on, Frauenfelder and Fenimore focused on explaining slaving and the role of the hydration shell (the thin layer of water surrounding the protein) in proteins, publishing a series of studies.[87-89] They argued that hydration facilitates essential processes such as ligand binding and migration, whereas, on the contrary, dehydrated proteins were found to be essentially non-functional. The authors claimed that dehydration halts or significantly slows down the protein internal motions, but did not adequately support this argument. They also categorized the processes

found in the mixtures and proposed a unified model for protein dynamics. According to their findings,[90] large-scale protein motions are slaved to the α-fluctuations in the bulk solvent, i.e., are dependent on the presence of bulk-like water, while internal protein motions are slaved to the β-fluctuations of the hydration shell, i.e., are coupled to surface-bound water. In addition, they observed a critical temperature at ~ 200 K where these two processes cross.

In the following years, this crossover became the subject of intense study in protein/solvent mixtures.[91,92] In one of the first studies in 2006, Swenson et al. investigated the hydration water around proteins.[91] The results showed two distinct relaxation processes, one for the protein (myoglobin) and one for the solvent (water), both of which exhibited the same VFT *T*-dependence. Interestingly, the crossover was detected at about 180 K. The authors attributed this to the disappearance of the strong cooperative motions of the water (Figure 1.14). At this temperature, the dependence of the two processes changes to an Arrhenius dependence at lower temperatures. Although, no differential scanning calorimetry (DSC) results were presented, these observations led the authors to conclude that the solvent completely controls the protein dynamics and that only local protein motions can occur in the absence of an α-relaxation in the solvent. However, the results should have been treated more critically, particularly the claim of "slaving" between protein and water dynamics. The idea of a strong slaving effect is questionable when considering that the two processes differ in their time scales by two orders of magnitude.

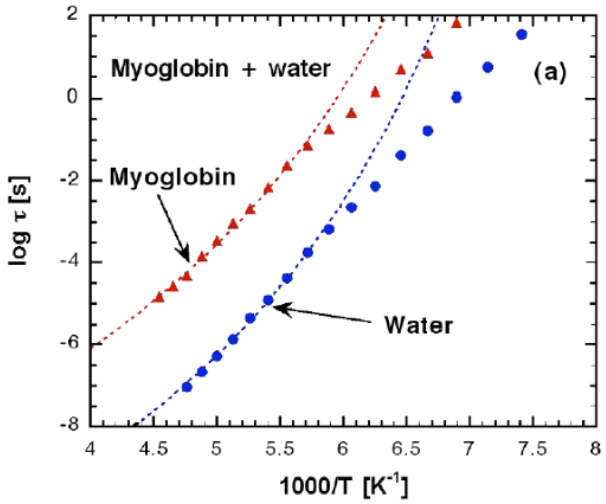

Figure 1.14. (a) Temperature dependence of the relaxation times for the two dielectric processes of hydrated myoglobin (0.8 g water per g protein). The blue symbols were assigned to the interfacial water dynamics, while the red symbols to the slaved protein dynamics. A crossover was detected at about 180 K, changing the temperature dependence of both processes, from an VFT to an Arrhenius behavior. [91]

Since then, several studies have identified up to four processes for protein/water (or protein/water-glycerol) mixtures, with up to five orders of magnitude difference from the solvent

dynamics. All of these processes were claimed to originate from the motions of the solvent.[92] Regarding the origin of the "glass transition" of the system, it was suggested, through comparisons between DSC and DS results, that the primary T_g is due to the freezing-in of the protein motions.[92,93] Notably, these studies on hydrated protein were published several years after seminal works on solvent-free polypeptides, which had already established T_g as an intrinsic feature of peptide dynamics (see Chapter 2 for details).[94,95] In cases where the calorimetric transition was asymmetric, i.e., in protein/water-glycerol mixtures (Figure 1.15),[93] researchers proposed that the solvent also contributes to the transition, which, according to authors, was not observed in protein/water mixtures. In a later study of lysine-water solutions, Swenson et al.[96] showed a well-defined step in the DSC results, with the data clearly suggesting that it is directly related to the "α-like" relaxation of the peptide lysine, as shown in Figure 1.16a. However, while the study primarily concerned the fast water dynamics, it did not address the concept of "solvent slaving".

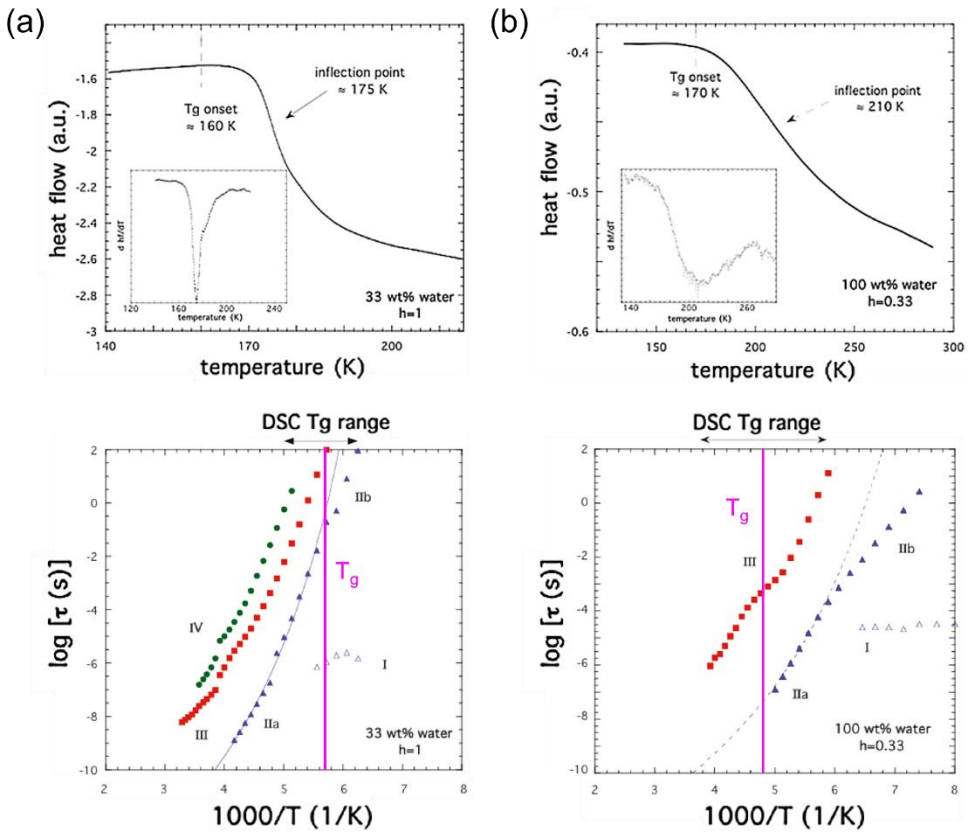

Figure 1.15. DSC traces (up) and relaxation times (down) as a function of temperature for (a) the myoglobin/water-glycerol mixture and (b) the myoglobin/water mixture. The magenta line indicates the glass temperature of the system. Processes I and II were attributed to the water dynamics, whereas III and IV to the slaved protein dynamics. [93]

In contrast, Cerveny et al. provided a more detailed analysis of the peptide-water solutions, focusing on the dynamics above T_g.[97] By keeping the water concentration constant (c_w = 40 wt%) and varying the peptide size, from oligopeptides to polypeptides, the study provided two important insights. First, the glass temperature of the system increased with increasing peptide molar mass (Figure 1.16b). This finding suggested that the T_g is intrinsically linked to the peptide, and not to the water. Again, this work was significantly later than the studies on the T_g of dry polypeptides.[94,95] Second, the observation that the peptide and the water relaxations (above T_g) share the same fragility parameters suggested an important influence of the surrounding water on the peptide, leading to the so-called "slaving" behavior. However, the two timescales differed by about two orders of magnitude. This means that the peptide conformational changes do not respond instantly to single water fluctuations. Instead, multiple water fluctuations occur before a single peptide undergoes a conformational transition, reinforcing the idea of a dynamic coupling rather than perfect ″synchronization″ between the two components. Thus, the term "slaving" describes a phenomenon in which the peptide relaxation times are influenced by the solvent dynamics, reflecting a dependence on the mobility of the surrounding water, rather than being strictly dictated by it.

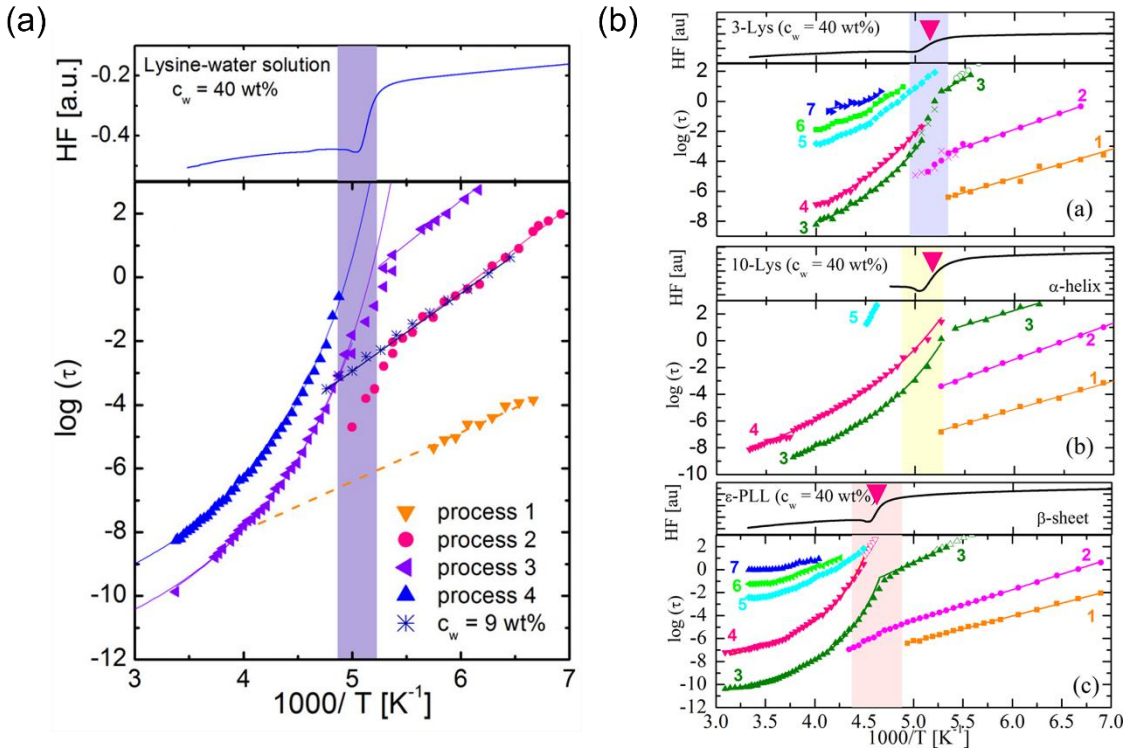

Figure 1.16. (a) (up) DSC trace of lysine-water solution (c_w = 40 wt%) and relaxation times (down) as a function of temperature for the same sample. Processes 1, 2, 3 were attributed to water dynamics, whereas process 4 indicates the "α-like" relaxation of lysine. Crossed symbols correspond to process 2 of hydrated lysine powder (c_w = 9 wt%), and are shown for comparison purposes only (not relevant to the present study). [96] (b) Arrhenius plots of (a) 3-lysine, (b) 10-lysine, and (c) ε-PLL (c_w = 40 wt% in all samples), with their corresponding DSC traces. Vertical colored lines show the width of the glass "transition", while arrows indicate the glass temperatures. [97]

An important observation from this study[97] was the influence, or lack thereof, of the secondary structure on peptide dynamics. Notably, ε-PLL was the only peptide examined (in the study) that exclusively adopted β-sheets. First, the "slaving" effect was found independent of the secondary structure, as it was present in all investigated peptides. Second, a glass temperature and a peptide-related α-relaxation was evident in all samples, again independent of the secondary structure. These findings suggested that the role of secondary structure in peptide glass temperature should be examined more thoroughly, which is one of the main scopes of this Thesis.

The work by Palacios et al. provided further understanding of the "slaving".[98] The authors examined the effects of different solvent concentrations, particularly in the low range, on water mixtures with a variety of solutes, including proteins and peptides. The results revealed a dual behavior of water depending on its content (Figure 1.17). At low water concentrations (< 15-20 wt%), the solvent acted as a plasticizer, lowering the glass temperature and the viscosity of the solute, compared to its bulk values. Under these conditions, the temperature dependence of the solute dynamics was independent of the solvent and no α-relaxation of the water was detected. At higher water concentrations, the results indicated a shift to the slaving behavior. This argument was supported by the same temperature dependence of the relaxation times of the two components, solute and solvent, implying a strong coupling. The authors proposed that the collective water motions were responsible for the global protein motions, making the "slaving effect" directly tied to the emergence of the slow coupled water-solute relaxation. Furthermore, the intrinsic dynamics of the solute also seemed to play a crucial role in this interaction, as the slaving behavior was inconsistent among different solutes. The dynamics of the slow water process was found to depend on the specific type of solute present, highlighting the complexity of these interactions. Additional annealing experiments above T_g revealed that partial ice formation has only a minor effect on the glass temperature, indicating that the dynamic crossover remains largely unaffected by the

presence of ice.[99] A certain hydration level, i.e., a certain level of cooperativity between the water molecules,[100] is required before peptide dynamics becomes "slaved" by water, meaning that slaving is a dynamic, hydration-dependent phenomenon.

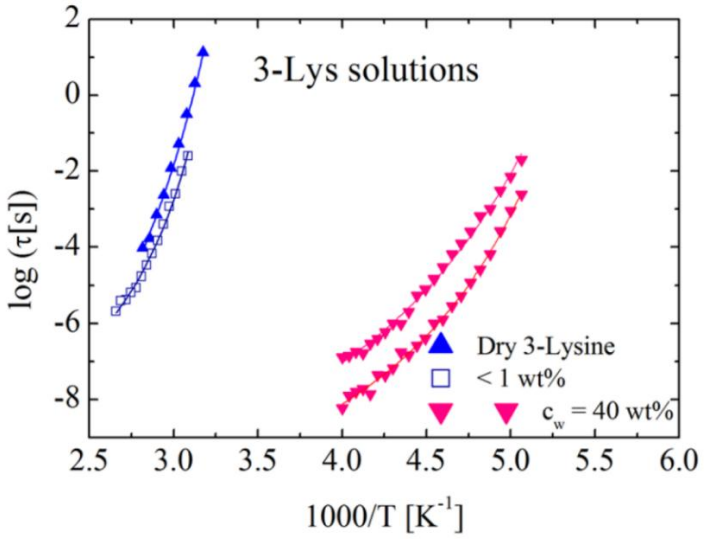

Figure 1.17. Relaxation times of the α-relaxation as a function of the inverse temperature. At low water content, the filled blue symbols are attributed to the α-relaxation of the dry 3-lysine, while the open blue symbols to the α-relaxation of the 3-lysine in a mixture with less than 1 wt% water. The magenta symbols show the α-related relaxations found in the mixture with a water concentration of 40 wt%. The faster one corresponds to the water relaxation, while the slower one to the slaved protein relaxation. [98]

From the detailed review of theoretical and experimental studies presented so far, it is now clear that nearly dry peptides, whether natural or synthetic, exhibit a liquid-to-glass "transition". In protein/water systems, however, the dynamics is more complex. The presence of hydration water appears to significantly modulate the peptide molecular mobility, leading to the so-called "slaving" of the peptide dynamics. However, the exact definition of "slaving" remains somewhat ambiguous. Although similarities in the temperature dependence of protein and solvent relaxations suggest dynamic coupling, the processes involved often differ in timescale by several orders of magnitude, while the hydration level strongly controls the extent of the effect.

1.4.1 The case of β-sheet proteins

The molecular origin of the liquid-to-glass "transition" in proteins has long been debated, but early studies established its presence in β-sheet-rich proteins. Magoshi and colleagues conducted a series of studies exploring the physical properties and structural transitions of silk fibroin from *Bombyx*

mori and *Antheraea pernyi* (tussah silk).[101-104] Using DSC and thermal expansion measurements, the authors suggested a glass temperature of approximately 175 °C in nearly – but not completely – dehydrated silk fibroin (Figure 1.18a). They attributed this T_g to random-coil configurations within the protein. However, the DSC traces showed the existence of water, with an endothermic peak at 100 °C indicating the water evaporation. Upon further heating above T_g, a cold crystallization was observed at around 200 °C in the DSC thermogram. This was interpreted as a transition from random-coil to the β-sheet secondary structure. Complementary evidence from X-ray, FTIR and DS supported this transition (Figure 1.18). They also extended their work to seed proteins, which exhibited similar thermal and structural behaviors, suggesting that glass formation and thermally induced ordering may be general features of globular and fibrous protein systems.[105]

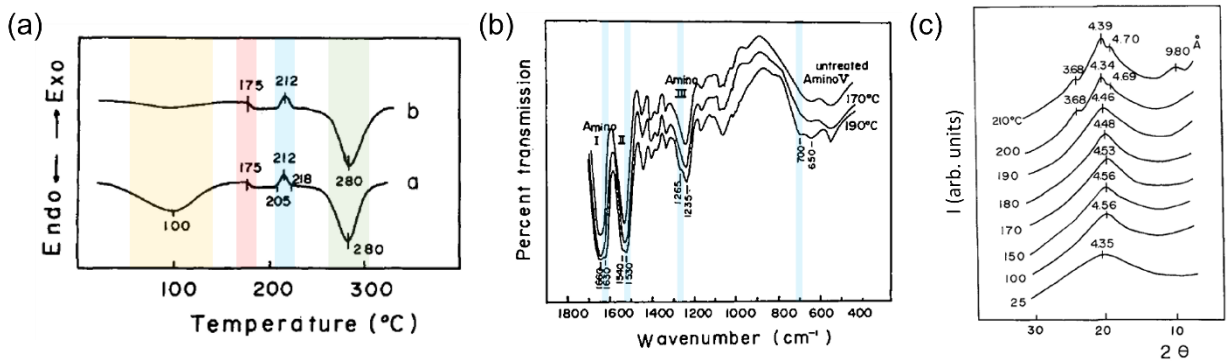

Figure 1.18. (a) DSC traces of amorphous silk fibroin (top) untreated and (bottom) after being kept in a desiccator containing silica gel for two weeks, obtained at a rate 8 K·min^{-1}. The different colors indicate the different thermodynamic events. Starting from lower temperatures: water evaporation (yellow), glass temperature (red), random-coil to β-sheet transition (blue), and degradation (green). [101] (b) FTIR spectra of (top) amorphous silk fibroin, and after heat-treated (middle) at 170 °C and (bottom) at 190 °C for 20 min. A comparison between the three reveals that only the sample treated at 190 °C exhibits amino bands indicative of a β-sheet structure. [102] (c) X-ray curves of silk fibroin at different temperatures. The main peak at low temperatures indicates the amorphous configurations, while the additional peaks at high temperatures, above 190 °C, reveal the formation of the β-sheet crystals. [104]

Further studies examined the influence of moisture content on the glass temperature of silk fibroin films using DSC.[106] Reference samples were dried at 150 °C for two hours under vacuum, producing films with presumed negligible residual moisture (though not analytically verified). The dried samples exhibited a thermal transition at ~ 180 °C, that posed interpretation challenges; while assigned to a "glass transition", the signal could also reflect some kind of melting (Figure 1.19). For the hydrated samples (despite unspecified thermal protocols), the results showed significant

water-induced plasticization, with the T_g decreasing progressively as hydration increased. Specifically, at 13 % relative humidity, T_g dropped by 40 °C compared to dry samples. At 75 % relative humidity, the reduction reached approximately 140 °C, shifting the transition from 180 °C to near ambient temperatures (Figure 1.19). The plasticization effect was found to be fully reversible upon drying, confirming water's transient role in disrupting the hydrogen-bonded network of the amorphous regions. These results highlighted how water content dynamically modulates the thermal properties of silk fibroin. However, the temperature scan ranges differed between the hydrated and dry samples. Therefore, it is not possible to observe the full thermal behavior of the hydrated samples within the temperature range where the dry-state T_g or the random-coil to β-sheet transition typically occurs.

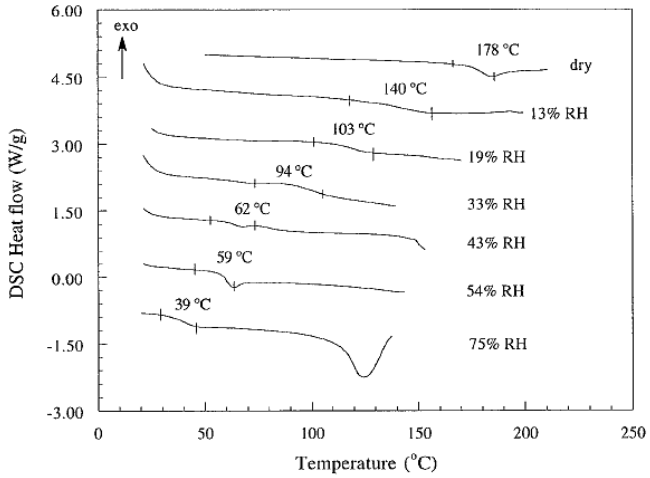

Figure 1.19. DSC traces of silk films with different relative humidity (RH) concentrations. The glass temperature is indicated for each sample. The endothermic peak at 75 % relative humidity indicates water evaporation. [106]

The Cebe group has extensively investigated the crystallization of β-sheets in silk fibroin and the influence of water on the β-sheet secondary structure, yielding important insights.[107] In an early study, they analyzed the heat capacity of isothermally crystallized samples using temperature modulated DSC (TM-DSC). They observed that crystallization suppressed the heat capacity increment at T_g, reflecting the loss of mobile, amorphous domains as β-sheet crystallinity increased (Figure 1.20). Based on these observations, they proposed a direct thermal method for quantifying β-sheet crystallinity (ϕ_C), and a two phase model (crystalline and amorphous regions only). The model was described by the equation $\Delta C_p = 0.475 - 0.494\phi_C$. These thermodynamic observations could be reinforced by using WAXS to quantify the degree of crystallinity statically through the β-sheet diffraction peaks, and by using DS to dynamically probe the relaxation of the remaining amorphous regions. Such a multimodal approach would cross-validate the TM-DSC

results, while determining how order (crystalline domains) affects local chain mobility and clarifying whether the reduced ΔC_p results solely from reduced amorphous regions or, in addition, from constrained dynamics in interfacial regions (i.e., restricted amorphous regions).

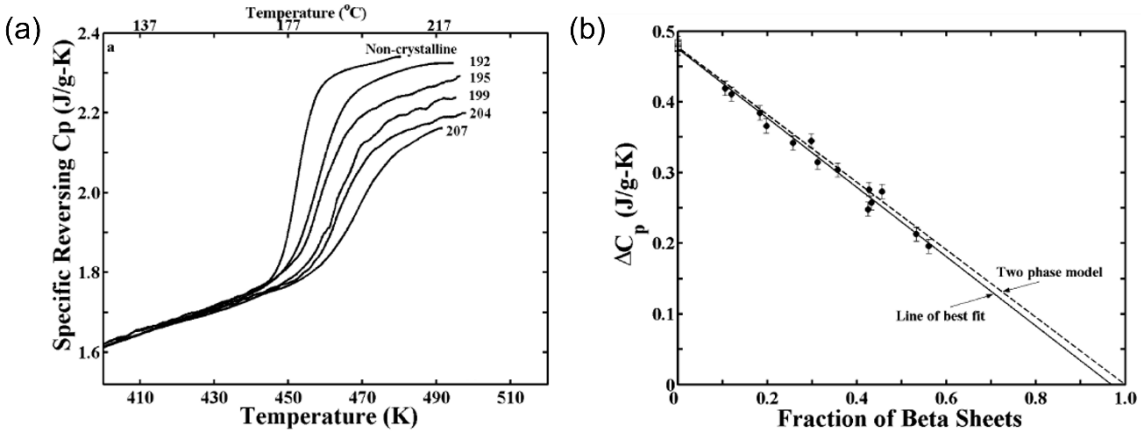

Figure 1.20. (a) Temperature dependence of the specific reversing heat capacity of silk fibroin at a rate of 2 °C·min^{-1}. The non-crystalline sample was scanned before the isothermal crystallization protocol, whereas the other samples were scanned after they had been isothermally crystallized at the respective temperatures. (b) Specific reversing heat capacity increment as a function of the β-sheet crystallinity. Filled and empty symbols represent the crystalline and noncrystalline samples, respectively. The solid line is a linear fit to the data. The dashed line represents the extrapolation of ΔC_p from a noncrystalline sample to a fully crystalline one (two phase model). [107]

In a follow-up study by the same group, silk fibroin samples containing 5.5 wt% bound water were analyzed again over a broad temperature range (from 170 K to 553 K).[108] The results revealed a more complex thermal behavior than had been previously observed (Figure 1.21a). At low temperatures, the hydrated samples exhibited a "glass transition" at around 353 K, which was attributed to a transient silk-water network. This was followed by a prominent endothermic peak corresponding to bound water evaporation. Following water removal during the DSC heating cycle (residual moisture may persist due the brief timescale and constrained sample environment of in-situ dehydration), a second "glass transition" – identical to that of (nearly) dry silk fibroin ($T_g \approx$ 451 K) – became apparent. The authors explained that bound water acted as a plasticizer, inducing a low-temperature T_g, which reverted to the native dry state upon dehydration. Complementary FTIR analysis during isothermal crystallization at 200 °C for 60 minutes revealed progressive structural reorganization (Figure 1.21b). In the amide I region, the researchers observed a clear transition from random coils and α-helices to β-pleated-sheet crystals. β-sheet absorbance bands increased, while random-coil and α-helix signals decreased, confirming β-sheet formation during

thermal treatment. The authors drew an analogy to Strobl's crystallization model for synthetic polymers, which posits an intermediate precursor phase before the three-dimensional crystalline lamellae. However, significant differences were noted. Silk fibroin's precursor structure formation critically depended on bound water, and its β-sheet crystals degrade before melting. This prevented the reversible melting-recrystallization behavior of thermoplastic polymers, demonstrating a distinctive feature of this natural biopolymer.

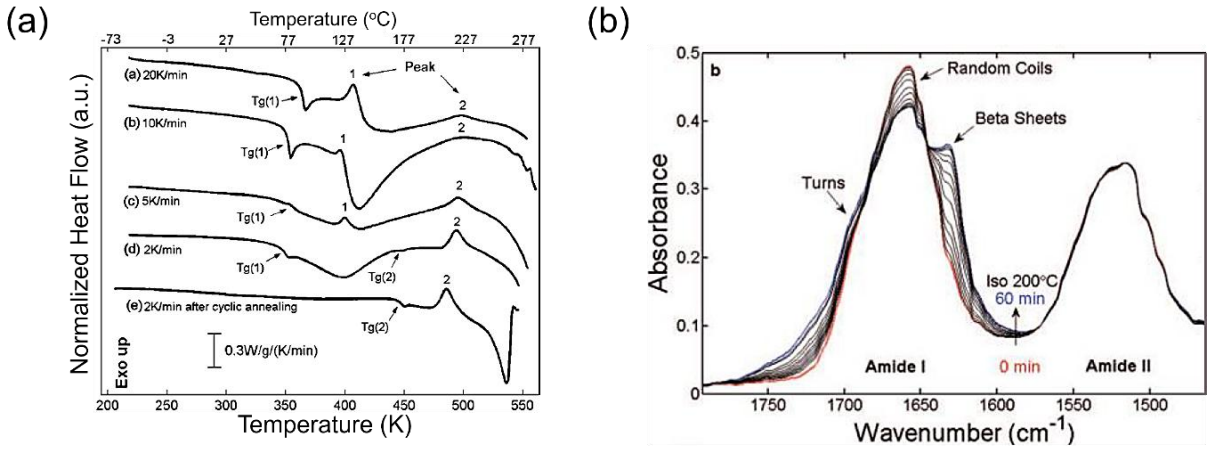

Figure 1.21. (a) DSC traces of silk fibroin films with different heating rates, as indicated. The samples (a) to (b) contain 5.5 wt% bound water, whereas sample (e) is in the dry state. $T_g(1)$ indicates the water-induced glass temperature. The large endothermic peak at about 130 °C corresponds to the water evaporation, whereas the exothermic peak (1) is also water-related. $T_g(2)$ corresponds to the (nearly) dry-state glass temperature and peak (2) indicates the random-coil to β-sheet transition. The endothermic peak around 260 °C indicates the degradation. (b) FTIR spectra of silk fibroin film during isothermal crystallization at 200 °C from 0 min (red) to 60 min (blue). The region from 1600 to 1640 cm^{-1} arises from the β-sheets, the region from 1640 to 1660 cm^{-1} includes contributions from random coils and α-helix structures, whereas the region from 1660 to 1690 cm^{-1} arises from the β-turns. [108]

In 2010, Yu et al. investigated the molecular dynamics of silk proteins using DS, comparing hydrated and dry systems.[109] For the hydrated samples, two distinct relaxation processes (β and α') were identified, both water-dependent as they disappeared upon dehydration. During isothermal crystallization experiments, the dielectric loss modulus (M'') revealed two high-temperature processes: conductivity effected and the α-relaxation, associated with the amorphous silk regions. Analysis of the relaxation dynamics showed that post-crystallization, the α-process exhibited slower kinetics and reduced dielectric strength, indicating either constrained mobility in the remaining amorphous domains or a decreased amorphous fraction. However, further analysis of

the α-process was precluded due to its overlap with conductivity contributions, limiting the in-depth characterization of the dynamics. Real-time DS monitoring of crystallization demonstrated progressive decrease in both the dielectric permittivity (ε') and conductivity (σ) under isothermal conditions. The most rapid changes occurred during the initial stages of crystallization, suggesting predominant β-sheet formation early in the process. The observed reduction in dielectric permittivity was attributed to a reduction in the number of effective dipole moments as α-helices (with net dipoles) "transitioned" into antiparallel β-sheets (with canceled dipole moments).

The research was later extended to recombinant spider silk-like block copolymers with 5 % bound water.[110] Through TM-DSC measurements (analyzing both total and reversing heat flow) and theoretical baseline modeling, the researchers again consistently observed two distinct glass temperatures in all of the studied protein-water systems (Figure 1.22). $T_g(1)$ was called a water-mediated T_g involving both bound water removal and a conformational change of the plasticized protein to a more compact structure. Further heating resulted in (in-situ) water removal, leaving the protein in its (nearly) dry state. $T_g(2)$ represented subsequent conformational changes from the "dry solid state" (between $T_g(1)$ and $T_g(2)$) to the "dry liquid state" (above $T_g(2)$) (Figure 1.23). In a complementary FTIR analysis,[111] the authors assigned $T_g(1)$ to a secondary-structure rearrangement from random-coil to β-turns (water-mediated), and $T_g(2)$ to an α-helix to β-turn transition.

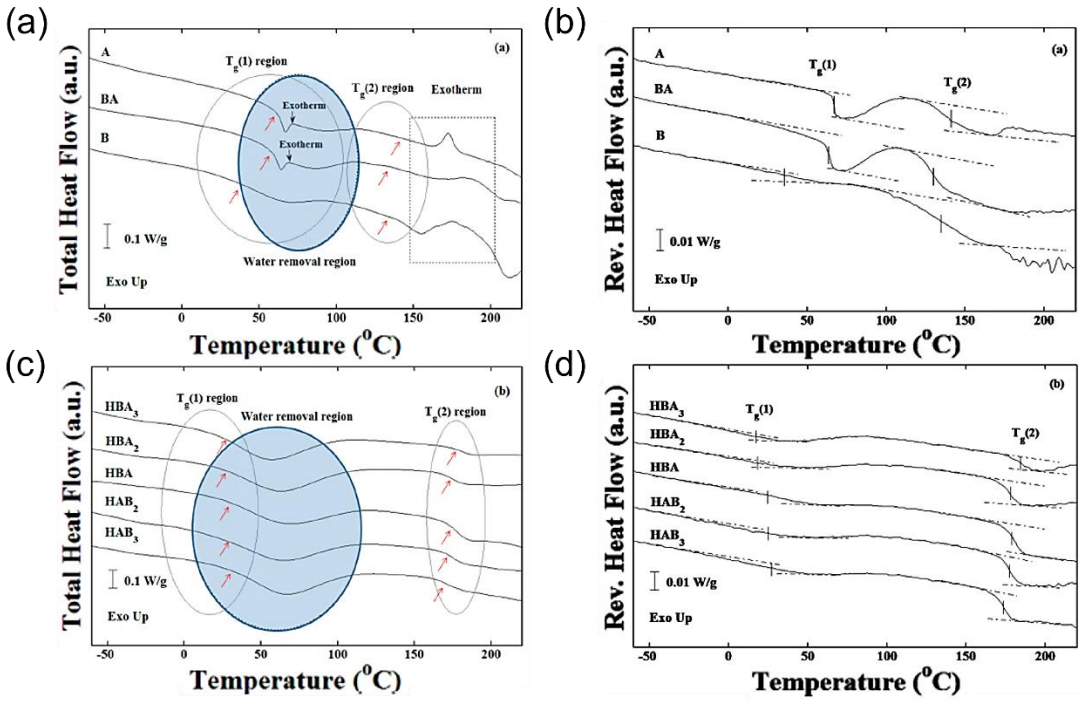

Figure 1.22. Temperature dependence of the (a), (c) total heat flow and (b), (d) reversing heat flow of recombinant spider silk-like block copolymers, obtained during the same heating at a rate 2 $K \cdot min^{-1}$ (modulation period of 60 s). Different names (i.e., A, BA, B, HBA_3, HBA_2, HBA, HAB_2, and HAB_3) were assigned according to the molar mass and the structure of the samples (see ref [100]). The two glass temperatures, $T_g(1)$ and $T_g(2)$, are indicated for each sample. Additional peaks are evident in the total heat flow: an exothermic peak assigned to the formation of a precursor state associated to with water removal, an endothermic peak assigned to the water removal, and at high T, an exothermic peak assigned to crystallization or crosslinking, depending on the sample. [110]

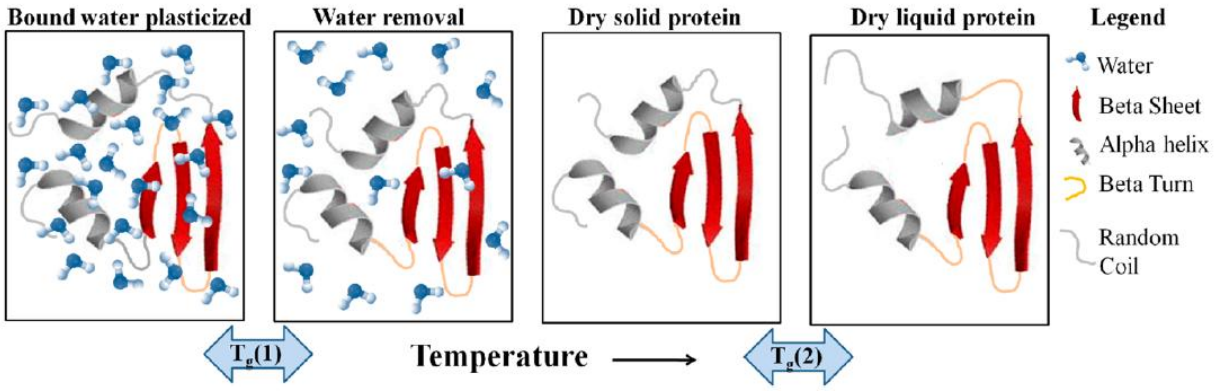

Figure 1.23. Schematic representation of the different states of the protein-water system as temperature increases. $T_g(1)$ was attributed to the bound water removal and to a conformational change of the plasticized protein to a more compact structure. $T_g(2)$ was assigned to the conformational changes from the dry solid state to the dry liquid state. [110]

Around the same time, another study[112] examined the macrodipole moments of polypeptides in β-sheet conformations, focusing on systems composed of glycine and alanine residues. Recognizing the importance of dipole-dipole interactions in protein structure and function, the authors developed a predictive model called VSHBβ (Vectorial Summation of Hydrogen-Bonded β-strands). The model estimates the macrodipole moment of a β-sheet by vectorially summing the dipole moments of individual amino acid residues, which are treated as building blocks, while accounting for their local hydrogen-bonding environment. The study systematically evaluated the dipole moments of both antiparallel and parallel β-sheets with varying numbers of amino acid residues and strands. Contrary to the prevailing assumption that the β-sheet macrodipole moments are negligible, due to the alternating residue orientations, the results showed that the macrodipole moment depends strongly on the number of strands, their length, and their arrangement (Figure 1.24). In antiparallel β-sheets, the dipole moments largely cancel out when an even number of strands are present. In contrast, parallel β-sheets exhibit significant macrodipole moments that scale with strand number and length. The predictions from the VSHBβ model showed excellent agreement with those obtained from *ab initio* molecular orbital (MO) calculations. Additionally, the model accurately predicted the direction of the macrodipole moment. The study also revealed that the dipole moment of an amino acid residue in a β-sheet is smaller than in an α-helix, suggesting weaker polarization in β-sheets due to interstrand hydrogen bonding compared to the more cooperative hydrogen bonding in α-helices.

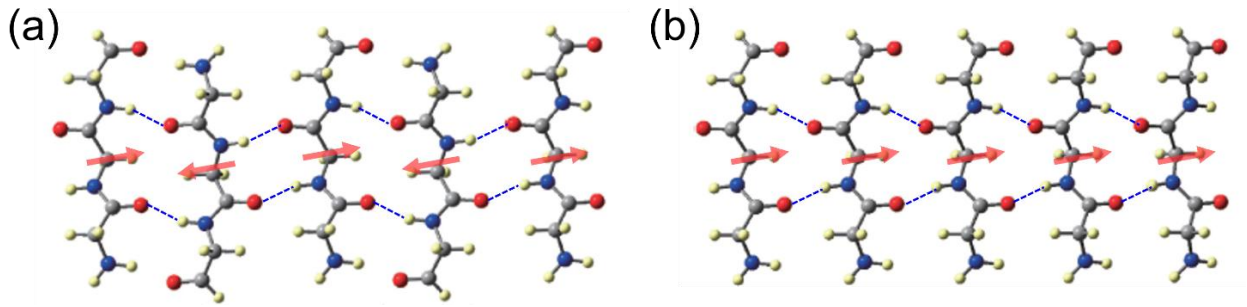

Figure 1.24. Geometries and dipole moment vectors of the central residues in (a) antiparallel and (b) parallel β-sheets of glycine. Each strand consists of three amino acids, while the β-sheet structures consist of five β-strands. Different colors indicate the different atoms: carbon (gray), nitrogen (blue), oxygen (red), hydrogen yellow. The hydrogen bonds are indicated with blue dashed lines. Red arrows indicate the axes of the central residue dipole moments. [112]

Literature studies have confirmed the presence of a liquid-to-glass "transition" in hydrated proteins with α-helical secondary structure. There are far fewer studies of the same "transition" in β-sheet forming proteins. Even so, complete de-hydration in proteins may be problematic. Hence, despite the significant advances in the study of α-helical and β-sheet proteins, fundamental questions remain unresolved regarding potential differences in their glass "transition" behavior. These secondary structures have distinct hydrogen bonding and packing self-assemblies that could result in different T_g characteristics and dynamic behavior, though this hypothesis remains untested. Additionally, the influence of thermodynamic parameters beyond temperature – particularly pressure – on these dynamic "transitions" remains largely unexplored. Resolving these questions requires a systematic investigation of model systems under controlled conditions and with several techniques probing the distinct (thermal-thermodynamic (TM-DSC), structural (X-rays), dynamical (NMR, DS) and viscoelastic (rheology)) features. Synthetic polypeptides, such as poly(γ-benzyl-L-glutamate) (PBLG), that can adopt both α-helical and β-sheet structures, offer particularly valuable insights for such comparative studies. The next chapter provides an overview of the self-assembly and dynamics of PBLG homopolypeptides and PBLG-based systems, that have been investigated thus far, establishing the framework for the experimental results that will be presented in the subsequent sections.

1.5 References

1. Parry, D. A. D.; Baker, E. N. Biopolymers. *Rep. Prog. Phys.* **1984**, *47*, 1133-1232.
2. Branden, C. I.; Tooze, J. *Introduction to Protein Structure* (2nd ed.). Garland Science. (**1998**).
3. Wade, L. G. Amino acids, peptides, and proteins. In *Organic chemistry*; Prentice Hall, **2010**.
4. McKee, T.; McKee, J. R. Amino Acids, Peptides, and Proteins. In *Biochemistry*; Oxford University Press, **2013**.
5. Pauling, L.; Corey, R. B.; Branson, H. R. The structure of proteins: two hydrogen-bonded helical configurations of the polypeptide chain. *Proc. Natl. Acad. Sci.* **1951**, *37*, 205-211.
6. Lupas, A. N.; Gruber, M., The structure of α-helical coiled coils. *Adv. Protein Chem.* **2005**, 70, 37-38.
7. Lee, A. How lipids affect the activities of integral membrane proteins. *Biochim. Biophys. Acta Biomembr.* **2004**, *1666*, 62-87.
8. White, S. H.; Wimley, W. C. Membrane Protein Folding and Stability: Physical Principles. *Annu. Rev. Biophys. Biomol. Struct.* **1999**, *28*, 319-365.
9. Dill, K. A.; Bromberg, S.; Yue, K.; Chan, H. S.; Ftebig, K. M.; Yee, D. P.; Thomas, P. D. Principles of protein folding - A perspective from simple exact models. *Protein Sci.* **2008**, *4*, 561-602.
10. Karplus, M.; Kuriyan, J. Molecular dynamics and protein function. *Proc. Natl. Acad. Sci.* **2005**, *102*, 6679-6685.
11. Weissbluth, M. Hemoglobin. In *Hemoglobin. Molecular Biology Biochemistry and Biophysics*, vol 15. Springer, Berlin, Heidelberg, **1974**.
12. Stefani, M.; Dobson, C. M. Protein aggregation and aggregate toxicity: new insights into protein folding, misfolding diseases and biological evolution. *J. Mol. Med.* **2003**, *81*, 678-699.
13. Chiti, F.; Dobson, C. M. Protein Misfolding, Functional Amyloid, and Human Disease. *Annu. Rev. Biochem.* **2006**, *75*, 333-366
14. Dobson, C. M. Protein misfolding, evolution and disease. *Trends Biochem. Sci.* **1999**, *24*, 329-332.
15. Prusiner, S. Molecular biology of prion diseases. *Science* **1991**, *252*, 1515-1522.
16. Pan, K. M.; Baldwin, M.; Nguyen, J.; Gasset, M.; Serban, A.; Groth, D.; Mehlhorn, I.; Huang, Z.; Fletterick, R. J.; Cohen, F. E.; Prusiner, S. B. Conversion of a-helices into b-sheets features in the formation of the scrapie prion proteins. *Proc. Natl Acad. Sci.* **1993**, *90*, 10962-10966.
17. Cohen, F. E. Protein misfolding and prion diseases. *J. Mol. Biol.* **1999**, *293*, 313-320.
18. Moore, R. A.; Taubner, L. M.; Priola, S. A. Prion protein misfolding and disease. *Curr. Opin. Struct. Biol.* **2009**, *19*, 14-22.
19. Oldfield, C. J.; Dunker, A. K. Intrinsically Disordered Proteins and Intrinsically Disordered Protein Regions. *Annu. Rev. Biochem.* **2014**, *83*, 553-584.
20. Wright, P. E.; Dyson, H. J. Intrinsically disordered proteins in cellular signalling and regulation. *Nat. Rev. Mol. Cell Biol.* **2015**, *16*, 18-29.
21. Uversky, V. N. Intrinsically Disordered Proteins and Their “Mysterious” (Meta) Physics. *Frontiers in Physics* **2019**, *7*, 1.

22. Wright, P. E.; Dyson, H. J. Intrinsically disordered proteins in cellular signalling and regulation. *Nat. Rev. Mol. Cell Biol.* **2015**, *16*, 18-29.
23. Heesink, G.; Marseille, M. J.; Fakhree, M. A. A.; Driver, M. D.; Leijenhorst-Groener, K. A.; Onck, P. R.; Blum, C.; Claessens, M. M. A. E. *Biomacromolecules* **2023**, *24*, 3680-3688.
24. Zimm, B. H.; Bragg, J. K. Theory of the Phase Transition between Helix and Random Coil in Polypeptide Chains. *J. Chem. Phys.* **1959**, *31*, 526-535.
25. McCammon, J.A.; Northrup, S.H.; Karplus, M.; Levy, R.M. Helix–coil transitions in a simple polypeptide model. *Biopolymers: Original Research on Biomolecules* **1980**, *19*, 2033-2045.
26. Muñoz, V.; Serrano, L. Elucidating the folding problem of helical peptides using empirical parameters. *Nat. Struct. Biol.* **1994**, *1*, 399-409.
27. Ballew, R.M.; Sabelko, J.; Gruebele, M. Direct observation of fast protein folding: the initial collapse of apomyoglobin. *Proc. Natl. Acad. Sci.* **1996**, *93*, 5759-5764.
28. Gilmanshin, R.; Williams, S.; Callender, R.H.; Woodruff, W.H; Dyer, R.B. Fast events in protein folding: relaxation dynamics of secondary and tertiary structure in native apomyoglobin. *Proc. Natl. Acad. Sci.* **1997**, *94*, 3709-3713.
29. Daggett, V.; Kollman, P.A.; Kuntz, I.D. A molecular dynamics simulation of polyalanine: an analysis of equilibrium motions and helix–coil transitions. *Biopolymers: Original Research on Biomolecules* **1991**, *31*, 1115-1134.
30. Daggett, V.; Levitt, M. Protein unfolding pathways explored through molecular dynamics simulations. *J. Mol. Biol.* **1993**, *232*, 600-619.
31. Schenck, H.L.; Gellman, S.H. Use of a designed triple-stranded antiparallel β-sheet to probe β-sheet cooperativity in aqueous solution. *J. Am. Chem. Soc.* **1998**, *120*, 4869-4870.
32. Yapa, K.;Weaver, D.L.; Karplus, M. β-Sheet coil transitions in a simple polypeptide model. *Proteins: Structure, Function, and Bioinformatics* **1992**, *12*, 237-265.
33. Blanco, F.J.; Rivas, G.; Serrano, L. A short linear peptide that folds into a native stable β-hairpin in aqueous solution. *Nat. Struct. Biol.* **1994**, *1*, 584-590.
34. Gellman, S.H. Minimal model systems for β-sheet secondary structure in proteins. *Current Opinion in Chemical Biology* **1998**, *2*, 717-725.
35. Nesloney, C.L.; Kelly, J.W. Progress towards understanding β-sheet structure. *Bioorganic & medicinal chemistry* **1996**, *4*, 739-766.
36. Munoz, V.; Thompson, P.A.; Hofrichter, J.; Eaton, W.A. Folding dynamics and mechanism of β-hairpin formation. *Nature* **1997**, *390*, 196-199.
37. de Alba, E.; Santoro, J.; Rico, M.; Jiménez, M.A. De novo design of a monomeric three-stranded antiparallel β-sheet. *Protein Science* **1999**, *8*, 854-865.
38. Lazaridis, T.; Karplus, M. "New view" of protein folding reconciled with the old through multiple unfolding simulations. *Science* **1997**, *278*, 1928-1931.
39. Dinner, A.R.; Lazaridis, T.; Karplus, M. Understanding β-hairpin formation. *Proc. Natl. Acad. Sci.* **1999**, *96*, 9068-9073.
40. Klimov, D.K.; Thirumalai, D. Viscosity dependence of the folding rates of proteins. *Phys. Rev. Lett.* **1997**, *79*, 317.

41. Shin, W.H.; Kihara, D. 55 Years of the Rossmann fold. "Protein Supersecondary Structures: Methods and Protocols", Humana Press, New York, **2019**.
42. Rao, S. T.; Rossmann, M. G. Comparison of super-secondary structures in proteins. *J. Mol. Biol.* **1973**, *76*, 241-256.
43. Gerstein, M.; Lesk, A. M.; Chothia, C. Structural mechanisms for domain movements in proteins. *Biochemistry* **1994**, *33*, 6739-6749.
44. Perona, J. J.; Craik, C. S. Structural basis of substrate specificity in the serine proteases. *Protein Science* **1995**, *4*, 337-360.
45. Bork, P.; Holm, L.; Sander, C. The immunoglobulin fold: structural classification, sequence patterns and common core. *J. Mol. Biol.* **1994**, *242*, 309-320.
46. Padlan, E. A. Anatomy of the antibody molecule. *Molecular immunology* **1994**, *31*, 169-217.
47. Schulz, G. E. The structure of bacterial outer membrane proteins. *Biochim. Biophys. Acta Biomembr.* **2002**, *1565*, 308-317.
48. Varghese, J. N.; Laver, W. G.; Colman, P. M. Structure of the influenza virus glycoprotein antigen neuraminidase at 2.9 Å resolution. *Nature* **1983**, *303*, 35-40.
49. Knowles, T. P.; Fitzpatrick, A. W.; Meehan, S.; Mott, H. R.; Vendruscolo, M.; Dobson, C. M.; Welland, M. E. Role of intermolecular forces in defining material properties of protein nanofibrils. *Science* **2007**, *318*, 1900-1903.
50. Gremer, L.; Schölzel, D.; Schenk, C.; Reinartz, E.; Labahn, J.; Ravelli, R. B.; Tusche, M.; Lopez-Iglesias, C.; Hoyer, W.; Heise, H.; Willbold, D. Fibril structure of amyloid-β (1–42) by cryo–electron microscopy. *Science* **2017**, *358*, 116-119.
51. Sawaya, M. R.; Sambashivan, S.; Nelson, R.; Ivanova, M. I.; Sievers, S. A.; Apostol, M. I.; Thompson, M. J.; Balbirnie, M.; Wiltzius, J. J.; McFarlane, H. T.; Madsen, A. Ø. Atomic structures of amyloid cross-β spines reveal varied steric zippers. *Nature* **2007**, *447*, 453-457.
52. Kendrew, J.C.; Bodo, G.; Dintzis, H.; Parrish, R.G., Wyckoff, H.; Phillips, D.C. A Three-Dimensional Model of the Myoglobin Molecule Obtained by X-Ray Analysis. *Nature* **1958**, *181*, 662-666.
53. Pesce, A.; Bolognesi, M.; Bocedi, A.; Ascenzi, P.; Dewilde, S.; Moens, L.; Hankeln, T.; Burmester, T. Neuroglobin and cytoglobin. *EMBO reports* **2002**, *3*, 1146-1151.
54. Perutz, M. F. Stereochemistry of cooperative effects in haemoglobin: haem–haem interaction and the problem of allostery. *Nature* **1970**, *228*, 726-734.
55. Harbury, P. B.; Zhang, T.; Kim, P. S.; Alber, T. A switch between two-, three-, and four-stranded coiled coils in GCN4 leucine zipper mutants. *Science* **1993**, *262*, 1401-1407.
56. Manna, P.R.; Dyson, M.T.; Stocco, D.M. Role of basic leucine zipper proteins in transcriptional regulation of the steroidogenic acute regulatory protein gene. *Mol. Cell. Endocrinol.* **2009**, *302*, 1-11.
57. Rasmussen, S. G.; DeVree, B. T.; Zou, Y.; Kruse, A. C.; Chung, K. Y.; Kobilka, T. S.; Thian, F. S.; Chae, P. S.; Pardon, E.; Calinski, D.; Mathiesen, J. M.; Shah, S. T. A.; Lyons, J. A.; Caffrey, M.; Gellman, S. H.; Steyaert, J.; Skiniotis, G.; Weis, W. I.; Sunahara, R. K.; Kobilka,

B. K. Crystal structure of the β_2 adrenergic receptor-Gs protein complex. *Nature* **2011**, *477*, 549-555.

58. Mackin, K.A.; Roy, R.A.; Theobald, D.L. An empirical test of convergent evolution in rhodopsins. *Mol. Biol. Evol.* **2014**, *31*, 85-95.
59. Koga, N.; Tatsumi-Koga, R.; Liu, G.; Xiao, R.; Acton, T. B.; Montelione, G. T.; Baker, D. Principles for designing ideal protein structures. *Nature* **2012**, *491*, 222-227.
60. Grigoryan, G.; DeGrado, W. F. Probing designability via a generalized model of helical bundle geometry. *J. Mol. Biol.* **2011**, *405*, 1079-1100.
61. Jumper, J; Evans, R.; Pritzel, A; Green, T.; Figurnov, M.; Ronneberger, O.; Tunyasuvunakool, K.; Bates, R.; Žídek, A.; Potapenko, A.; Bridgland, A.; Meyer, C.; Kohl, S.A.A.; Ballard, A.J.; Cowie, A.; Romera-Paredes, B.; Nikolov, S.; Jain, R.; Adler, J.; Back, T.; Petersen, S.; Reiman, D.; Clancy, E.; Zielinski, M.; Steinegger, M.; Pacholska, M.; Berghammer, T.; Bodenstein, S.; Silver, D.; Vinyals, O.; Senior, A.W.; Kavukcuoglu, K.; Kohli, P.; Hassabis, D. Highly accurate protein structure prediction with AlphaFold. *Nature* **2021**, *596*, 583-589.
62. Senior, A.W.; Evans, R.; Jumper, J.; Kirkpatrick, J.; Sifre, L.; Green, T.; Qin, C.; Žídek, A.; Nelson, A.W.R.; Bridgland, A.; Penedones, H.; Petersen, S.; Simonyan, K.; Crossan, S.; Kohli, P.; Jones, D.T.; Silver, D.; Kavukcuoglu, K.; Hassabis, D. Improved protein structure prediction using potentials from deep learning. *Nature* **2020**, *577*, 706-710.
63. Baek, M.; DiMaio, F.; Anishchenko, I.; Dauparas, J.; Ovchinnikov, S.; Lee, G.R.; Wang, J.; Cong, Q.; Kinch, L.N.; Schaeffe, R.D.; Millán, C.; Park, H.; Adams, C.; Glassman, C.R.; DeGiovanni, A.; Pereira, J.H.; Rodrigues, A.V.; van Dijk, A.A.; Ebrecht, A.C.; Opperman, D.J.; Sagmeister, T.; Buhlheller, C.; Pavkov-Keller, T.; Rathinaswamy, M.K.; Dalwadi, U.; Yip, C.K.; Burke, J.E.; Garcia, K.C.; Grishin, N.V.; Adams, P.D.; Read, R.J.; Baker, D. Accurate prediction of protein structures and interactions using a three-track neural network. *Science* **2021**, *373*, 871-876.
64. Peng, C.X.; Liang, F.; Xia, Y.H.; Zhao, K.L.; Hou, M.H.; Zhang, G.J. Recent advances and challenges in protein structure prediction. *J. Chem. Inf. Model.* **2024**, *64*, 76-95.
65. Gligorijević, V.; Renfrew, P.D.; Kosciolek, T. et al. Structure-based protein function prediction using graph convolutional networks. *Nat. Commun.* **2021**, *12*, 3168.
66. Karplus, M.; McCammon, J. A. The Dynamics of Proteins. *Sci. Am.* **1986**, *254*, 42-51.
67. McCammon, J. A. Protein dynamics. *Reports on Progress in Physics* **1984**, *47*, 1-46.
68. Doster, W.; Cusack, S.; Petry, W. Dynamical transition of myoglobin revealed by inelastic neutron scattering. *Nature* **1989**, *337*, 754-756.
69. Doster, W.; Cusack, S.; Petry, W. Structural dynamics of proteins, scaling behaviour and liquid glass transition. *J. Non-Cryst. Solids.* **1991**, *131*, 357-361.
70. Smith, J.; Kuczera, K.; Karplus, M. Dynamics of myoglobin: comparison of simulation results with neutron scattering spectra. *Proc. Natl. Acad. Sci.* **1990**, *87*, 1601-1605.
71. Schmidt, M.; Achterhold, K.; Prusakov, V.; Parak, F. G. Protein dynamics of a β-sheet protein. *Eur. Biophys. J.* **2009**, *38*, 687-700.

72. Iben, I. E. T.; Braunstein, D.; Doster, W.; Frauenfelder, H.; Hong, M. K.; Johnson, J. B.; Luck. S.; Ormos, P.; Schulte, A.; Steinback, P. J.; Xie, A. H.; Young, R. D. Glassy behavior of a protein. *Phys. Rev. Lett.* **1989**, *62*, 1916-1919.
73. Rasmussen, B. F.; Stock, A. M.; Ringe, D.; Petsko, G. A. Crystalline ribonuclease A loses function below the dynamical transition at 220 K. *Nature* **1992**, *357*, 423-424.
74. Norberg, J.; Nilsson, L. Glass transition in DNA from molecular dynamics simulations. *Proc. Natl. Acad. Sci.* **1996**, *93*, 10173-10176.
75. Laudát, J.; Laudát, F. Indications of Glass Transition in DNA. *Europhys. Lett.* **1992**, *20*, 663-667.
76. Careri, G.; Consolini, G.; Bruni, F. Proton tunneling in hydrated biological tissues near 200 K. *Biophys. Chem.* **1990**, *37*, 165-170.
77. Doster, W.; Bachleitner, A.; Dunau, R.; Hiebl, M.; Lüscher, E. Thermal properties of water in myoglobin crystals and solutions at subzero temperatures. *Biophys. J.* **1986**, *50*, 213-219.
78. Green, J. L.; Fan, J.; Angell, C. A. The protein-glass analogy: New insight from homopeptide comparisons. *J. Phys. Chem.* **1994**, *98*, 13780-13790.
79. Rupley, J. A.; Careri, G. Protein Hydration and Function. *Adv. Protein Chem.* **1991**, *41*, 37-172.
80. Gregory, RB. Protein hydration and glass transition behavior. In *Protein-Solvent Interactions*, ed. RB. Gregory, Marcel Dekker, New York, **1995**.
81. Kurkal, V.; Daniel, R. M.; Finney, J. L.; Tehei, M.; Dunn, R. V.; Smith, J. C. Enzyme Activity and Flexibility at Very Low Hydration. *Biophys. J.* **2005**, *89*, 1282-1287.
82. Vitkup, D.; Ringe, D.; Petsko, G. A.; Karplus, M. Solvent Mobility and the Protein 'Glass' Transition. *Nat. Struct. Biol.* **2000**, *7*, 34-38.
83. Karplus, M.; McCammon, J. A. Molecular dynamics simulations of biomolecules. *Nat. Struct. Biol.* **2002**, *9*, 646-652.
84. Brooks, B. R.; Bruccoleri, R. E.; Olafson, B. D.; States, D. J.; Swaminathan, S. A.; Karplus, M. CHARMM: a program for macromolecular energy, minimization, and dynamics calculations. *J. Comput. Chem.* **1983**, *4*, 187-217.
85. Karplus, M.; Kuriyan, J. Molecular dynamics and protein function. *Proc. Natl. Acad. Sci.* **2005**, *102*, 6679-6685.
86. McCammon, J., Gelin, B.; Karplus, M. Dynamics of folded proteins. *Nature* **1977**, *267*, 585-590.
87. Frauenfelder, H.; Fenimore, P.; McMahon, B. H. Hydration, slaving and protein function. *Biophys. Chem.* **2002**, *98*, 35-48.
88. Fenimore, P. W.; Frauenfelder, H.; McMahon, B. H.; Parak, F. G. Slaving: Solvent fluctuations dominate protein dynamics and functions. *Proc. Natl. Acad. Sci.* **2002**, *99*, 16047-16051.
89. Fenimore, P. W.; Frauenfelder, H.; McMahon, B. H.; Young, R. D. Bulk-solvent and hydration-shell fluctuations, similar to α - and β -fluctuations in glasses, control protein motions and functions. *Proc. Natl. Acad. Sci.* **2004**, *101*, 14408-14413.

90. Frauenfelder, H.; Chen, G.; Berendzen, J.; Fenimore, P. W.; Jansson, H.; McMahon, B. H.; Stroe, I. R.; Swenson, J.; Young, R. D. A unified model of protein dynamics. *Proc. Natl. Acad. Sci.* **2009**, *106*, 5129-5134.
91. Swenson, J.; Jansson, H.; Bergman, R. Relaxation Processes in Supercooled Confined Water and Implications for Protein Dynamics. *Phys. Rev. Lett.* **2006**, *96*, 247802.
92. Jansson, H.; Swenson, J. The protein glass transition as measured by dielectric spectroscopy and differential scanning calorimetry. *Biochim. Biophys. Acta Proteins Proteomics* **2010**, *1804*, 20-26.
93. Jansson, H.; Bergman, R.; Swenson, J. Role of Solvent for the Dynamics and the Glass Transition of Proteins. *J. Phys. Chem. B* **2011**, *115*, 4099-4109.
94. Papadopoulos, P.; Floudas, G.; Klok, H.-A.; Schnell, I.; Pakula, T. Self-Assembly and Dynamics of Poly(γ-benzyl-L-glutamate) Peptides. *Biomacromolecules* **2004**, *5*, 81.
95. Papadopoulos, P.; Floudas, G.; Schnell, I.; Klok, H.-A.; Aliferis, T.; Iatrou. H.; Hadjichristidis, N. "Glass transition" in peptides: Temperature and pressure effects. *J. Chem. Phys.* **2005**, *122*, 224906.
96. Swenson, J.; Cerveny, S. Dynamics of deeply supercooled interfacial water. *J. Phys.: Condens. Matter* **2014**, *27*, 033102.
97. Cerveny, S.; Combarro-Palacios, I.; Swenson, J. Evidence of Coupling between the Motions of Water and Peptides. *J. Phys. Chem. Lett.* **2016**, *7*, 4093-4098.
98. Combarro-Palacios, I.; Olsson, C.; Kamma-Lorger, C. S.; Swenson, J.; Cerveny, S. Motions of water and solutes—Slaving versus plasticization phenomena. *J. Chem. Phys.* **2019**, *150*, 124902.
99. Melillo, J.H.; Swenson, J.; Cerveny, S. Influence of ice formation on the dynamic and thermodynamic properties of aqueous solutions. *Journal of Molecular Liquids* **2022**, *356*, 119039.
100. Cerveny, S.; Swenson, J. Water dynamics in the hydration shells of biological and non-biological polymers. *J. Chem. Phys.* **2019**, *150*, 234904.
101. Magoshi, J.; Nakamura, S. Studies on physical properties and structure of silk. Glass transition and crystallization of silk fibroin. *J. Appl. Polym. Sci.* **1975**, *19*, 1013-1015.
102. Magoshi, J.; Magoshi, Y. Physical properties and structure of silk. II. Dynamic mechanical and dielectric properties of silk fibroin. *J. Polym. Sci. Polym. Phys. Ed.* **1975**, *13*, 1347-1351.
103. Magoshi, J.; Magoshi, Y.; Nakamura, S. Physical properties and structure of silk. III. The glass transition and conformational changes of tussah silk fibroin. *J. Appl. Polym. Sci.* **1977**, *21*, 2405-2407.
104. Magoshi, J.; Magoshi, Y.; Nakamura, S.; Kasai, N.; Kakudo, M. Physical properties and structure of silk. V. Thermal behavior of silk fibroin in the random-coil conformation. *J. Polym. Sci. Polym. Phys. Ed.* **1977**, *15*, 1675-1683.
105. Magoshi, J.; Nakamura, S.; Murakami, K.I. Structure and physical properties of seed proteins. I. Glass transition and crystallization of zein protein from corn. *J. Appl. Polym. Sci.* **1992**, *45*, 2043-2048.

106. Agarwal, N.; Hoagland, D.A.; Farris, R.J. Effect of moisture absorption on the thermal properties of Bombyx mori silk fibroin films. *J. Appl. Polym. Sci.* **1997**, *63*, .401-410.
107. Hu, X.; Kaplan, D.; Cebe, P. Determining beta-sheet crystallinity in fibrous proteins by thermal analysis and infrared spectroscopy. *Macromolecules* **2006**, *39*, 6161-6170.
108. Hu, X.; Kaplan, D.; Cebe, P. Dynamic protein-water relationships during β-sheet formation. *Macromolecules* **2008**, *41*, 3939-3948.
109. Yu, L.; Hu, X.; Kaplan, D.; Cebe, P. Dielectric relaxation spectroscopy of hydrated and dehydrated silk fibroin cast from aqueous solution. *Biomacromolecules* **2010**, *11*, 2766-2775.
110. Huang, W.; Krishnaji, S.; Tokareva, O.R.; Kaplan, D.; Cebe, P. Influence of Water on Protein Transitions: Thermal Analysis. *Macromolecules* **2014**, *47*, 8098-8106.
111. Huang, W.; Krishnaji, S.; Tokareva, O.R.; Kaplan, D.; Cebe, P. Influence of Water on Protein Transitions: Morphology and Secondary Structure. *Macromolecules* **2014**, *47*, 8107-8114.
112. Mieda, S.; Aida, M. Macrodipole Moment of Polypeptides in *β*-Sheet and Its Prediction from Dipole Moments of Amino Acid Residues as Building Blocks: Alanine and Glycine in *β*-Strand. *Chemistry Letters* **2013**, *42*, 473-475.

Chapter 2. Synthetic polypeptides

2.1 Introduction

As the complexity of protein dynamics posed significant challenges towards understanding their behavior, scientists turned to polypeptides as simplified models of natural systems.[1,2] Polypeptides provide a simplified framework for studying fundamental biological processes and the principles that govern protein function. Unlike natural proteins, which are influenced by intricate structures, diverse sequences and complex solvent interactions, synthetic polypeptides offer a controlled environment for exploration. This reduction in complexity allows the study of specific aspects of molecular motion, self-assembly, and interactions without the confounding variables (e.g., solvent) present in full-length proteins.

Apart from their simplicity, polypeptides are increasingly recognized as a promising class of drugs, due to their unique combination of properties that bridge the gap between small molecules and proteins, yet are biochemically and therapeutically distinct from both.[3,4] Polypeptides have found wide application in a variety of fields, including pharmaceuticals (e.g., oncology, endocrinology, analgesics, neurotherapeutics), cosmetics, food and nutrition, diagnostics and biotechnology, demonstrating their versatility and potential. However, natural peptides have important limitations, that make their role as therapeutic agents challenging.[5] These include low stability and bioavailability, limited cellular capacity, the potential to induce immune responses and, finally, the cost and complexity of large-scale production, all of which point to the need for a suitable alternative. Synthetic peptides overcome many of the risks associated with natural peptides. As a result, they are increasingly replacing natural peptides in drug development, providing greater control and precision in treatment outcomes. In particular, small synthetic peptides consisting of a few amino acids can easily be administered to the human body due to their low molar mass.[6]

Synthetic polypeptides are created artificially under controlled laboratory conditions by chemically linking amino acids in a specific sequence, a process that mimics the natural biosynthesis of polypeptides in living cells.[7-10] Synthetic polypeptides vary in length from just a few amino acids to longer chains that resemble the size of smaller proteins. One of the main reasons

synthetic polypeptides are important is their structural and functional similarity to proteins, and in particular to intrinsically disordered proteins (IDPs).

This similarity enables synthetic polypeptides to mimic the dynamic conformational states of IDPs, making them valuable for various biomedical and nanotechnology applications. By carefully designing their amino acid sequences, researchers can control properties such as solubility, responsiveness to environmental stimuli, and self-assembly behavior. For example, elastin-like polypeptides (ELPs) undergo temperature-dependent phase transitions, making them useful for drug delivery and tissue engineering.[11] Similarly, silk-inspired polypeptides mimic the mechanical strength and flexibility of natural silk, contributing to the development of biomaterials for medical implants and sutures.[12] Another example is β-sheet-forming polypeptides, that self-assemble into nanofibers and hydrogels for regenerative medicine applications.[13]

More specifically, poly-γ-benzyl-L-glutamate (PBLG) is a model synthetic polypeptide known for its ability to form well-defined secondary structures, α-helices and β-sheets.[14] Due to its highly stable α-helical configuration, it is considered a model rigid-rod polymer and an excellent candidate for understanding polypeptide behavior. At the same time, PBLG has a hydrophobic character that allows for studies in completely non-aqueous and organic solvents. These two characteristics make PBLG a promising candidate for studying the physical, chemical, and conformational properties of helical peptides, as well as their response to external factors (e.g., temperature, pressure, and solvent content), without the complexity and variability inherent in natural proteins.

In the bulk, PBLG organizes into a nematic-like paracrystalline structure, with a periodic packing of helices in the direction lateral to the chain axis, while along the chain axis the mutual levels of the chains are irregular.[16] This semi-ordered arrangement of polymer chains is characteristic of many biological and synthetic polypeptides that do not form perfectly ordered structures. The α-helix of PBLG is described as a 18/5 helix, which is a right-handed for L-α-amino acids, with 18 repeat units in 5 turns (3.6 repeat units per turn). However, the polypeptide can also form a metastable 7/2 helix that irreversibly converts to a 18/5 helix upon heating.[17] The pitch of the helix, i.e., the axial length of one complete helix turn, is 0.54 nm. In solution, a recent study reported an α-to-PPII helix transition for PBLG in THF/water solutions.[18] The PPII (polyproline-

II) helix, commonly found in proline-rich peptides, is a left-handed, extended helical conformation known for its enhanced flexibility compared to the typical α-helix.

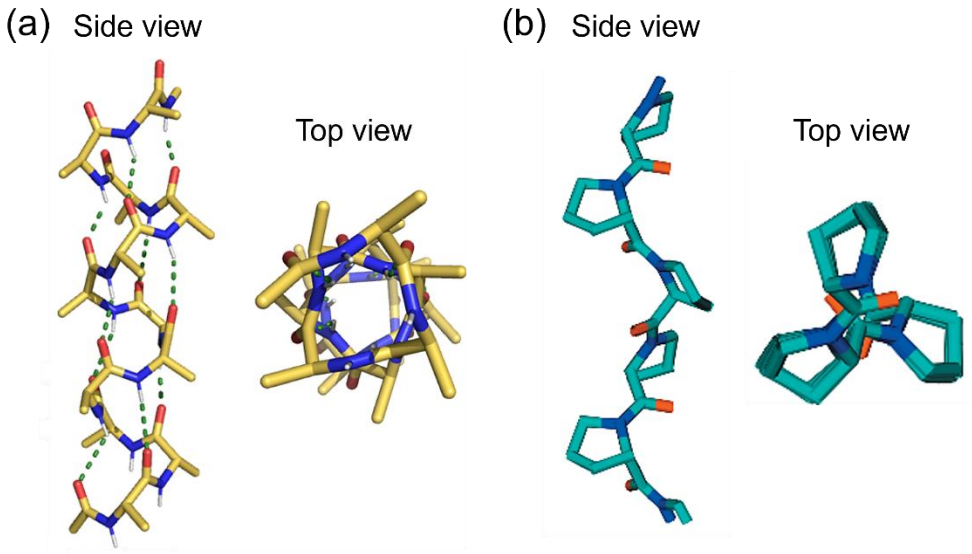

Figure 2.1. Side and top view of a three-dimensional structural representation of (a) an α-helix (18/5 or 7/2 helix) [19] and (b) a PPII helix [20]. In both structures, nitrogen and oxygen atoms are colored blue, and red, respectively. The α-helix backbone is highlighted in yellow, and the PPII helix backbone is indicated with green.

2.2 Self-assembly and dynamics

Among polypeptides, PBLG has been extensively studied due to its ability to adopt a stable α-helical conformation.[14] Early work by Wada showed that in helicogenic solvents such as dioxane, the α-helix exhibits a pronounced dipole moment along its axis that scales with the degree of polymerization.[21-23] Subsequent research, based on theoretical and simulation studies, explored the conformational flexibility of PBLG in the bulk and in solution, revealing deviations from perfect helices.[24-28] A widely used theoretical model to describe the structural transitions of polypeptides is the Zimm-Bragg model, which provides a statistical framework for predicting a phase transition in polypeptide chains.[24,25]

The Zimm-Bragg framework describes the helix-coil transition, the process by which a polymer changes from an ordered, helical structure to a disordered, random coil conformation, or vice versa, in response to changes in environmental conditions such as temperature or solvent composition. According to the model, the helix-coil transition can be sharp, resembling a phase transition, especially for long polymer chains. This sharpness is a result of the cooperative

interactions between adjacent segments. In each case, the system tries to balance entropy, which favors the flexible coil, and enthalpy, that stabilizes the structured helices through hydrogen bonding. To describe this process, Zimm and Bragg introduced two fundamental parameters; the nucleation parameter, σ, and the propagation parameter, s.[25] The nucleation parameter controls the difficulty in the formation of a helical segment. A small value of σ ($\ll 1$) means that nucleation is (highly) energetically unfavorable, since forming the first turn of a helix results in a significant loss of entropy. However, once a helical segment forms, it stabilizes adjacent regions, making helix propagation much easier. This process is controlled by the propagation parameter, which determines how easily the helix grows. When $s > 1$, subsequent turns are easily added, allowing helices to form more readily. Depending on the values of these parameters, one of the following conformations dominates: random conformations, single helices with occasional disorder at the ends, and, for longer chains, helices randomly interrupted by amorphous segments (Figure 2.2a).

This model provides a fundamental explanation of how helical structures form and how peptides transition between ordered and disordered states in response to specific changes. In biological systems, polypeptides rarely exist as either fully helical or fully coiled structures. Instead, they exhibit a combination of conformations, that reflects the energetic equilibrium described by the Zimm-Bragg model.[24,25] The explanation is that helices do not break randomly, but rather tend to break at specific boundaries, forming helical and coiled regions. This behavior is governed by nucleation effects and the boundary tension. The boundaries between helical and coiled regions are sharp and well-defined due to their strong dependence on the neighboring residues. Consequently, there is a preference for large helical regions separated by well-defined coil domains, and, therefore, long polypeptides tend to have alternating structured and unstructured regions.

The study by Muroga et al. demonstrated an application of the Zimm-Bragg model.[28] The authors investigated the structural behavior of PBLG peptides of different molar masses in helicogenic solvents as a function of radius of gyration (R_g) (Figure 2.2b). Deviations in R_g from that of an intact, rigid α-helix were observed: a downward deviation in the higher molar mass region and an upward deviation in the lower molar mass region. The Zimm-Bragg model explained the unwound chain ends of the low molar mass PBLG, as the high nucleation barrier prevented the helix formation. However, experimental data showed that long PBLG chains behave more like

semiflexible wormlike coils, rather than perfectly rigid helices, resulting in a decrease in R_g compared to the rigid-rod values. The reason is because, at high molar masses, chain bending or thermal fluctuations become significant, requiring the use of other theoretical models, such as the wormlike chain model or the freely jointed rod model. Thus, although helicogenic solvents ensure the formation of helices, they do not ensure that PBLG behaves like a rigid rod.

Ongoing research into the dynamics of homopolypeptides in the bulk has revealed a glass "transition" similar to that observed in amorphous polymers.[29-32] This "transition" was identified through static (X-ray) and dynamic (thermodynamic, dielectric and mechanical) measurements. Many dielectric measurements identified a relaxation that froze at T_g, very reminiscent of the segmental relaxation of amorphous polymers. However, the interpretations of its origin varied. Early studies erroneously attributed the process to the relaxation of the side groups.[30] As for the α-helices, it was assumed that they were either highly ordered, with no possible conformational motions, or that they rotated as a rigid rod.[30-32] In the latter case, the helix motion was described by the Doi and Edwards's ″chopstick″ model,[31] where polymer segments, considered as connected rigid rods (chopsticks), could move independently within a tube formed by the surrounding polymer chains, or later by the Wang and Pecora model.[32] The model described the restricted rotational diffusion of rigid rod-like molecules that are geometrically confined to a limited angular range, e.g., a polymer or a helical segment oscillating in a cone, due to interactions with its environment (Figure 2.2c). This was discussed in the study of Hartmann et al.,[33] in which the dielectric relaxation of grafted PBLG was in agreement with the model's predictions. However, a detailed understanding of the exact origin of T_g in polypeptides or the dynamics and the persistence length of helices was still lacking.

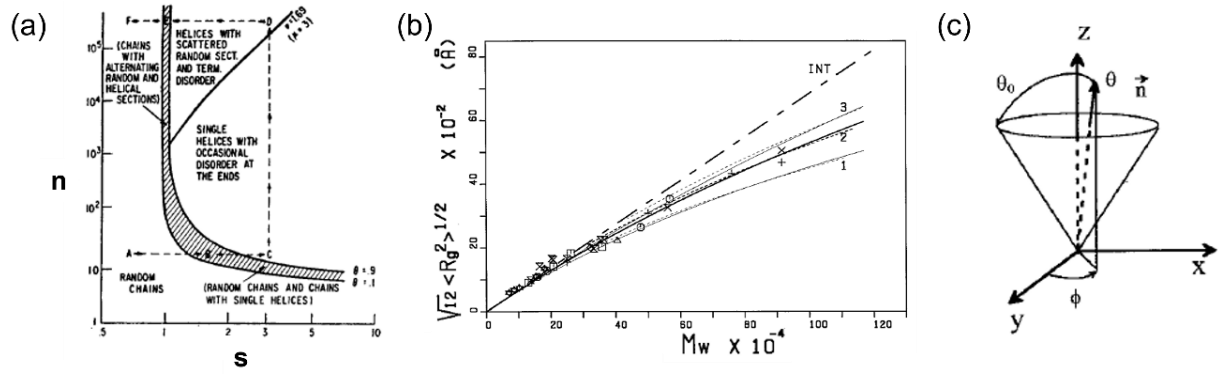

Figure 2.2 (a) Peptide phase diagram according to Zimm and Bragg theory. The n denotes the peptide chain length, while s is an equilibrium constant for the formation of hydrogen bonds. The shadowed area corresponds to the helix-to-coil transition region. [24] (b) The root-mean-square radius of gyration as a function of the average molar mass for PBLG in various helicogenic solvents, i.e. dichloroacetic acid, chloroform-formamide, dimethylformamide, ethylene dichloride, dioxane, pyridine, m-cresol, dichloroethane and dichloroacetic acid with cyclohexanol. The dashed line (INT) shows the theoretical dependence of the ideal α-helix. [28] (c) A schematic representation of the restricted rotational diffusion model of rod-shaped molecules within a cone of angle θ, by Wang and Pecora. [32]

The first comprehensive study to elucidate the self-assembly and dynamics of PBLG homopolypeptides in the absence of solvent was ref[15]. PBLG was synthesized via ring-opening polymerization (ROP) of γ-benzyl-L-glutamate *N*-carboxyanhydride (BLG-NCA) using established methods (peptide synthesizer).[34] The purified NCA was polymerized using a primary amine initiator, *n*-hexylamine, in an inert atmosphere, to produce PBLG with controlled molecular masses. The static analysis, using solid-state nuclear magnetic resonance (NMR), wide-angle X-ray scattering (WAXS) and fourier transform infrared spectroscopy (FTIR), revealed that PBLG forms both secondary structures, α-helices and β-sheets, depending on the degree of polymerization. Low degrees of polymerization stabilized β-sheets in a lamellar structure, while longer chains ($N > 18$) stabilized α-helical conformations ordered in hexagonally packed cylinders (Figure 2.3a). Dynamic analysis by differential scanning calorimetry (DSC), revealed a step-like reduction in the specific heat, indicative of a liquid-to-glass temperature. Complementary results from dielectric spectroscopy (DS) revealed five active relaxation processes. It is important to note that the following results refer to the dynamics of $PBLG_{14}$, a polypeptide with both secondary structures, while the dynamics of lower molecular masses was not presented in the study.

Within the glassy state, two processes were identified, reflecting localized motions of the side groups (Figure 2.3b). At temperatures higher than T_g, three processes were present. The first

was the segmental relaxation, that froze at the liquid-to-glass temperature. This process was found in all polypeptides, regardless of molar mass, indicating an intrinsic feature of the peptide dynamics. It was attributed to the amorphous segments interrupting the α-helices and at the chain ends. This finding was further supported by the Vogel-Fulcher-Tammann (VFT) temperature dependence of the relaxation times of the segmental process ($\tau = \tau_o^{\#} exp(B/T - T_o)$, where $\tau_o^{\#}$ is the relaxation time in the limit of very high temperatures, B is the activation parameter and T_o is the "ideal" glass temperature), which confirms the cooperative nature of the segmental motions, and by the Fox-Flory relation of the glass temperatures ($T_g(K) = T_g^{\infty} - K/M_n$, where T_g^{∞} is the glass temperature at infinite molar mass, and K is an empirical constant) as a function of the degree of polymerization (Figure 2.3c). However, mechanical measurements showed that the segmental process of polypeptides is not identical to that of amorphous polymers, since the formers do not flow, even at temperatures well above the glass temperature. The authors attributed this behavior to the formation of aggregates at the intersections of the amorphous segments of the chains. The next active process was the intermediate process, which, based on its low dielectric strength, was assigned to the motion of few completely amorphous chains, while the slower process, based on its higher dielectric strength, was attributed to the relaxation of the helical parts. These helical parts were found to be interrupted by amorphous segments (″defected helices″), since estimates of the effective dipole moment of the helices (based on the dielectric strength of the slower process) showed significantly lower values than those of an ideal helix (μ_{ideal} = 3.4 D per repeat unit) (Figure 2.3d). The results implied a strong coupling between the origin of the segmental process, i.e., the amorphous segments interrupting the helical parts, and the persistence length of these helical parts.

In this context, the ″defected helix″ model was proposed.[35] According to this model, the helix is assumed to be composed of ideal helical parts of the same correlation length, ξ, that can rotate on the surface of a cone of angle θ, each independently of the others, but with their axes parallel to each other (Figure 2.3e). The dielectric strength associated with the relaxation of helical segments is

$$\Delta\varepsilon = \frac{N_A \rho}{3\varepsilon_0 kTM_0}(3.4Debye)^2(\xi/0.15\ nm)sin^2\theta \qquad (2.1)$$

Here, M_0 is the molar mass of the repeat unit of the polypeptide, ρ is the density, whereas the dipole moment of each helical part is μ = 3.4 D ($\xi/0.15\ nm$), as the step length of the helix is 0.15 nm per repeat unit. X-ray scattering from oriented fibers provided an upper value for θ, which allowed extracting the correlation length, ξ, of α- helices. The latter was estimated at ~ 2 nm.

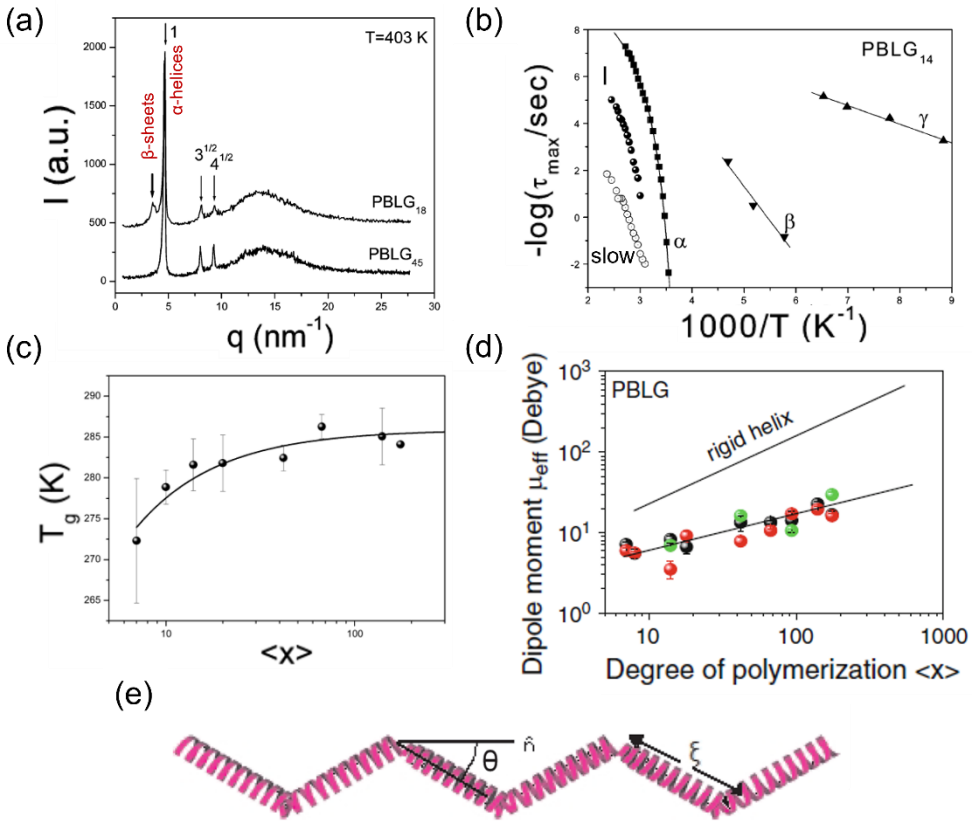

Figure 2.3. (a) WAXS patterns of PBLG$_{18}$ (top) and PBLG$_{45}$ (bottom). The arrows indicate the Bragg reflections that correspond to the lamellar spacing of β-sheets and the hexagonally packed α-helices. [15] (b) Arrhenius relaxation map of PBLG$_{14}$. Five processes are depicted. Starting from low temperatures: the γ- and β- local processes, the segmental α-relaxation, the intermediate (I) process and the slow helical process. [15] (c) Glass temperature of PBLG as a function of molar mass. [15] (b) Effective dipole moment of the slow helical process as a function of the degree of polymerization of PBLG. The solid upper line represents the theoretical values for ideal helices. [36] (e) Schematic representation of the ″defected helix″ model. [35]

The DS results of PBLG were later complemented by temperature-dependent ^{13}C NMR spectra, which provided insight into the molecular geometry underlying the observed dielectric processes.[36] Analysis of the integrated peak intensities revealed that the fast dielectric β-process, observed below T_g, corresponded to the dynamics of the ester C=O and OCH_2 groups (Figure 2.4).

In addition, the backbone dynamics was detected by NMR. It was slower than the DS segmental process but faster than the DS "slow" process. Since this process was not detected in DS, due to low intensity, it was attributed to the backbone motions within the ordered helical regions and was considered to be a precursor to the unfreezing of the DS helical dynamics.

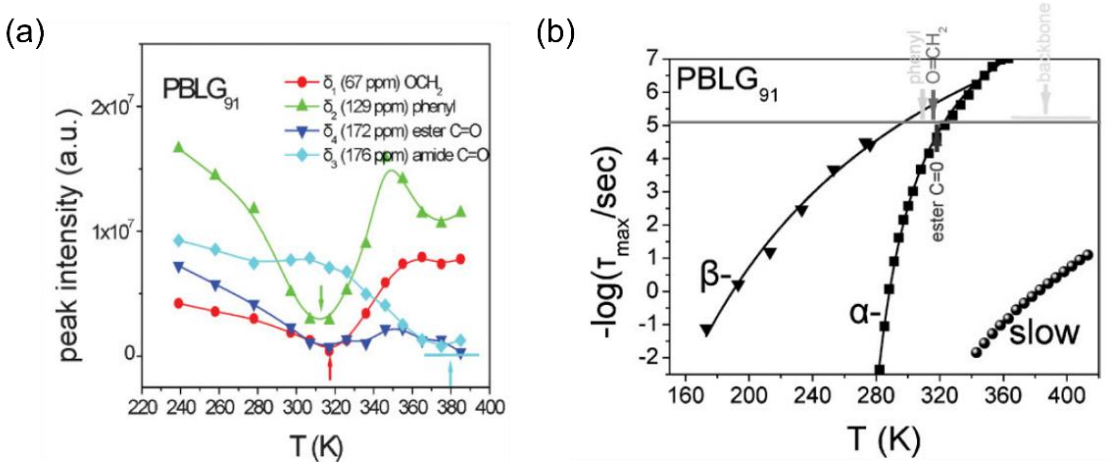

Figure 2.4. (a) Integrated peak intensities as a function of temperature for the resonances at $\delta_1 \approx$ 67 ppm, $\delta_2 \approx$ 129 ppm, $\delta_3 \approx$ 176 ppm, and $\delta_4 \approx$ 172 ppm, corresponding to the OCH_2, phenyl, amide C=O and ester C=O, respectively, of the ^{31}C NMR spectra of $PBLG_{91}$. The arrows indicate the temperature of minimum peak intensity, which suggests the rate of the underlying molecular motions at f = 20 kHz. (b) Arrhenius plot of the dielectrically active processes for $PBLG_{91}$. The ^{13}C NMR resonances are indicated with arrows at the relevant NMR frequency. [36]

Additional dielectric measurements were performed as a function of temperature and pressure on three polypeptides, PBLG, PZLL (poly-(ϵ-carbobenzoxy-L-lysine)), and PGly (polyglycine) aiming to the origin of the segmental dynamics and the associated T_g.[37] The choice of polypeptides was made in order to study all possible cases, since the polypeptides PBLG and PZLL only form α-helices, whereas PGly forms β-sheets. The results showed that the secondary structure affected both the fragility and the apparent activation volume ($\Delta V^{\#}$) (a quantity accessible only through pressure experiments) of the segmental process of the polypeptides (Figure 2.5a,b). Helical polypeptides exhibited a more fragile behavior compared to the more compact β-sheet polypeptides. Furthermore, the $\Delta V^{\#}$ for PBLG and PZLL was found to be much higher and strongly temperature-dependent than the $\Delta V^{\#}$ of PGly, which was almost constant with temperature.

An important part of the study focused on determining whether the liquid-to-glass temperature is primarily driven by the thermal energy (temperature effect) or by the available volume (pressure effect). Two parameters were introduced; E_V represented the energy barrier for

molecular relaxation at constant volume, while, E_P is the apparent activation energy at constant pressure. The ratio $E_V/E_P \left(= 1 - \left(\frac{\partial ln\tau}{\partial V}\right)_T \cdot \left(\frac{\partial V}{\partial T}\right)_P / \left(\frac{\partial ln\tau}{\partial T}\right)_P\right)$ is a critical parameter. A ratio close to 1 indicates that molecular mobility is primarily limited by insufficient thermal energy rather than by volume constraints, meaning that the glass "transition" is primarily temperature-controlled (thermal energy effects). On the other hand, a ratio close to 0 would indicate that the transition is primarily volume-controlled (as in free-volume theories). This would mean that densification (reduction of free volume) is the main factor resulting in the liquid-to-glass "transition". The analysis revealed ratios between 0.78 and 0.80, indicating that thermal energy is the dominant control parameter for the segmental dynamics (Figure 2.5c). This result links the origin of glass formation in the polypeptides to the breaking/weakening of the hydrogen bonds at specific defect areas, mainly due to reduced thermal energy rather than lack of free volume. This behavior was consistent across different polypeptides, regardless of their secondary structure. This suggested that temperature similarly affects the strength of intramolecular (α-helices) bonds in PBLG and PZLL, and the intermolecular (β-sheets) hydrogen bonds in PGly.

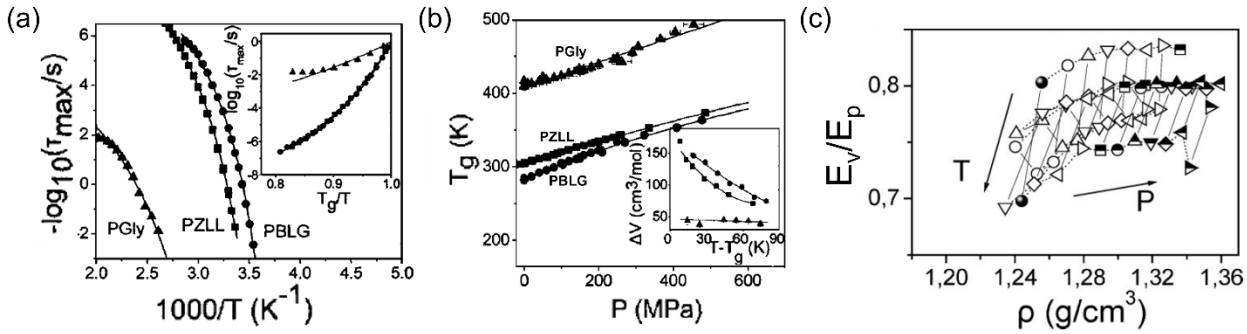

Figure 2.5. (a) Arrhenius map of the segmental relaxations for $PBLG_{45}$ (circles), $PZLL_{135}$ (squares), and $PGly_{342}$ (triangles). The inset shows the corresponding segmental relaxations as a function of T_g/T. (b) Pressure dependence of the glass transition (at τ = 1 s) for the three polypeptides. The inset shows the apparent activation volume ($\Delta V^{\#}$) as a function of temperature. (c) Ratio (E_v/E_p) of the apparent activation energies of the segmental relaxation at constant volume (E_v) and pressure (E_p) as a function of density for the $PBLG_{45}$. [37]

Despite these advances, key questions about the dynamics of synthetic peptides remain unanswered. For example, can we detect the dynamics of β-sheets and α-helices in the same polypeptide (same chemistry) only by varying the molar mass? If so, what are their length- and timescales? Do β-sheets have slower dynamics as α-helices do, and if so, what is the origin? How do different secondary structures or even different α-helix-to-β-sheet ratios affect the peptide

dynamics? How does pressure affect the dynamics of α-helices and β-sheets? Are there any similarities in the dynamic behavior of these two secondary structures? This study addresses these questions, in an effort to deepen our understanding of the relationship between secondary structure and dynamics.

2.3 Poly(*γ*-benzyl-L-glutamate) copolymers

Polypeptide-based materials are a rapidly growing area of research and innovation, driven by their unique ability to combine protein-like backbones, functional side-chains, and biodegradability.[38-41] These materials offer a wide range of properties, that make them highly valuable for applications in drug delivery, tissue engineering, stimuli-responsive materials, and nanotechnology. Within this field, PBLG-based materials can be broadly categorized into two types: copolypeptides, which are composed of blocks of different polypeptides, and hybrid materials, in which peptides are polymerized with amorphous or semicrystalline polymers. Copolypeptides combine the unique properties of the individual polypeptide blocks into a single material, creating well-defined nanoscale morphologies in highly versatile systems. In contrast, combining PBLG with amorphous polymers, such as poly(ethylene glycol) or polystyrene, creates unique combinations of biological and synthetic properties that often improve material processability and expand practical applications.

The stability of PBLG secondary structures in copolypeptides has been well documented over the years.[36] One of the earliest systems studied was the PBLG-*b*-PGly diblock copolymer, composed of polypeptides with different packing efficiencies and different secondary structures.[42] Nuclear magnetic resonance (NMR) and wide angle X-ray scattering (WAXS) experiments revealed that PBLG predominantly adopts α-helical structures arranged in a hexagonal lattice, while PGly – a polypeptide composed of the simplest amino acid – forms β-sheets. The self-assembly of the copolymer was found to vary with the degree of polymerization, revealing two distinct morphological regimes: a hexagonal morphology for $0.86 \leq f_{PBLG} \leq 0.94$, and a lamellar morphology of α-helices for $0.67 \leq f_{PBLG} \leq 0.79$. Notably, the authors did not elaborate on the broad feature in the scattered intensity, which is likely related to the form factor of the PBLG helices (Figure 2.6a). Further analysis of the SAXS data enabled a comparison of the PBLG and PGly domain spacings to the theoretical distances calculated for ideal α-helices (0.15 nm per residue) and fully extended β-sheets (0.35 nm per residue) (Figure 2.6b). The PBLG spacing

was consistent with an arrangement intermediate between monolayer and bilayer packing, while the PGly spacing was significantly smaller than predicted for fully extended chains. This finding was corroborated by the broadened resonance (δ ~ 45 ppm) of the copolymer in NMR, characteristic of PGly β-sheet structure. These results suggested that PGly chains adopt multiply folded β-sheet conformations (Figure 2.6c). This folding behavior was driven by thermodynamic confinement within the nanodomains and the disparity in packing efficiency between the two blocks. Consequently, a lamellar nanodomain morphology was stabilized even at highly asymmetric compositions – an effect reminiscent of the stability of the crystalline lamellar phase in semicrystalline-amorphous block copolymers.

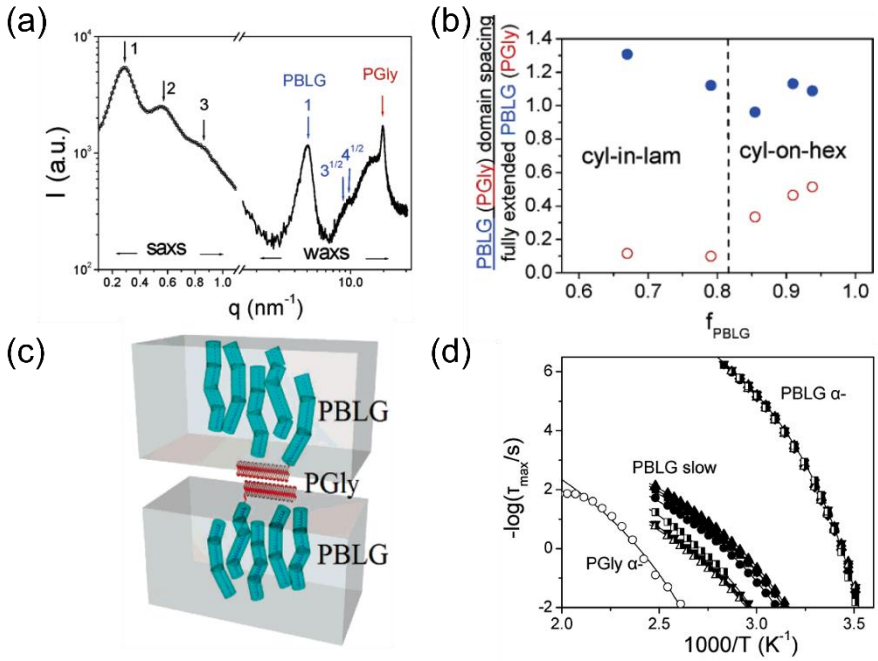

Figure 2.6. (a) WAXS and SAXS curves for the PBLG-*b*-PGly copolymer with f_{PBLG} = 0.79. The black arrows indicate a lamellar nanodomain block copolymer morphology, the blue arrows indicate the hexagonal packing of the PBLG α-helices, and the red arrow indicates the lamellar spacing of the PGly β-sheets. (b) Normalized domain spacings, obtained from SAXS, of PBLG (filled symbols) and PGly (empty symbols) to the length of the fully extended secondary structures, of the same molecular weight, as a function of f_{PBLG}. The vertical line indicated the two nanodomain morphologies found in the copolymers. (c) Schematic representation of the lamellar nanodomain morphology of PBLG-*b*-PGly copolymers with $f_{PBLG} < 0.8$. The defects of the PBLG α-helices, as well as the induced folding of PGly β-sheets are indicated. (d) Arrhenius plot of the PBLG-*b*-PGly copolymers. Filled squares represent the bulk PBLG, while open circles represent the bulk PGly. [42]

WAXS further revealed that the inter-helical distance of the PBLG helices increases with increasing PGly content, while the inter-sheet distance of PGly decreases with increasing PBLG content, suggesting possible interfacial mixing between the two blocks. Although the authors questioned this interpretation, dielectric studies provided support for interfacial effects, showing that for PGly, the segmental relaxation appeared to be masked by the slow helical process, suggesting a faster-than-bulk dynamics (Figure 2.6d). An analysis of the normalized effective dipole moments showed that thermodynamic confinement reduces helical defects in PBLG, while promoting chain folding in PGly β-sheets. Furthermore, it was possible to estimate the correlation length of α-helices from the dielectric strength of the PBLG slow process.

A subsequent study investigated PBLG-*b*-PAla (PAla: polyalanine) copolypeptides.[43] In this case, both polypeptides can form both secondary structures, α-helices and β-sheets. The study showed that thermodynamic confinement suppresses the formation of PAla β-sheets, leading both blocks to adopt exclusively α-helical configurations, as evidenced by NMR results. The WAXS data suggested that confinement affects the hexagonal packing of both polypeptides, reducing their lateral correlation length. This effect was more pronounced in the PAla block, where the helices were less tightly packed, as evidenced by their remarkably broader reflection. The DS analysis revealed that all PBLG processes were active. However, the absence of a detectable segmental process for PAla, combined with the lack of SAXS data prevented the exclusion of possible some degree of mixing between the two components.

The effects of nanophase separation in PBLG-based diblock copolymers were further investigated by comparing α-helical PLeu (poly(L-leucine)) and β-sheet POBT (poly(*O*-benzyl-L-tyrosine) blocks.[44] WAXS results showed that nanoscale confinement promotes the lateral packing of the secondary structures, albeit without long-range order. SAXS analysis of PBLG-*b*-POBT copolymers revealed multiple folded β-sheet conformations in the POBT domain. For both α-helical blocks, PBLG and PLeu, defected α-helices were reported.

Subsequently, a notable study investigated PBLG-*b*-PLP (poly-L-proline) copolypeptides and highlighted the special role of proline in helix stabilization.[45] The homopolypeptides and copolypeptides were synthesized using high-vacuum techniques developed by Iatrou and coworkers.[46,47] Unlike most peptides, proline stabilizes α-helices through steric hindrance rather than hydrogen bonding. Both the PBLG and the PLP blocks were found to stabilize hexagonally

packed helices, but with significantly different hexagonal unit cells. The results showed that the predominant helical conformation of proline is PPII, while PPI is favored near the interface. Further NMR analysis revealed a *trans*-to-*cis* conformational change of PLP at the interface of the two blocks, a result of thermodynamic confinement. This change alleviated packing frustration and allowed each block to maintain its bulk properties. Given the observed structural complexity, dielectric spectroscopy could provide valuable insights into the properties of these "different" secondary structures and further enrich the understanding of their conformational behavior.

When exploring more complex macromolecular architectures, two studies provided compelling examples of how topology influences the properties of polypeptide-based materials. The first study examined the self-assembly and dynamics of PBLG-*b*-PZLL copolymers, with both diblock and star architectures.[48] In the diblock copolymers, both peptides adopted α-helices organized in a hexagonal lattice, while the nanodomain morphology of the system indicated the formation of a lamellar structure (Figure 2.7a). The authors observed that increasing the molar mass of the peptides resulted in an increased lamellar spacing. Conversely, in the star architecture, the peptides again formed α-helices, but now the helices exhibited hexagonal packing without long-range order. In addition, phase mixing was shown by SAXS results (Figure 2.7a). The dielectric spectra revealed the segmental dynamics of both components. Interestingly, a single slow relaxation process was identified (Figure 2.7a) (not discussed in the paper). This may represent a merging of the two slow processes of PBLG and PZLL, suggesting a similar helical relaxation. Lastly, effective dipole moment calculations revealed more helical defects in the star copolymer architecture than in the diblock copolymer.

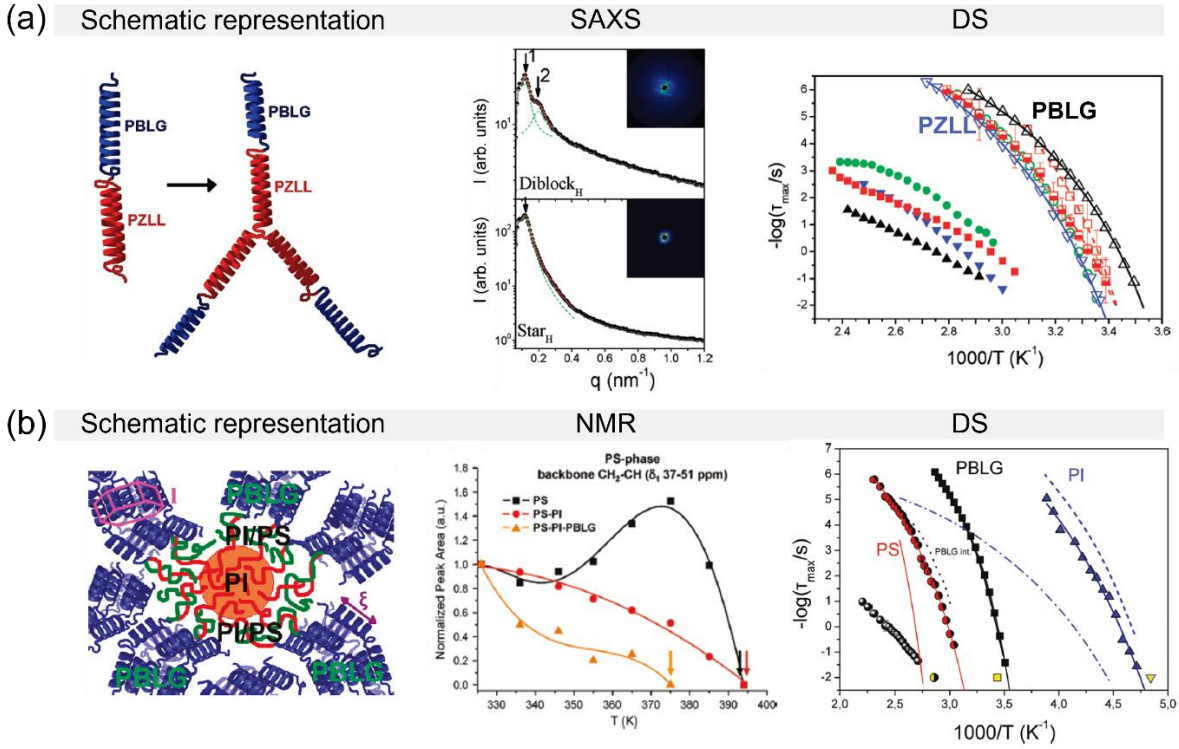

Figure 2.7. (a) (left) Schematic representation of the PBLG/PZLL diblock copolymer and star architecture. (middle) SAXS patterns for the PBLG/PZLL diblock copolymer (up) and star architecture (bottom). In the copolymer, a lamellar nanodomain morphology is shown, while in the star the two blocks appear phase mixed. (right) Arrhenius map as a function of the inverse temperature. The open symbols represent the segmental dynamics, while the filled symbols indicate the slow helical process. The up and down triangles correspond to the bulk PBLG and PZLL, respectively. The red symbols represent the dynamics of the diblock copolymer, while the green symbols show the dynamics of the star. [48] (b) (left) Schematic representation of the of the miktoarm star structure of (PS)(PI)(PBLG). (middle) Peak area of the PS backbone CH_2-CH region at 37-51 ppm region in the ^{13}C NMR spectra as a function of temperature for the (PS)(PI)(PBLG) system (orange), as well as the PS homopolymer (black) and the PS-PI diblock copolymer (red) for comparison. The $\Delta T \sim 20$ K difference in the temperatures (indicated with arrows), at which the ^{13}C signal completely loses intensity, indicates the mixing between the PS and the PI blocks in the (PS)(PI)(PBLG) system. (right) Arrhenius map for the investigated system. Each color represents the segmental dynamics of each block: PI (blue), PBLG (black), PS (red). The slow α-helix process is indicated with spheres. Solid lines represent the segmental dynamics of PBLG (black) and PS (red) homopolymers, while the blue dashed and dashed-dotted lines show the segmental and normal mode of the PI homopolymer. [49]

The second study focused on a (PS)(PI)(PBLG) miktoarm star rod-coil chimera.[49] The synthesis was conducted by H. Iatrou et al., who combined living anionic and ring-opening polymerization (ROP) techniques under high vacuum. The study used a combination of five complementary experimental techniques to provide a comprehensive analysis of the structural and

dynamic behavior. NMR, WAXS, and DS revealed that the amorphous regions of the PBLG block remained largely unaffected by the complex star architecture; but, the ordered helical parts were affected. WAXS revealed broader Bragg reflections, indicating a less well-defined hexagonal packing, and a smaller persistence length of the α-helices, compared to the PBLG homopolymer. These results suggested that the long-range order and rigidity of the helices is affected by the star topology. NMR and DS measurements examined all three segmental dynamics (PS, PBLG, and PI) and in addition the slower α-helical dynamics in PBLG (Figure 2.7b). They revealed local mixing of the amorphous segments, as indicated by the slower segmental dynamics for PS and the faster dynamics for PI relative to their respective homopolymers. Analogous systems with a lower degree of polymerization for the PBLG block, where both α-helical and β-sheet structures coexist, would be particularly interesting to study.

When PBLG is copolymerized with amorphous or semicrystalline polymers, the resulting hybrid materials exhibit distinct structural and dynamic properties, that are influenced by the interplay between the peptide secondary structures and the non-peptide block properties. Early studies of PBLG diblock copolymers with amorphous polymers such as PB (polybutadiene),[50,51] PI (polyisoprene),[52] and PS (polystyrene)[53-55] focused primarily on the secondary structure of the peptide block and the nanodomain morphology of the copolymer. Depending on the value of the interaction parameter and the particular architecture, these studies reported nanophase separation to phase mixing, especially for high peptide molar masses. Based on these findings, PS-*b*-PBLG oligomers exhibited particularly interesting behavior. In the study by Lecommandoux et al.,[55] low molar mass PBLG homopolypeptides were found to destabilize α-helices at high temperatures by undergoing a helix-to-sheet transition. However, the incorporation of the PS block enhanced helical stability. For low molar mass copolymers, the lamellar β-sheet morphology was the predominant organization of the peptide chains at high *T*, while two other distinct nanodomain morphologies were observed at low *T* and high molar masses.

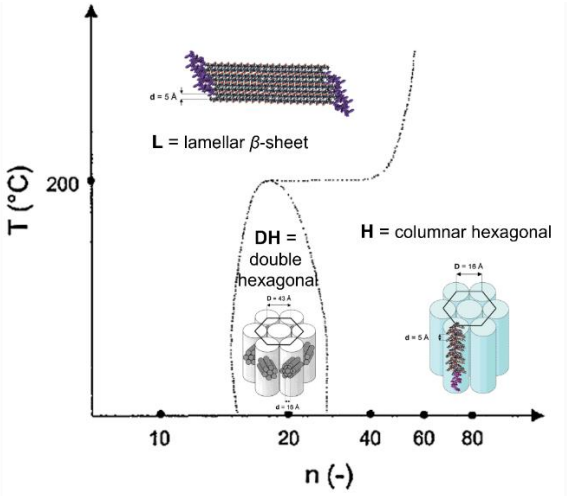

Figure 2.8. Phase diagram of PS-*b*-PBLG diblock copolymers as a function of the average degree of polymerization. Three nanodomain morphologies can be identified: columnar hexagonal (H), double hexagonal (DH) and lamellar β-sheet (L). [55]

Results regarding the favored secondary structure depend mainly on the degree of polymerization of the peptide block. In this context, the self-assembly and dynamics of PBLG-*b*-PDMS-*b*-PBLG (PDMS: poly(dimethyl siloxane)) triblock copolymers were studied, where, PDMS was amorphous, despite typically being semicrystalline.[56] Two cases were identified. Copolymers with high PBLG content exhibited phase separated blocks, as confirmed by NMR and SAXS, while those with low PBLG content exhibited phase mixing. WAXS data confirmed the presence of both α-helices and β-sheets in the PBLG block, depending on the degree of polymerization. The data also indicated a reduced coherence length of the hexagonal packing within the block. The dynamics revealed distinct segmental processes for each block, with *T*-dependencies similar to those of bulk materials, reinforcing the evidence for strong nanophase separation. Calculations of effective dipole moments suggested that the helices have an increased persistence length in the copolymer. Interestingly, the PBLG slow helical process appeared asymmetric in the copolymers; however, the study did not explain this observation. Similar structural and morphological behavior was later observed in thin films of highly asymmetric PBLG-*b*-PDMS-*b*-PBLG samples.[57]

An important class of peptide-based block copolymers includes PBLG copolymerized with poly(ethylene glycol) (PEG), a well-studied model semi-crystalline polymer.[58,59] PEG combines excellent biocompatibility, hydrophilicity, and structural flexibility, and is widely used in biomedical applications, such as for drug delivery or tissue engineering. Early investigations of PBLG-PEG diblock and triblock copolymers mainly focused on self-assembly.[60-62] The first detailed study investigated triblock copolymers of PBLG-*b*-PEG-*b*-PBLG.[63] For $f_{PBLG} < 0.26$, the

copolymers exhibited a lamellar morphology, that allowed the PEG block to crystallize albeit under significant undercooling (Figure 2.9a). For $f_{PBLG} > 0.26$, the components were phase mixed (Figure 2.9b), resulting in an absence of PEG crystallization and a shift in the glass temperature of PBLG to lower values. However, the effect of the degree of polymerization of the peptide block on the T_g of PBLG was not addressed. Regarding the PBLG secondary structure, nanophase separation allowed the formation of β-sheets in PBLG with a low degree of polymerization. It was shown that mixing only allows the formation of α-helices in a hexagonal lattice. The authors also investigated the effect of annealing on the PBLG secondary structure and revealed that higher temperatures result in more coherent β-sheet and α-helical structures, with a stronger effect for the latter.

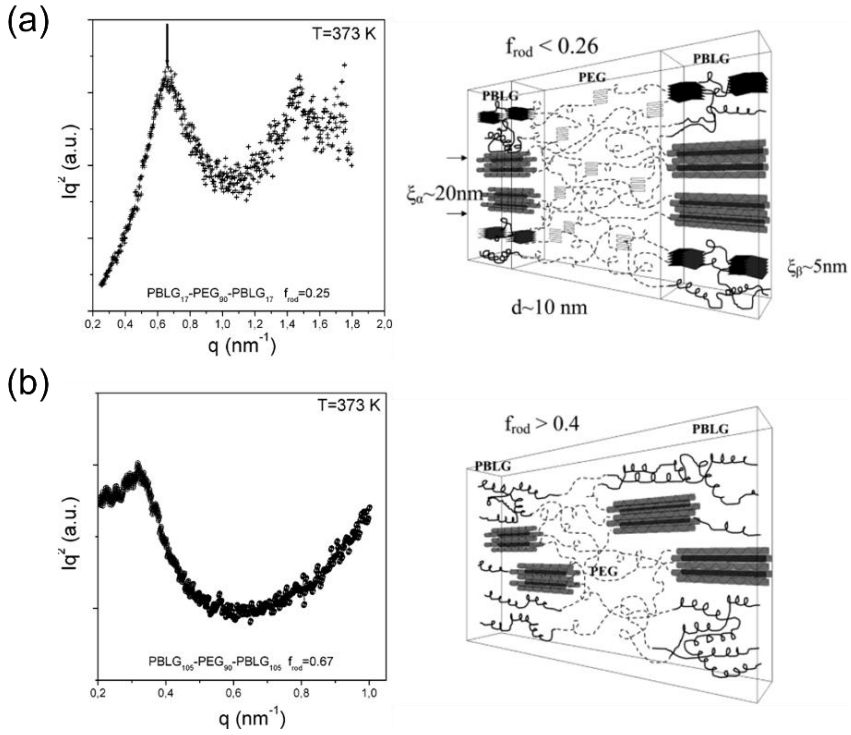

Figure 2.9. SAXS curves of the PBLG-*b*-PEG-*b*-PBLG copolymers with (a) $f_{PBLG} < 0.26$ and (b) $f_{PBLG} > 0.26$. Schematic representations of the self-assembly of the corresponding copolymers are also shown. [63]

A subsequent study on triblock PBLG-*b*-PEG-*b*-PBLG copolymers by a different group further investigated the nanodomain morphology and the secondary structure of the peptide block, using primarily atomic force microscopy (AFM) and transmission electron microscopy (TEM).[64] The authors identified three distinct regions in the phase diagram. Highly asymmetric samples appeared disordered, while copolymers with intermediate f_{PBLG} exhibited nanophase separation.

The observed nanodomain morphologies included cylindrical, lamellar, and broken lamellar morphologies (Figure 2.10). Furthermore, the results revealed distorted helices in copolymers with a higher degree of polymerization of the peptide block. However, while AFM and TEM are useful for visualizing the overall morphology, they are less effective at resolving molecular-level details of secondary structures, such as α-helices or β-sheets. These probes lack the sensitivity to detect specific periodicities or structural arrangements. Contrast this with SAXS and WAXS that offer more comprehensive analyses, providing a bulk-level representations of copolymers self-assembly and structural properties.

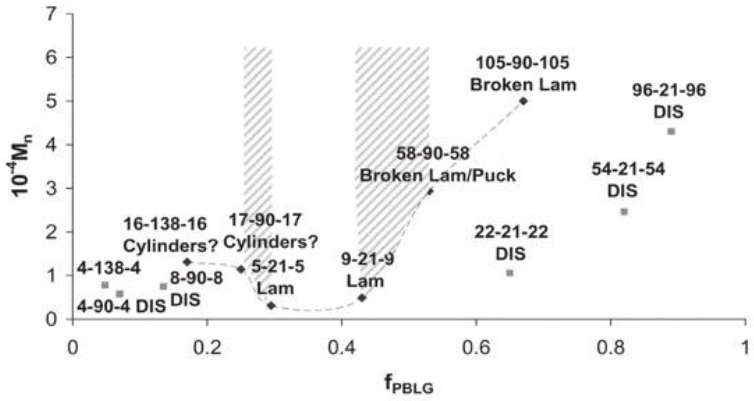

Figure 2.10. Phase diagram for PBLG-*b*-PEG-*b*-PBLG copolymers. The different phases are: Cylinders, Lamellae (Lam), Broken Lam/Puck, Broken Lam and Disordered (DIS). [64]

To provide an overview of the PBLG-based copolymers that have been studied over the years, we summarize all of the above results on the peptide secondary structures and the nanodomain morphologies of the copolymers in Table 2.1.

Table 2.1. Nanodomain morphology and peptide secondary structures for the different PBLG-based copolymers.

	PBLG-based copolymers	Nanodomain Morphology	Peptide secondary structure
copolypeptides	PBLG-*b*-PGly[42]	$0.86 \leq f_{PBLG} \leq 0.94$: hexagonal morphology $0.67 \leq f_{PBLG} \leq 0.79$: lamellar morphology	PBLG: hexagonally packed α-helices PGly: β-sheets with induced chain folding
	PBLG-*b*-PAla[43]	nanophase separation	PBLG: α-helices organized in hexagonal lattice with lower coherence length PAla: weakly hexagonally packed α-helices
	PBLG-*b*-PLEU[44]	weak lamellar morphology	both peptides: weakly hexagonally packed α-helices
	PBLG-*b*-POBT[44]	weak lamellar morphology	PBLG: weakly hexagonally packed α-helices POBT: β-sheets with induced chain folding
	PBLG-*b*-PLP[45]	nanophase separation with interphase mixing	both peptides: hexagonally packed α-helices
	PBLG-*b*-PZLL[48]	diblock copolymer: lamellar morphology	both peptides: α-helices organized in a hexagonal lattice
		star architecture: phase mixing	both peptides: hexagonal packing α-helices (absent of long-range order)
	(PS)(PI)(PBLG) miktoarm[49]	PBLG block: nanophase separated PS/PI blocks: local mixing	hexagonally packed α-helices with increased number of defects
PBLG wth amorphous/semicrystalline polymers	PB-*b*-PBLG[50]	nanophase separation	hexagonally packed α-helices
	PBLG-*b*-PB-*b*-PBLG[51]	nanophase separation	hexagonally packed α-helices
	PBLG-*b*-PI-*b*-PBLG[52]	nanophase separation	hexagonally packed α-helices
	PS-*b*-PBLG[55]	low N_{PBLG}: lamellar β-sheet morphology intermediate N_{PBLG}: double hexagonal high N_{PBLG}: columnar hexagonal morphology	low N_{PBLG}: β-sheets / α-helices (hexagonally packed) high N_{PBLG}: hexagonally packed α-helices
	PBLG-*b*-PDMS-*b*-PBLG[56]	low N_{PBLG}: lamellar morphology high N_{PBLG}: mixing	low N_{PBLG}: β-sheets / α-helices (hexagonally packed) high N_{PBLG}: hexagonally packed α-helices
	PBLG-*b*-PEG[61]	nanophase separation	hexagonally packed α-helices
	PBLG-*b*-PEG-*b*-PBLG[63]	$f_{PBLG} < 0.26$: lamellar morphology $f_{PBLG} > 0.26$: interfacial mixing	$f_{PBLG} < 0.26$: β-sheets / α-helices (hexagonally packed) $f_{PBLG} > 0.26$: hexagonally packed α-helices

In summary, synthetic polypeptides provide a simplified and controllable framework for investigating the structural and dynamic properties of complex systems, such as proteins. PBLG is an ideal system for studying secondary structure-related behavior under varying thermodynamic conditions and thermodynamic confinement, as it stabilizes both α-helices and β-sheets. This

chapter has reviewed the self-assembly, morphology, and molecular dynamics of homopolypeptides and block copolypeptides, with a focus on the relationship between structural motifs and dynamic processes, particularly the "glass transition" of peptides. Studies show that the structured α-helical segments contribute to a slow relaxation process, while amorphous α-helical regions are associated with the segmental dynamics. In copolymers, both secondary structure stabilization and dynamic behavior were strongly influenced by confinement, chain topology, and the chemical nature of the adjacent blocks. It was shown that the more complex topologies (star, miktoarms) induce mixing that destabilizes some secondary structures.

In this Thesis we address two scientific questions that relate to homopolypeptides and copolypeptides:

(I) homopolypeptides: Dynamics of β-sheets: Do β-sheets exhibit a liquid-to-glass "transition" analogous to that of α-helices, and if so, what is its molecular origin? We investigate this by probing completely non-hydrated oligopeptides and polypeptides of PBLG. For the first time, we characterize the dynamics of β-sheets in dry systems. We identify relaxation timescales and lengthscales of β-sheets, that differ from those of the α-helices. The two secondary structures (α-helices and β-sheets) exhibit distinct dynamic properties (fragility and pressure dependence) and viscoelastic signatures, determined by their different structural environment and type of hydrogen bonding (intermolecular vs intramolecular).

(II) copolypeptides: The scientific question here is how many levels of organization exist in copolypeptides? Recent synthesis protocols identified new conditions (polymerization-induced self-assembly (PISA)) for producing amphiphilic block copolymers. The method affords the in-situ one-step growth of a living amphiphilic polymer chain during its self-assembly into nanostructures. A variation of the method is based on the ring-opening polymerization-induced self-assembly (ROPISA) in aqueous buffer. Here we explore ROPISA with respect to the tunability towards nanostructures. We show that the latter method gives rise to polypeptide copolymers of PEG-*b*-PBLG with unprecedented levels of organization. These levels of organization could not be obtained in earlier morphology investigations of copolymers based on PEG and PBLG prepared by different methods.

2.4 References

1. Groß, A.; Hashimoto, C.; Sticht, H.; Eichler, J. Synthetic Peptides as Protein Mimics. *Front. Bioeng. Biotechnol.* **2016**, *3*, 211.
2. Walton, A. G.; Blackwell, J. *Biopolymers*. Elsevier, New York, **1973**.
3. Henninot, A.; Collins, J. C.; Nuss, J. M. The Current State of Peptide Drug Discovery: Back to the Future? *J. Med. Chem.* **2017**, *61*, 1382-1414.
4. Lau, J. L.; Dunn, M. K. Therapeutic peptides: Historical perspectives, current development trends, and future directions. *Bioorg. Med. Chem.* **2018**, *26*, 2700-2707.
5. Muttenthaler, M.; King, G. F.; Adams, D.J.; Alewood, P.F. Trends in peptide drug discovery. *Nat. Rev. Drug Discov.* **2021**, *20*, 309-325.
6. Santos, S.; Torcato, I.; Castanho, M. A. R. B. Biomedical applications of dipeptides and tripeptides. *Biopolymers* **2012**, *98*, 288-293.
7. Deming, T. J. Living polymerization of α-amino acid-N-carboxyanhydrides. *J. Polym. Sci. A Polym. Chem.* **2000**, *38*, 3011-3018.
8. Deming, T. J. Polypeptide and Polypeptide Hybrid Copolymer Synthesis via NCA Polymerization. *Adv. Polym. Sci.* **2006**, *202*, 1-18.
9. Kricheldorf, H. R. Polypeptides and 100 Years of Chemistry of α-Amino Acid N-Carboxyanhydrides. *Angew. Chem. Int. Ed.* **2006**, *45*, 5752-5784.
10. Aliferis, T.; Iatrou, H.; Hadjichristidis, N. Living Polypeptides. *Biomacromolecules* **2004**, *5*, 1653-1656.
11. Roberts, S.; Dzuricky, M.; Chilkoti, A. Elastin-like polypeptides as models of intrinsically disordered proteins. *FEBS letters* **2015**, *589*, 2477-2486.
12. Hardy, J.G.; Scheibel, T.R. Silk-inspired polymers and proteins. *Biochem. Soc. Trans.* **2009**, *37*, 677-681.
13. Cai, L.; Liu, S.; Guo, J.; Jia, Y. G. Polypeptide-based self-healing hydrogels: Design and biomedical applications. *Acta Biomaterialia* **2020**, *113*, 84-100.
14. Block, H. Poly(γ-benzyl-L-glutamate) and Other Glutamic Acid Containing Polymers. Gordon and Breach Science, New York, **1983**.
15. Papadopoulos, P.; Floudas, G.; Klok, H.-A.; Schnell, I.; Pakula, T. Self-Assembly and Dynamics of Poly(γ-benzyl-L-glutamate) Peptides. *Biomacromolecules* **2004**, *5*, 81.
16. Watanabe, J.; Imai, K.; Gehani, R.; Uematsu, I. Structural differences between two crystal modifications of poly(γ-benzyl-L-glutamate). *J. Polym. Sci., Polym. Phys. Ed.* **1981**, *19*, 653-665.
17. Watanabe, J.; Uematsu, I. Anomalous properties of poly(γ-benzyl-L-glutamate) film composed of unusual 7/2 helices. *Polymer* **1984**, *25*, 1711.
18. Liu, Z.; Shi, X.; Shu, W.; Qi, S.; Wang, X.; He, X. The effect of hydration and dehydration on the conformation, assembling behavior and photoluminescence of PBLG. *Soft Matter* **2022**, *18*, 4396-4401.
19. Núñez-Villanueva, D. Revisiting 310-helices: biological relevance, mimetics and applications. *Explor Drug Sci.* **2024**, *2*, 6-37.

20. Moradi, M.; Babin, V.; Roland, C.; Sagui, C. A classical molecular dynamics investigation of the free energy and structure of short polyproline conformers. *J. Chem. Phys.* **2010**, *133*, 125104.
21. Wada, A. Dielectric Properties of Polypeptide Solutions. I. The Electric Dipole Moment of α Helix in Dioxane. *J. Chem. Phys.* **1958**, *29*, 674.
22. Wada, A. Dielectric Properties of Polypeptide Solutions. II. Relation between the Electric Dipole Moment and the Molecular Weight of α Helix. *J. Chem. Phys.* **1959**, *30*, 328-329.
23. Wada, A. Dielectric Properties of Polypeptide Solutions. III. Elucidation of the Critical Frequency of Dielectric Dispersion from the Molecular Shape of the α Helix. *J. Chem. Phys.* **1959**, *30*, 329-330.
24. Zimm, B. H.; Bragg, J. K. Theory of the Phase Transition between Helix and Random Coil in Polypeptide Chains. *J. Chem. Phys.* **1959**, *31*, 526-535.
25. Zimm, B.H.; Doty, P.; Iso, K. Determination of the parameters for helix formation in poly-γ-benzyl-L-glutamate. *Proc. Natl. Acad. Sci.* **1959**, *45*, 1601-1607.
26. Flory, P. J. Statistical Thermodynamics of Mixtures of Rodlike Particles. 6. Rods Connected by Flexible Joints. Macromolecules **1978**, *11*, 1141-1144.
27. Flory P. J.; Frost, R. S. Statistical Thermodynamics of Mixtures of Rodlike Particles. 3. The Most Probable Distribution. Macromolecules **1978**, *11*, 1126-1133.
28. Muroga, Y.; Nagasawa, M. On the Flexibility of Poly(*γ*-Benzyl L-Glutamate) in Helicogenic Solvents. *Biopolymers* **1998**, *45*, 281-288.
29. Kakizaki, M.; Nakayama, H.; Hideshima, T. Dielectric Relaxations in Poly(*γ*-*n*-alkyl-L-glutamate) II. Study of Relaxation due to Motion of the Side Chain and that due to Motion of the Main Chain. *Polym. J.* **1986**, *18*, 141-151.
30. Colomer, F. R.; Gómez Ribelles, J. L. Structural relaxation of poly(*γ*-benzyl-L-glutamate). *Polymer* **1989**, *30*, 849-855.
31. Doi, M.; Edwards, S. F. *The Theory of Polymer Dynamics*, Oxford University Press Inc., New York, **1986**.
32. Wang, C. C.; Pecora, R. Time-correlation functions for restricted rotational diffusion. *J. Chem. Phys.* **1980**, *72*, 5333-5340.
33. Hartmann, L.; Kratzmüller, T.; Braun, H.-G.; Kremer, F. Molecular dynamics of grafted PBLG in the swollen and in the dried state. *Macromol. Rapid Commun.* **2000**, *21*, 814-819.
34. Poche, D.S.; Moore, M.J.; Bowles, J.L. An unconventional method for purifying the N-carboxyanhydride derivatives of γ-alkyl-L-glutamates. *Synth. Commun.* **1999**, *29*, 843-854.
35. Papadopoulos, P. and Floudas, G. Polypeptide dynamics: Glass "transition" and "broken" helices. *Dielectric Newsletter* **2005**, Issue Nov.
36. Floudas, G.; Spiess, H. W. Self-Assembly and Dynamics of Polypeptides. *Macromol. Rapid Commun.* **2009**, *30*, 278-298.
37. Papadopoulos, P.; Floudas, G.; Schnell, I.; Klok, H.-A.; Aliferis, T.; Iatrou. H.; Hadjichristidis, N. “Glass transition” in peptides: Temperature and pressure effects. *J. Chem. Phys.* **2005**, *122*, 224906.

38. Deming, T. J. Synthetic polypeptides for biomedical applications. *Prog. Polym. Sci.* **2007**, *32*, 858-875.
39. Song, Z.; Han, Z.; Lv, S.; Chen, C.; Chen, L.; Yin, L.; Cheng, J. Synthetic polypeptides: from polymer design to supramolecular assembly and biomedical application. *Chem. Soc. Rev.* **2017**, *46*, 6570-6599.
40. Bonduelle, C. Secondary structures of synthetic polypeptide polymers. *Polym. Chem.* **2018**, *9*, 1517-1529.
41. Song, Z.; Fu, H.; Wang, R.; Pacheco, L.A.; Wang, X.; Lin, Y.; Cheng, J. Secondary structures in synthetic polypeptides from N-carboxyanhydrides: design, modulation, association, and material applications. *Chem. Soc. Rev.* **2018**, *47*, 7401-7425.
42. Papadopoulos, P.; Floudas, G.; Schnell, I.; Aliferis, T.; Iatrou, H.; Hadjichristidis, N. Nanodomain-Induced Chain Folding in Poly(*γ*-benzyl-L-glutamate)-*b*-polyglycine Diblock Copolymers. *Biomacromolecules* **2005**, *6*, 2352-236.
43. Gitsas, A.; Floudas, G.; Mondeshki, M.; Spiess, H.W.; Iatrou, H.; Hadjichristidis, N. Control of Peptide Secondary Structure and Dynamics in Poly(*γ*-benzyl-L-glutamate)-*b*-polyalanine Peptides. *Biomacromolecules* **2008**, *41*, 8072-8080.
44. Mondeshki, M.; Spiess, H. W.; Aliferis, T.; Iatrou, H.; Hadjichristidis, N.; Floudas, G. Hierarchical self-assembly in diblock copolypeptides of poly(*γ*-benzyl-L-glutamate) with poly(L-leucine) and poly(O-benzyl-L-tyrosine). *Eur. Pol. J.* **2011**, *47*, 668-674.
45. Graf, R.; Spiess, H. W.; Floudas, G.; Butt, H.-J.; Gkikas, M.; Iatrou, H. Conformational Transitions of Poly(L-proline) in Copolypeptides with Poly(*γ*-benzyl-L-glutamate) induced by Packing. *Macromolecules* **2012**, *45*, 9326-9332.
46. Hadjichristidis, N.; Iatrou, H.; Pispas, S.; Pitsikalis, M. Anionic polymerization: High vacuum techniques. *J. Polym. Sci., Part A: Polym. Chem.* **2000**, *38*, 3211-3234.
47. Gkikas, M.; Iatrou, H.; Thomaidis, N.S.; Alexandridis, P.; Hadjichristidis, N. Well-defined homopolypeptides, copolypeptides, and hybrids of poly(L-proline). *Biomacromolecules* **2011**, *12*, 2396-2406.
48. Gitsas, A.; Floudas, G.; Mondeshki, M.; Butt, H.-J.; Spiess, H. W.; Iatrou, H.; Hadjichristidis, N. Effect of Chain Topology on the Self-Organization and Dynamics of Block Copolypeptides: From Diblock Copolymers to Stars. *Biomacromolecules* **2008**, *9*, 1959-1966.
49. Gitsas, A.; Floudas, G.; Mondeshki, M.; Lieberwirth, I.; Spiess, H. W.; Iatrou, H.; Hadjichristidis, N.; Hirao, A. Hierarchical self-assembly and dynamics of a miktoarm star chimera composed of poly (*γ*-benzyl-L-glutamate), polystyrene, and polyisoprene. *Macromolecules* **2010**, *43*, 1874-1881.
50. Perly, B.; Douy, A.; Gallot, B. Block Copolymers Polybutadiene/Poly(benzyl-L-glutamate) and Polybutadiene/Poly(N5-hydroxypropylglutamine) Preparation and Structural Study by X-Ray and Electron Microscopy. *Die Makromol. Chem.* **1976**, *177*, 2569-2589.
51. Nakajima, A.; Hayashi, T.; Kugo, K.; Shinoda, K. Synthesis and Structural Study of the ABA Type Block Copolymer Consisting of Poly(*γ*-benzyl-L-glutamate) as the A Component and Polybutadiene as the B Component. *Macromolecules* **1979**, *12*, 840-843.

52. Yoda, R.; Komatsuzaki, S.; Nakanishi, E.; Hayashi, T. Microheterophase structure of A-B-A type block copolymer consisting of poly(γ-benzyl-L-glutamate) as the A component and polyisoprene as the B component. *Eur. Polym. J.* **1995**, *31*, 335-339.
53. Douy, A.; Gallot, B. Block copolymers with a polyvinyl and a polypeptide block: factors governing the folding of the polypeptide chains. *Polymer* **1982**, *23*, 1039-1044.
54. Klok, H.-A.; Langenwalter, J. F.; Lecommandoux, S. Self-Assembly of Peptide-Based Diblock Oligomers. *Macromolecules* **2000**, *33*, 7819-7826.
55. Lecommandoux, S.; Achard, M.-F.; Langenwalter, J. F.; Klok, H.-A. Self-Assembly of Rod−Coil Diblock Oligomers Based on α-Helical Peptides. *Macromolecules* **2001**, *34*, 9100-9111.
56. Papadopoulos, P.; Floudas, G.; Schnell, I.; Lieberwirth, I.; Nguyen, T. Q.; Klok, H.-A. Thermodynamic Confinement and α-Helix Persistence Length in Poly(γ-benzyl-L-glutamate)-*b*-poly(dimethyl siloxane)-*b*-poly(γ-benzyl-L-glutamate) Triblock Copolymers. *Biomacromolecules* **2006**, *7*, 618-626.
57. Ibarboure, E.; Rodríguez-Hernández, J. Supramolecular structures from self-assembled poly(γ-benzyl-L-glutamate)–polydimethylsiloxane–poly(γ-benzyl-L-glutamate) triblock copolypeptides in thin films. *Eur. Polym. J.* **2010**, *46*, 891-899.
58. D'souza, A.A.; Shegokar, R. Polyethylene glycol (PEG): a versatile polymer for pharmaceutical applications. *Expert Opin. Drug Deliv.* **2016**, *13*, 1257-1275.
59. Osada, K.; Kataoka, K. Drug and Gene Delivery Based on Supramolecular Assembly of PEG-Polypeptide Hybrid Block Copolymers. *Adv. Polym. Sci.* **2006**, *202*, 113-153.
60. Kugo, K.; Ohji, A.; Uno, T.; Nishino, J. Synthesis and Conformations of A-B-A Tri-Block Copolymers with Hydrophobic Poly(γ-benzyl-L-glutamate) and Hydrophilic Poly(ethylene oxide). *Polym. J.* **1987**, *19*, 375-381.
61. Cho, C.-S.; Kim, S.-W.; Komoto, T. Synthesis and structural study of an ABA block copolymer consisting of poly(γ-benzyl-L-glutamate) as the A block and poly(ethylene oxide) as the B block. *Die Makromol. Chem.* **1990**, *191*, 981-991.
62. Cho, C.-S.; Nah, J.-W.; Jeong, Y.-I.; Cheon, J.-B.; Asayama, S.; Ise, H.; Akaike, T. Conformational transition of nanoparticles composed of poly(γ-benzyl-L-glutamate) as the core and poly(ethylene oxide) as the shell. *Polymer* **1999**, *40*, 6769-6775.
63. Floudas, G.; Papadopoulos, P.; Klok, H.A.; Vandermeulen, G.W.M.; Rodriguez-Hermamdez, J. Hierarchical Self-Assembly of Poly(γ-benzyl-L-glutamate)-Poly(ethyleneglycol)-Poly(γ-benzyl-L-glutamate) Rod-Coil-Rod Triblock Copolymers. *Macromolecules* **2003**, *36*, 3676-3683.
64. Parras, P.; Castelletto, V.; Hamley, I. W.; Klok, H.-A. Nanostructure formation in poly(γ-benzyl-L-glutamate)–poly(ethylene glycol)–poly(γ-benzyl-L-glutamate) triblock copolymers in the solid state. *Soft Matter* **2005**, *1*, 284.

Chapter 3. Experimental Techniques and Methods of Analysis

The following experimental techniques were employed in the present work: Dielectric Spectroscopy (DS), Differential Scanning Calorimetry (DSC), Temperature-Modulated Differential Scanning Calorimetry (TM-DSC), Small-Angle X-ray Scattering (SAXS), Wide-Angle X-ray Scattering (WAXS), ^{13}C Solid-State NMR, Polarizing Optical Microscopy (POM) and Rheology. Below, we report on the technical characteristics of these techniques and their respective measurement protocols.

3.1 Dielectric spectroscopy

The interaction of electromagnetic radiation with molecular systems results in quantized transitions between the electronic, vibrational and rotational molecular energy states, that can be observed by UV, visible and infrared absorption spectroscopy at frequencies above about 1 THz (10^{12} Hz). The interaction of electromagnetic waves with matter in the frequency range between 10^{-6} and 10^{12} Hz is the domain of broadband dielectric spectroscopy.[1,2] In this extended dynamic range, molecular and collective dipolar fluctuations, charge transport and polarization effects at the inner and outer boundaries take place, and determine the dielectric properties of the sample. Broadband dielectric spectroscopy can therefore provide a wealth of information about: (i) dipole relaxation resulting from the reorientational motions of molecular dipoles and (ii) electrical conduction arising from the translational motions of electrical charges (e.g., ions). Each material responds differently in the presence of an external alternating electric field and different dielectric absorption mechanisms are observed at a specific resonance frequency, ω, or relaxation time, $\tau = 1/\omega$, as illustrated in Figure 3.1.

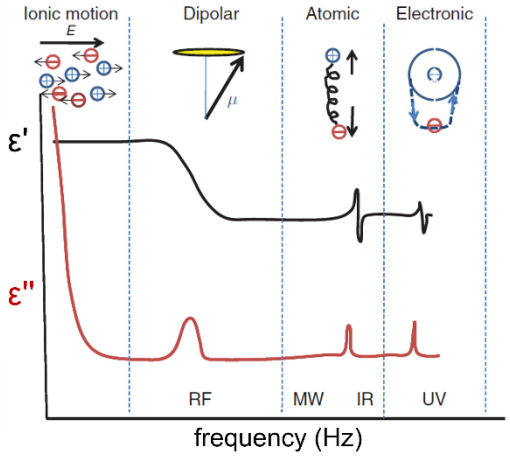

Figure 3.1. Diagram of dielectric relaxation mechanisms as they appear in the dielectric permittivity (ε') and dielectric losses (ε'') as a function of frequency. Different types of polarization (dipolar, ionic, atomic and electronic) appear depending on the frequency range of the external electric field.

In general, dielectric mechanisms can be divided into relaxation and resonance processes, at low and high frequencies, respectively. The most common mechanisms, starting from high frequencies, are:

(i) *Electronic polarization*: this resonant process appears when isolated atoms or molecules are placed in an electric field ($f = 10^{15}$ Hz).

(ii) *Atomic polarization*: it is also a resonant process found in ionic or partially ionic substances whose molecules are formed of atoms having excess charges of opposite polarities ($f \sim 10^{13}$ Hz, infrared regime) (i.e., ionic crystals).

(iii) *Dipolar relaxation*: it is associated with the relaxation of intrinsic dipoles with respect to the external electric field ($f = 10^{-2}$ Hz – 10^{9} Hz).

(iv) *Ionic relaxation*: it comprises ionic conductivity and interfacial or space-charge polarization. Ionic conductivity dominates at low frequencies and high temperatures. Interfacial polarization occurs when charge carriers are trapped at interfaces in heterogeneous systems or when they are trapped by the electrode surface (electrode polarization (EP)).

3.1.1 Response in a static electric field

The polarization, $\boldsymbol{P}$, is defined as the difference between the electric displacement, $\boldsymbol{D}$, due to bound charges and the electric field strength, $\boldsymbol{E}$, due to free charges[3]

$$\boldsymbol{P} = \frac{\boldsymbol{D} - \boldsymbol{E}}{4\pi} \tag{3.1}$$

Molecules with a permanent dipole moment $\boldsymbol{\mu}$ can be oriented by an external electric field $\boldsymbol{E}$. Hence, for a system containing only one kind of dipoles, a macroscopic polarization $\boldsymbol{P}$ of the molecules within a volume $\boldsymbol{V}$ becomes

$$\boldsymbol{P} = \frac{1}{V}\sum_i \boldsymbol{\mu}_i + \boldsymbol{P}_\infty = \frac{N}{V}\langle\boldsymbol{\mu}\rangle + \boldsymbol{P}_\infty \tag{3.2}$$

where N denotes the total number of dipoles in the system, $\langle\boldsymbol{\mu}\rangle$ is the mean dipole moment and $\boldsymbol{P}_\infty$ is an induced polarization (electronic and atomic polarization). The dielectric permittivity, $\varepsilon^* = \varepsilon'(\omega) - i\varepsilon''(\omega)$, where $\varepsilon'(\omega)$ is the real part that is proportional to the energy stored reversibly in the system per period and the imaginary part $\varepsilon''(\omega)$ is proportional to the dissipated energy per period, is related to the macroscopic polarization by

$$\boldsymbol{P} = (\varepsilon^* - 1)\varepsilon_0\boldsymbol{E} \tag{3.3}$$

where $\varepsilon_0 \left(= 8.854 \times 10^{-12}\,\frac{F}{m}\right)$ is the dielectric permittivity of vacuum. Eq. 3.3 describes only the dielectric properties in the linear regime, ($E < 10^6 Vm^{-1}$), which we consider in the present work.

Assuming non-interacting dipoles and in the absence of local-filed corrections, the mean value of the dipole moment is given by the counterbalance of the thermal energy and the interaction energy U of a dipole with the electric field given by $U = -\boldsymbol{\mu}\cdot\boldsymbol{E}$. According to Boltzmann statistics, the ensemble average of the dipole moment is given by

$$\langle\boldsymbol{\mu}\rangle = \frac{\int_{4\pi}\boldsymbol{\mu}\,exp\left(\frac{\boldsymbol{u}\cdot\boldsymbol{E}}{k_BT}\right)d\Omega}{\int_{4\pi}exp\left(\frac{\boldsymbol{\mu}\cdot\boldsymbol{E}}{k_BT}\right)d\Omega} \tag{3.4a}$$

where T is the temperature, k_B is the Boltzmann constant and $d\Omega$ the differential space angle. Only the dipole moment component which is parallel to the direction of the external electric field contributes to the polarization. Therefore, the interaction energy is given by $U = -|\mu||E|\cos\theta$ where, θ is the angle between the orientation of the dipole moment $\boldsymbol{\mu}$ and the electric field $\boldsymbol{E}$. So Eq. (3.4a) simplifies to

$$\langle\boldsymbol{\mu}\rangle = \frac{\int_0^\pi \boldsymbol{\mu}\cos\theta\,exp\left(\frac{|\boldsymbol{\mu}||\boldsymbol{E}|\cos\theta}{k_BT}\right)\frac{1}{2}sin\,\theta\,d\theta}{\int_0^\pi exp\left(\frac{|\boldsymbol{\mu}||\boldsymbol{E}|\cos\theta}{k_BT}\right)\frac{1}{2}sin\,\theta\,d\theta} \tag{3.4b}$$

The term , $\frac{1}{2} sin\,\theta\, d\theta$, corresponds to components of the space-angle in θ direction. With $a = \frac{|\mu||E|}{k_B T}$ and $x = \frac{|\mu||E|\,cos\,\theta}{k_B T}$, it results $\langle \mu \rangle = \mu \langle cos\,\theta \rangle$, where

$$\langle cos\,\theta \rangle = \frac{1}{a}\frac{\int_{-a}^{a} x\, exp(x)\, dx}{\int_{-a}^{a} exp(x)\, dx} = \frac{exp(a) + exp(-a)}{exp(a) - exp(-a)} - \frac{1}{a} = coth(a) - \frac{1}{a} = \Lambda(\alpha) \tag{3.5}$$

where $\Lambda(\alpha)$ is the Langevin function that can be written in a Taylor series $\Lambda(\alpha) = \frac{1}{3}\alpha - \frac{1}{45}\alpha^3 + \frac{2}{945}\alpha^5 - \frac{1}{4725}\alpha^7 + \cdots$ .... For small values of the electric field (i.e., $E \ll k_B T/\mu$, e.g., for $\mu\sim$ 1 D and $k_B T \sim 0.025\ eV$ we get $E \ll 10^6 \frac{V}{m}$, and $a = \frac{|\mu||E|}{k_B T} = 0.83 \times 10^{-3} < 0.1$) the approximation $\Lambda(\alpha) \approx \frac{\alpha}{3}$ is valid. Hence, the dipole moment will obey a linear dependence with the electric field, therefore Eq(3.4b) reduces to

$$\langle \boldsymbol{\mu} \rangle \cong \frac{\mu^2}{3k_B T}\boldsymbol{E} \tag{3.6}$$

The intensity of the electric field that was applied in the experiments of this work was ~ 10^4 V/m (the sample thickness was ~ 50 μm and the applied voltage was ~ 1Volt), i.e., within the linear regime.

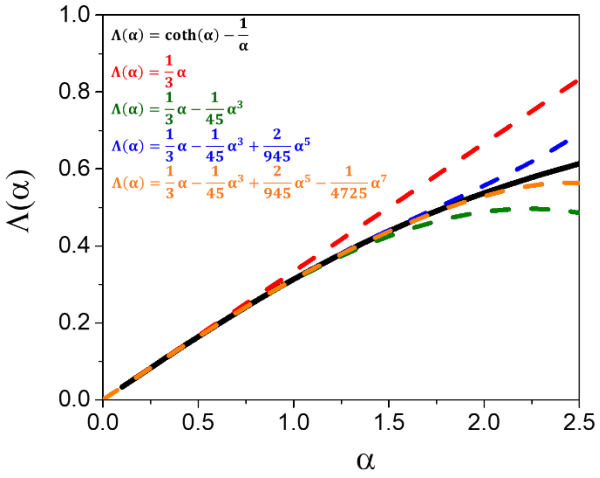

Figure 3.2. Dependence of the Langevin function $\Lambda(\alpha)$ (solid line), together with the expansion up to the fourth order of the Taylor series.

From Eq. (3.2), (3.3), and (3.6) the contribution of the orientational polarization to the dielectric function can be calculated as

$$\varepsilon_S - \varepsilon_\infty = \frac{1}{3\varepsilon_0}\frac{\mu^2}{k_B T}\frac{N}{V}, \quad \varepsilon_\infty = 1 + \frac{P_\infty}{\varepsilon_0 E} \tag{3.7}$$

where $\varepsilon_S = \lim_{\omega\to 0}\varepsilon'(\omega)$ and $\varepsilon_\infty = \lim_{\omega\to\infty}\varepsilon'(\omega)$ are the limits of the dielectric constant, ε', at low- and high- frequencies, respectively.

Eq. (3.7) allows one to estimate the mean molecular dipole moment, $\langle\mu^2\rangle^{\frac{1}{2}}$, from dielectric spectra, provided that: (i) the dipoles do not interact with each other (true only for very dilute systems) and (ii) local field effects (shielding of the external electric field) are negligible. Onsager treated the problem of the local field effects for polar molecules by considering the enhancement of the permanent dipole moment of a molecule, $\boldsymbol{\mu}$, by the polarization of the environment (reaction field). The detailed calculation gives[4]

$$\varepsilon_S - \varepsilon_\infty = \frac{1}{3\varepsilon_0} F \frac{\mu^2}{k_B T}\frac{N}{V}, \qquad F = \frac{\varepsilon_S(\varepsilon_\infty + 2)^2}{3(2\varepsilon_S + \varepsilon_\infty)} \tag{3.8}$$

where F is the factor of local field. Eq. (3.8) can be used to estimate dipole moments for non-associating organic liquids, but fails for polar associating liquids. The reason is the static orientation correlations between molecules, that are not considered in the derivation of the Onsager equation. Therefore, Kirkwood and Fröhlich introduced the correlation factor, g, to model the interaction between dipoles with respect to the ideal case of noninteracting dipoles. In general, the Kirkwood/Fröhlich correlation factor is defined by[5,6]

$$\mathrm{g} = \frac{\langle\sum_i \boldsymbol{\mu}_i \sum_j \boldsymbol{\mu}_i\rangle}{N|\boldsymbol{\mu}|^2} = 1 + \frac{\langle\sum_i \sum_{i<\mathrm{j}} \boldsymbol{\mu}_i\boldsymbol{\mu}_j\rangle}{N|\boldsymbol{\mu}|^2} \tag{3.9}$$

where μ^2 is the mean square dipole moment for noninteracting isolated dipoles that can be measured. It was found experimentally that the g-factor can be less that or greater than unity depending on the tendency of neighboring dipoles to align parallel or antiparallel to each other. The contribution of the Kirkwood/Fröhlich correlation factor g to the dielectric function can be calculated as

$$\varepsilon_S - \varepsilon_\infty = \frac{1}{3\varepsilon_0}\mathrm{g}F\frac{\mu^2}{k_B T}\frac{N}{V} \tag{3.10}$$

with

$$\mathrm{g} = 1 + z\langle\cos\gamma\rangle \tag{3.11}$$

where z is the coordination number and γ is the angle between the test dipole and a neighbor. Usually, the g-factor is difficult to be measured and the effective dipole moment μ_{eff} can only be measured as

$$\mu_{eff} = (g\mu^2)^{\frac{1}{2}} \tag{3.12}$$

3.1.2 Response to an alternating electric field

The polarization that is created by an alternating electric field, $E(t)$, in the framework of linear response theory (i.e., small electric fields), is given by

$$P(t) = P_\infty + \varepsilon_0 \int_{-\infty}^{t} \varepsilon(t - t') \frac{dE(t')}{dt'} dt' \tag{3.13}$$

where $\varepsilon(t)$ is the time-dependent dielectric function and P_∞ covers all contributions arising from induced polarization. Eq. (3.13) is based only on linearity and causality. $P(t)$ can be measured directly as the time-dependent response caused by a step-like change of the external electrical field.

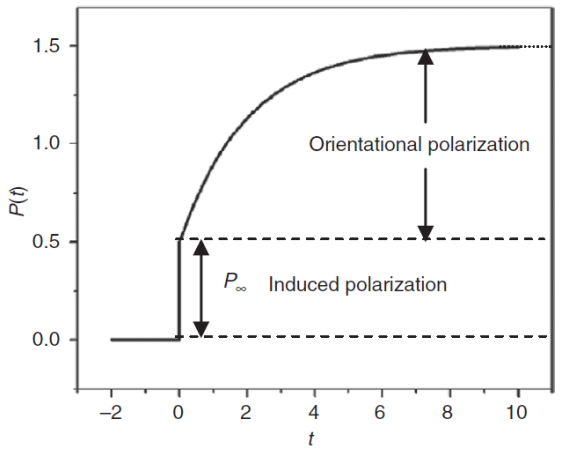

Figure 3.3. Schematic illustration of the time dependence of the polarization. At $t = 0$, the time-dependence polarization, $P(t)$, is equal to the induced polarization, P_∞, while at $t > 0$, it is equal to the orientational polarization. [6]

If a stationary periodic electric field $E(t, \omega) = E_0\, exp(-i\omega t)$, where $\omega = 2\pi f$ is the angular frequency, is applied to the system, Eq. (3.13) can be written as

$$P(t, \omega) = \varepsilon_0(\varepsilon^*(\omega) - 1)E(t, \omega) \tag{3.14}$$

The relationship of $\varepsilon^*(\omega)$ to the time dependent dielectric function $\varepsilon(t)$ is given by

$$\varepsilon^*(\omega) = \varepsilon'(\omega) - i\varepsilon''(\omega) = \varepsilon_\infty - \int_0^\infty \frac{d\varepsilon(t)}{dt} exp(-i\omega t)\, dt \tag{3.15}$$

Eq. (3.15) is a one-sided Fourier transformation. The real and the imaginary part of $\varepsilon^*(\omega)$ are related to each other by the Kramers-Krönig relations[6]

$$\varepsilon'(\omega) - \varepsilon_\infty = \frac{2}{\pi}\int_0^\infty \frac{\xi\varepsilon''(\xi)}{\xi^2 - \omega^2} d\xi$$

$$\varepsilon''(\omega) = \frac{2}{\pi}\int_0^\infty \frac{\xi(\varepsilon'(\xi) - \varepsilon_\infty)}{\xi^2 - \omega^2} d\xi + \frac{\sigma}{\varepsilon_0\omega} \tag{3.16}$$

where ξ is a complex quantity. From an experimental point of view, Eq. (3.16) means that both $\varepsilon'(t)$ and ε''(t) ideally carry the same information, but this is only the case in the absence of interfacial polarization or EP. In addition, the second equation contains a conductivity term, $\sigma/\varepsilon_0\omega$, that is the dominant mechanism at low frequencies.

The response of a system can also be expressed in terms of the complex electric modulus, $M^*(\omega)$, which is related to the complex dielectric function as

$$M^*(\omega)\varepsilon^*(\omega) = 1 \tag{3.17}$$

The fluctuation-dissipation theorem (FDT)[6] states a general relationship between the response of a given system to an external disturbance and the internal fluctuation of the system in the absence of the disturbance. Such a response is characterized by a response function or equivalently by an admittance, or an impedance. For dielectric relaxation, the complex dielectric function, is related to the dipole moment correlation function, $\Phi(t)$, via Fourier transformation

$$\Phi(t) = \frac{\varepsilon(t) - \varepsilon_\infty}{\varepsilon_0 - \varepsilon_\infty} = \frac{\langle\mu(t)\cdot\mu(0)\rangle}{\langle\mu^2\rangle} \tag{3.18}$$

where t denoted the time variable. The $\varepsilon(t)$ and $\varepsilon^*(\omega)$ are related to the correlation function $\Phi(t)$ of the dipolar fluctuations by

$$\frac{\varepsilon^*(\omega) - \varepsilon_\infty}{\varepsilon_S - \varepsilon_\infty} = 1 - i\omega\int_0^\infty \Phi(t)\, exp(-i\omega t)\, dt \tag{3.19}$$

The real, $\varepsilon'(\omega)$, and imaginary, $\varepsilon''(\omega)$, parts of the complex dielectric function can be calculated from the correlation function

$$\frac{\varepsilon'^{(\omega)} - \varepsilon_\infty}{\varepsilon_S - \varepsilon_\infty} = 1 - \omega\int_0^\infty \Phi(t)\, sin(\omega t) dt$$

$$\frac{\varepsilon''(\omega)}{\varepsilon_S - \varepsilon_\infty} = \omega \int_0^\infty \Phi(t)\, cos(\,\omega t) dt \tag{3.20}$$

3.1.3 Distribution of relaxation times

Assuming that the decrease of the polarization in the absence of an electric field, due to the occurrence of a field in the past, depends only on the value of the orientation polarization at that instant, and denoting the proportionality constant by $1/\tau_D$, one obtains the following differential equation for the orientation polarization in the absence of an electric field

$$\frac{d\boldsymbol{P}(t)}{dt} = -\frac{1}{\tau_D}\boldsymbol{P}(t) \tag{3.21}$$

where τ_D is a characteristic relaxation time. The solution of the first order differential Eq. (3.21) leads to an exponential decay for the correlation function Φ(t)

$$\Phi(t) = exp\left(-\frac{t}{\tau_D}\right) \tag{3.22}$$

Inserting Eq. (3.22) into Eq. (3.19), one gets for the complex dielectric function $\varepsilon^*(\omega)$

$$\varepsilon^*(\omega) = \varepsilon_\infty + (\varepsilon_S - \varepsilon_\infty)\left(1 - i\omega \int_0^\infty exp\left(\frac{-t}{\tau_D}\right) exp(-i\omega t)\, dt\right) \tag{3.23a}$$

$$= \varepsilon_\infty + (\varepsilon_S - \varepsilon_\infty)\left(1 - \frac{i\omega\tau_D}{1 + i\omega\tau_D}\right) = \varepsilon_\infty + (\varepsilon_S - \varepsilon_\infty)\frac{1}{1 + i\omega\tau_D}$$

$$\varepsilon^*(\omega) = \varepsilon_\infty + \frac{\Delta\varepsilon}{1 + i\omega\tau_D} \begin{cases} \varepsilon'(\omega) = \varepsilon_\infty + \dfrac{\Delta\varepsilon}{1 + \omega^2{\tau_D}^2} \\ \varepsilon''(\omega) = \Delta\varepsilon \dfrac{\omega\tau_D}{1 + \omega^2{\tau_D}^2} \end{cases} \tag{3.23b}$$

These relations are known as the Debye formulas. The Debye process has a relaxation time distribution, which is symmetrical around $f_{max} = \omega_{max}/2\pi = 1/2\pi\tau_{max}$ and with a full-width at half- maximum of ~ 1.14 decades in frequency for the dielectric loss. In most cases, the half width of the measured loss peaks is much broader than the predicted by Eq. (3.23) and in addition, their shapes are asymmetric and have a high-frequency tail. This is called non-Debye (or non-ideal)

relaxation behavior. In the literature, several empirical model functions, mostly generalizations of the Debye function, have been developed and tested to describe broadened and/or asymmetric loss peaks. Among these empirical model functions, the most important are the Kohlrausch-Williams-Watts (KWW), Cole-Cole (CC), Cole-Davidson (CD) and the Havriliak-Negami function (HN). The HN function, with two shape parameters, is most commonly used in the frequency domain, as will be discussed in detail later in the section on analyzing dielectric spectra.

Table 3.1. Time-scale relations of the dielectric permittivity, ε^*, and the electric modulus, M^*, for the Debye and the non-Debye processes.

Debye:	$\varepsilon^*(\omega) = \varepsilon_\infty + (\varepsilon_S - \varepsilon_\infty)\frac{1}{1+i\omega\tau}$	$\tau_M = \tau_\varepsilon \times \left(\frac{\varepsilon_\infty}{\varepsilon_S}\right)$
KWW:	$\varepsilon^*(\omega) = \varepsilon_\infty + (\varepsilon_S - \varepsilon_\infty) \times \left[1 - exp\left[-\left(\frac{t}{\tau}\right)^\beta\right]\right]$	$\tau_M \sim \tau_\varepsilon \times \left(\frac{\varepsilon_\infty}{\varepsilon_S}\right)^{\frac{1}{\beta}}$
CC:	$\varepsilon^*(\omega) = \varepsilon_\infty + (\varepsilon_S - \varepsilon_\infty)\frac{1}{1+(i\omega\tau)^a}$	$\tau_M = \tau_\varepsilon \times \left(\frac{\varepsilon_\infty}{\varepsilon_S}\right)^{\frac{1}{a}}$
CD:	$\varepsilon^*(\omega) = \varepsilon_\infty + (\varepsilon_S - \varepsilon_\infty)\frac{1}{(1+i\omega\tau)^\gamma}$	$\tau_M \sim \tau_\varepsilon \times \left(\frac{\varepsilon_\infty}{\varepsilon_S}\right)^{\frac{1}{\gamma}}$
HN:	$\varepsilon^*(\omega) = \varepsilon_\infty + (\varepsilon_S - \varepsilon_\infty)\frac{1}{[1+(i\omega\tau)^a]^\gamma}$	$\tau_M \sim \tau_\varepsilon \times \left(\frac{\Delta\varepsilon}{\varepsilon_\infty}\right)^{-\frac{1}{a}}$

3.1.4 Experimental Setup

Dielectric Spectroscopy (DS) measurements as a function of temperature (T) and pressure (P) were performed with a Novocontrol Alpha frequency analyzer (Figure 3.4). The temperature protocol involved "isobaric" measurements at atmospheric pressure within the temperature range from 183.15 to 423.15 K in steps of 5 K for frequencies in the range from 10^{-2} to 10^7 Hz. All samples were prepared under vacuum by pressing the electrodes to the spacer thickness where necessary. The sample cell consisted of two electrodes, 20 mm (or 10 mm when the sample quantity was limited) in diameter and 50 μm in thickness for all polymers, the latter maintained by Teflon spacers. Measurements under hydrostatic pressure (e.g. "isothermal") were carried out with a Novocontrol pressure cell. The pressure protocol involved "isothermal" measurements within the pressure range from 0.1 to 240 MPa for temperatures in the range 293 – 423 K. The pressure setup consisted of a T-controlled cell, hydraulic closing press with air pump, and air pump for hydrostatic test pressure. For the P-dependent measurements, samples were placed between 20 mm electrodes and Teflon spacers were used to maintain the thickness. Subsequently, the capacitor was wrapped

with Teflon tape and placed inside a Teflon ring, in order to prevent the flow of silicone oil (DOW CORNING 550 Fluid) into the sample. The silicone oil is the liquid that uniformly transmits the pressure to the capacitor. The isothermal measurements of relaxation times were performed with temperature stability better than 0.1 K and pressure stability better than 2 MPa. The complex dielectric permittivity, $\varepsilon^* = \varepsilon' - i\varepsilon''$, where ε' is the real and ε'' is the imaginary part, was obtained as a function of angular frequency, ω *(*$= 2\pi f = 1/\tau$*)*, temperature, and pressure, i.e., $\varepsilon^*(T, P, \omega)$.[1,2]

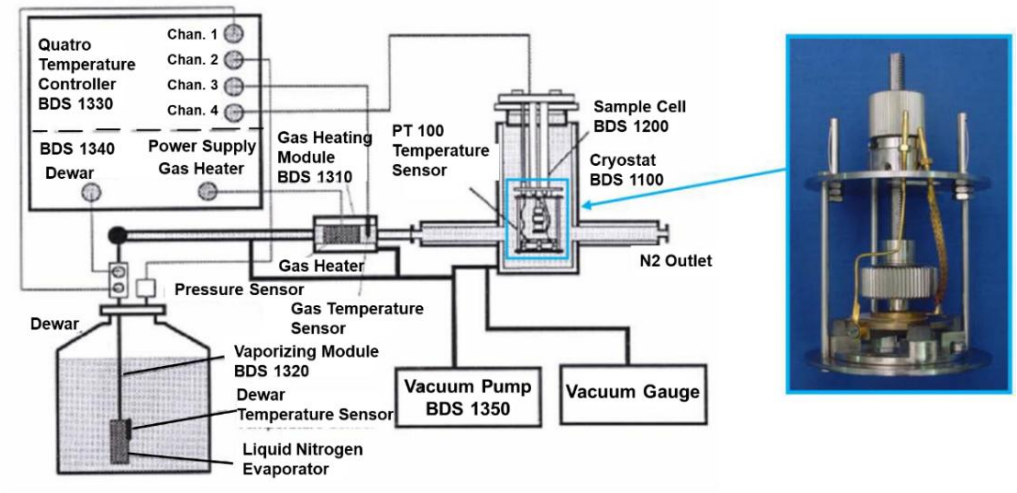

Figure 3.4. (Left) The experimental setup for dielectric spectroscopy measurements under atmospheric pressure with variable temperature, along with the temperature control system. (Right) Enlarged view of a section of the measurement cell with the two electrodes.

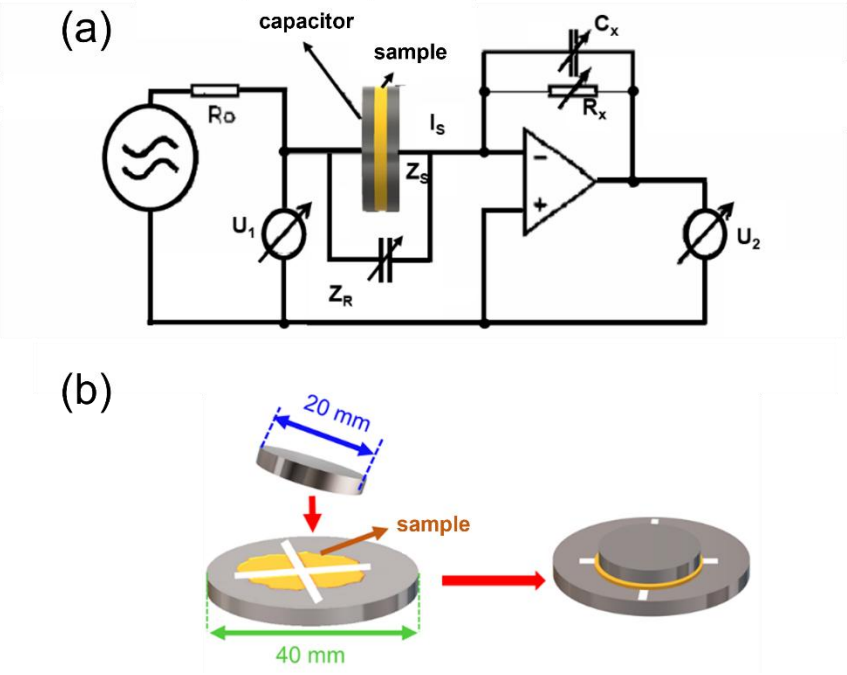

Figure 3.5.(a) Schematic representation of the experimental setup. The sample under investigation is placed between the electrodes of a capacitor, and its complex impedance is recorded, to obtain the dielectric function $\varepsilon^*(\omega)$. (b) Schematic representation of the sample preparation process.

Figure 3.5 illustrates the setup used for measuring the complex impedance of a capacitor, in which the dielectric material is the sample under investigation. If Z_x is a variable impedance which can be changed in resistance R_x, and capacitance C_x, the sample impedance $Z^*(\omega)$ of a direct measurements is given by

$$Z^*(\omega) = Z'' + iZ'' = \frac{U_1}{I_S} = -\frac{U_1}{U_2} Z_X \tag{3.24}$$

where the voltage U_1 applied from the generator to the sample and the sample current I_S are directly measured by the analyzer. The complex dielectric function $\varepsilon^*(\omega)$ is related to the sample impedance $Z^*(\omega)$ by

$$\varepsilon^*(\omega) = \frac{1}{i\omega C_0 Z^*(\omega)} \Rightarrow \begin{cases} \varepsilon' = \dfrac{Z''}{\omega C_0 |Z|^2} \\ \varepsilon'' = \dfrac{Z''}{\omega C_0 |Z|^2} \end{cases} \tag{3.25}$$

where C_0 is the capacity of the empty sample capacitor. At $\varepsilon' = 0$, the sample impedance Z will represent a resistor R, i.e., $Z = R$, therefore $\varepsilon''=1/\omega R C_0$ which reflects that the ionic conductivity is presented only in the imaginary part.

In the frequency domain, the complex dielectric function $\varepsilon^*(\omega)$ is related to the complex electric modulus $M^*(\omega)$ through

$$M^*(\omega) \equiv M' + iM'' = \frac{1}{\varepsilon^*(\omega)} \Rightarrow \begin{cases} M' = \dfrac{\varepsilon'}{\varepsilon'^2 + \varepsilon''^2} \\ M'' = \dfrac{\varepsilon''}{\varepsilon'^2 + \varepsilon''^2} \end{cases} \tag{3.26}$$

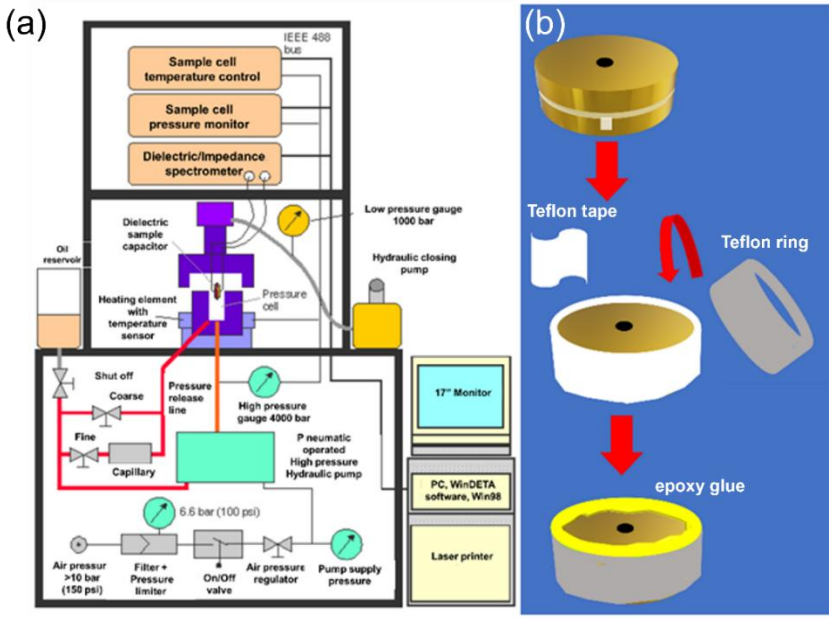

Figure 3.6. Schematic representation of (a) the dielectric measurement setup under varying pressures, and (b) the sample preparation process.

For the pressure-dependent measurements (Figure 3.6), a hydraulic system was used to apply hydrostatic pressure to the sample via silicone oil. The samples were prepared similarly, and then insulated with Teflon tape, a Teflon ring and epoxy glue to prevent the silicone oil from penetrating. The system is capable of applying pressures ranging from 0.1 to 300 MPa within a temperature range of 293 K to 523 K. The results of the pressure-dependent measurements were used to determine the characteristic volumes associated with the processes studied.

3.1.5 Analysis of dielectric spectra

The isothermal dielectric loss spectra ε'' were used to determine the relaxation times and their distributions at each temperature and pressure. The analysis was made with the empirical equation of Havriliak and Negami (HN):

$$\varepsilon^*(\omega,T) = \varepsilon_\infty + \sum_k \frac{\Delta\varepsilon_k(T)}{[1+(i\cdot\omega\cdot\tau_{HN,k}(T))^{m_k}]^{n_k}} + \frac{\sigma_0(T)}{i\varepsilon_0\omega} \tag{3.27}$$

where $\Delta\varepsilon_k$ is the dielectric strength, $\tau_{HN,k}$ is the H-N characteristic relaxation time, m_k, n_k (with limits $0.2 < m_k$, $mn_k \leq 1$) describe, respectively, the symmetrical and asymmetrical broadening of the distribution of relaxation times and the index k indicates the process under investigation. At lower frequencies, the dielectric loss sharply rises due to conductivity contribution as $\sigma_0/\varepsilon_0\omega$, where σ_0 is the dc-conductivity and ε_0 (= 8.854×10^{-12} F·m^{-1}) is the permittivity of free space. From $\tau_{HN,k}$, the relaxation times at maximum loss, τ_{max}, were obtained analytically from the HN equation as follows

$$\tau_{max,k} = \tau_{HN,k}[sin\left(\frac{\pi m_k n_k}{2(1+n_k)}\right) / sin\left(\frac{\pi m_k}{2(1+n_k)}\right)]^{1/m_k} \tag{3.28}$$

These relaxation times correspond to the relaxation times of the segmental processes. Except for the measured ε'', the derivative of the real part of the dielectric permittivity, ε', ($\frac{d\varepsilon'}{dln\omega} \approx -(2/\pi)\varepsilon''$) was used in the analysis of the dynamic behavior.[7]

3.2 Differential Scanning Calorimetry

Differential Scanning Calorimetry (DSC) is a widely used thermoanalytical technique for studying the thermal properties of materials. It measures the difference in the amount of heat required to increase (or decrease) the temperature of a sample and a reference as a function of temperature. The sample and reference are subjected to a controlled temperature program, and the resulting heat flow difference reveals critical thermal events such as phase transitions. Melting (T_m) and crystallization (T_c) appear as endothermic and exothermic peaks, respectively, while the liquid-to-glass "transition" appears as a step in the DSC baseline, due to a change in the heat capacity of the material.

The thermal measurements were performed using a Q2000 DSC system (TA Instruments), calibrated for optimal performance. The calibration procedure involved three steps: (i) system conditioning to ensure proper gas flow and remove residual moisture, (ii) baseline calibration using a sapphire standard to determine time constants and heat capacities of the sensors, and (iii) calibration of enthalpy and transition temperatures using indium as a standard (ΔH = 28.71 J·g^{-1}, T_m = 428.8 K). As a final check, the system response was measured with empty pans to verify the change in baseline. Measurements were performed using sealed aluminum pans (Tzero Aluminum Hermetic Pan/Lid) with an empty pan as the reference. The thermal protocol included two full cycles of heating and cooling between 223 K and 423 K at 10 K·min^{-1}. During the experiment, differences in heat flow between the sample and reference were recorded, allowing the determination of enthalpy changes associated with phase transitions. These differences occur because, during a phase transition, the sample requires more (or less) heat to maintain the same temperature as the reference. The heat flow is governed by the energy balance

$$\frac{dH}{dt} = mc_P \frac{dT}{dt} \tag{3.29}$$

where $\Delta H = \int c_p dt$, is enthalpy, m is the mass of the sample, $c_p = \frac{1}{m}\left(\frac{dQ}{dT}\right)_P$ is specific heat capacity, and $\frac{dT}{dt}$ is the temperature ramp rate.

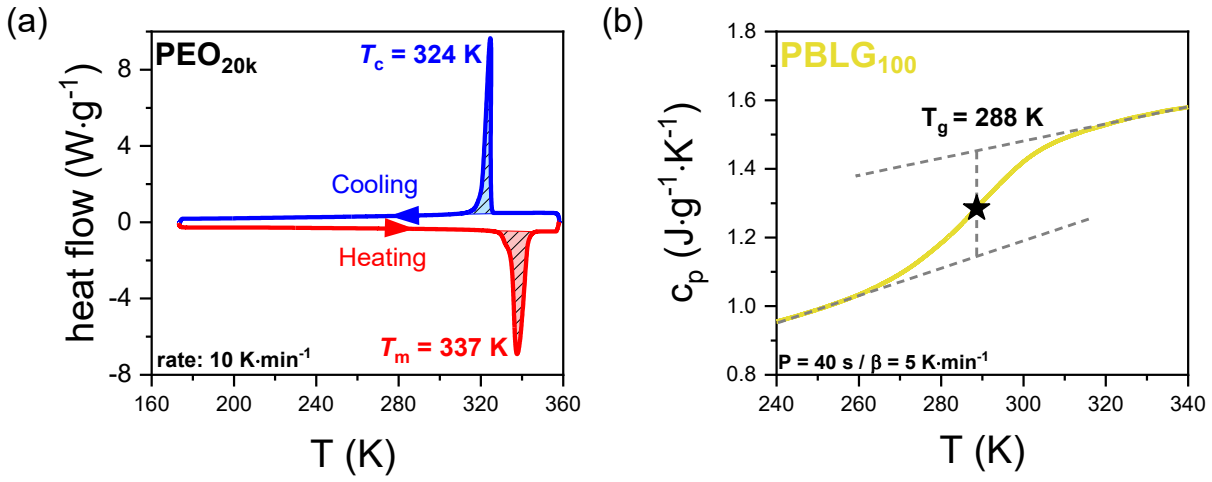

Figure 3.7. (a) Temperature dependence of the heat flow for polyethylene oxide (PEO) during the second cooling and subsequent heating. The exothermic and endothermic peaks correspond to the crystallization temperature (T_c) and melting temperature (T_m), respectively. (b) Temperature

dependence of the specific (reversing) heat capacity of $PBLG_{100}$, obtained from TM-DSC at a period of modulation of $P = 40$ s ($\beta = 5$ K·s^{-1}). Star symbol corresponds to the glass temperature (T_g).

DSC thermograms provide areas corresponding to enthalpy changes. For example, in the case of PEO_{20k}, an exothermic peak during cooling indicates crystallization, while upon heating, an endothermic melting peak is observed with $\Delta H_m = 164$ J·g^{-1}. For amorphous or semi-crystalline polymers, the glass temperature is determined by extrapolating the baseline before and after the step, and drawing a vertical line such that the shaded areas on either side are equal. The intersection defines the T_g.

3.3 Temperature-Modulated Differential Scanning Calorimetry

Temperature-modulated differential scanning calorimetry (TM-DSC) measurements were employed with the same Q2000 (TA Instruments). A low frequency sinusoidal signal is applied to the standard DSC profile as $T=T_0+\beta t+A_T\cdot\sin(\omega t)$,[8] where β is the rate, A_T is the amplitude (typically 1 K) and ω is the angular frequency. Figure 3.8 shows the linear and modulated (harmonic) heating rates for the $PBLG_{46}$.

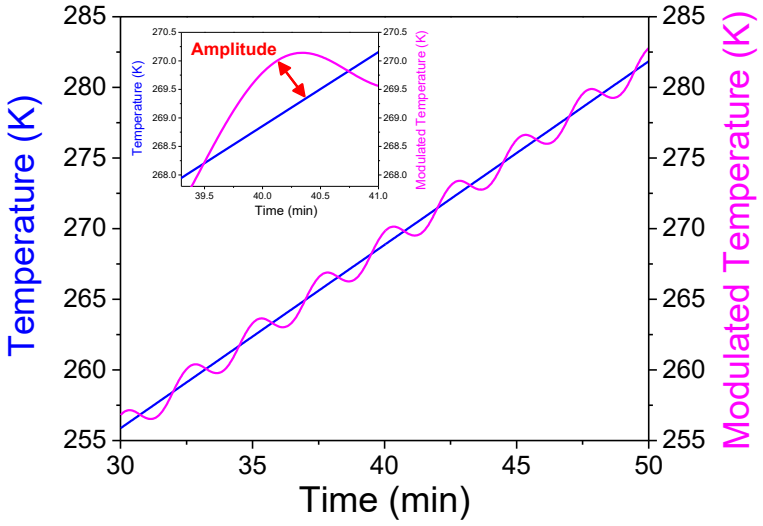

Figure 3.8. Temperature dependence over time for $PBLG_{46}$. The linear and harmonic heating rates are shown, from which the amplitude (inset) and period of the harmonic heating rate can be extracted.

The application of a sinusoidal modulation to the temperature variation allows the separation of the in-phase and out-of-phase components of the complex heat capacity, C_p^*. This separation is described by the phase difference, δ, between the sinusoidal temperature rate, dT_{sin}/dt, and the sinusoidal heat flow, dQ_{sin}/dt:[9]

$$\frac{dT_{sin}}{dt} = A_{HR}\cos\omega t \tag{3.30}$$

$$\frac{dQ_{sin}}{dt} = A_{HRF}\cos(\omega t + \delta) \tag{3.31}$$

where A_{HR} and A_{HF} are the respective amplitudes. A complex representation is used to describe the in-phase and out-of-phase components of the heat capacity, expressed in terms of the real part, C_p' (storage), and the imaginary part, C_p'' (loss):[9]

$$C_p^* = C_p' - iC_p'' \Rightarrow \begin{cases} C_p' = \dfrac{A_{HF}}{A_{HR}}\cos\delta & (\text{in}-\text{phase}) \\ C_p'' = \dfrac{A_{HF}}{A_{HR}}\sin\delta & (\text{out}-\text{of}-\text{phase}) \end{cases} \tag{3.32}$$

Changes observed in C_p' correspond to phenomena associated with reversible processes that are fully synchronized (in-phase) with the sinusoidal modulation. Such phenomena include crystal melting or changes in C_p' at the glass transition temperature. On the other hand, changes in C_p'' are associated with irreversible kinetic processes that occur out of equilibrium, such as crystallization and enthalpy recovery on heating from the glassy state. In modulated DSC measurements, an oscillation amplitude of 1 K was used, with periods ranging from 20 to 60 seconds, corresponding to linear heating/cooling rates from 10 K·min⁻¹ to 3.3 K·min⁻¹. The rate/period pair was employed for each measurement according to $\beta = \frac{\Delta T_g}{cP}60s/min$.[8] Here, ΔT_g is the breadth of T_g, c is the number of cycles across the T_g width, and P is the oscillation period. The period/rate pairs used were as follows: 20 s / 10 K·min^{-1}; 40 s / 5 K·min^{-1}; 60 s / 3.3 K·min^{-1}. The temperature range for the TM-DSC measurements was also from 223 to 350 K. According to the fluctuation-dissipation theorem, the cooperativity region is related to thermal fluctuations. Therefore, the characteristic

relaxation times for the segmental relaxations were extracted using the relation $\tau_{\alpha,\mathrm{TMDSC}} = \frac{1}{2\pi f^{\mathrm{TMDSC}}} = \frac{T_{\mathrm{TMDSC}}}{2\pi}$. These values were later compared with the DS results.

3.4 Small-Angle X-ray Scattering

Small-angle X-ray scattering (SAXS) measurements were made with the N8 Horizon vertical setup (Bruker), using a 50W CuKα radiation (IμS micro-focus source with integrated MONTEL optics). The diffraction patterns were recorded on the VÅNTEC-500 2D detector (Bruker) at a sample-detector distance of 660 mm. The samples were placed in the form of powder within borosilicate glass capillaries with a diameter of 1 mm. Intensity distributions as a function of the modulus of the scattering vector, $q = (4\pi/\lambda)\cdot\sin(2\theta/2)$, where 2θ is the scattering angle and $\lambda = 0.154$ nm is the wavelength, were obtained by radial averaging of the 2D datasets. Temperature-dependent measurements of 1 hour long were made by slowly heating the samples from 303 K to 423 K in 5 K steps – with 1 hour equilibration time at each temperature- and subsequent cooling aiming at obtaining the disorder-to-order temperature.

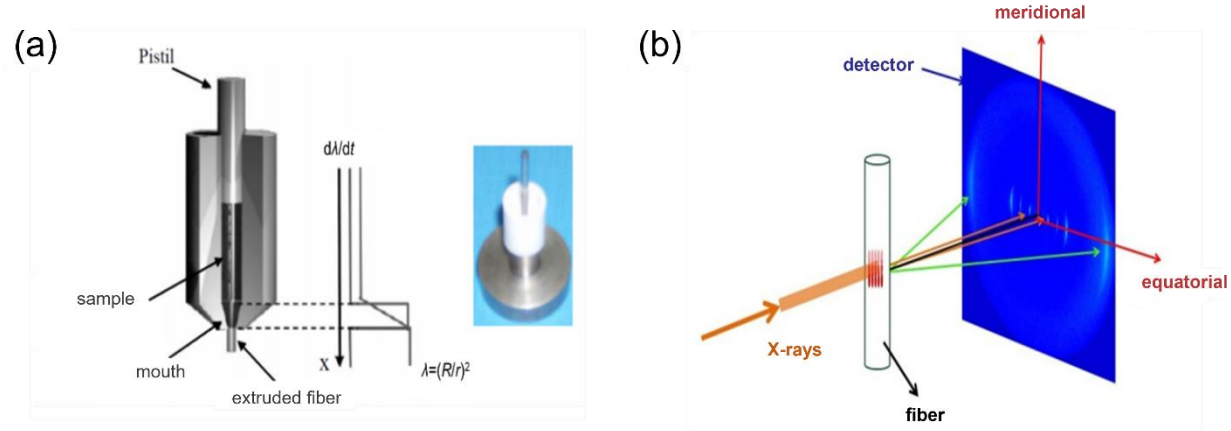

Figure 3.9. (a) Schematic representation of the extrusion setup used for the production of oriented copolypeptide fibers, including a photograph of the extruder, and (b) the experimental setup for two-dimensional wide-angle X-ray scattering (WAXS) measurements.

The measured scattered intensity $I(q)$ arises from the interaction of X-rays with the electron density inhomogeneities in the sample. The scattering pattern contains contributions from both the form factor, $P(q)$, and the structure factor, $S(q)$, which encode information about the size, shape, and organization of the scattering objects. In this case, the total scattered intensity can be expressed as[10,11]

$$I(q) \sim K \cdot P(q) \cdot S(q) \tag{3.33}$$

The combined analysis of the form and structure factors provides a comprehensive understanding of the nanomorphology of the material.

The structure factor, $S(q)$, describes the spatial correlations and interference effects resulting from the arrangement of particles or domains relative to each other. It is particularly important in concentrated systems or self-assembled materials, where long-range or short-range order is present. Peaks in $S(q)$ indicate the domain spacing or periodicity and can be used to determine characteristic distances via the relation $d = 2\pi/q$, where q is the position of the primary scattering peak. For example, block copolymers that exhibit microphase separation into lamellar, cylindrical, or gyroid structures display distinct sets of Bragg reflections in the SAXS pattern, corresponding to their ordered morphologies. At low q, $S(q)$ provides insight into long-range ordering. In dilute systems, $S(q) \to 1$, indicating negligible interparticle effects.

The form factor, $P(q)$, represents the scattering contribution from an isolated particle or domain and reflects its internal structure, shape, and size. It depends on the electron density contrast between the scatterer and the surrounding medium, as well as on the geometry of the scatterer. The form factor dominates at high q, where interparticle interference is negligible. Different morphologies, such as spheres, cylinders, ellipsoids, or core-shell particles, exhibit characteristic $P(q)$ profiles. Among the most common geometries encountered in materials are spheres and cylinders, which can be broadly divided into two groups: non-interacting monodisperse particles and interacting monodisperse particles. The distinction is critical, as the presence of interparticle interactions significantly modifies the scattering intensity, especially at low scattering vectors (q).

Non-interacting monodisperse "particles"

For monodisperse spheres, in the absence of interactions, the form factor is given by

$$P(q,R) = \left| 3\frac{\sin(qR) - qRcol(qR)}{(qR)^3} \right|^2 \tag{3.34}$$

where R is the radius of the sphere, and q is the scattering vector. This equation describes the characteristic oscillatory decay pattern of the scattered intensity for spherical objects.

For monodisperse cylinders, the form factor is more complex due to the additional geometric parameter (length, L) and the cylindrical symmetry. The form factor is expressed as

$$P(q,R,L) = 16\int_0^1 \left(\frac{J_1\left(qR\sqrt{1-x^2}\right)}{qR\sqrt{1-x^2}}\frac{\sin(qL\,x/2)}{qLx}\right)^2 dx \qquad (3.34)$$

where J_1 is the first-order Bessel function, R is the cylinder radius, L is the length, and the integration accounts for orientation averaging in the random ensemble of cylinders.

To illustrate the behavior of these form factors, simulations were performed for selected values of R and L, and the resulting scattering curves are presented in Figure 3.10.

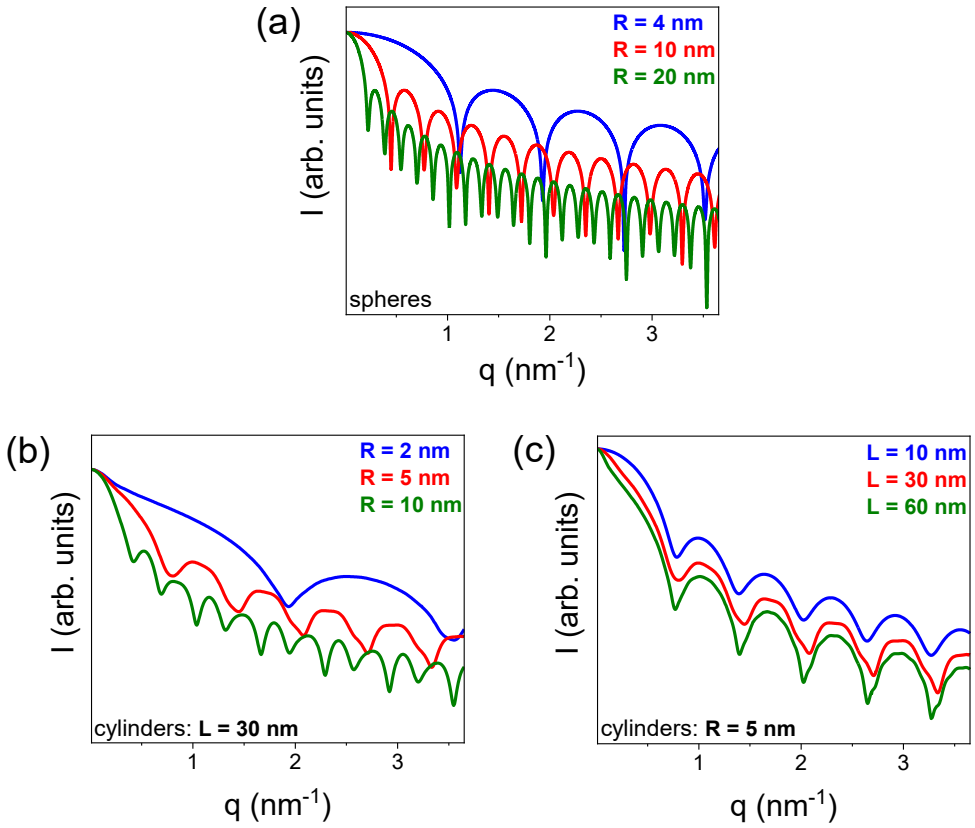

Figure 3.10. Simulated scattered intensity, $I(q)$, for non-interacting monodisperse "particles". (a) Scattered intensity of spheres of different radii. (b) Scattered intensity of cylinders of the same length, L, but differing in the radius, R. (c) Scattered intensity of cylinders of the same radius, R, but differing in the length, L.

Interacting monodisperse "particles"

When interparticle interactions become significant, typically due to higher concentrations or structural organization, the structure factor, $S(q)$, must be included in the analysis. For monodisperse spheres or cylinders with hard-sphere interactions, the interference effects at low q can be described by the Percus-Yevick approximation. This approach assumes that particles interact through a hard-sphere potential and that interactions are independent of size or orientation. The structure factor under this model is given by[10,11]

$$S(q, R_{\mathrm{h}}, f_{\mathrm{h}}) = \frac{1}{1 + \frac{24 f_{\mathrm{h}} G(A)}{A}} \tag{3.35}$$

where $A = 2qR_{\mathrm{h}}$, R_{h} and f_{h} are the effective interaction hard-sphere radius and volume fraction parameters describing the interference effects between the "particles", and

$$\begin{aligned} G(A) = \frac{\alpha}{A^2}(sinA - AcosA) + \frac{\beta}{A^3}(2AsinA + (2 - A^2)cosA - 2) \\ + \frac{\gamma}{A^5}[-A^4 cosA + 4(3A^2 - 6)cosA + (A^3 - 6A)sinA + 6] \end{aligned} \tag{3.36}$$

Where,

$$\begin{aligned} \alpha &= (1 + 2f_{\mathrm{h}})^2/(1 - f_{\mathrm{h}})^4 \\ \beta &= -6f_{\mathrm{h}}\,(1 + f_{\mathrm{h}}/2)^2/(1 - f_{\mathrm{h}})^4 \\ \gamma &= {}^1\!/_2\, f_{\mathrm{h}}\,(1 + 2f_{\mathrm{h}})^2/(1 - f_{\mathrm{h}})^4 \end{aligned} \tag{3.37}$$

Thus, the form factor of interacting monodisperse particles is

for spheres: $$P(q, R) = \left(\frac{4}{3}\pi R^3\right)^2 \left| 3\frac{\sin(qR) - qRcol(qR)}{(qR)^3} \right|^2 \tag{3.38a}$$

for cylinders: $$P(q,R,L) = \int_0^1 \left(2\frac{J_1\left(qR\sqrt{1-x^2}\right)}{qR\sqrt{1-x^2}}\frac{\sin(qL\,x/2)}{qL\,x/2}\right)^2 dx \qquad (3.38b)$$

In order to demonstrate the effect of interparticle interference on the scattering profiles, simulations were performed incorporating values of the interaction parameters (R_h, f_h). The results of these simulations are shown in Figure 3.11, highlighting the evolution of the low q peak.

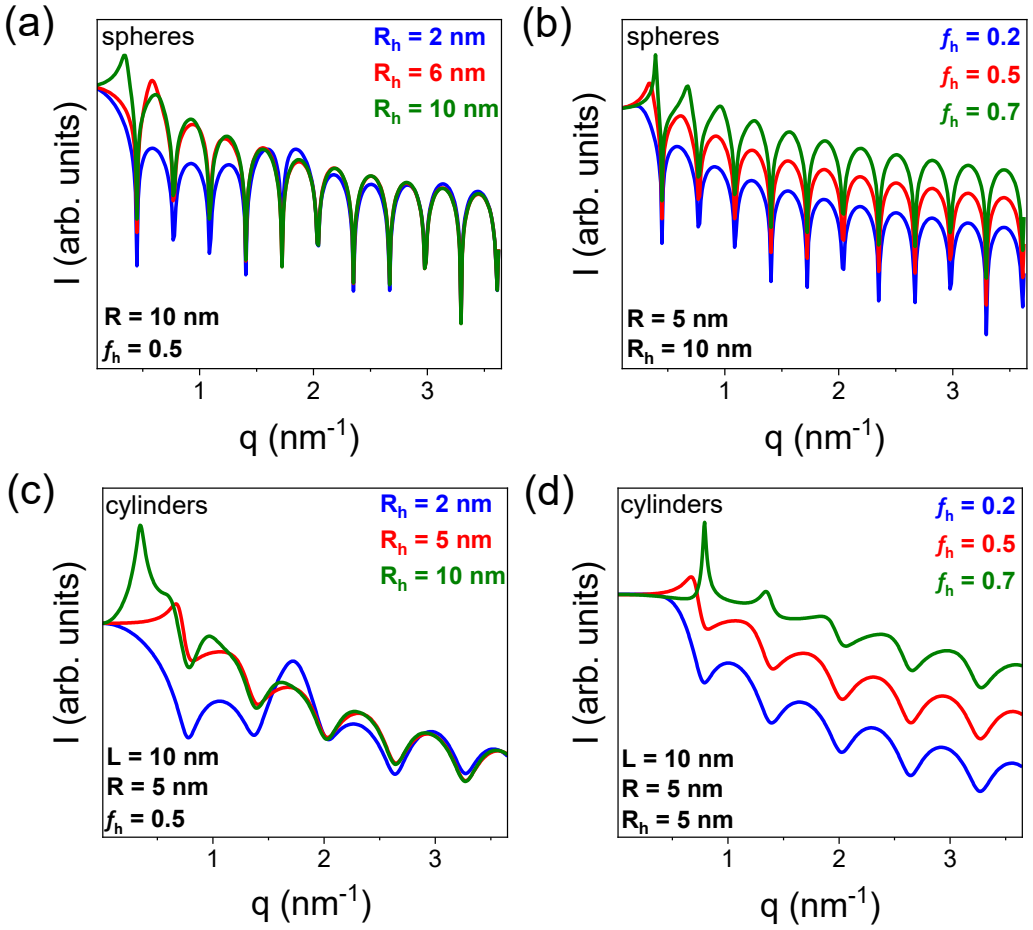

Figure 3.11. Simulated scattered intensity, $I(q)$, for interacting monodisperse "particles", under a hard-sphere interaction potential, using the Percus-Yevick approximation. (a), (b) Scattered intensity of spheres and (b), (c) scattered intensity of cylinders.

3.5 Wide-Angle X-ray Scattering

Wide-angle X-ray scattering (WAXS) measurements were performed with a D8 Advance Bruker diffractometer, CuKα (40 kV, 40 mA) radiation, equipped with a secondary beam graphite monochromator (λ = 1.54184 nm). The system employed a Bragg-Brentano geometry in a θ-θ

configuration. Patterns were obtained over the range of 2θ from 2 deg to 60 deg in steps of 0.01 deg, and the rate was 2 s per step for all samples. The recorded intensity distributions are presented as a function of the modulus of the scattering vector. Scattering curves were taken at a temperature of 303 K.

3.6 ^{13}C Solid-State NMR

Nuclear Magnetic Resonance (NMR) spectroscopy is one of the primary methods used to determine the secondary structures of polypeptides. The magnetic spin properties of atomic nuclei are used in NMR to determine the distances between atoms in the molecule, which in turn allows the determination of the three-dimensional structure of the polypeptide. The chemical shifts observed experimentally are the result of nuclear shielding, which affects the charge distribution, bonds, and conformations of macromolecules. The correlations between the repeating structural units allow the assignment of chemical shifts to the exact type and state of the atoms in the polypeptide chain. The ^{13}C NMR spectra of a polypeptide depend on the mobility of the carbon atoms and are distinct for each polypeptide. ^{13}C CP MAS NMR spectra have been recorded with a Bruker Avance III NMR console operating at 500.20 MHz 1H Larmor frequency at a 11.7 T Oxford-Instruments wide-bore NMR magnet using a commercial double-resonance CP-MAS probe supporting zirconia MAS NMR rotors with 2.5 mm out diameter at 25 kHz magic angle spinning frequency. The rf-power has been adjusted on both channels, ^{1}H and ^{13}C, to 100 kHz rf-nutation frequency. A 90-100% ramped CP-contact pulse has been used on the ^{1}H channel, in order to account for possible rf instability and off-resonance conditions, and the duration of the CP contact time was 1 ms. High power swept-frequency TPPM decoupling[12] with 100 kHz rf-nutation frequency has been applied on the 1H channel during acquisition. The sample temperatures under fast MAS spinning conditions have been corrected for frictional heating in the air bearings using the temperature dependent chemical shift of lead nitrate.[13] The conformation dependent NMR signals of the polypeptides have been assigned according to Shoji et al. (Figure 3.12).[14] The quantitative analysis of the NMR spectra has been performed spectral fitting using the DMfit software.[15] The molecular dynamics investigations were performed by recording ^{13}C-^{1}H REREDOR spinning sideband patterns[16,17] at 80 μs recoupling time and 25 kHz magic angle spinning (MAS) on a Bruker Avance 500 spectrometer using a Bruker double-resonance probe supporting rotors of 2.5 mm outer diameter. All experimental temperatures were corrected for the frictional heating effects arising from the fast rotor spinning.[18]

	C_α			C_β			C=O			
polypeptide	α-helix	β-sheet	Δ[a]	α-helix	β-sheet	Δ[a]	α-helix	β-sheet	Δ[a]	ref
$(Ala)_n$	52.4	48.2	4.2	14.9	19.9	−5.0	176.4	171.8	4.6	2
	52.3	48.7	3.6	14.8	20.0	−5.2	176.2	171.6	4.6	8
	52.8	49.3	3.5	15.5	20.3	−4.8	176.8	172.2	4.6	9
$(Leu)_n$	55.7	50.5	5.2	39.5	43.3	−3.8	175.7	170.5	5.2	1, 2
	55.8	51.2	4.6	43.7[d]	39.6[d]	(4.1)	175.8	171.3	4.5	9
$[Glu(OBzl)]_n$	56.4	51.2	5.2	25.6	29.0	−3.4	175.6	171.0	4.6	this work
	56.8	51.1	5.7	25.9	29.7	−3.8	175.4	172.2	3.2	9
$[Glu(OMe)]_n$	57.0	51.4	5.6				175.7	172.5	3.2	this work
	47.0[d]	51.2	(−4.2)	26.3	29.8	−3.5	175.9	172.2	3.7	9
$(B, M)_n$[b]	56.4	50.8	5.6	25.7	28.5	−2.8	176.1	171.7	4.4	this work
$[Asp(OBzl)]_n$	53.4	49.2	4.2	33.8	38.1	−4.3	174.9	169.8	5.1	4
	53.6			34.2			174.9			9
$(Val)_n$	65.5	58.4	7.1	28.7	32.4	−3.7	174.9	171.8	3.1	1
		58.2			32.4			171.5		9
$(Ile)_n$	63.9	57.8	6.1	34.8	39.4	−4.6	174.9	172.7	2.2	1
		57.1			33.1			171.0		9
$(Lys)_n$[c]	57.4			29.9			176.5			43
$[Lys(Z)]_n$	57.6	51.4	6.2	29.3	28.5	−0.8	175.7	170.4	5.3	9
$(Arg)_n$[c]	57.1			28.9			176.8			43
$(Phe)_n$	61.3	53.2	8.1	35.0	39.3	−4.3	175.2	169.0	6.2	9
$(Met)_n$	57.2	52.2	5.0	30.2	34.8	−4.6	175.1	170.6	4.5	9
$(Tyr)_n$	54.8	52.1	6.5	36.1	39.3	−3.2	176.7	169.6	7.1	9
	~58.6		~2.7							
$(Gly)_n$		43.2						168.4		3
		44.3						169.2		9
			5.1 ± 1.0[e]			−4.1 ± 0.7[e]	175.8 ± 0.8[e]	170.9 ± 1.2[e]	4.5 ± 1.1[e]	

Figure 3.12. Characteristic ^{13}C chemical shifts of the C_α carbon, C_β carbon and amide C=O for the α-helical and β-sheet secondary structures for different polypeptides. The abbreviations are: $(Ala)_n$, poly(L-alanine); $(Leu)_n$, poly(L-leucine); $[Glu(OBzl)]_n$, PBLG; $[Glu(OMe)]_n$, poly(γ-methyl-L-glutamate); $(B,M)_n$, sequential copolymer consisting of γ-benzyl-L-glutamate (B) and γ-methyl-L-glutamate (M) units; $[Asp(OBzl)]_n$, poly(β-benzyl-L-aspartate); $(Val)_n$, poly(L-valine); $(Ile)_n$, poly(L-isoleucine); $(Lys)_n$, poly(L-lysine); $[Lys(Z)]_n$, poly(benzyloxycarbonyl-L-lysine); $(Arg)_n$, poly(L-arginine); $(Phe)_n$, poly(L-phenylalanine); $(Met)_n$, poly(L-methionine); $(Tyr)_n$, poly(L-tyrosine); $(Gly)_n$, poly(L-glycine). Highlighted are the chemical shifts for PBLG used for our studies. The resonances have an error of ± 0.5 ppm. [14]

3.7 Polarizing Optical Microscopy

Polarizing optical microscopy (POM) is ideal for studying the macroscopic structure of materials that exhibit birefringence, i.e., a refractive index that depends on the polarization and direction of light propagation. The microscope setup is shown in Figure 3.13a. The sample to be examined is placed between a polarizer and an analyzer, which are perpendicular to each other. In the absence of a sample, the perpendicular arrangement of the polarizer and analyzer blocks the transmission of light. Similarly, when an optically isotropic sample (e.g., an amorphous material) is placed between the polarizer and analyzer, no change in polarization occurs. However, birefringent materials (e.g., liquid crystals) rotate the plane of the polarized light passing through the polarizer. This rotation allows the light to pass through the analyzer, resulting in distinctive optical patterns.

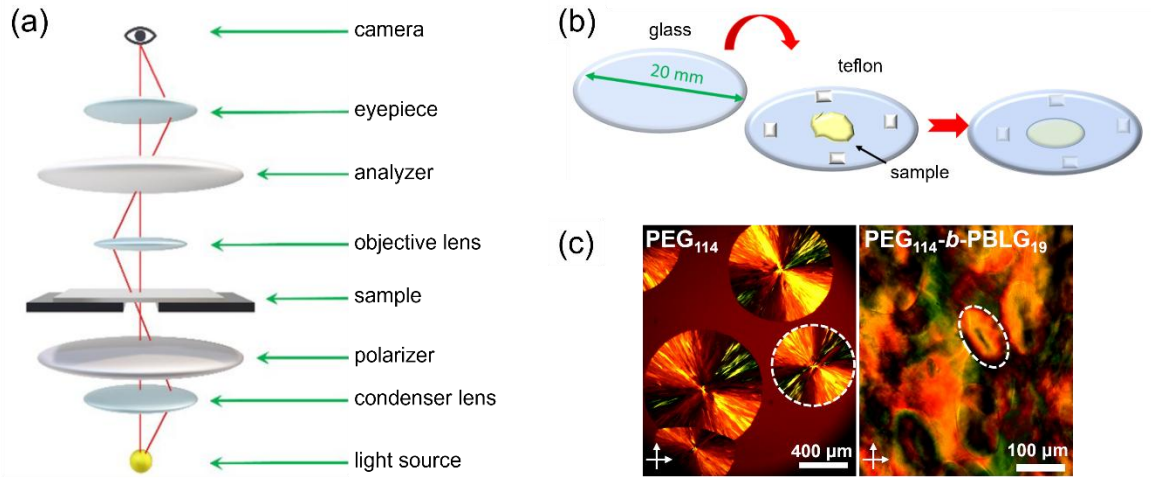

Figure 3.13. (a) Schematic representation of the positions of the lenses and polarizers. (b) Sample preparation. (c) POM images, obtained under isothermal conditions for bulk PEG_{114} at 311 K and the PEG_{114}-*b*-$PBLG_{19}$ copolymer at 286 K.

A Zeiss Axioskop40 polarizing optical microscope was used, equipped with a video camera capable of capturing fast snapshots (up to 2 ms), which were recorded using appropriate software. The Linkam THMS600 heating/cooling stage has a temperature range of 77 K to 8713 K with a temperature stability of 0.1 K, while the LNP94/2 liquid nitrogen pump cooling system allows controlled cooling rates. The sample was placed between two glasses and mounted on a highly polished silver heating element to ensure high heat transfer. Teflon with a thickness of 25 µm was used as a spacer, ensuring uniformity in the sample thickness (Figure 3.13b). The kinetics of superstructure formation was investigated by performing *T*-jumps from high temperatures (above PEG melting) to different final crystallization temperatures where the growth of the axialites was followed. Subsequently, the system was heated with 1 $K \cdot min^{-1}$ and the apparent melting temperature of the superstructure was recorded. Representative POM images of PEG-*b*-PBLG copolymers are shown in Figure 3.13c.

3.8 Rheology

A TA Instruments, AR-G2, with a magnetic bearing that allows for nanotorque control was used to record the viscoelastic properties of PBLG as a function of molar mass. Measurements were made with the environmental test chamber (ETC) as a function of temperature. Samples were prepared on the lower plate of the 8 mm diameter parallel plate geometry. Temperature control was achieved within 0.1 K with a nitrogen convection oven.

The operating principle of the rheometer is based on the application of a controlled shear stress, σ, which induces a corresponding shear strain, γ. The shear modulus, G, is defined as $G = \sigma/\gamma$. In the oscillatory mode of the rheometric system, the angle of rotation, θ, and consequently all quantities dependent on it, vary sinusoidally with time (Figure 2.22(b)). Therefore, a sinusoidal shear strain deforms the sample according to

$$\left.\begin{aligned} \theta &= \theta_0\, sin(\omega t) \\ \gamma &= \frac{\theta_0 r}{h} sin(\omega t) \end{aligned}\right\} \Rightarrow \gamma = \gamma_0\, sin(\omega t) \tag{3.39}$$

where γ_0 is the strain amplitude and ω is the angular frequency. The response of the material is also a sinusoidal shear stress shifted by a phase angle δ in respect to the strain:

$$\sigma = \sigma_0\, sin(\omega t + \delta) = \sigma_0 cos\delta \cdot sin\omega t + \sigma_0 sin\delta \cdot cos\omega t \tag{3.40}$$

where σ_0 is the stress amplitude. This sinusoidal motion can be represented in the complex plane and can define the complex strain (γ^*) and complex stress (σ^*) according to

$$\begin{aligned} \gamma^* &= \gamma_0\, exp(i\omega t) \\ \sigma^* &= \sigma_0\, exp(i\omega t + i\delta) \end{aligned} \tag{3.41}$$

The resulting complex shear modulus is

$$G^* = G' + iG'' \Rightarrow G^* = \frac{\sigma^*}{\gamma^*} \xrightarrow{\text{eq 3.41}} G^* = \frac{\sigma_0}{\gamma_0} e^{i\delta} \Rightarrow$$

$$\Longrightarrow G^* = \frac{\sigma_0}{\gamma_0}(cos\delta + isin\delta) \xrightarrow{\text{eq 3.40}} \begin{cases} G' = \dfrac{\sigma_0}{\gamma_0} cos\delta \\ G'' = \dfrac{\sigma_0}{\gamma_0} sin\delta \end{cases} \tag{3.42}$$

$$\Rightarrow \begin{cases} |G^*| = \sqrt{(G')^2 + (G'')^2} = \dfrac{\sigma_0}{\gamma_0} \\ \dfrac{G''}{G'} = tan\delta \end{cases}$$

The linear and nonlinear viscoelastic regions were determined by the strain amplitude dependence of the complex shear modulus $|G^*|$ at ω = 10 rad·s^{-1}. The storage (G') and loss (G'') shear moduli were measured as a function of frequency, ω, within the range of 10^{-1} to 10^{2} rad·s^{-1} at several temperatures from 293 to 493 K. The ratio of the two moduli, tan(δ), describes the degree of viscoelasticity of the material. Master curves were constructed by using the time-temperature superposition principle (*tT*s). The shift factors, α_T, were fitted according to the Williams-Landel-Ferry (WLF) equation as $\alpha_T = \frac{-C_1^{\mathrm{ref}}(T-T_{\mathrm{ref}})}{C_2^{\mathrm{ref}}+(T-T_{\mathrm{ref}})}$, where C_1^{ref} and C_2^{ref} are empirical parameters at T_{ref}.

3.9 References

1. Kremer, F.; Schönhals, A. "*Broadband Dielectric Spectroscopy*", Springer, Berlin, **2002**.
2. Floudas, G.; Paluch, M.; Grzybowski, A.; Ngai, K. L. "*Molecular Dynamics of Glassforming systems: Effects of Pressure",* Springer-Verlag, Berlin, **2011**.
3. McCrum, N. G.; Read, B. E.; Williams, G. *Anelastic and Dielectric Effects in Polymeric Solids*, Dover, New York, **1991**.
4. Onsager, L. *J. Am. Chem. Soc.* **1938**, *58*, 1486.
5. (a): Kirkwood, J. G. *J. Chem. Phys.* **1939** *58*, 911. (b): Kirkwood, J. G. *Ann. NY Acad. Sci.* **1940**, 40, 315. (c): Kirkwood, J. G. *Trans. Faraday Soc.* **1946**, *42A*, 7. (d): Fröhlich, H. "*Theory of Dielectrics*", Oxford University Press, London, **1958**.
6. (a) Kohlrausch, R. *Pogg. Ann. Phys.* **1847**, *12*, 393. (b) Williams, G.; Watts, D. C. *Trans. Faraday Soc.* **1970**, *66*, 80. (c) Williams, G.; Watts, D. C.; Dev, S. B.; North, A. M. *Trans. Faraday Soc.* **1971**, *67*, 1323.
7. Wubbenhorst, M.; van Turnhout, J. Analysis of Complex Dielectric Spectra. I. One-Dimensional Derivative Techniques and Three-Dimensional Modelling. *J. Non-Cryst. Solids* **2002**, *305*, 40-49.
8. Hensel, A.; Debbertin, J.; Schawe, J.E.K.; Boller, A.; Schick, C. Temperature-Modulated Calorimetry and Dielectric Spectroscopy in the Glass Transition Region of Polymers. *J. Thermal Anal.* **1996**, *46*, 935-954.
9. Simon, S. Temperature-modulated differential scanning calorimetry: theory and application. *Thermochimica Acta* **2001**, *374*, 55-71.
10. Kinning, D. J.; Thomas, E. L. Hard-Sphere Interactions Between Spherical Domains in Diblock Copolymers. *Macromolecules* **1984**, *17*, 1712-1718.
11. Pedersen, J. S. Determination of Size Distributions from Small-Angle Scattering Data for Systems with Effective Hard-Sphere Interactions. *J. Appl. Cryst.* **1994**, *27*, 595-608.
12. Vinod Chandran, C.; Madhu, P.K.; Kurur, N.D.; Bräuniger, T. Swept-Frequency Two-Pulse Phase Modulation (SWf-TPPM) Sequences with Linear Sweep Profile for Heteronuclear Decoupling in Solid-State NMR. *Magn. Reson. Chem*. **2008**, *46*, 943-947.
13. Guan, X.; Stark, R.E. A General Protocol for Temperature Calibration of MAS NMR Probes at Arbitrary Spinning Speeds, *Solid State Nuclear Magnetic Resonance,* **2010**, *38*, 74-76.

14. Shoji, A.; Ozaki, T.; Saito, H.; Tabeta, R.; Ando, I. Conformational Characterization of Solid Polypeptides by ^{13}C NMR Recorded by the Cross Polarization-Magic Angle Spinning Method: Conformation-Dependent ^{13}C Chemical Shifts of Oligo-and Poly(*γ*-benzyl L-glutamates) and Sequential Copolymers of *γ*-Benzyl and *γ*-Methyl L-Glutamates and Qualitative Evaluation of Side-Chain Orientation *Macromolecules*, **1984**, *17*, 1472.
15. Massiot, D.; Fayon, F.; Capron, M.; King, I.; Lecalve, S.; Alonso, B.; Durand, J.O.; Bujoli, B.; Gan, Z.; Hoatson, G. Modelling One-and Two-Dimensional Solid-State NMR Spectra, *Magnetic Resonance in Chemistry*, **2002**, *40*, 70-76.
16. Saalwächter, K.; Schnell, I. *Solid State Nucl. Magn. Reson*. **2002**, 22, 154–187.
17. Saalwächter, K.; Spiess, H. W. *J. Chem. Phys.* **2001**, *114*, 5707-5728.
18. Langer, B.; Schnell, I.; Spiess, H. W.; Grimmer, A.-R. *J. Magn. Reson.* **1999**, *138*, 182-186.

Chapter 4. Distinct Dynamic Signatures of α-helices and β-sheets in Poly(γ-benzyl-L-glutamate) peptides

4.1 Introduction

Proteins achieve their remarkable functional diversity due to the specialized roles of their secondary structural motifs, primarily α-helices and β-sheets.[1] α-helices (found in globins and GPCRs, for example)[2,3] provide mechanical flexibility for dynamic processes, such as oxygen binding and signal transduction. In contrast, β-sheets (found in immunoglobulins and bacterial porins, for example)[4,5] provide rigidity and extended interaction surfaces. This enables resilience in harsh environments and supports functions such as antigen recognition and solute transport. These motifs often coexist in mixed α/β domains, such as Rossmann folds or serine proteases,[6,7] where balancing flexibility and stability is essential for proper function. These characteristics are currently being leveraged in protein engineering to develop biomaterials and therapeutics, highlighting the relationship between secondary structure and biological function.

The temperature-dependent nature of these protein functions has driven decades of research into protein dynamics. Early solution studies revealed that proteins undergo a liquid-to-glass "transition," regardless of their secondary structure.[8,9] The nature of this "transition" was long debated: is it an intrinsic property of the protein, or a water-mediated effect? To address this question, studies were conducted on model polypeptides, the simplified analogues of natural proteins.[10,11] These studies revealed that "glass transitions" are intrinsic features of such biological polymers. In α-helical polypeptides, "glass transitions" were observed in the dry state and were attributed to amorphous regions associated with amorphous peptide segments that interrupt the helices and with segments at the chain ends. Furthermore, the α-helices themselves were found to be dielectrically active due to their axial dipole moment.[11,12] This gave rise to a characteristic relaxation process known as the "slow helix process", which provided insight into the timescales and lengthscales of ordered helical domains.

For β-sheet proteins, such as *Bombyx mori* silk, the presence of a high-temperature liquid-to-glass "transition" was discussed.[13] However, looking closely to the preparation conditions it is likely that the weak feature seen in DSC is probably associated with bound water. Subsequent research has explored how hydration, bound water, and β-sheet crystallinity influence the observed

T_g.[14-16] The strong conductivity contribution induced at high *T*s hindered a clear dielectric characterization of the associated relaxation.[17] As a result, the dynamics of the ordered β-sheet regions remains largely unexplored, despite recent simulations suggesting that β-sheet structures also possess a dipole moment.[18]

This background raises several scientific questions:

- *Do β-sheets exhibit a liquid-to-glass "transition" analogous to that of α-helices, and if so, what is its molecular origin?* Directly comparing the dielectric profiles of α-helical and β-sheet polypeptides could elucidate molecular-level similarities and differences between the two secondary structures.

- *What are the characteristic length and timescales associated with the relaxation of β-sheets?* Beyond the amorphous contributions responsible for T_g, we aim to investigate the intrinsic relaxation of ordered β-sheets. Recent simulations have indicated that they process a significant dipole moment[18] and thus have the potential for a distinct dielectric response.

- *How β-sheets are affected by pressure?* Studies that consider both temperature and pressure are crucial, as β-sheets operate in diverse environments (e.g., silk's responsiveness to humidity and amyloid pathology under cellular stress). The T_g controls the "transition" between functional flexibility and rigidity. Understanding this threshold could enable control of β-sheet assembly for applications ranging from tunable biomaterials to the inhibition of amyloidogenesis.

- *Do β-sheets exhibit a distinct viscoelastic signature compared to α-helices?* Understanding their mechanical behavior could reveal how β-sheet-rich and α-helix-rich materials align with the stiffness of various biological tissues. How do their moduli compare to those of classical biomedical materials, such as drug delivery matrices (typically in the kPa range, designed to be soft for biocompatibility and degradation) or plastic surgery implants (designed stiffer, ranging from kPa to GPa, for structural support)? Representative examples include:[19,20] human femur (~ 15 GPa), Achilles tendon (~ 1 GPa), retina (~ 20 kPa), epithelial tissues (~ 1 kPa), or anterior basement membranes (~ 4 kPa)?

To address these questions, we employ poly(γ-benzyl-L-glutamate) (PBLG), as a model synthetic polypeptide, with different end-groups and controlled degrees of polymerization. Two series of PBLG samples were examined; PBLG samples terminated with a dimethylamino group

($-N(CH_3)_2$) synthesized by Prof. H.-A. Klok (synthesis at the Max Planck Institute for Polymer Research, Mainz), and the n-hexyl terminated PBLG samples synthesized by Prof. E. Iatrou and his group (National and Kapodistrian University of Athens). These well-defined polymers, with controlled degrees of polymerization, enable systematic investigation of the various secondary structure regimes. The series include short to intermediate oligopeptides (n = 4, 6, 7, 8, 10, 12, 14, 16, 18, 20), that stabilize both secondary structures, and polypeptides (n = 40, 60, 80, 100) dominated by α-helical structures. We use a multi-technique approach that combines both *static* (SAXS and ^{13}C solid-state NMR to identify the secondary structure and their corresponding fractions) and *dynamic probes* (TM-DSC to access the thermodynamic properties; ^{13}C solid-state NMR to measure the mobility differences between the two secondary structures; DS as a function of temperature and pressure to study their dynamic behavior; Rheology to assess their viscoelastic response).

The results show two distinct glass temperatures (T_gs) in polypeptides that form both secondary structures. The lower T_g is attributed to the amorphous α-helical segments, while the high T_g to the amorphous β-sheet segments. A slower segmental dynamics of the β-sheets is observed, indicating significantly more restricted dynamics. In addition, the relaxation of the α-helical and β-sheet macrodipoles is also evident at even longer timescales. The different fragility values and pressure dependences of the α-helices and β-sheets are discussed in terms of the different structural environments imposed by the type of the secondary structure. Specifically, the network-like structure of β-sheets imposes stronger constraints on the nearby amorphous segments. Lastly, we find an elastic response ($G' > G''$) across all samples. The analysis of the van Gurp-Palmen (vGP) plots revealed two minima in δ associated with, (i) the plateau modulus G_N^0 reflecting the elastic properties of the entanglement "network" ($\sim 10^5$ Pa) and, (ii) the freezing of the amorphous segments at T_g ($\sim 10^9$ Pa). We show that the different secondary structures have a clear viscoelastic signature at the segmental level and a similar fingerprint at the domain level, which reflects the emergence of a "tertiary structure", i.e., a "mesh", that decreases in size with increasing molar mass.

4.2 Results and Discussion

Poly(γ-benzyl-L-glutamate) (PBLG) is a model synthetic polypeptide that adopts both secondary structures, α-helices and β-sheets, with the relative fraction depending on molecular parameters such as the degree of polymerization and the chain end-group chemistry. These structures, stabilized by intramolecular and intermolecular hydrogen bonds in α-helices and β-sheets, respectively, have an effect on the self-assembly, the dynamics and the viscoelastic response of the material. In this study, two series of PBLG samples were investigated through precise oligomer synthesis having different chain ends; PBLG samples terminated with a dimethylamino group (–$N(CH_3)_2$) synthesized by Prof. H.-A. Klok (synthesis at the Max Planck Institute for Polymer Research, Mainz), and the n-hexyl terminated PBLG samples synthesized by Prof. E. Iatrou and his group (National and Kapodistrian University of Athens). The first set of PBLG samples terminate with a dimethylamino group (–$N(CH_3)_2$) at one end and a hydrogen atom at the other. The second set carries a bulkier end group consisting of a secondary amine substituted with an n-hexyl chain (–NH–$(CH_2)_6CH_3$) at one end and a hydrogen atom at the other. Because of the low molar masses, chain-end chemistry may influence local mobility, packing efficiency, and the stabilization of specific secondary structures. The chemical structures of both series are shown in Figure 4.1.

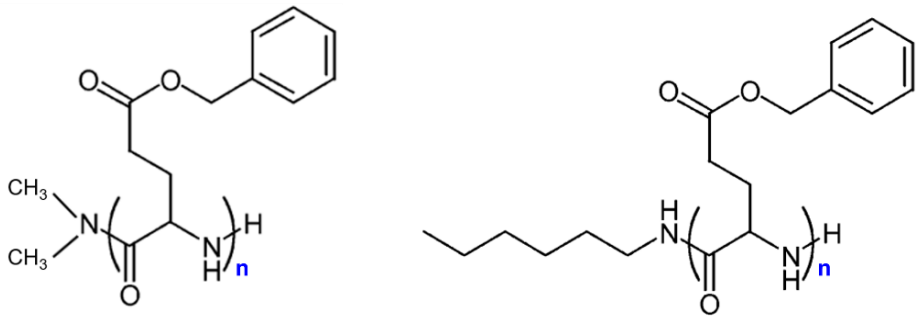

Figure 4.1. Chemical structures of two poly(γ-benzyl-L-glutamate) (PBLG) series synthesized via conventional ring-opening polymerization used in this study. (Left) PBLG, terminated with a dimethylamino group (–$N(CH_3)_2$) at one end and a hydrogen atom at the other. (Right) PBLG, terminated with a secondary amine substituted with an n-hexyl chain (–NH–$(CH_2)_6CH_3$) at one end and a hydrogen atom at the other. The end groups result from the different initiators used during synthesis.

4.2.1 Thermodynamics and Self-assembly.

The thermodynamics of PBLG depend on molar mass and end-group chemistry. The DSC traces are shown in Figure 4.2 (the absolute values of c_p for three characteristic molar masses are presented in Figure 4.3). TM-DSC measurements were performed for three oscillation periods and the characteristic relaxation times were extracted using the relation $\tau_{\alpha,\mathrm{TMDSC}} = \frac{1}{2\pi f^{\mathrm{TMDSC}}} = \frac{T_{\mathrm{TMDSC}}}{2\pi}$. These values will be compared later with the DS results. At low degrees of polymerization, n, two steps corresponding to distinct glass temperatures are observed. The lower T_g is present in all samples, regardless of molar mass. It is attributed to the relaxation of amorphous peptide segments that interrupt the helices and to segments at the helical chain ends.[10] This liquid-to-glass "transition" follows a Fox-Flory dependence (shown in Figure 4.18). Interestingly, a second, higher T_g is observed in oligopeptides, especially in the derivative representation of c_p (Figure 4.2b). This glass temperature is assigned to the dynamics of segments located in less-ordered or completely disordered parts of β-sheets. To our knowledge, this is the first time that a β-sheet-associated T_g is reported in a completely non-hydrated (hydrophobic) polypeptide. The presence of two T_gs confirms that the corresponding relaxation processes – here referred to as α and α^* segmental dynamics – are both thermodynamically active and contribute significantly to the configurational entropy of the system. Unlike previous reports on PBLG,[12] we did not observe an irreversible first-order transition from a 7/2 helix to the more thermodynamically stable 18/5 α-helix during the first heating (Figure 4.5).

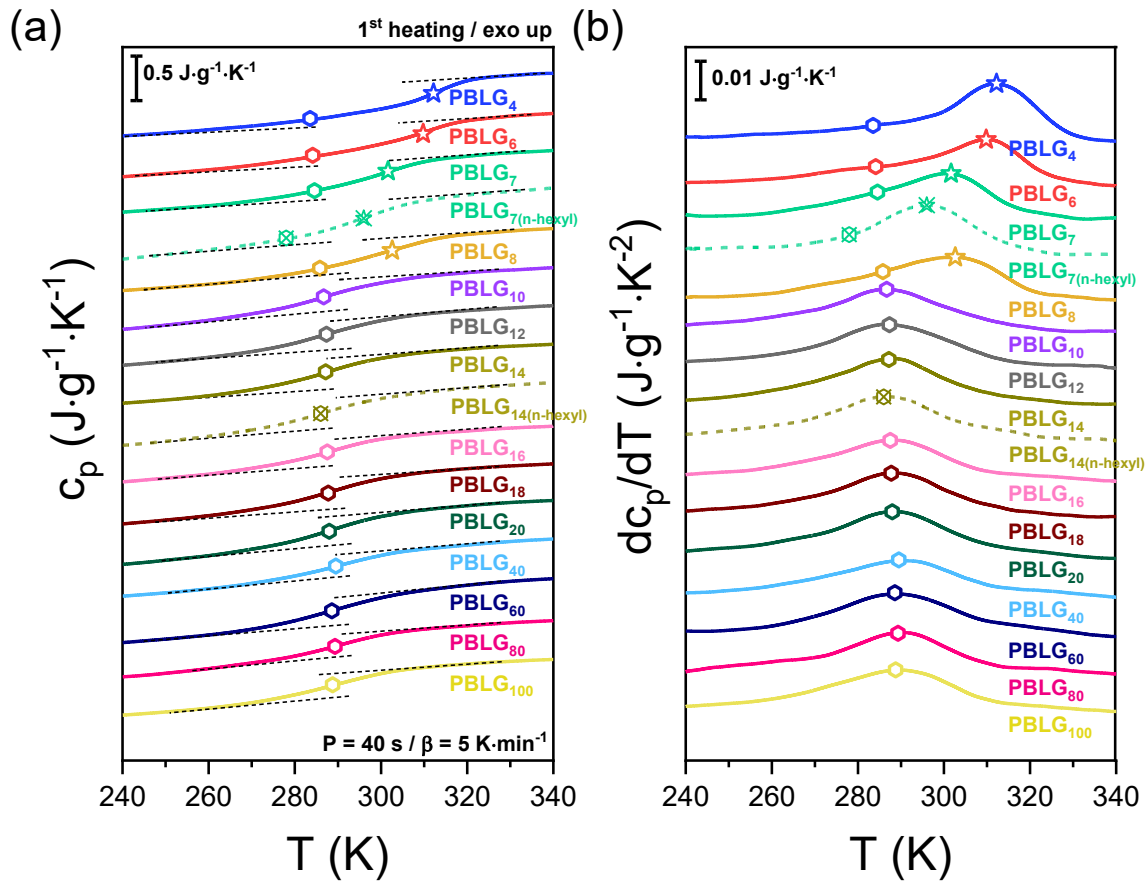

Figure 4.2. (a) Temperature dependence of the specific (reversing) heat for a series of PBLGs with different molar masses, obtained from TM-DSC at a period of modulation of P = 40 s (β = 5 K·s^{-1}). Dashed lines correspond to the n-hexyl terminated samples. Data are shifted for clarity. (b) Derivative of the specific heat capacity with respect to temperature plotted as a function of temperature. Polygons indicate the main liquid-to-glass temperature of PBLG. Star symbols correspond to the additional glass temperature, e.g., the high T_g, evident only in low molar mass PBLG.

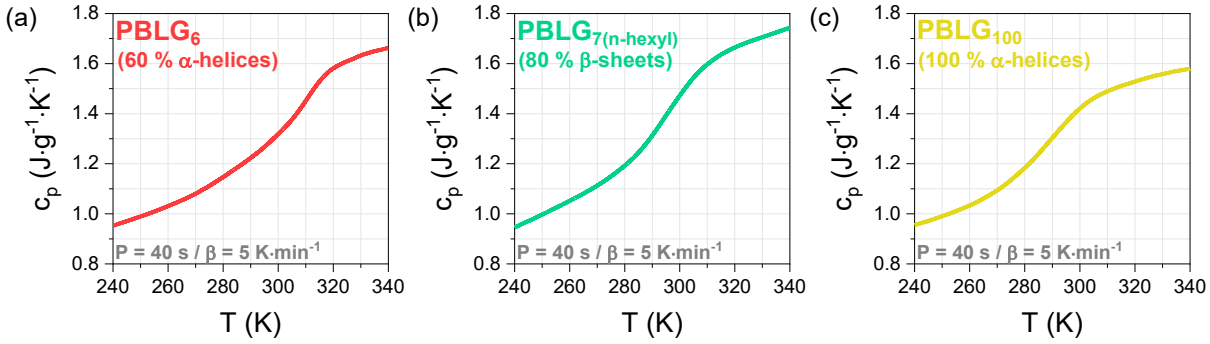

Figure 4.3. Temperature dependence of the specific (reversing) heat (absolute values) of PBLG$_6$ (red), PBLG$_{7(n\text{-hexyl})}$ (green) and PBLG$_{100}$ (yellow), obtained from TM-DSC at a period of modulation of P = 40 s (β = 5 K·s^{-1}).

To quantify the contribution of each secondary structure and to extract the relative α-helical and β-sheet fractions for the oligopeptides, the derivative representation of the c_p was fitted to a summation of two Lorentzian functions (Figure 4.4). As discussed, the lower T_g was assigned to the amorphous α-helical segments, while the higher T_g to the amorphous β-sheet segments. The relative contribution of each T_g can be estimated from the integrated areas under each Lorentzian peak ($A_{\alpha-helix}$ and $A_{\beta-sheet}$, respectively), according to $f_{\alpha-helix}^{DSC} = \frac{A_{\alpha-helix}}{A_{\alpha-helix}+A_{\beta-sheet}}$ and $f_{\beta-sheet}^{DSC} = \frac{A_{\beta-sheet}}{A_{\beta-sheet}+A_{\alpha-helix}}$. The results are summarized in Table 4.1. They reveal good agreement with the WAXS and NMR results (discussed below with respect to Figure 4.10). Interestingly, a significant distinction is evident between the oligopeptide $PBLG_{7(n\text{-}hexyl)}$ and its analog $PBLG_7$ terminated by the dimethylamino group. Specifically, $PBLG_{7(n\text{-}hexyl)}$ exhibits a substantially higher β-sheet fraction (Figure 4.4d), nearly twice that of α-helices. Quantitatively, the n-hexyl terminated sample consists of approximately 65 % β-sheets and 35 % α-helices. In comparison, the dimethylamino terminated $PBLG_7$ has approximately 60 % α-helices and ~ 40 % β-sheets. These results highlight the critical effect of end-groups on the secondary structure. On the other hand, for $PBLG_{14(n\text{-}hexyl)}$ and its dimethylamino terminated analog, it is difficult to identify two distinct glass temperatures in the thermodynamic traces. Overall, the results indicate that increasing *n* promotes the stabilization of α-helices, whereas β-sheet formation is favored at low *n*. In the dimethylamino terminated samples, however, the α-helices are the predominant secondary structure, as $f_{\alpha-helix}^{DSC} > f_{\beta-sheet}^{DSC}$, for all molar masses investigated.

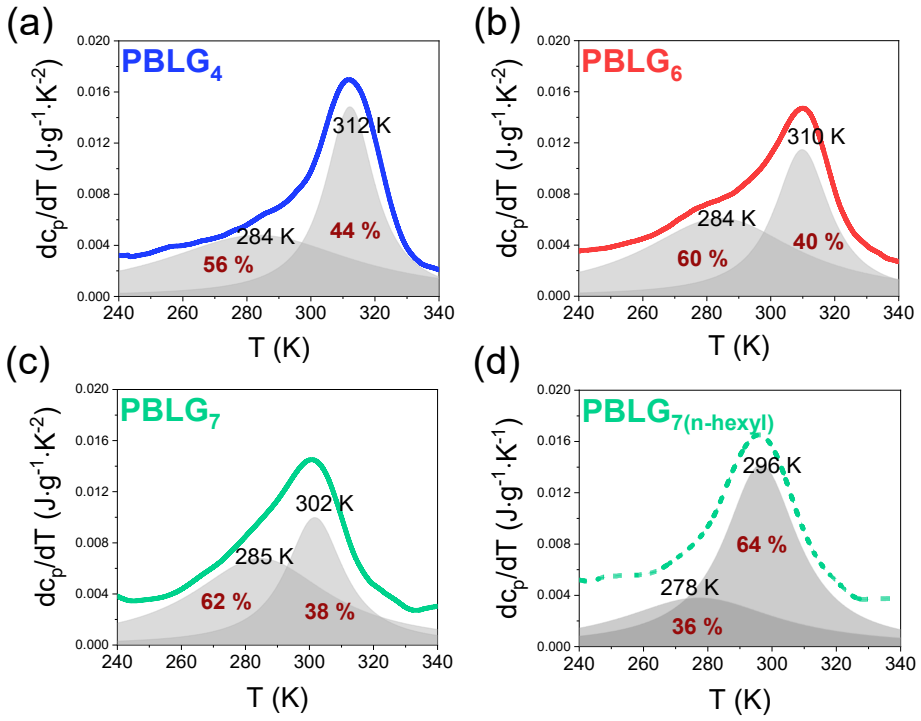

Figure 4.4. Derivative of the specific heat (obtained from TM-DSC at a period of modulation of P = 40 s) with respect to temperature plotted as a function of temperature for (a) $PBLG_4$, (b) $PBLG_6$, (c) $PBLG_7$ and (d) $PBLG_{7(n\text{-hexyl})}$. Gray integrated areas under each Lorentzian peak were used to estimate the relative $f_{\alpha-\text{helix}}^{\text{DSC}}$ and $f_{\beta-\text{sheet}}^{\text{DSC}}$ of the oligopeptides.

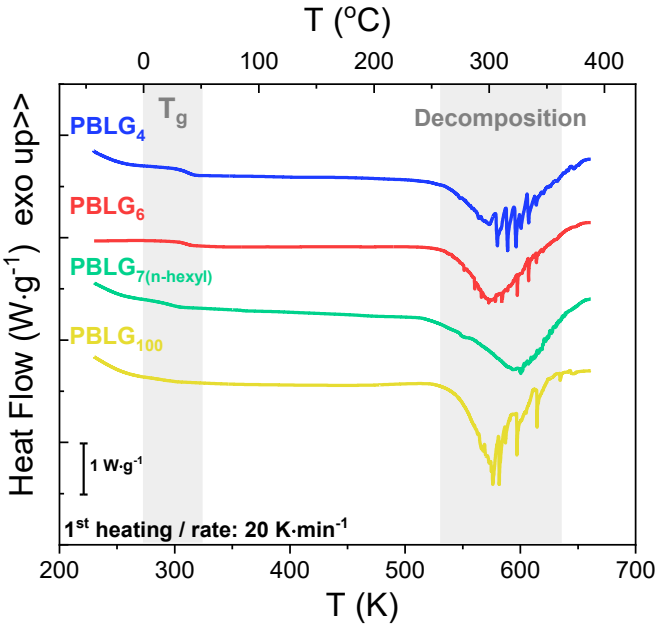

Figure 4.5. DSC traces of $PBLG_4$ (blue), $PBLG_6$ (red), $PBLG_{7(n\text{-hexyl})}$ (green) and $PBLG_{100}$ (yellow), obtained during first heating at a rate of 20 K·min^{-1}. Gray areas indicate the respective glass temperature area (low T) and the thermal degradation (high T). Curves are shifted for clarity.

Lastly, no other thermal transition was detected in any of the DSC traces over the entire temperature range (Figure 4.5) (Regardless of the degree of polymerization or chain end-group chemistry, only thermal degradation was detected above 573 K). This suggests that although both α-helices and β-sheets in PBLG are ordered structures, they do not undergo classical first-order transitions such as melting or crystallization.

Table 4.1. Relative fractions of *α*-helices and *β*-sheets for the investigated PBLG, as obtained from DSC and WAXS, and absolute fractions of *α*-helices, *β*-sheets and random coils, as obtained from NMR (at 320 K).

	DSC		**WAXS**		**NMR**	
Samples	$f_{\beta-\text{sheet}}$	$f_{\alpha-\text{helix}}$	$f_{\beta-\text{sheet}}$	$f_{\alpha-\text{helix}}$	$f_{\beta-\text{sheet}}$ $(f_{\beta-\text{ends}})$	$f_{\alpha-\text{helix}}$
$PBLG_4$	0.44	0.56	0.40	0.60	0.34 (0.10)	0.56
$PBLG_6$	0.40	0.60	0.40	0.60	0.33 (0.08)	0.59
$PBLG_7$	0.38	0.62	0.40	0.60	-	-
$PBLG_{7(\text{n-hexyl})}$	0.64	0.36	1	0	0.81	0.19
$PBLG_8$	0.36	0.64	0.40	0.60	0.29 (0.05)	0.66
$PBLG_{10}$	-	-	0.37	0.63	-	-
$PBLG_{12}$	-	-	0.36	0.64	-	-
$PBLG_{14}$	-	-	0.35	0.65	0.21	0.79
$PBLG_{14(\text{n-hexyl})}$	-	-	0.52	0.48	0.57	0.43
$PBLG_{16}$	-	-	0.33	0.67	-	-
$PBLG_{18}$	-	-	0.28	0.72	-	-
$PBLG_{20}$	-	-	0.30	0.70	-	-
$PBLG_{40}$	-	-	0	1	0.03	0.97
$PBLG_{60}$	-	-	0	1	-	-
$PBLG_{80}$	-	-	0	1	-	-
$PBLG_{100}$	-	-	0	1	-	-

The self-assembly of PBLG was investigated as a function of the degree of polymerization employing WAXS and ^{13}C solid state NMR. The WAXS patterns for four representative n-hexyl terminated samples, along with their dimethylamino terminated analogs, are presented in Figure 4.6 (and Figure 4.7 for the remaining samples). Two distinct groups can be identified: (i) short to intermediate oligopeptides (n = 4, 6, 7, 8, 10, 12, 14, 16, 18, 20) that stabilize both secondary structures, and (ii) polypeptides (n = 40, 60, 80, 100) where only the α-helical secondary structure is stabilized. In the WAXS curves, all dimethylamino terminated samples exhibit, at low scattering vector, a set of strong Bragg reflections with characteristic ratios $1:3^{1/2}:4^{1/2}$, with the primary peak at $q \sim 4.7$ nm^{-1} (intercylinder distance of ~ 1.54 nm), indicating the hexagonal packing of the 18/5 α-helices. This structure of PBLG, known as the nematic-like paracrystalline form C, describes a

periodic packing of α-helices in the direction lateral to the chain axis with a nematic-like paracrystalline order.[11,12] In the polypeptides, an additional sharp reflection is observed at higher q (= 12.6 nm^{-1}) corresponding to the helical pitch of 0.5 nm along the chain axis. Oligopeptides show an additional Bragg reflection at q = 3.7 nm^{-1} (d = 1.7 nm), corresponding to the lamellar spacing or the inter-sheet spacing of β-sheets. The PBLG$_{7(\text{n-hexyl})}$ displays reflections exclusively associated with the β-sheet structure, consistent with its high β-sheet fraction (~ 80 % according to NMR results). In addition, n-hexyl terminated oligopeptides show an additional peak at q = 13.4 nm^{-1}, corresponding to an inter-strand spacing of 0.47 nm between adjacent peptide chains within the β-sheets. The broad peak (amorphous halo or van der Waals peak) at around 14 nm^{-1}, evident in all samples, is assigned to correlations between the side-group atoms and contributions from the amorphous PBLG regions.

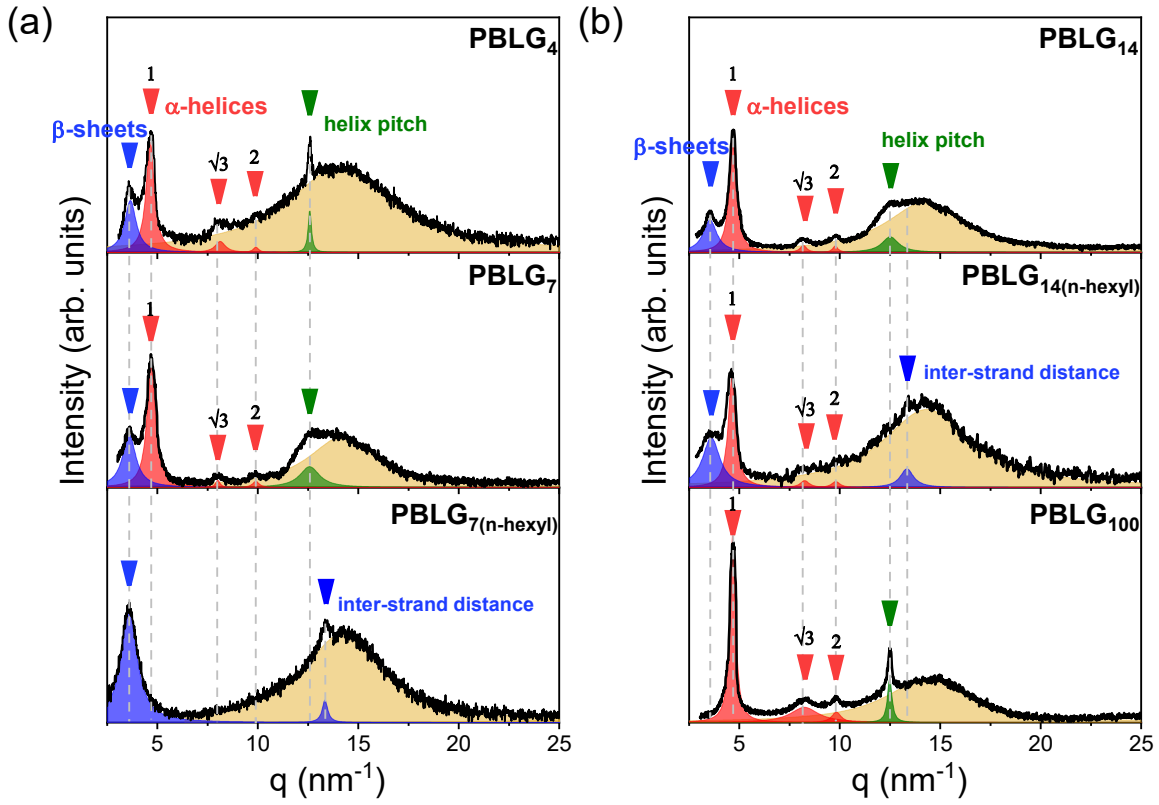

Figure 4.6. WAXS patterns of the investigated samples (a) top: PBLG$_4$, middle: PBLG$_7$, bottom: PBLG7$_{(\text{n-hexyl})}$ and (b) top: PBLG$_{14}$, middle: PBLG$_{14(\text{n-hexyl})}$, bottom: PBLG$_{100}$. Blue arrows correspond to the lamellar spacing of β-sheet secondary structure and the inter-stand distance of β-sheets, respectively. Red arrows indicate the Bragg reflections of the hexagonally packed α-helices, while green arrows give the reflection corresponding to the pitch of the α-helix. The amorphous halo is indicated in yellow.

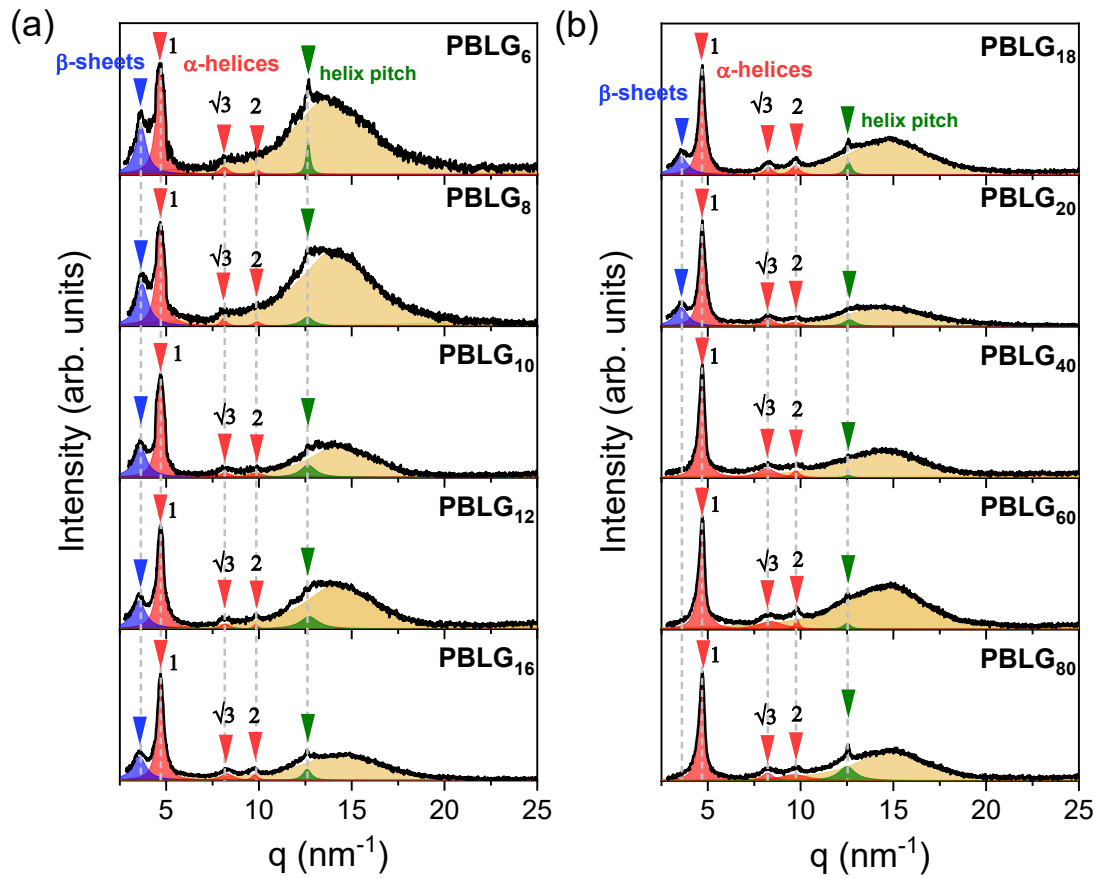

Figure 4.7. WAXS patterns of the investigated samples. Left: $PBLG_{10}$, $PBLG_{12}$, $PBLG_{16}$, $PBLG_{18}$. Right: $PBLG_{20}$, $PBLG_{40}$, $PBLG_{60}$, $PBLG_{80}$. Blue arrows correspond to the lamellar spacing of *β*-sheet secondary structure. Red arrows indicate the Bragg reflections of the hexagonally packed *α*-helices, while green arrows give the reflection corresponding to the pitch of the *α*-helix. The amorphous halo is indicated in yellow.

The relative fractions of α-helices and β-sheets were determined from the integrated intensities of respective Bragg peaks. This analysis assumes that there are only two ordered populations (α-helices and β-sheets) contributing to the scattering. Prior to integration, all curves were corrected for the background. The values are summarized in Table 4.1 and also presented in Figure 4.8a. The dimethylamino terminated PBLGs display a consistently higher α-helical fraction over all chain lengths. The evolution of both $f_{\alpha-\mathrm{helix}}^{\mathrm{WAXS}}$ and $f_{\beta-\mathrm{sheet}}^{\mathrm{WAXS}}$ as a function of the degree of polymerization was fitted to a generalized sigmoidal function as $y = \mathrm{A} - (\mathrm{A} - \mathrm{B})\mathrm{e}^{-(\mathrm{k}x)^{\mathrm{d}}}$, where A is the final (asymptotic) value, B is the initial value, k is a rate parameter, and d is a shape parameter controlling the sharpness of the "transition". The fit to the α-helical fraction data yields the equation $f_{\alpha-\mathrm{helix}} = 1 - 0.4\,\mathrm{e}^{-(0.04n)^{3.2}}$, while for the β-sheet fraction data $f_{\beta-\mathrm{sheet}} =$

$0.4\left(1-\mathrm{e}^{-(0.05n)^{-3.6}}\right)$. Both shape parameters indicate a progressive transformation in the secondary fractions. On the other hand, the n-hexyl terminated samples exhibit a different trend (a sigmoidal curve is shown in Figure 4.8a). At low *n*, the β-sheet fraction dominates, presumably reflecting the inability of short chains to stabilize the 18/5 helix.

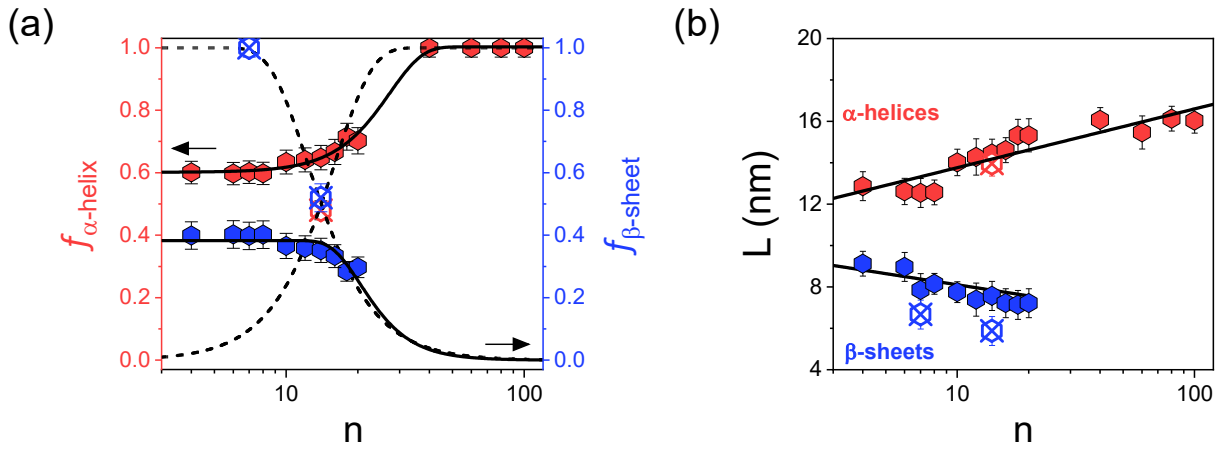

Figure 4.8. (a) Relative fractions of α-helices (red) and β-sheets (blue), as obtained from the integrated intensity of the first characteristic Bragg reflection, as a function of the number of peptide repeat units. Crossed symbols correspond to the n-hexyl terminated samples. Black lines are sigmoidal fits (see text). (b) Coherence length of the hexagonally packed α-helices (red) and of the lamellar assembly of the β-sheets (blue) over molar mass. Black lines are a guide for the eye.

A key parameter characterizing the self-assembly of the secondary structures is the lateral coherence length of their ordered domains in their lamellar β-sheets and the hexagonal packed α-helices.[11] This parameter can be extracted from the FWHM of the corresponding primary Bragg reflections, as $L = 2\pi/w$ (where w = FWHM). The calculated lengths are presented in Figure 4.8b. The results, seen together with Figure 4.8a, reveal a connection between the increasing (decreasing) fraction of α-helices (β-sheets) and the lateral coherence of the respective domains.

The structural behavior was further investigated by ^{13}C solid state NMR.[21,22] Representative samples, i.e., $PBLG_4$, $PBLG_6$ and $PBLG_8$ from the oligomers, $PBLG_{14}$ from the intermediate *n*, and $PBLG_{40}$ from the polypeptides, were selected to investigate the evolution of the secondary structure with the chain length through the characteristic chemical shifts. Corresponding NMR traces are shown in Figure 4.9. As well-established in literature,[23] each secondary structure exhibits distinct chemical resonances. α-helices can be identified by the

resonances at chemical shifts $\delta \sim 176$ ppm and $\delta \sim 58$ ppm, corresponding to the amide C=O and C_α carbon, respectively. In contrast, β-sheets are evident by the upfield shifted amide C=O and C_α carbon resonances at $\delta \sim 172$ ppm and $\delta \sim 53$ ppm, respectively. In addition, different from WAXS, the chain ends of β-sheets can be distinguished from the resonance at ~ 49 ppm of the C_α carbon.

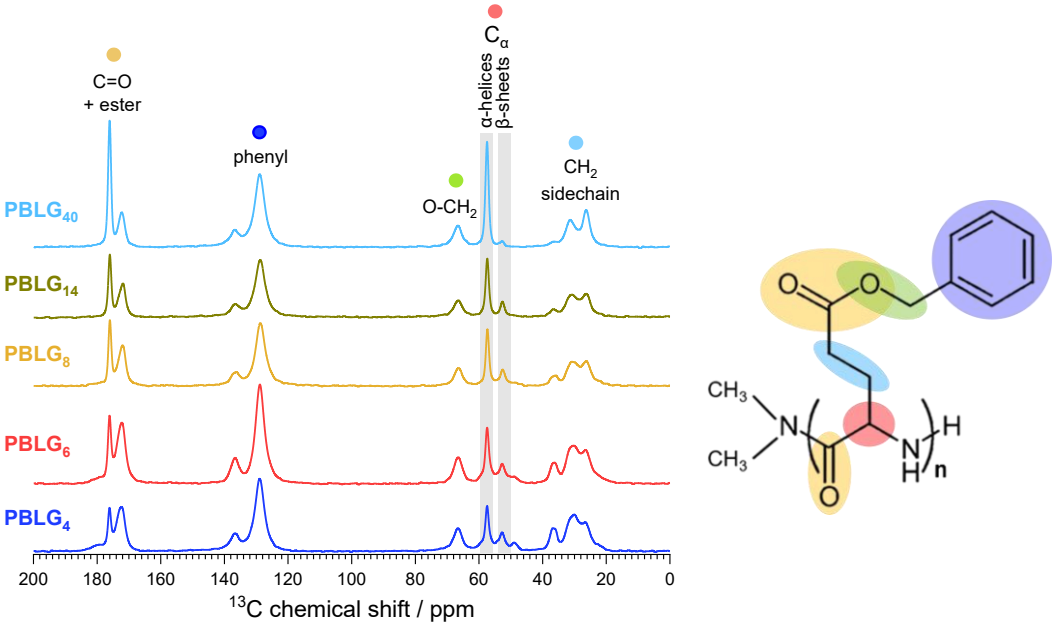

Figure 4.9. ^{13}C solid state NMR traces of the dimethylamino terminated samples: $PBLG_4$ (blue), $PBLG_6$ (red), $PBLG_8$ (yellow), $PBLG_{14}$ (dark yellow) and $PBLG_{40}$ (light blue). The highlighted areas refer to the chemical shifts used for the calculation of the absolute fractions of peptide secondary structures. The molecular structure of the repeat unit is also shown, including the color scheme employed for assignment purposes.

The calculated absolute fractions of the α-helices and β-sheets, as well as the chain-end contributions, are presented in Table 4.1, together with the corresponding DSC and WAXS data. In NMR, the fractions were calculated based solely in the C_α carbon resonances. The NMR curves show a progressive increase in the intensity of the α-helical resonances with increasing n, accompanied by a corresponding decrease in the β-sheet signals.[12] For the dimethylamino terminated samples, this trend can be described by the dependencies $f_{\alpha-\mathrm{helix}} = 0.28 + 0.43 \cdot \log n$ and $f_{\beta-\mathrm{sheet}} = 0.57 - 0.33 \cdot \log n$. Notably, β-sheet associated resonances decrease substantially and eventually disappear at $n \geq 40$, indicating that β-sheets become structurally unstable in this regime. These results indicate the systematic stabilization of 18/5 α-helices at higher chain lengths, while oligomers preferentially adopt β-sheet conformations. For the n-hexyl terminated samples,

although the available data are limited, the observed fits are indicative of a similar trend. For intermediate *n*, as expected, both secondary structure signals are evident, revealing coexisting α-helical and β-sheet domains. These observations are in relative agreement with the structural insights from WAXS and the thermodynamic results observed from TM-DSC. The combined results of the three techniques are summarized in Figure 4.10. It depicts the secondary structure evolution with molar mass: from β-sheet-rich domains at low *n* to purely α-helical structures at high *n*.

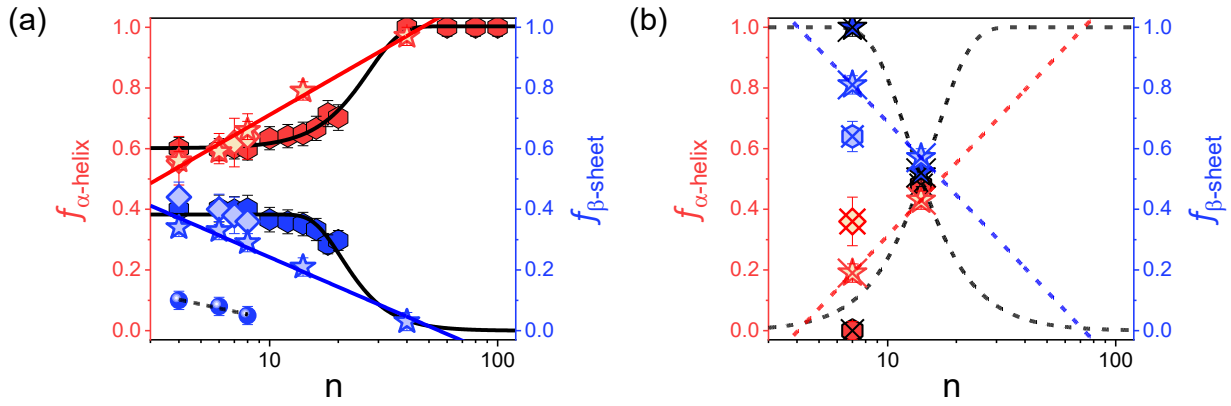

Figure 4.10. Relative (TM-DSC: rhombi, WAXS: hexagons) and absolute (NMR: stars) fractions of *α*-helices (red) and *β*-sheets (blue) of the (a) dimethylamino terminated and (b) n-hexyl terminated samples as a function of the degree of polymerization. The chain ends of the β-sheets are also indicated by spheres. Black lines are sigmoidal fits to the WAXS results (see text). Red and blue lines are linear fits to the NMR data.

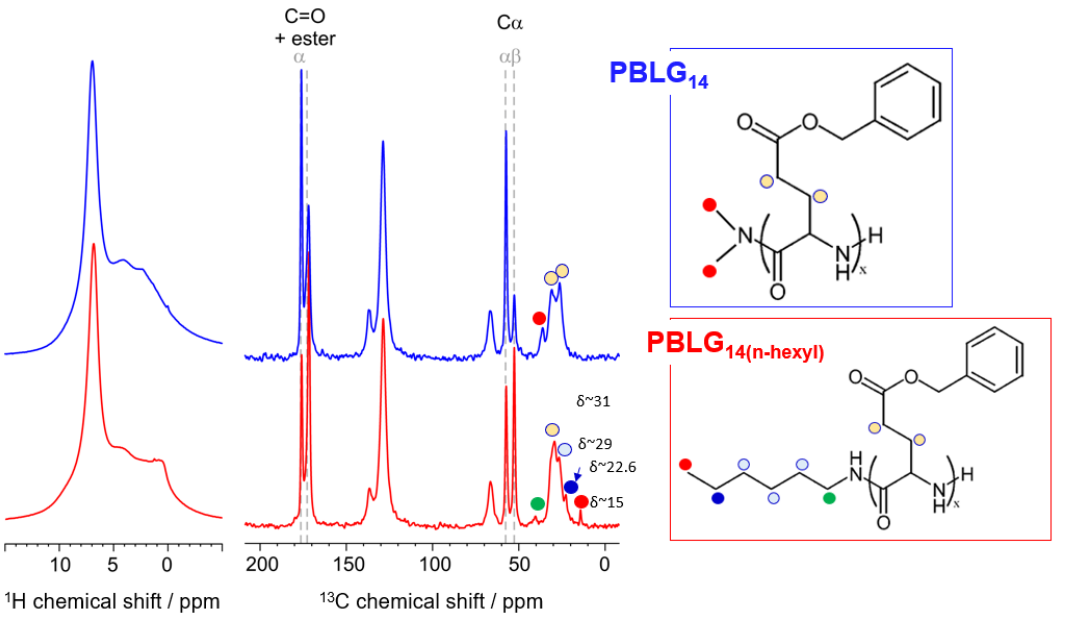

Figure 4.11. (middle) ^{13}C solid state NMR traces and (left) ^{1}H NMR traces of $PBLG_{14}$ and $PBLG_{14(n\text{-}hexyl)}$ at $T = 320$ K. The molecular structures of the repeat units of the dimethylamino (up) and n-hexyl (down) terminated samples are also shown, (right) including the color scheme employed for assignment purposes.

How do these results depend on end group chemistry? To further probe the role of end-group chemistry and its influence on the self-assembly, detailed ^{13}C solid state NMR spectra, together with the corresponding ^{1}H NMR spectra, were acquired for $PBLG_{14}$ and its n-hexyl terminated analog, $PBLG_{14(n\text{-}hexyl)}$ (Figure 4.11). Although both samples share the same degree average of polymerization, the nature of their end groups is different. $PBLG_{14}$ features a hydrogen atom at one end and a dimethylamino group ($–N(CH_3)_2$) at the other end, while $PBLG_{14(n\text{-}hexyl)}$ has a hydrogen atom at one terminus and a longer, bulkier end group consisting of a secondary amine substituted with an n-hexyl chain ($–NH–(CH_2)_6CH_3$) at the other end. The ^{13}C NMR traces reveal distinct resonances in the upfield region, corresponding to the terminal carbons of these end groups, along with the two carbons of the side group. These assignments are further supported by the ^{1}H NMR spectra, which display the corresponding proton signals of the terminal moieties. $PBLG_{14}$ has predominantly α-helical structures, whereas $PBLG_{14(n\text{-}hexyl)}$ shows a majority of β-sheets. Hence, chain-end chemistry contributes significantly to the stabilization of a certain secondary structure.

4.2.2 Molecular dynamics

a. Solid-State NMR

Important insights into the dynamics of PBLG can be obtained by examining the temperature dependence of the NMR spectra, shown in Figure 4.12.[24] As can be seen from the evolution of the C_α resonances of $PBLG_6$ and $PBLG_{14}$, the α-helical signal ($\delta \sim 58$ ppm) exhibits a significant broadening and a decrease in intensity with increasing temperature. This behavior reflects a temperature-induced softening of the helical segments, especially at the ends of the helices where they are connected to more disordered or amorphous segments. As the system approaches the segmental (α) process (the relative timescales are presented below in Figure 4.17), the segmental motions fall within the dynamic window of NMR. These thermally activated motions reduce the local rigidity of the helices, leading to a broadening of resonances and to a reduction in signal intensity. On the contrary, the β-sheet resonances remain sharp and even increase with temperature (e.g., in $PBLG_{14}$, Figure 4.12b). The absence of a similar softening or dynamic broadening implies

that the segmental dynamics associated with the β-sheets – hereafter referred to as the α^* process – is not thermally activated in the temperature range studied by the specific NMR frequency ($f \sim 10^5$ Hz). Hence, the results of the T-dependent NMR study suggest that, up to the highest measurement temperature (T = 360 K), the dynamics of β-sheets remain practically frozen at the NMR frequency.

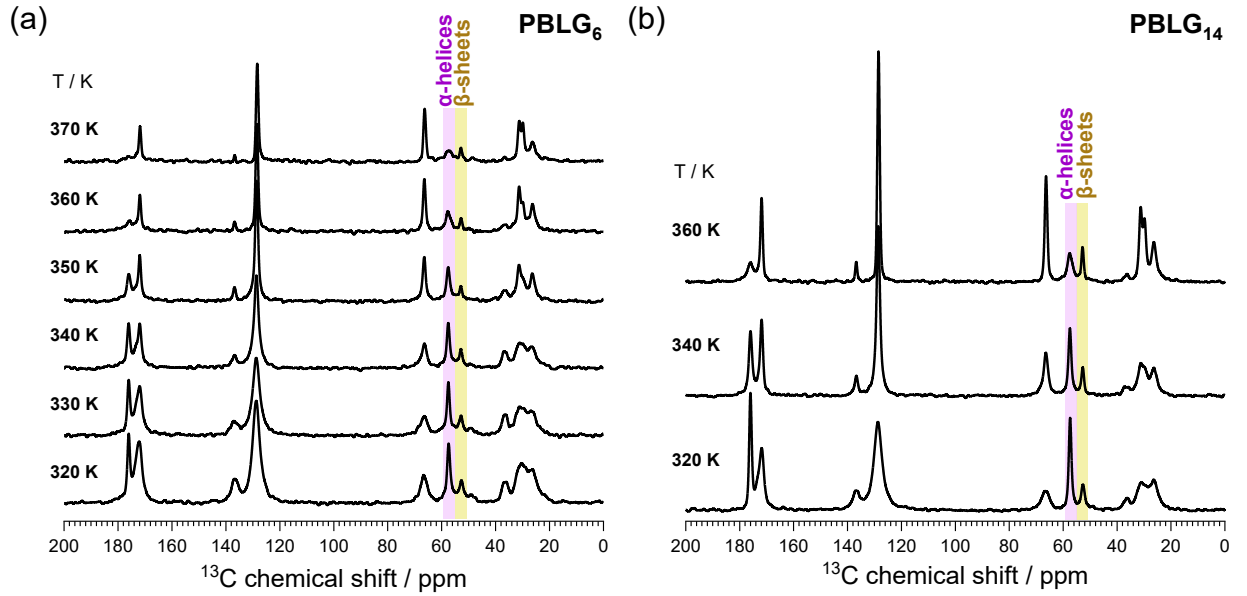

Figure 4.12. ^{13}C solid state NMR traces of (a) $PBLG_6$ and (b) $PBLG_{14}$ as a function of temperature. The highlighted areas refer to the chemical shifts used for the calculation of the absolute fractions of α-helices and β-sheets.

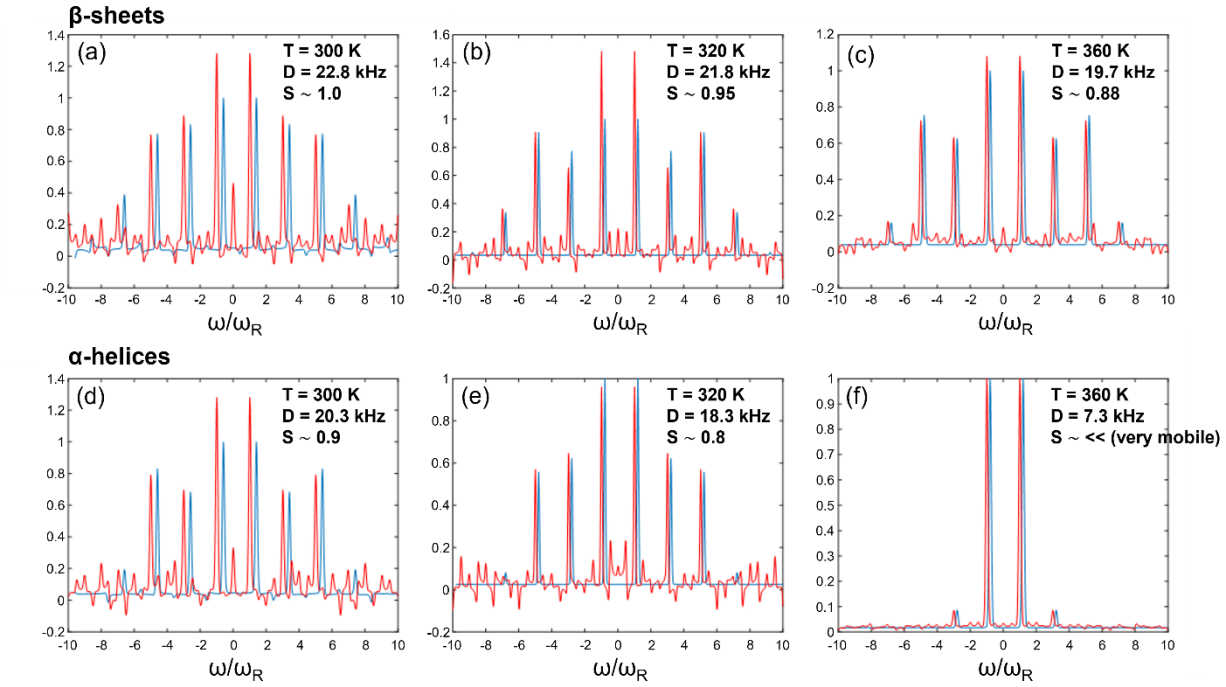

Figure 4.13. ^{13}C-^{1}H REREDOR spinning sideband patterns recorded at 25 kHz spinning at the magic angle for $PBLG_{14}$ shown for different temperatures.

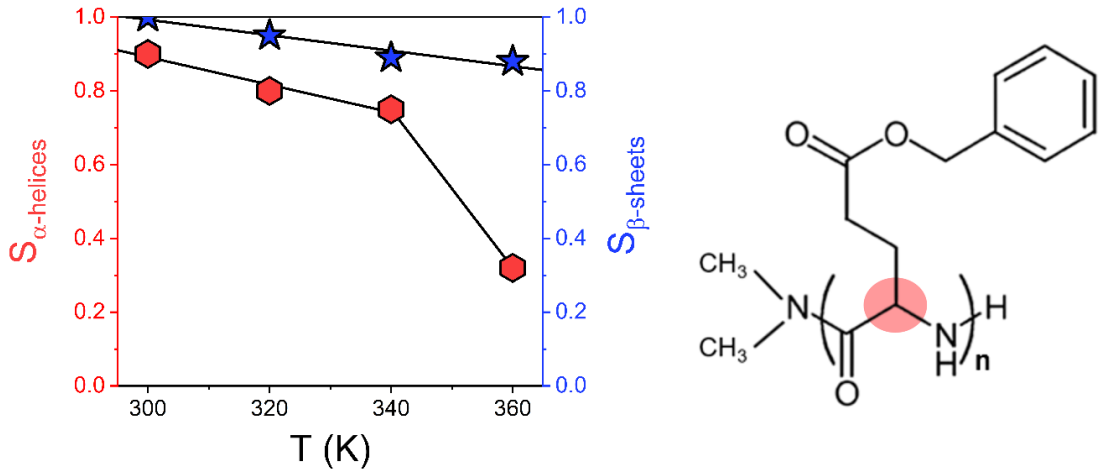

Figure 4.14. (left) Temperature dependence of the dynamics order parameter, *S*, for the C_α-H bonds in the two secondary structures, α-helices and β-sheets. $S = 0$ indicates isotropic motion, while $S = 0.1$ indicates nearly anisotropic motion. (right) The molecular structure is also shown, including the color scheme employed for clarity.

Additional information on the rigidity and the mobility differences of the β-sheet and α-helical segments of $PBLG_{14}$ can be obtained by site specific ^{13}C-^{1}H REDEROR spinning sideband pattern measurements as a function of temperature (Figure 4.13).[25,26] These experiments provide

access to the dipolar coupling constants, D_{CH}, from which the local dynamic order parameter, S, is derived. The parameter S, defined in terms of the time-averaged second order Legendre polynomial, quantifies the residual motional anisotropy of a given molecular segment:

$$S_{CH} = \langle \frac{1}{2}(3\cos^2\theta_{CH}(t) - 1)\rangle_t = \frac{\langle D_{CH}(t)\rangle_t}{D_{CH,static}} \quad (4.1)$$

A value of $S = 1$ indicates complete rigidity, while lower values reflect increasing amplitudes of molecular motion at the NMR timescale. As the resonances for α-helices/β-sheets are well resolved, S can be calculated *for each* secondary structure (Figure 4.14). For the β-sheets, S remains nearly constant over the entire temperature range studied, with only a small decrease from 1.0 (D = 22.8 kHz) at 300 K to 0.88 (D = 19.7 kHz) at 360 K. This slight decrease reflects the onset of limited local mobility, but overall confirms that the β-sheets remain highly rigid and dynamically arrested up to 360 K. These findings are consistent with the glassy behavior of the β-sheets. The α-helical segments show a significantly different response. Starting from a slightly lower S value of 0.90 (D = 20.3 kHz) at 300 K, the order parameter gradually decreases with increasing temperature, reaching 0.75 at 340 K. This continuous decrease indicates increasing local mobility and partial dynamic softening of the helical parts. Importantly, a "transition" occurs between 340 K and 360 K, where S drops abruptly to 0.32 (D = 7.3 kHz), indicating the onset of large-amplitude segmental dynamics. As we will show bellow with DS, this reflects the onset of the segmental (α) process, e.g., the segmental motion in α-helical peptides. The distinct S (T) profiles displayed in Figure 4.14 quantitatively demonstrate this divergence in mobility: while β-sheets remain largely immobilized, α-helices undergo a temperature-driven relaxation into a dynamically softened state.

b. Dielectric spectroscopy

The thermodynamic (TM-DSC) and structural characterization (WAXS, solid-state NMR) of PBLG as a function of the degree of polymerization identified distinct self-assembly motifs. In addition, temperature-dependent solid-state NMR identified dynamic changes in the NMR frequency, especially for the α-helices, whereas β-sheets were found to be "glassy" up to about 360 K. Although NMR could identify glassy vs mobile segments, it was not possible to extract timescales of motions. This inherent difficulty of NMR can be surpassed by employing the

technique which is most sensitive to dynamics; Dielectric Spectroscopy. Here we discuss the molecular dynamics as a function of temperature and pressure by employing DS.

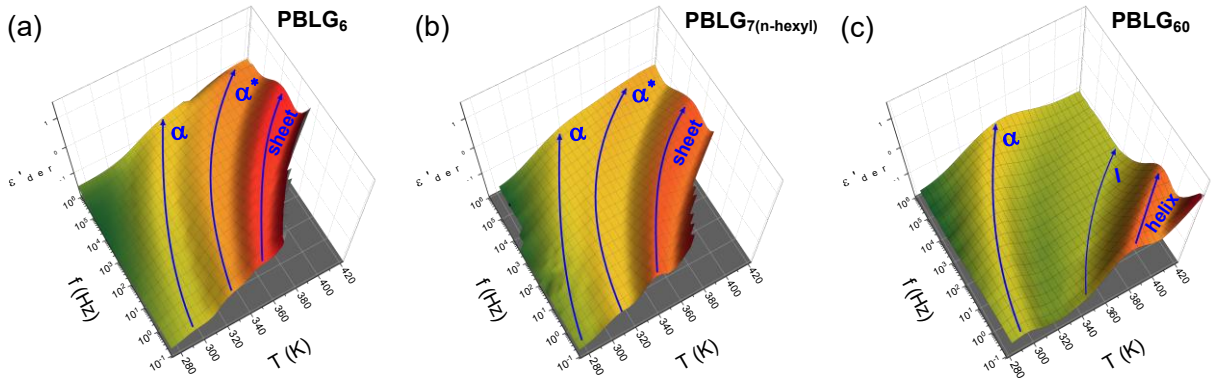

Figure 4.15. Three-dimensional representation of the derivative of dielectric permittivity as a function of frequency and temperature, for (a) $PBLG_6$, (b) $PBLG_{7(n\text{-hexyl})}$ and (c) $PBLG_{60}$. Three processes are visible in each case; for the oligopeptides, $PBLG_6$ and $PBLG_{7(n\text{-hexyl})}$, the indicative lines correspond to the α process, the α^* process and the slow β-sheet process, while for $PBLG_{60}$ the lines give the α process, a weak intermediate process and the slower relaxation of α-helices.

First, we examined the molecular dynamics as a function of temperature for different molar masses. Figure 4.15 shows a three-dimensional plot of the derivative of dielectric permittivity as a function of frequency and temperature for three representative samples: $PBLG_6$, $PBLG_{7(n\text{-hexyl})}$, and $PBLG_{60}$. Starting from lower temperatures, all samples, regardless of the degree of polymerization and end-group, exhibit the α process.[11,12] This process originates from the amorphous segments that interrupt the α-helices, as well as from segments at the helical chain ends. It corresponds to the lowest glass temperature detected in TM-DSC. For peptides with low and intermediate molar masses ($n \leq 20$), that stabilize both α-helical and β-sheet secondary structures, two additional relaxations are evident. The first is the α^* process, attributed to the dynamics of segments located in less-ordered or completely disordered parts of β-sheets. This is the first experimental observation of a segmental relaxation directly associated with the β-sheets (Figure 4.15a,b). Interestingly, the α^*process occurs at lower frequencies, i.e., longer timescales, than the α process at the same temperature (Figure 4.16). This indicates that the associated motions are significantly more restricted. The second process, termed "slow" process, is associated with a global relaxation of β-sheets. This process will be discussed in detail below, in the context of its dielectric strength.

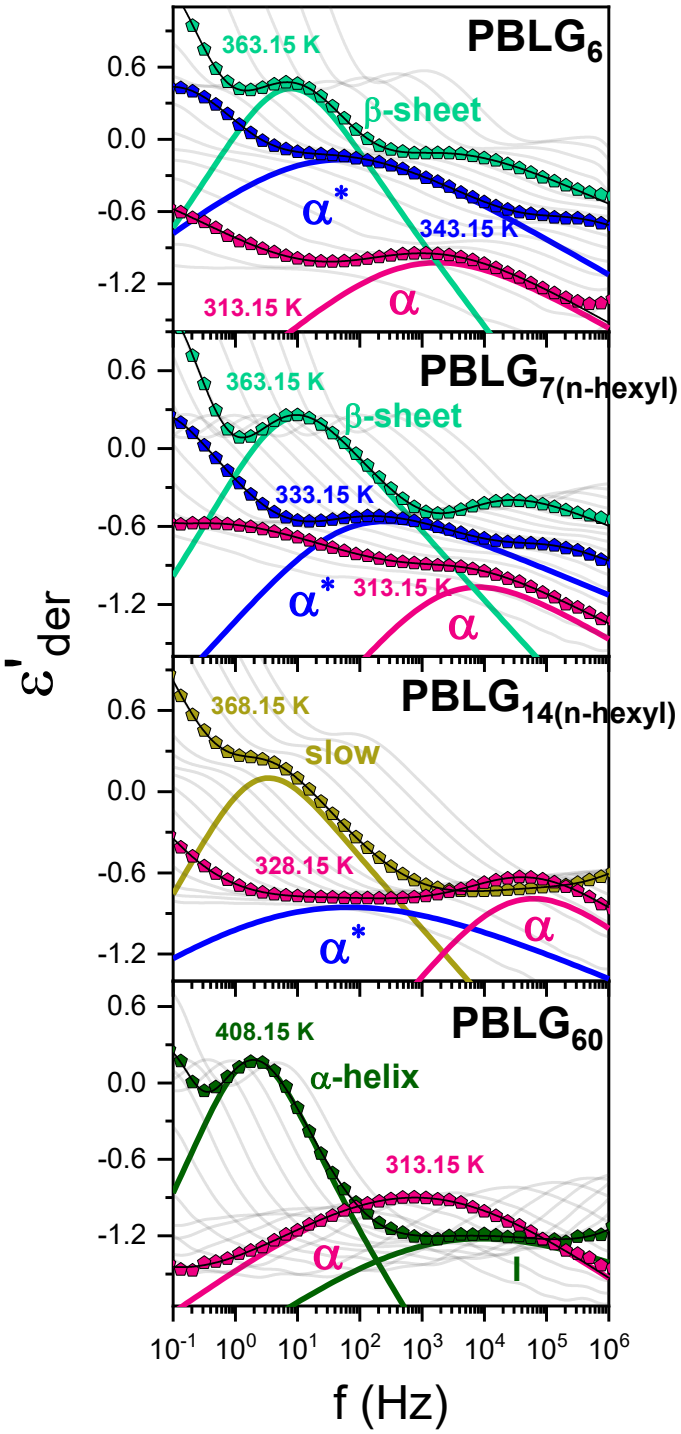

Figure 4.16. Derivative of dielectric permittivity as a function of frequency at selected temperatures, for four distinct samples PBLG$_6$, PBLG$_{7(n\text{-hexyl})}$, PBLG$_{14(n\text{-hexyl})}$ and PBLG$_{60}$. Some temperatures are highlighted for each sample showing simulations of the HN function for the respective processes: α segmental process (pink), α^* segmental process (blue), β-sheet process (green), slow process (yellow), α-helix process (dark green).

For polypeptides ($40 \leq n \leq 100$), that exclusively adopt α-helical structures, the results are consistent with the previous studies on PBLG polypeptides (Figure 4.15c). At intermediate temperatures, a weak process is detected, that could associate with the relaxation of the amorphous chains. At higher T, a slower and intense process is observed. It is assigned to the relaxation of the helical parts, the so-called α-helix process. According to the "defected helix" model, the α-helix can be conceptualized as consisting of distinct "ideal" helical parts of uniform correlation length, denoted as ξ_{helix}, which are capable of rotating on the surface of a cone at a defined angle θ. Due to the hexagonal packing of helices, it is assumed that each part rotates independently, while the axes of the rotational cones remain parallel. The dipole moment associated with each helical part is $\mu = 3.4\ D\ (\xi/0.15\ nm)$, where 0.15 nm is the helix length per repeat unit. This model allows the estimation of the ξ_{helix} from the dielectric strength of the slow helical process as, $\Delta\varepsilon = \frac{N_A \rho}{3\varepsilon_0 kTM_0}(3.4Debye)^2(\xi/0.15\ nm)sin^2\theta$. X-ray scattering from oriented fibers provides an upper value for θ, which is then used to estimate the helical correlation length. This value is approximately 2 nm, significantly smaller than the theoretical length of an "ideal" helix. This suggests that α-helices consist of broken helices rather than behaving as a single rigid unit.

The extracted relaxation times for the aforementioned processes are presented in the Arrhenius plot of Figure 4.17. The α and α^* processes conform to the usual Vogel-Fulcher-Tammann (VFT) equation

$$\tau = \tau_o^{\#} exp\left(\frac{B}{T - T_o}\right) \tag{4.2}$$

where $\tau_o^{\#}$ is the relaxation time in the limit of very high temperatures, B is the activation parameter and T_o is the "ideal" glass temperature. The VFT parameters of the two segmental processes in the oligopeptides and the polypeptides with the different terminated groups are summarized in Table 4.2.

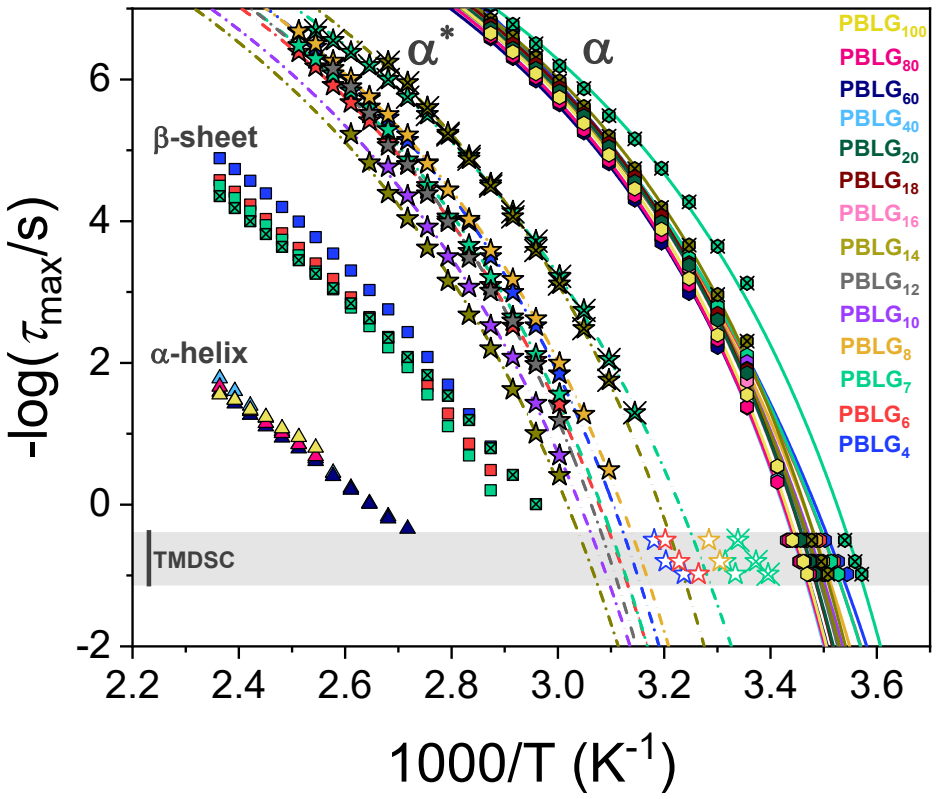

Figure 4.17. Characteristic relaxation times as a function of the inverse temperature of PBLGs with different degrees of polymerization: $PBLG_4$ (blue), $PBLG_6$ (red), $PBLG_7$ (green), $PBLG_8$ (orange), $PBLG_{10}$ (purple), $PBLG_{12}$ (gray), $PBLG_{14}$ (dark yellow), $PBLG_{16}$ (pink), $PBLG_{18}$ (wine), $PBLG_{20}$ (dark green), $PBLG_{40}$ (light blue), $PBLG_{60}$ (navy), $PBLG_{80}$ (magenta), $PBLG_{100}$ (yellow). Crossed symbols correspond to $PBLG_{7(n\text{-hexyl})}$ (green) and $PBLG_{14(n\text{-hexyl})}$ (dark yellow). Hexagons represent the α process, stars the α^* process, squares the slow β-sheet process and triangles the slow α-helical process (see text). TM-DSC data are also shown. The lines represent fits to the VFT equation (parameters are summarized in Table 4.2).

Table 4.2. VFT parameters for the segmental α and α^* processes, along with the corresponding T_g values extracted from DS (at τ = 100 s) and DSC.

	Sample	-log(τ_0/s)	B (K)	T_0 (K)	T_g^{DS} (K)	T_g^{DSC} (K)
α process	$PBLG_4$	-14*	2015 ± 20	225 ± 1	279 ± 1	284 ± 3
	$PBLG_6$	-13.4 ± 0.3	1800 ± 85	229 ± 2	280 ± 1	284 ± 3
	$PBLG_7$	-13.2 ± 0.2	1710 ± 65	230 ± 1	281 ± 1	285 ± 3
	$PBLG_{7(n\text{-hexyl})}$	-12	1250 ± 15	238 ± 1	277 ± 1	278 ± 3
	$PBLG_8$	-12.6 ± 0.1	1490 ± 45	237 ± 1	282 ± 1	286 ± 3
	$PBLG_{10}$	-12.3 ± 0.5	1384 ± 55	241 ± 3	283 ± 1	287 ± 1
	$PBLG_{12}$	-12*	1265 ± 5	244 ± 1	284 ± 1	287 ± 1
	$PBLG_{14}$	-12*	1280 ± 10	244 ± 1	283 ± 1	287 ± 1
	$PBLG_{14(n\text{-hexyl})}$	-12*	1225 ± 15	244 ± 1	282 ± 1	286 ± 1
	$PBLG_{16}$	-12*	1235 ± 15	246 ± 1	284 ± 1	288 ± 1
	$PBLG_{18}$	-12*	1210 ± 20	247 ± 1	284 ± 1	288 ± 1

	$PBLG_{20}$	-12*	1235 ± 10	246 ± 1	284 ± 1	288 ± 1
	$PBLG_{40}$	-12*	1260 ± 20	247 ± 1	286 ± 1	289 ± 1
	$PBLG_{60}$	-12*	1295 ± 20	245 ± 1	285 ± 1	289 ± 1
	$PBLG_{80}$	-12*	1265 ± 15	246 ± 1	286 ± 1	289 ± 1
	$PBLG_{100}$	-12*	1240 ± 10	247 ± 1	285 ± 1	289 ± 1
α* process	$PBLG_{4}$	-12*	1690 ± 10	261 ± 1	313 ± 1	312 ± 1
	$PBLG_{6}$	-12*	1795 ± 15	260 ± 1	316 ± 1	310 ± 1
	$PBLG_{7}$	-12*	1735 ± 25	262 ± 1	316 ± 1	302 ± 1
	$PBLG_{7(n\text{-}hexyl)}$	-12*	1760 ± 15	245 ± 1	301 ± 1	296 ± 1
	$PBLG_{8}$	-12*	1725 ± 10	258 ± 1	312 ± 1	302 ± 1
	$PBLG_{10}$	-12*	1920 ± 30	259 ± 1	319 ± 1	-
	$PBLG_{12}$	-12*	1700 ± 35	265 ± 2	318 ± 1	-
	$PBLG_{14}$	-12*	1980 ± 45	260 ± 2	321 ± 1	-
	$PBLG_{14(n\text{-}hexyl)}$	-12*	1570 ± 20	257 ± 1	305 ± 1	-

* value held fixed

As a next step, we examine the dependence of the glass temperatures on molar mass. The T_gs associated with the α and α^* segmental processes, as determined by both TM-DSC and DS, are plotted as a function of the degree of polymerization n in Figure 4.18. The T_g of the α process increases with increasing chain length, following an approximately Fox–Flory dependence, suggesting the influence of chain-ends on the segmental dynamics. Despite a more limited dataset, the T_g of the α^* process shows a similar trend. Both processes are attributed to the dynamics of amorphous segments, especially those located at the chain ends or in disordered regions in-between the more ordered domains. However, the key difference lies in their structural environment: the α^* process occurs at higher temperatures, suggesting that these amorphous segments are subject to additional constraints. This reduced mobility of segments associated with the α^* process in β-sheets is likely to associate with h.b. defects between different chains in their β-sheet secondary structure (although the exact assignment would require additional tools).

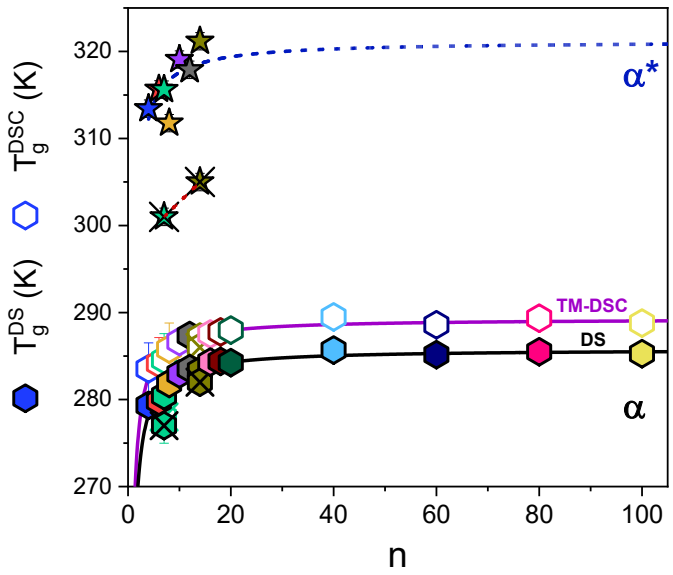

Figure 4.18. Liquid-to-glass temperatures of the α process (hexagons) and the α^* process (stars) as a function of the molar mass. Crossed symbols correspond to the n-hexyl terminated oligopeptides. Filled symbols refer to DS (T_g defined at $\tau = 100$ s) and open symbols to TM-DSC. Lines represent fits to the Fox-Flory equation.

Interestingly, the n-hexyl terminated samples exhibit lower T_gs, as compared to the dimethylamino terminated ones, both for the α-helical (α) and β-sheet (α^*) secondary structures.

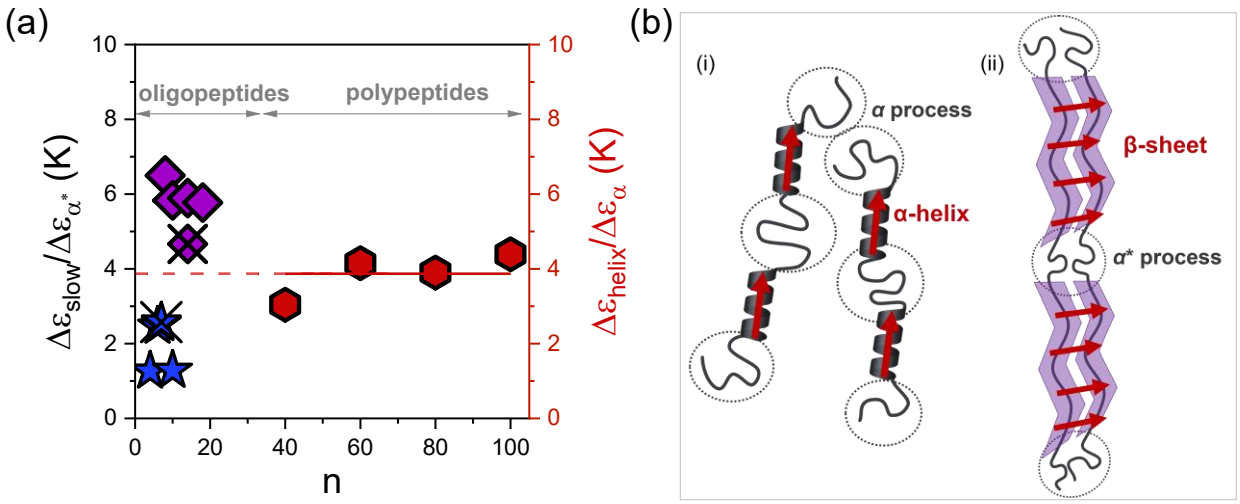

Figure 4.19. (a) Dielectric strength of the slow process (blue) normalized to the dielectric strength of the α^* (α) process and the α-helix process (red) normalized to the dielectric strength of the α process, for oligopeptides and polypeptides, as a function of molar mass. The case of polypeptides with intermediate n, where the dielectric strength of the slow process (purple) is normalized to the dielectric strength of the α^* process, is also indicated. Crossed symbols correspond to the n-hexyl terminated oligopeptides. (b) Schematic representation of two PBLG chains forming (i) α-helices

and (ii) a parallel β-sheet. The red arrows indicate the dipole moment vector. The dotted circles indicate regions where amorphous segments interrupt the α-helices/β-sheets, as well as segments at the chain ends.

We now turn to the analysis of the "slow" process, observed at elevated temperatures in PBLG with low and intermediate molar masses. In α-helical polypeptides, this process is attributed to the relaxation of the α-helical parts. The ratio of the dielectric strength of the slower process associated with the secondary structure relaxation (α-helix or β-sheet) to the dielectric strength of the corresponding segmental process (α or α^* process, respectively) (Figure 4.19b) is shown in Figure 4.19a as a function of molar mass. For high n ($\geq$ 40), the calculated ratio is $\Delta\varepsilon_{\alpha-\mathrm{helix}}/\Delta\varepsilon_{\alpha} \sim 4$, consistent with the relaxation of α-helical parts, with an effective dipole moment (macrodipole) larger than of the segmental process. Conversely, for low n ($4 \leq n \leq 10$), the ratio is $\Delta\varepsilon_{\beta-\mathrm{sheet}}/\Delta\varepsilon_{\alpha^*} \sim 2$. This is again suggestive of a relaxation exceeding a repeat unit in the β-sheet configuration. Such process can result from the parallel β-sheet structures, where the vectorial sum of individual amino acid residues in a β-sheet create a macrodipole. The dipole moments of polypeptides with alanine and glycine in β-strands have recently been discussed.[18] They were used as building blocks to predict the macrodipole moment of a β-sheet. Furthermore, it was shown that the dipole moment of an amino acid residue in a β-sheet is smaller than in an α-helix, as experimentally observed. The effect was discussed in terms of a smaller polarization caused by the interstrand hydrogen bonding in a β-sheet as compared to that in an α-helix. Interestingly, in the case of peptides with intermediate degrees of polymerization ($12 \leq n \leq 20$), we observe a significantly higher ratio, $\Delta\varepsilon_{\mathrm{slow}}/\Delta\varepsilon_{\alpha^*} \sim 5$. The higher value suggests that, the slow process likely arises from a convolution of both β-sheet and α-helical macrodipoles. This interpretation is further supported by the dielectric loss data presented in Figure 4.16. The representative fits at a selected temperature reveal that the slow process in peptides with intermediate n appears less well-resolved compared to the distinct secondary structure relaxations observed in either oligopeptides (β-sheets) or polypeptides (α-helices).

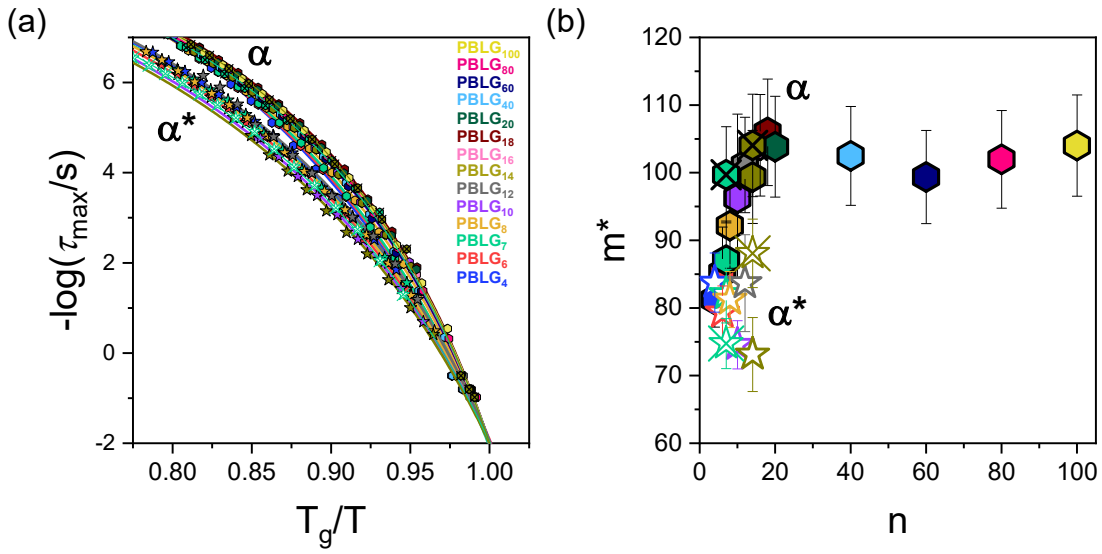

Figure 4.20. (a) Segmental α and α^* relaxations as a function of T_g/T for the different degrees of polymerization. Crossed data correspond to n-hexyl terminated samples. (b) Fragility or steepness index, m^*, of the two segmental relaxations as a function of molar mass. N-hexyl terminated samples are indicated with crossed symbols.

A parameter that provides insight into the dynamic behavior of the β-sheets versus the α-helices is the fragility of the corresponding segmental process. The fragility or steepness index, m,[27,28] is defined as $\vartheta \log\tau / \vartheta (T_g/T)|_{T=T_g}$. It quantifies the deviation of the temperature dependence of the relaxation times from the Arrhenius behavior at $T > T_g$. It can be calculated using the VFT parameters as $m^* = \frac{BT_g}{2.303(T_g - T_o)^2}$. A higher (lower) value of fragility corresponds to a steeper increase in the relaxation times near T_g, indicating a more "fragile" ("strong") glass-forming system. The temperature dependence of the relaxation times for the α and α^* processes is shown in Figure 4.20a in a T_g-scaled plot. The corresponding values of fragility are presented in Figure 4.20b. Notably, the steepness index increases systematically with increasing molar mass, a trend that is particularly evident for the α process. This observation aligns with results from various homopolymers, where higher molar mass polymers typically correlates with higher fragility. This implies that, as the degree of polymerization increases, the influence of the mobile chain-ends decreases, leading to a steeper temperature dependence near T_g. The results suggest that the chain-ends determine both the absolute value of T_g and the temperature sensitivity of the segmental dynamics in polypeptides. Regarding the effect of secondary structure on the fragility, it can be seen that the slower process (α^*), associated with the local relaxation of β-sheets, exhibits

consistently lower fragility than the faster process (α), associated with the local relaxation in α-helices, indicating a stronger glass behavior.[10] Both processes originate from amorphous segments located in structurally different environments. The β-sheet secondary structures are stabilized by intermolecular hydrogen bonds, forming a network-like structure. The constraints induced by the latter give rise to the restricted α^* process and to a lower fragility. Conversely, the α-helical secondary structures are stabilized by intramolecular hydrogen bonds. The disordered segments next to the helical segmental have more freedom to reconfigure, leading to a more thermally sensitive dynamics. Thus, while both processes originate from disordered segments, it is the structural environment, and, in particular, the extent and type of hydrogen bonding (inter vs intra), that determines their fragility.

Next, the nature of the α and α^* processes, as well as of the slower processes associated with the α-helical and β-sheet secondary structures, were investigated by pressure-dependent measurements (Figure 4.21). Two representative peptides were selected: $PBLG_{7(n\text{-hexyl})}$, an oligopeptide consisting a majority of β-sheets, and $PBLG_{40}$, which forms exclusively α-helices.

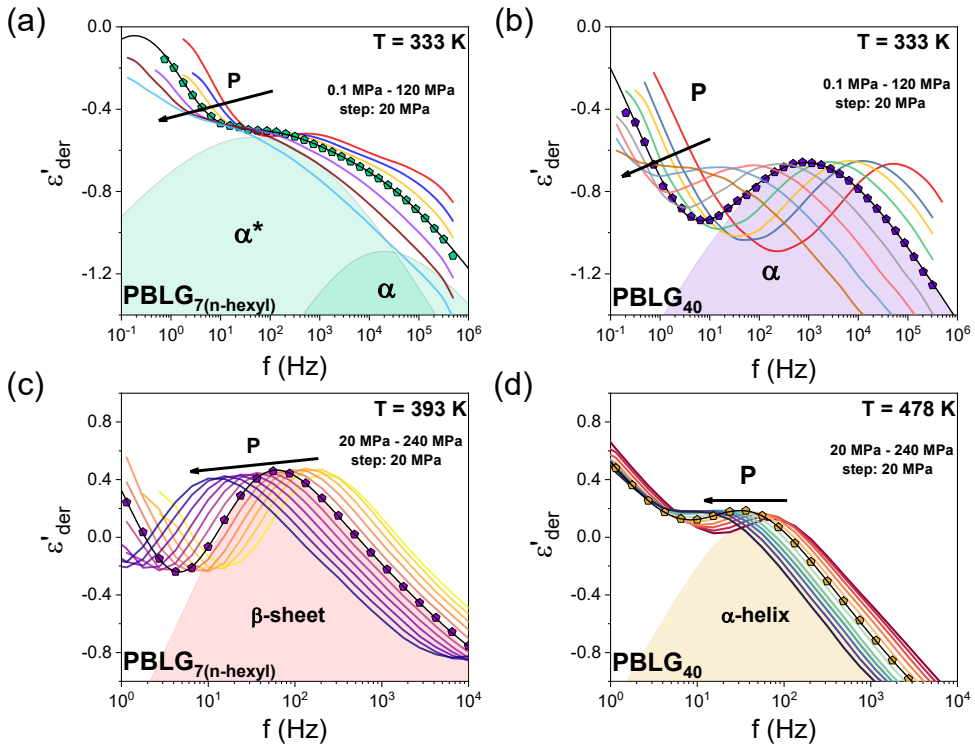

Figure 4.21. Derivative of dielectric permittivity as a function of frequency under isothermal conditions at (a) 333 K and (c) 393 K for $PBLG_{7(n\text{-hexyl})}$ and at (b) 333 K and (d) 478 K for $PBLG_{40}$. Pressure increases in the direction of the arrow. The colored areas for the highlighted pressures (indicated with symbols) represent fits (simulations) to eq (5) for the respective processes.

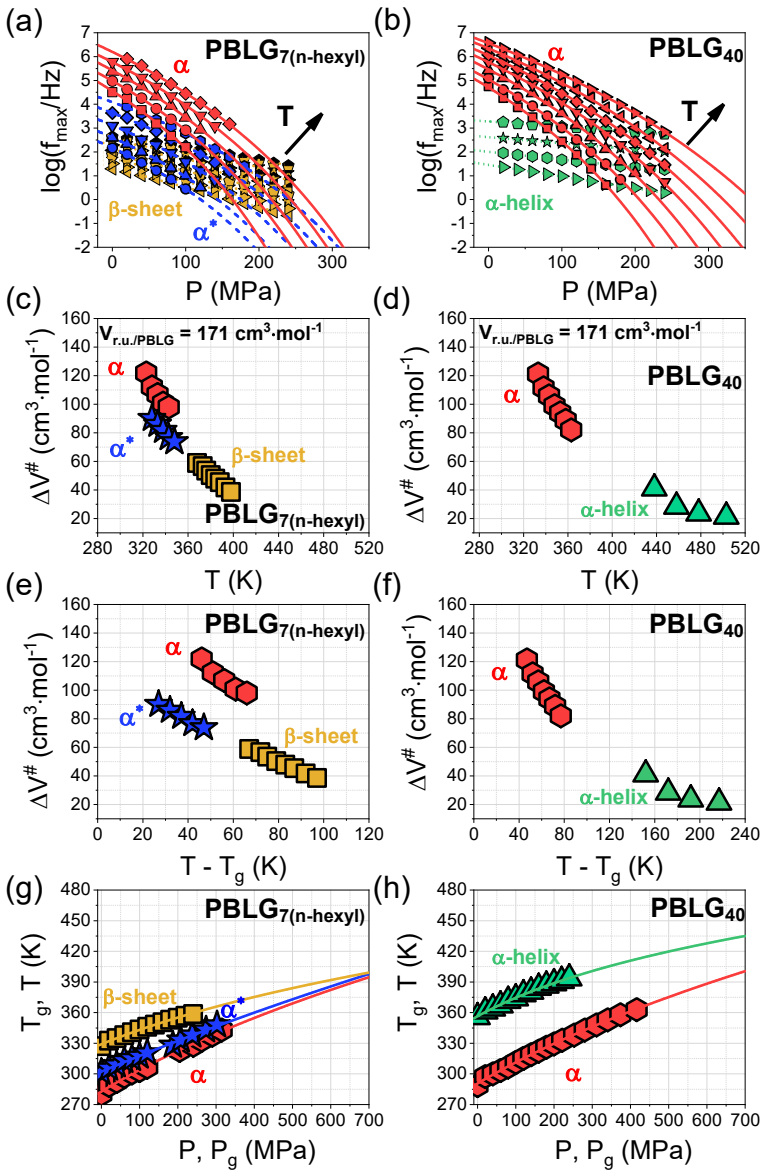

Figure 4.22. (a) Frequency at a maximum loss as a function of pressure for $PBLG_{7(n\text{-hexyl})}$, corresponding to the segmental (α) process (red); from 323 K to 343 K in 5 K steps, α^* process (blue); from 328 K to 348 K in 5 K steps, and β-sheet process (orange); for temperatures 368 K, 373 K, 376 K, 380 K, 384 K, 388 K, 393 K, and 398 K. The solid and dashed lines are fits to eq 4.3, while the dotted lines are fits to an Arrhenius dependence. (b) Pressure dependence of the characteristic frequencies at maximum loss for the $PBLG_{40}$, indicating the segmental (α) process (red); from 333 K to 363 K in 5 K steps, and the α-helix process (green); for temperatures 438 K, 458 K, 478 K, and 503 K. The solid and dotted lines are fits to eq 4.3 and to an Arrhenius dependence, respectively. (c), (d) Temperature dependence of the apparent activation volumes ($\Delta V^{\#}$) for the α (red), α^* (blue), β-sheet (orange) and α-helix (green) processes. (e), (f) Apparent activation volumes ($\Delta V^{\#}$) in a T-T_g representation for the respective processes. (g), (h) Pressure dependence of the glass temperatures (T_g) as obtained from the isothermal and isobaric representation, corresponding to the freezing of the respective processes, at a characteristic time of τ = 10 s. Solid and dashed lines represent fits to eq 4.5.

The pressure dependence of the relaxation times, under isothermal conditions, is presented in Figure 4.22a,b for the two samples. The *P*-dependence of the α and α^* processes can be described by the pressure equivalent to the VFT equation as[29]

$$f_{\max} = f_{\infty} exp\left(-\frac{D_P P}{P_0 - P}\right) \tag{4.3}$$

where τ_o is the segmental relaxation time at atmospheric pressure at a given temperature, D_P is a dimensionless parameter, P is the pressure corresponding to the "ideal" glass. In $PBLG_{7(n\text{-}hexyl)}$, the segmental (α) process exhibits a stronger pressure dependence than the α^* process. In contrast, the slow processes attributed to macrodipole relaxation in the β-sheet and α-helical secondary structures show much weaker pressure dependences.

To gain further insight into the pressure-induced behavior of the different relaxation processes, the normalized dielectric strength $\Delta\varepsilon/\rho$ was examined as a function of pressure. The density was calculated using the Tait equation,[10] $V(P,T) = V(0,T)\left\{1 - 0.0894 \ln\left(1 + \frac{P}{B(T)}\right)\right\}$, where $V(0,T) = A_0 + A_1 T + A_2 T^2$ is the perfect volume at atmospheric pressure and $B(T) = B_0 \exp(-B_1 T)$, where T is in °C (A_0 = 0.788 cm^3, $A_1 = 4.92 \cdot 10^{-4}$ $cm^3 \cdot °C^{-1}$, $A_2 = 7.57 \cdot 10^{-7}$ $cm^3 \cdot °C^{-1}$, $A_2 = 7.57 \cdot 10^{-7}$ $cm^3 \cdot °C^{-1}$, B_0 = 142 MPa, $B_1 = 4.3 \cdot 10^{-3}$ $°C^{-1}$). The dielectric strength of a relaxation process is given by[30]

$$\Delta\varepsilon = \frac{1}{3\varepsilon_o} g F \frac{\mu^2 N}{k_B T V} \tag{4.4}$$

where, ε_o is the dielectric permittivity of vacuum, N/V is the number density of dipoles expressed as $(\rho/M)N_A$, ρ is the density, M is the molar mass of the repeat unit, μ is the dipole moment, F is the local field factor, and g is the Kirkwood-Fröhlich correlation factor.

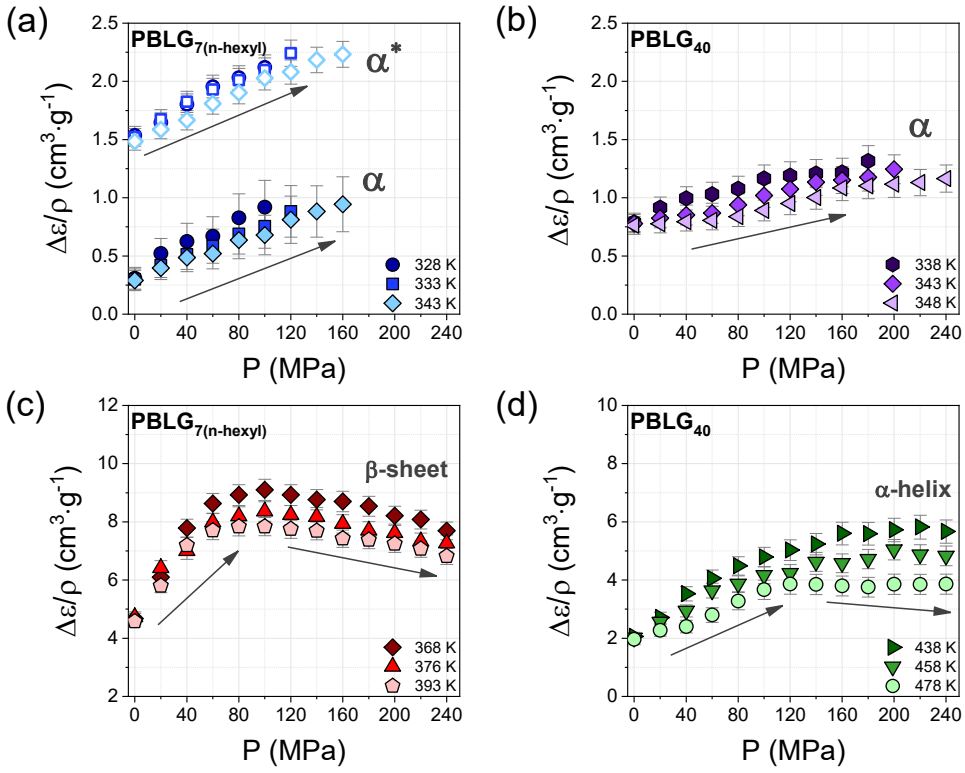

Figure 4.23. Normalized dielectric strengths, $\Delta\varepsilon/\rho$ for $PBLG_{7(n\text{-}hexyl)}$ corresponding to (a) the α and α^* process and (c) the β-sheet process, and for $PBLG_{40}$ indicating (b) the α process and (d) the α-helix process at some selected temperatures.

The normalized dielectric strengths of the aforementioned processes for $PBLG_{7(n\text{-}hexyl)}$ and $PBLG_{40}$ are presented in Figure 4.23. For both the α and α^* processes, the normalized dielectric strength, $\Delta\varepsilon/\rho$, for lower pressures increases beyond densification. In the absence of dipole-dipole interactions (g), this implies that pressure induces structural defects (increase of N in eq 4.4) that are incorporated in the segmental processes (i.e., increasing number density of amorphous segments). Following the same reasoning, $\Delta\varepsilon/\rho$ for the organized structures should decrease with increasing pressure. This is indeed observed but only for pressures exceeding ~ 120 MPa. For $P <$ 120 MPa, the normalized dielectric strengths for the α-helix and β-sheet processes also reveal an increase. This could imply dipole-dipole interactions (g > 1) of larger entities (i.e., macrodipoles in α-helices).

Pressure dependent measurements provide access to the apparent activation volume, $\Delta V^{\#}$.[31] This quantity is extracted from the pressure dependence of the relaxation times (Figure 4.22a,b), as the slope at each pressure, according to $\Delta V^{\#} = 2.303RT\left(\frac{\partial \log\tau}{\partial P}\right)_T$. In the absence of

hydrogen bonding, $\Delta V^{\#}$ has been interpreted as reflecting the molecular volume of the underlying dynamic processes. In the presence of h.b., it could associate with a characteristic volume of defects. The apparent activation volume at ambient pressure can be calculated as a function of the temperature for the investigated processes, with the results plotted in Figure 4.22c,d (and also in Figure 4.22e,f). For all processes studied, the calculated $\Delta V^{\#}$ values were found to be smaller than the molecular volume of PBLG repeat unit ($\Delta V^{\#}_{\text{r.u.}} = 171$ cm^3·mol^{-1}). However, at T_g, $\Delta V^{\#}(\alpha) \approx \Delta V^{\#}_{\text{r.u.}}$ and $\Delta V^{\#}(\alpha^*) < \Delta V^{\#}_{\text{r.u.}}$. The α process exhibits comparable activation volumes in both $PBLG_{7(\text{n-hexyl})}$ and $PBLG_{40}$, supporting the notion that it originates from the relaxation of amorphous segments in the α-helical peptides. In $PBLG_{7(\text{n-hexyl})}$, the α^* process displays a lower activation volume than of the α process at the same temperature, but a similar temperature dependence. This could reflect a smaller defect volume in the case of β-sheets.

Lastly, we examine the pressure sensitivity of the glass temperature, extracted for each process at $\tau = 10$ s (to avoid long extrapolations). Figure 4.22g,h presents the P and T dependence of T_g and P_g, respectively. The data fitted using the empirical equation[32]

$$T_g(P) = T_g(0)\left(1 + \frac{\nu}{\mu}P\right)^{1/\nu} \tag{4.5}$$

with $T_g(0)$ being the glass temperature at atmospheric pressure and μ and ν are fitting parameters. The fitting parameters are shown in Table 4.3. The pressure sensitivity of T_g, can be discussed from the $\left(dT_g/dP\right)_{P\to 0}$ coefficient. For amorphous polymers and van der Waals liquids, $\left(dT_g/dP\right)_{P\to 0}$ is in the range from 360 to 180 K·GPa^{-1}. On the other hand, hydrogen bonding systems show a weaker dependence, as $\left(dT_g/dP\right)_{P\to 0}$~ 100 to 20 K·GPa^{-1}.[33] The α process of both $PBLG_{7(\text{n-hexyl})}$ and $PBLG_{40}$ exhibit similar $\left(dT_g/dP\right)_{P\to 0}$ parameters (~ 200 K·GPa^{-1}), consistent with the values reported for α-helical polypeptides (PBLG and PZLL).[10] In contrast, the α^* process of $PBLG_{7(\text{n-hexyl})}$ exhibits a lower pressure coefficient of 158 K·GPa^{-1}, closely related to the behavior observed for the β-sheet-forming PGly.[10] These findings once again highlight the role of the secondary structure in governing pressure sensitivity. The network-like structure of β-sheets imposes stronger constraints on the amorphous segments, thereby limiting the pressure response of the α^* process.

Table 4.3. Parameters of the $T_g(P)$ dependence (eq 4.5)

Sample	ν	μ (MPa)	$\left(dT_g/dP\right)_{P\to 0}$ (K·GPa^{-1})
α process (PBLG$_{7(\text{n-hexyl})}$)	3.1 ± 0.9	1210 ± 150	234
α^* process (PBLG$_{7(\text{n-hexyl})}$)	2.2 ± 0.8	1910 ± 80	158
β-sheet (PBLG$_{7(\text{n-hexyl})}$)	6.5 ± 1.1	1705 ± 130	208
α process (PBLG$_{40}$)	2.9 ± 0.3	1320 ± 60	220
α-helix (PBLG$_{40}$)	5.1 ± 1.3	2151 ± 140	153

So far, the dynamics has revealed two distinct glass temperatures in polypeptides that form both secondary structures, each corresponding to the relaxation of α-helical- and β-sheet-associated amorphous segments. ^{13}C NMR and DS showed that β-sheets relax on longer timescales, indicating a more restricted structural environment. The relaxation of the α-helical and β-sheet macrodipoles was also evident at even longer timescales. Further analysis revealed consistently lower fragility values in β-sheets. This behavior was discussed in view of the constraints imposed by their inherent network-like structure stabilized by intermolecular hydrogen bonds. In contrast, α-helices (stabilized by intramolecular h.b.) allow for greater mobility in nearby amorphous segments, leading to a more thermally sensitive dynamics. These structural differences were also reflected in the weaker pressure sensitivity of the β-sheets compared to α-helices.

4.2.3 Viscoelastic response

Here, we examine the viscoelastic properties of PBLG as a function of molar mass and chain end-group chemistry. Figure 4.24 depicts master curves of the storage (G') and the loss (G'') moduli as a function of frequency. For both oligopeptides and polypeptides, the storage modulus consistently exceeds the loss modulus ($G' > G''$), indicating a solid-like (elastic) behavior. This solid-like response indicates the underlying structural organization, i.e., the α-helical and β-sheet secondary structures and their supramolecular self-assembly into ordered domains. The respective van Gurp-Palmen (vGP) plot of the phase angle (δ) versus the complex modulus ($|G^*|$), shown in Figure 4.25, is more informative of the applicability of time-Temperature superposition (*tT*s) and of the elastic plateau. For homopolymers following the *tT*s, all isothermal data in a vGP plot overlap in a single master curve. There exist two minima in δ. One at the plateau modulus G_N^0 reflecting the elastic properties of the entanglement "network" (typically $G_N^0 \sim 10^5$ Pa) and another in the vicinity of the liquid-to-glass temperature (T_g) where $|G^*| \sim 10^9$ Pa. Between the two minima, δ increases and goes through a maximum.

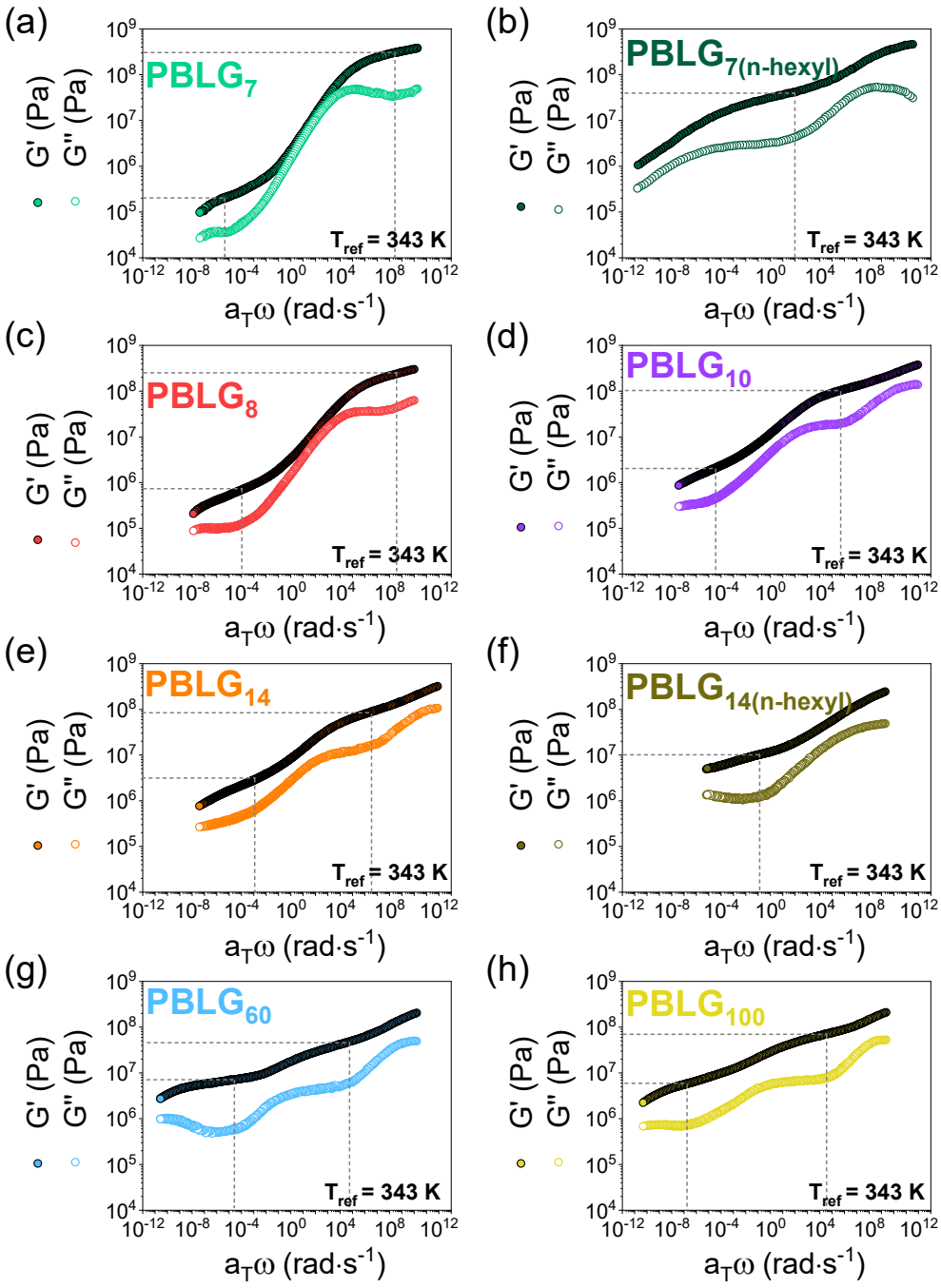

Figure 4.24. Master curves of the storage (filled circles) and loss (open circles) moduli of $PBLG_{7}$ (green), $PBLG_{7(n\text{-}hexyl)}$ (dark green), $PBLG_{8}$ (red), $PBLG_{10}$ (purple), $PBLG_{14}$ (orange), $PBLG_{14(n\text{-}hexyl)}$ (dark yellow), $PBLG_{60}$ (blue) and $PBLG_{100}$ (yellow). There is a solid-like behavior ($G' > G''$) across all measured frequencies.

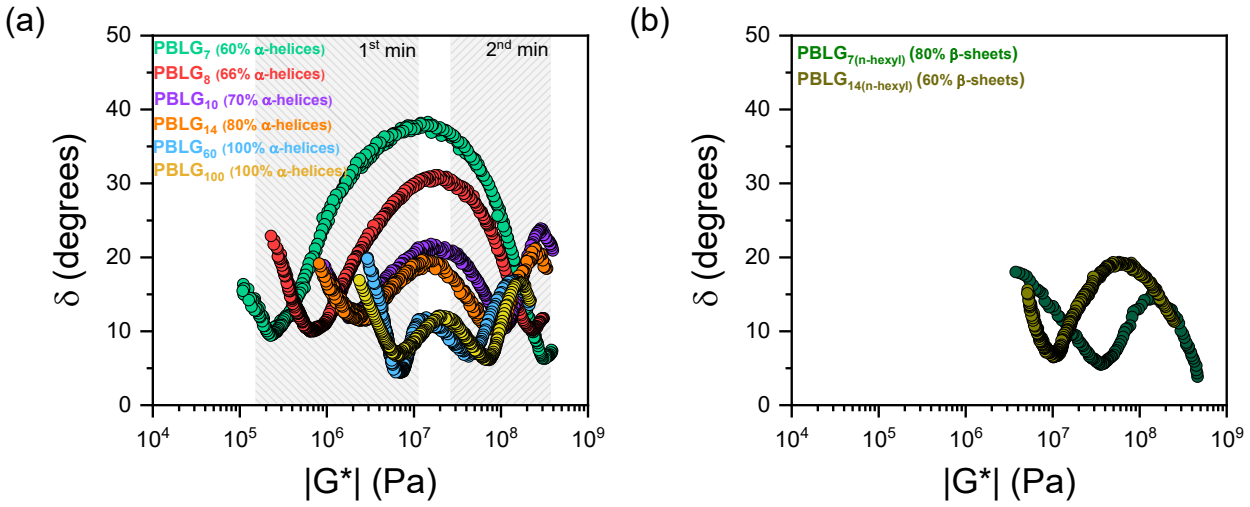

Figure 4.25. The van Gurp-Palmen plot for the investigated (a) dimethylamino terminated and (b) n-hexyl terminated samples. Colors indicate the different degrees of polymerization: $PBLG_7$ (green), $PBLG_{7(n\text{-hexyl})}$ (dark green), $PBLG_8$ (red), $PBLG_{10}$ (purple), $PBLG_{14}$ (orange), $PBLG_{14(n\text{-hexyl})}$ (dark yellow), $PBLG_{60}$ (blue) and $PBLG_{100}$ (yellow). In the former samples, two minima are evident, while in the latter a single minimum is shown.

In the dimethylamino terminated samples, the vGP plot (Figure 4.25a) reveals two distinct minima. In the case of $PBLG_7$ (60 % of α-helices) the first δ_{min} is at a modulus of $|G^*| \sim 2\text{x}10^5$ Pa, reminiscent to amorphous polymers. However, increasing molar mass brings about a large shift towards higher $|G^*|$ values; from $2\text{x}10^5$ Pa in $PBLG_7$ to $7\text{x}10^6$ Pa in $PBLG_{100}$. Naturally, we assign this first δ_{min} to the α-helical segments that grow in number and coherence with n. For polypeptides, where the hierarchical self-assembly (α-helices and their hexagonal packing) is more coherent, $\delta_{min} \sim 4$ ° and the plateau becomes more evident. The significant increase in the $|G^*|$ values with n suggests a percolation mechanism of the helical structures. To quantify the length scale of these structural constraints, we calculate an apparent molar mass, M_e, and the corresponding N_e, of the smallest structural unit that imparts rigidity using the equation $G_N^0 = \frac{4}{5}\frac{\rho RT_{ref}}{M_e}$,[34] where ρ is the density at the reference temperature (T_{ref} = 343 K). Interestingly, N_e decreases with increasing n (Figure 4.26a), ranging from about 60 repeat units in $PBLG_7$ to only 2 repeat units for $PBLG_{100}$, reflecting increasing topological constraints in the α-helical polypeptides with a decreasing "mesh" size. As an additional approach, the characteristic length of these constraints (i.e., the "mesh" size), d, can also be estimated using $G_N^0 = \frac{k_B T_{ref}}{d^3(\omega_c \tau)^2}$, where k_B is the Boltzmann constant, T_{ref} is the superposition reference temperature, and $\omega_c \tau = 1$. The results are shown in Figure 4.26b. The

consistency between the two approaches (Figure 4.26) reinforces the idea that increased chain length promotes tighter coupling between the helical segments, leading to a more rigid "network". This reflects the critical role of hierarchical ordering – from individual α-helices to their collective packing – in the viscoelastic properties of the system.

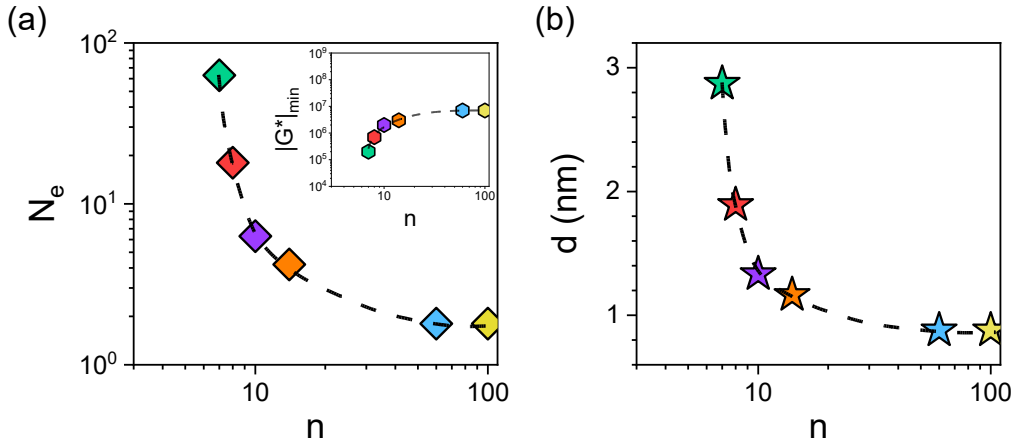

Figure 4.26. Dependence of the characteristic length (a) N_e and (b) d between the structural constraints (see text), as a function of molar mass. Different colors indicate the different peptides: $PBLG_7$ (green), $PBLG_8$ (red), $PBLG_{10}$ (purple), $PBLG_{14}$ (orange), $PBLG_{60}$ (blue) and $PBLG_{100}$ (yellow). The inset shows the absolute value of the complex shear modulus at the first minimum as a function of n. The dashed lines are guides for the eye.

In the case of the n-hexyl terminated samples (Figure 4.25b), the first minima in the vGP plot corresponds to high $|G^*|$ values. This high modulus elastic plateau is associated with the compact, network-like structures of the β-sheets. We can also observe that, well-ordered α-helices (in $PBLG_{60}$ and $PBLG_{100}$) and β-sheets (in $PBLG_{7(n\text{-hexyl})}$ and $PBLG_{14(n\text{-hexyl})}$) exhibit similar plateau values (~ 10^7 Pa), reflecting increasing topological constraints through percolation/aggregation.

At high $|G^*|$ (~ 10^9 Pa), a second minimum is evident, suggesting proximity to the liquid-to-glass "transition" regime. To verify its origin and possibly associate this feature with the two segmental processes (α and α^*), we extracted the relaxation times from G'' at low temperatures and compared it with DS (Figure 4.27). For low and intermediate degrees of polymerization, the second, well-resolved $\delta_{\min}$ reflects the freezing of the segments participating in the α^* process identified in DS. In polypeptides, the relaxation times extracted align with the weak intermediate process (indicated as I in Figure 4.27). Moreover, there is evidence for a second process at even higher frequencies associated with the α-process in the α-helical PBLGs.

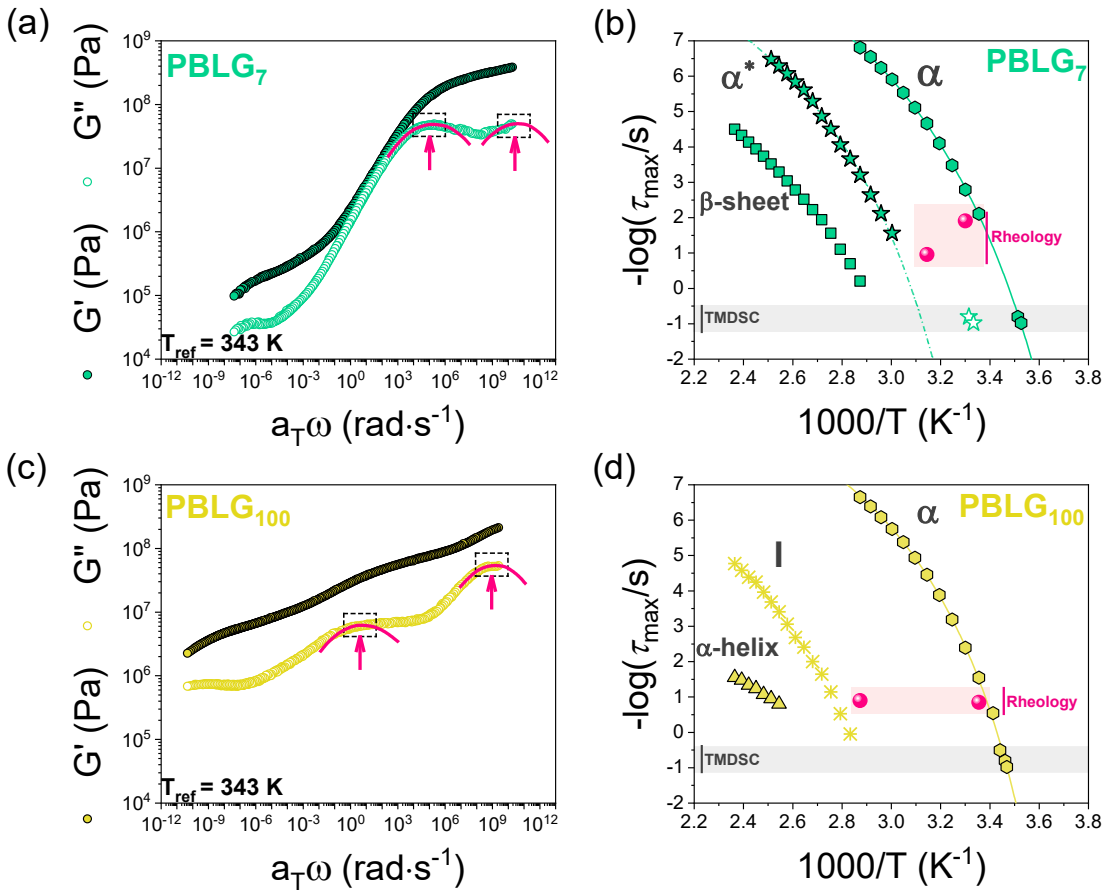

Figure 4.27. Master curves of the storage (filled circles) and loss (open circles) moduli of (a) $PBLG_7$ (green) and (c) $PBLG_{100}$ (yellow). The insets show the frequency of the maximum of G'' at the respective temperatures. The characteristic times obtained as $\tau = 1/\omega$ are indicated in the Arrhenius plots of (b) $PBLG_7$ and (d) $PBLG_{100}$.

These results are further contextualized in Figure 4.28, which illustrates the hierarchical organization of PBLG homopolypeptides. The primary structure is defined by the polypeptide backbone and its molar mass distribution. The secondary structure consists of α-helices and β-sheets, as previously identified. Rheological measurements reveal the emergence of a tertiary level of organization – an interconnected "mesh" of ordered domains – whose formation is driven by percolation or aggregation of these secondary motifs. This supramolecular structure imposes topological constraints on the material and governs its viscoelastic response.

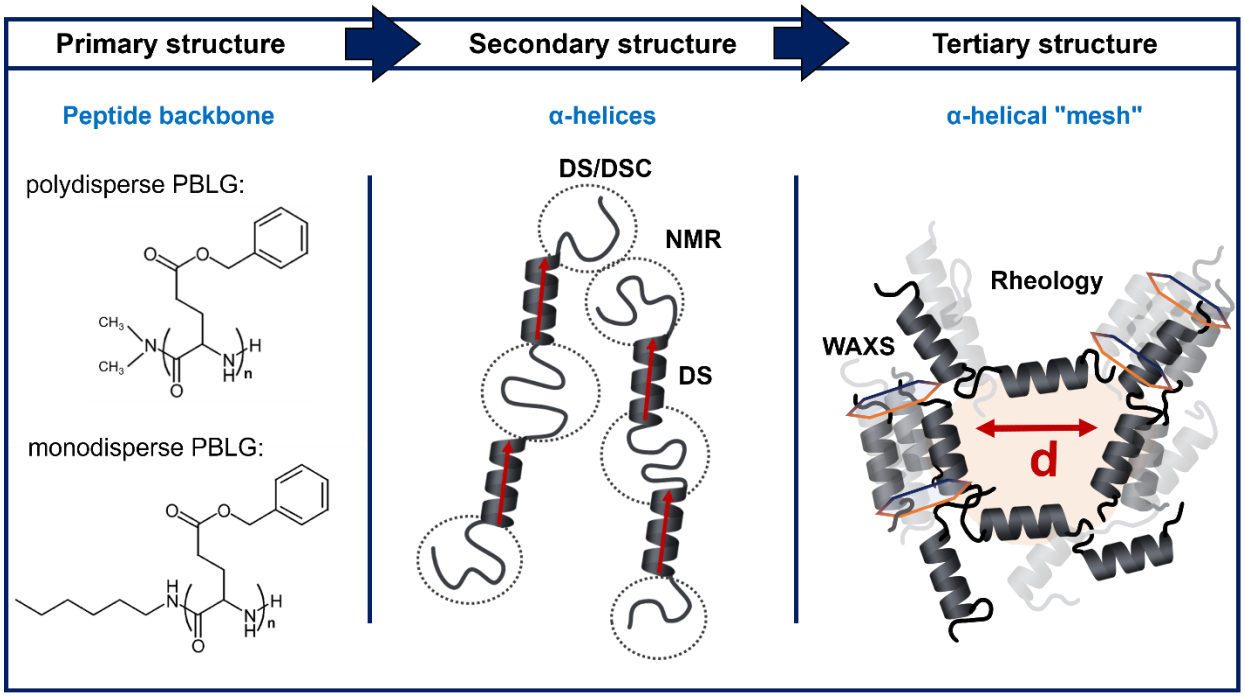

Figure 4.28. Hierarchical organization of α-helical PBLG homopolypeptides. Progressing from primary to higher-order structures: (i) the primary structure, i.e., the PBLG backbone, (ii) the secondary structure, α-helices, and (iii) the tertiary structure, i.e., the "mesh" of ordered domains with a size *d*.

In conclusion, polypeptides show in general an elastic response ($G' > G''$). The different secondary structures have a clear viscoelastic signature at the segmental level and a similar fingerprint at the domain level, with a decreasing "mesh" size by increasing molar mass. In addition, the high moduli of the oligopeptides with β-sheet motifs makes them ideal candidates as load-bearing scaffolds or implantable supports. On the other hand, α-helical polypeptides with low molar masses are suitable for applications involving compliant tissues such as epithelium, basement membranes, soft connective tissue, or even retinal substrates.[19,20]

4.3 Conclusion

A series of poly(*γ*-benzyl-L-glutamate) (PBLG) peptides was synthesized, with a broad range of molar masses: from oligopeptides with high β-sheet content, to polypeptides exclusively forming α-helical structures, including all intermediate structural regimes. By combining static (SAXS and ^{13}C solid-state NMR) with dynamic probes (^{13}C solid-state NMR, DS as a function of temperature and pressure, and Rheology), we achieved some understanding of the distinct dynamics of β-sheets and α-helices.

Thermodynamic results revealed two distinct glass temperatures (T_gs) in polypeptides that form both secondary structures. The lower T_g was assigned to the amorphous α-helical segments, while the higher T_g to the amorphous β-sheet segments. This is the first reported β-sheet-associated T_g in non-hydrated polypeptides. The self-assembly of PBLG was investigated as a function of the degree of polymerization and the absolute fractions of the α-helices and β-sheets were calculated. A connection was revealed between the increasing (decreasing) fraction of α-helices (β-sheets) and the lateral coherence of the respective domains, with the latter being consistently smaller for β-sheets. Chain end-group chemistry was also found to affect the stabilization of the secondary structure. N-hexyl terminated samples exhibited higher β-sheet fractions, whereas dimethylamino terminated samples displayed a consistently higher α-helical fraction across all chain lengths.

The analysis of the dynamics revealed two segmental processes: the α process for α-helices and the α^* process for β-sheets, each associated with the respective T_gs. A slower segmental dynamics of the β-sheets was observed, indicating significantly more restricted dynamics. The relaxation of the α-helical and β-sheet macrodipoles was also evident at even longer timescales. Moreover, β-sheets exhibit consistently lower fragility values that α-helices. This stronger glass behavior was explained by the constraints imposed by their inherent network-like structure stabilized by intermolecular hydrogen bonds. Conversely, α-helices, stabilized by intramolecular h.b., allow for more mobility in nearby amorphous segments, leading to a more thermally sensitive dynamics.

Pressure was found to induce structural defects that are incorporated in both segmental processes. The two processes were found to have different sensitivity to pressure, with pressure coefficients of T_g as 200 K·GPa^{-1} and 160 K·GPa^{-1} for the α and α^* processes, respectively. These

results were discussed in terms of the type of the secondary structure. The network-like structure of β-sheets imposes stronger constraints on the amorphous segments, thereby limiting the pressure response of the α^* process.

Lastly, an elastic response ($G' > G''$) was evident across all samples. Analysis of the van Gurp-Palmen (vGP) plots revealed clear correlations between the elastic modulus and the dominant secondary structure. Two minima in δ where identified: one at the plateau modulus G_N^0 reflecting the elastic properties of the entanglement "network" (typically $G_N^0 \sim 10^5$ Pa) and another in the vicinity of the T_g ($|G^*| \sim 10^9$ Pa). In dimethylamino terminated samples, where α-helices are the dominant secondary structure, the increase in the first minimum – and the corresponding decrease of its characteristic length – with molar mass suggested a tighter coupling between the helical segments, leading to a more rigid "mesh". In n-hexyl temrinated samples, where β-sheets dominate, this high elastic modulus was associated with the compact, network-like structures of β-sheets. These results provided evidence of a tertiary level of structural organization governed by percolation and aggregation of secondary motifs.

Overall, our results demonstrate that both end-groups and chain length can be used to selectively stabilize α-helices and/or β-sheets, enabling deliberate control over the structural, dynamical, and viscoelastic properties of the polypeptide. These findings possibly provide a framework for designing polypeptides tailored to specific biomedical applications; from rigid, load-bearing scaffolds, implantable supports, and drug delivery matrices (harnessing β-sheet rigidity) to soft tissue engineering platforms, such as cell-support matrices and biointerfaces (exploiting the tunability of α-helical networks).

4.4 References

1. Branden, C.; Tooze, J. *Introduction to protein structure*, Garland, New York (**1991**).
2. Kendrew, J.C.; Bodo, G.; Dintzis, H.; Parrish, R.G., Wyckoff, H.; Phillips, D.C. A Three-Dimensional Model of the Myoglobin Molecule Obtained by X-Ray Analysis. *Nature* **1958**, *181*, 662-666.
3. Rasmussen, S. G.; DeVree, B. T.; Zou, Y.; Kruse, A. C.; Chung, K. Y.; Kobilka, T. S.; Thian, F. S.; Chae, P. S.; Pardon, E.; Calinski, D.; Mathiesen, J. M.; Shah, S. T. A.; Lyons, J. A.; Caffrey, M.; Gellman, S. H.; Steyaert, J.; Skiniotis, G.; Weis, W. I.; Sunahara, R. K.; Kobilka, B. K. Crystal structure of the β_2 adrenergic receptor-Gs protein complex. *Nature* **2011**, *477*, 549-555.
4. Bork, P.; Holm, L.; Sander, C. The immunoglobulin fold: structural classification, sequence patterns and common core. *J. Mol. Biol.* **1994**, *242*, 309-320.
5. Schulz, G. E. The structure of bacterial outer membrane proteins. *Biochim. Biophys. Acta Biomembr.* **2002**, *1565*, 308-317.
6. Rao, S. T.; Rossmann, M. G. Comparison of super-secondary structures in proteins. *J. Mol. Biol.* **1973**, *76*, 241-256.
7. Perona, J. J.; Craik, C. S. Structural basis of substrate specificity in the serine proteases. *Protein Science* **1995**, *4*, 337-360.
8. Doster, W.; Cusack, S.; Petry, W. Dynamical transition of myoglobin revealed by inelastic neutron scattering. *Nature* **1989**, *337*, 754-756.
9. Schmidt, M.; Achterhold, K.; Prusakov, V.; Parak, F. G. Protein dynamics of a β-sheet protein. *Eur. Biophys. J.* **2009**, *38*, 687-700.
10. Papadopoulos, P.; Floudas, G.; Schnell, I.; Klok, H.-A.; Aliferis, T.; Iatrou. H.; Hadjichristidis, N. "Glass transition" in peptides: Temperature and pressure effects. *J. Chem. Phys.* **2005**, 122, 224906.
11. Floudas, G.; Spiess, H. W. Self-Assembly and Dynamics of Polypeptides. *Macromol. Rapid Commun.* **2009**, 30, 278–298.
12. Papadopoulos, P.; Floudas, G.; Klok, H.-A.; Schnell, I.; Pakula, T. Self-Assembly and Dynamics of Poly(*γ*-benzyl-L-glutamate) Peptides. *Biomacromolecules* **2004**, 5, 81.
13. Magoshi, J.; Nakamura, S. Studies on physical properties and structure of silk. Glass transition and crystallization of silk fibroin. *J. Appl. Polym. Sci.* **1975**, *19*, 1013-1015.
14. Agarwal, N.; Hoagland, D.A.; Farris, R.J. Effect of moisture absorption on the thermal properties of Bombyx mori silk fibroin films. *J. Appl. Polym. Sci.* **1997**, *63*, .401-410.
15. Hu, X.; Kaplan, D.; Cebe, P. Determining beta-sheet crystallinity in fibrous proteins by thermal analysis and infrared spectroscopy. *Macromolecules* **2006**, *39*, 6161-6170.
16. Hu, X.; Kaplan, D.; Cebe, P. Dynamic protein-water relationships during β-sheet formation. *Macromolecules* **2008**, *41*, 3939-3948.
17. Yu, L.; Hu, X.; Kaplan, D.; Cebe, P. Dielectric relaxation spectroscopy of hydrated and dehydrated silk fibroin cast from aqueous solution. *Biomacromolecules* **2010**, *11*, 2766-2775.

18. Mieda, S.; Aida, M. Macrodipole Moment of Polypeptides in *β*-Sheet and Its Prediction from Dipole Moments of Amino Acid Residues as Building Blocks: Alanine and Glycine in *β*-Strand. *Chemistry Letters* **2013**, *42*, 473-475.
19. Ratner, B.D.; Hoffman, A.S.; Schoen, F.J.; Lemons, J.E. "*Biomaterials science: an introduction to materials in medicine*", Elsevier, US, **2004**.
20. Thomasy, S.M.; Raghunathan, V.K.; Winkler, M.; Reilly, C.M.; Sadeli, A.R.; Russell, P.; Jester, J.V.; Murphy, C.J. Elastic modulus and collagen organization of the rabbit cornea: epithelium to endothelium. *Acta Biomater.* **2014**, *10*, 785-791.
21. van Beek, J.D.; Beaulieu, L.; Schafer, H.; Demura, M.; Asakura, T.; Meier, B.H. Solid-state NMR Determination of the Secondary Structure of Samia Cynthia Ricini Silk. *Nature* **2000**, *405*, 1077.
22. Tycko, R. Biomolecular Solid-State NMR: Advances in Structural Methodology and Applications to Peptide and Protein Fibrils. *Ann. Rev. Phys. Chem.* **2001**, *52*, 575.
23. Shoji, A.; Ozaki, T.; Saito, H.; Tabeta, R.; Ando, I. Conformational Characterization of Solid Polypeptides by ^{13}C NMR Recorded by the Cross Polarization-Magic Angle Spinning Method: Conformation-Dependent ^{13}C Chemical Shifts of Oligo-and Poly(γ-benzyl L-glutamates) and Sequential Copolymers of γ-Benzyl and γ-Methyl L-Glutamates and Qualitative Evaluation of Side-Chain Orientation *Macromolecules*, **1984**, *17*, 1472.
24. Gitsas, A.; Floudas, G.; Mondeshki, M.; Spiess, H.W.; Iatrou, H.; Hadjichristidis, N. Control of Peptide Secondary Structure and Dynamics in Poly(*γ*-benzyl-L-glutamate)-*b*-polyalanine Peptides. *Biomacromolecules* **2008**, 41, 8072-8080.
25. Saalwächter, K.; Schnell, I. *Solid State Nucl. Magn. Reson*. **2002**, 22, 154–187.
26. Saalwächter, K.; Spiess, H. W. *J. Chem. Phys.* **2001**, 114, 5707–5728.
27. Ngai, K. L.; Roland, C. M. Chemical Structure and Intermolecular Cooperativity: Dielectric Relaxation Results. *Macromolecules* **1993**, *26*, 6824–6830.
28. Dudowicz, J.; Freed, K.F.; Douglas, J.F. Fragility of Glass-Forming Polymer Liquids. *J. Phys. Chem. B* **2005**, *109*, 21350−21356.
29. Paluch, M.; Patkowski, A.; Fischer, E. W. Temperature and Pressure Scaling of the α Relaxation Process in Fragile Glass Formers: A Dynamic Light Scattering Study. *Phys. Rev. Lett.* **2000**, *85*, 2140.
30. Kremer, F. and Schönhals, A. in *Broadband Dielectric Spectroscopy*, Springer, Berlin, (**2002**).
31. Mpoukouvalas, K.; Floudas, G.; Williams, G. Origin of the α, β, (βα), and ″Slow″ Dielectric Processes in Poly(ethyl methacrylate). *Macromolecules* **2009**, *42*, 4690−4700.
32. Andersson, S. P.; Andersson, O. Relaxation Studies of Poly(propylene glycol) under High Pressure. *Macromolecules* **1998**, *31*, 2999−3006.
33. Floudas, G.; Paluch, M.; Grzybowski, A.; Ngai, K. Molecular Dynamics of Glass-Forming Systems − Effects of Pressure; Springer Verlag: Berlin, **2010**.
34. L. J. Fetters, D. J. Lohse, W. W. Graessley, J. Chain Dimensions and Entanglement Spacings in Dense Macromolecular Systems. *Polym. Sci. Part B: Polym. Phys.* **1999**, *37*, 1023-1033.

Chapter 5. Multiple Levels of Organization in Amphiphilic Diblock Copolymers Based on Poly(γ-benzyl-L-glutamate) Produced by Aqueous ROPISA

5.1 Introduction

In the effort to design new functional materials with precisely controlled – at the synthesis level – internal dimensions and structures ranging from nanometer to macroscopic scales, synthetic polypeptides play an important role. The latter combine the complexity of biological macromolecules found in nature with the simpler synthetic polymers.[1-9] In this respect, amphiphilic block copolymers based on the well-known synthetic polypeptide poly(γ-benzyl-L-glutamate) (PBLG)[10-14] and the water soluble poly(ethylene glycol) (PEG)[15] have been synthesized and investigated with respect to the self-assembly.[6,16-19] The presence of antagonistic tandem interactions between the two blocks (from one side the tendency of PEG to crystallize by chain folding, and from the other side, the propensity of PBLG to form α-helical/β-sheet peptide secondary structures, on top nanophase separation) gave rise to different levels of organization and structures of key in the design of new functional materials.

A recent method for producing amphiphilic block copolymers and nano-objects is polymerization-induced self-assembly (PISA).[20,21] The method affords the *in situ* one-step growth of a living amphiphilic polymer chain during its self-assembly into nanostructures. A variation of the method recently explored is based on the ring-opening polymerization-induced self-assembly (ROPISA) in aqueous buffer.[22,23,24] It was employed with PEG-NH_2 macroinitiator and either benzyl-L-glutamate or L-leucine NCA monomers to synthesize well-defined amphiphilic block copolymers of PEG-*b*-PBLG and PEG-*b*-PLeu in a rapid way. The latter were found to stabilize anisotropic rod-like nanostructures. It was thought that responsible for the different nanostructures were the peptide secondary structures (α-helical/β-sheet for PBLG and PLeu, respectively).

Herein we employ the same diblock copolymers (PEG-*b*-PBLG and PEG-*b*-PLeu) and explore the self-assembly and polypeptide dynamics over different length and timescales, as a function of molar mass and for different annealing and solvent treatment protocols. By employing a combination of static (^{13}C NMR, X-ray scattering, polarizing optical microscopy), thermodynamic (differential scanning calorimetry), and dynamic (dielectric spectroscopy) probes, we demonstrate a record of six levels of organization only found before in natural materials like

tendon.[25] They include (a) secondary structures of the polypeptides (α-helical/β-sheet), (b) the unit cell of PEG crystals, (c) the domain spacing of semicrystalline PEG, (d) the nanophase separation of unlike blocks, (e) an intermediate length-scale of rod-like objects (~ 100 nm in size), and (f) distorted slowly growing anisotropic crystalline superstructures (~ 100 μm). These structural motifs of the block copolymers prepared by the ROPISA method exceed both the structural integrity and the levels of organization found earlier in the same block copolymers[6,19] but synthesized by different methods. We discuss herein the role of reduced interfacial mixing in polypeptide-based nanomaterials produced by ROPISA. Furthermore, we discuss the effect of solvent treatment (slow solvent evaporation vs freeze-drying vs organic solvent precipitation) on the degree of nanophase separation and peptide secondary structure.

The synthesis was accomplished by Prof. S. Lecommandoux and his group, Dr. C. Bonduelle and H. Beauseroy, at the University of Bordeaux. The molecular characteristics of the samples are shown in Table 5.1. A part of the sample was then used as such for analysis (indicated below as FD), while another part was solubilized in DMF, precipitated in diethyl ether, and dried under vacuum overnight (indicated below as OSP).

Table 5.1. Molecular characteristics of the investigated copolymers.

Samples	$Đ$	N^{PEG}	$N^{peptide}$	f_{PEG}[a]	w_{PEG}
PEG_{114}-*b*-$PLeu_{32}$ (FD)[b]	1.05	114	32	0.60	0.63
PEG_{114}-*b*-$PLeu_{32}$ (OSP)[c]	1.05	114	32	0.60	0.63
PEG_{114}-*b*-$PBLG_{19}$ (FD)	1.06	114	19	0.52	0.49
PEG_{114}-*b*-$PBLG_{19}$ (OSP)	1.06	114	19	0.52	0.49
PEG_{228}-*b*-$PBLG_{19}$ (FD)	1.05	228	19	0.66	0.63
PEG_{228}-*b*-$PBLG_{19}$ (OSP)	1.05	228	19	0.66	0.63

[a] ρ_{PEG}[26] $= 1.064\ g \cdot cm^{-3}$, ρ_{PBLG}[27] $= 1.278\ g \cdot cm^{-3}$, ρ_{PLeu}[28] $= 1\ g \cdot cm^{-3}$

[b] FD = freeze drying

[c] OSP = organic solvent precipitation

5.2 Results and Discussion

The aim of the study is twofold: first to compare the diblock copolymer morphology prepared by ROPISA with earlier studies[6,19] on PEO-*b*-PBLG diblock copolymers and PBLG-*b*-PEO-*b*-PBLG triblock copolymers. To this end, we will show that the level of organization produced by ROPISA is superior to earlier morphology investigations of copolymers based on PEG and PBLG prepared by other methods. Second, within the ROPISA method we explore the effects of solvent treatment and the effect of molar mass (Table 5.1). The question here is how solvent treatment (slow water evaporation vs freeze-drying vs organic solvent annealing), as well as temperature, affects the degree of nanophase separation and peptide secondary structure. In the first protocol, the aqueous ROPISA polymerization was followed by a freeze-drying process (FD), while in the second protocol, a precipitation in organic solvent (OSP) was carried out right after freeze-drying. In general, slow water removal vs freeze-drying produce the same level of nanophase segregation and the same peptide secondary structure. However, OSP produced better equilibrated copolymers taking into account that this solvent may reduce the influence of the secondary structure coming from the aqueous process.[23] The results are presented in five sections below addressing the: thermodynamic properties, nanophase segregation, secondary structure, superstructure formation and molecular dynamics, each revealing the underlying complexity and multifaceted nature of the PEG-*b*-polypeptide copolymers prepared via the ROPISA mechanism. A schematic representation of the lamellar nanodomain morphology found in PEG-*b*-PBLG copolymers (by following either FD or OSP processes) is depicted in Scheme 5.1. Within each block there are multiple levels of organization. In the PEG block, the monoclinic unit cell of PEG, the well-defined crystalline lamellar, and, at much higher length scales, the PEG overarching axialitic superstructures can be identified, while the polypeptide domain embeds the two secondary structures, α- helices and β-sheets, with the former further packed in a hexagonal lattice.

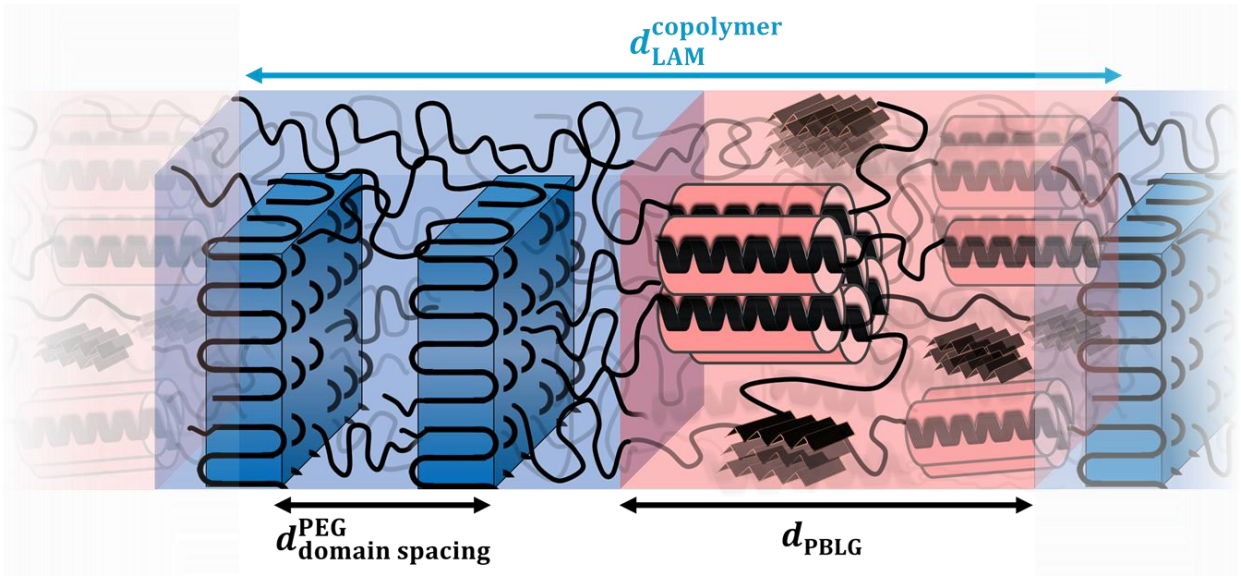

Scheme 5.1. Schematic representation of the nanodomain morphology of PEG-*b*-PBLG copolymer prepared via the ROPISA mechanism (by following either FD or OSP processes). The blue color corresponds to the PEG block, while the red color indicates the PBLG block.

5.2.1 Thermodynamic Properties

With DSC we address the degree of crystallinity, the melting temperatures, the possible liquid-to-glass temperatures and the order-to-disorder transition temperature of the copolymers prepared by FD and OSP protocols. The DSC heating traces are presented in Figure 5.1, where an endothermic peak appears revealing the melting of PEG crystals. In all copolymers, the melting of the PEG block appears weakly dependent on the peptide block, as it is observed at slightly lower temperatures to that in the respective homopolymer ($T_{\mathrm{m}}^{\mathrm{PEG}_{114}} = 333$ K). However, the results differ for the crystallization temperature. Especially in PEG_{114}-*b*-PBLG_{19} copolymer, the PEG compound crystallizes at 278 K (cooling traces shown in Figure 5.2), with a high degree of undercooling ($\Delta T \sim 30$ K), in contrast to bulk PEG ($T_{\mathrm{c}}^{\mathrm{PEG}_{114}} = 311$ K). The degree of crystallinity in the copolymers can be calculated from the heat of fusion, as $X_c = \frac{1}{w_{PEG}} \frac{\Delta H}{\Delta H_\infty}$, where $\Delta H_\infty = 196\ \mathrm{J \cdot g^{-1}}$.[29] The results are summarized in Table 5.2, along with the results of WAXS and NMR (to be discussed below).

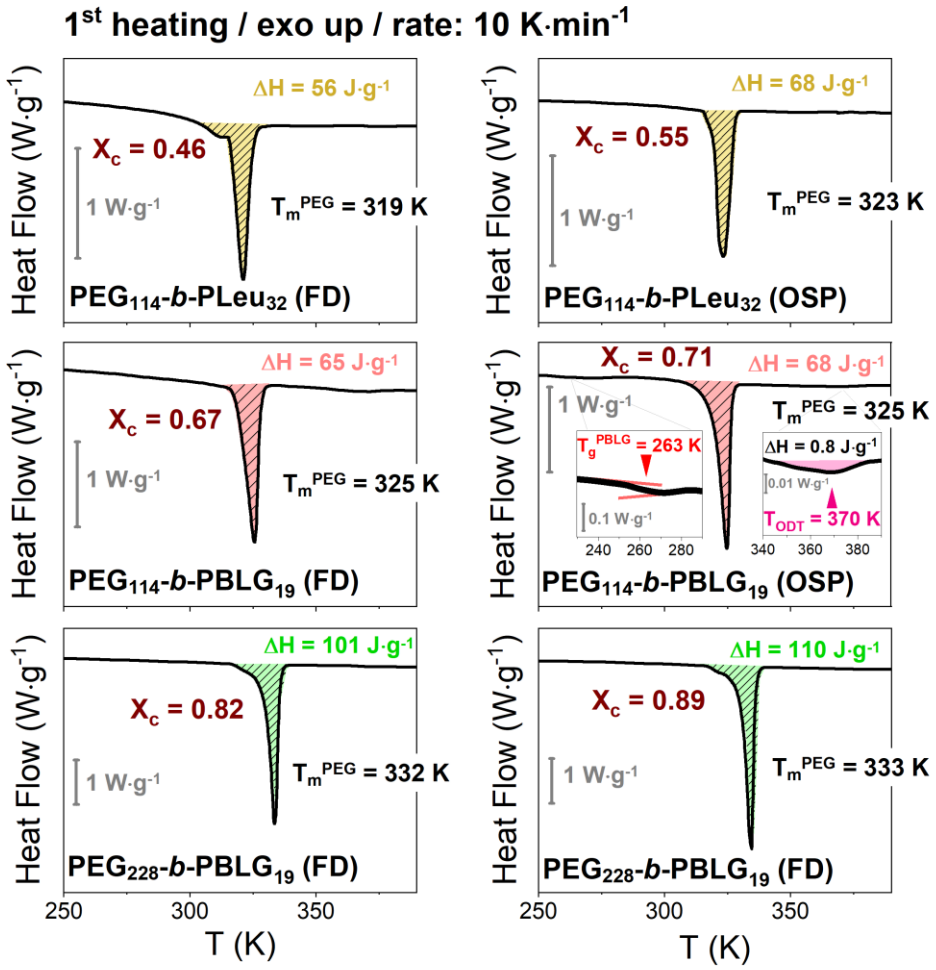

Figure 5.1. DSC traces of the copolymers, obtained during the first heating at a rate 10 K·min^{-1}. The shadowed areas represent the heat of fusion for the semicrystalline PEG. Melting temperatures T_m^{PEG} and degrees of crystallinity (X_c) are indicated. For PEG$_{114}$-*b*-PBLG$_{19}$ (OSP) the insets give the glass temperature of the PBLG block (left) and the order-to-disorder transition (with the heat of fusion) of the copolymer (right).

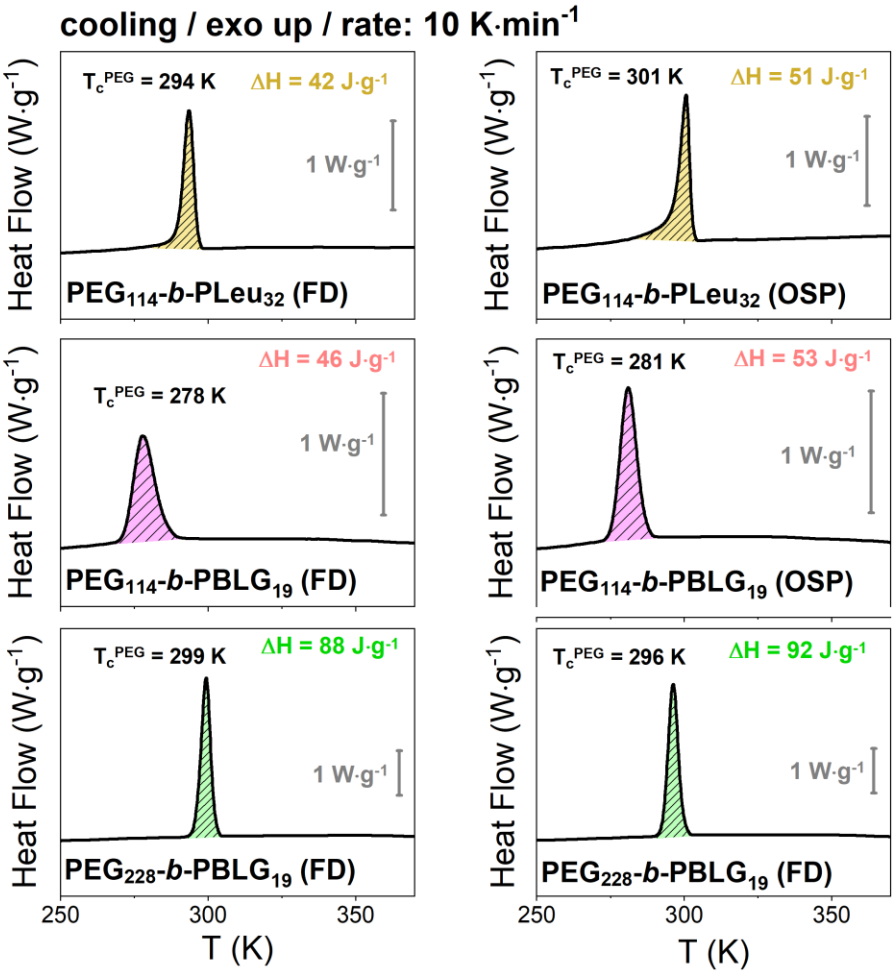

Figure 5.2. DSC traces of the copolymers, obtained during the cooling at a rate 10 K·min^{-1}. The shadowed areas represent the heat of fusion for the semicrystalline PEG for each sample. Crystallization temperatures are also indicated.

A closer look in the DSC trace of PEG$_{114}$-*b*-PBLG$_{19}$ (Figure 5.1 insets) can provide information about additional thermodynamic transitions. At temperature corresponding below the melting of PEG, the glass temperature of the PBLG block is evident (at 263 K), while at temperatures above PEG melting, a first-order transition is evident corresponding to the order-to-disorder transition at T_{ODT} = 370 ± 1 K (value is in agreement with the SAXS results below). An estimation of the $(\chi N)_{ODT}$ parameter can be obtained from[30-32] $\Delta H = RT_{ODT} f(1-f)(\chi N)_{ODT}/M_n$, where, ΔH (= 0.8 ± 0.2 J·g^{-1}) is the heat of fusion of the ODT transition, R is the gas constant, f (= 0.52) is the volume fraction of PEG, N (= 133) is the total degree of polymerization, and M_{n} (= 9160 g·mol^{-1}) is the total molar mass. This estimate provides $(\chi N)_{ODT} = 10 \pm 1$ at the transition, which is in

agreement (within the experimental error) with the MFT predictions for diblock copolymers.[33] Overall, the investigation of the thermodynamics revealed an influence of solvent treatment on the PEG degree of crystallinity. Samples prepared by the freeze-drying method display consistently lower degree of crystallinity. In addition, one of the copolymers prepared by OSP did show an ODT at higher temperatures.

5.2.2 Nanophase Separation

Precise information about the nanodomain morphology can be obtained by small-angle X-ray scattering. Some representative SAXS curves of PEG_{114}-*b*-$PBLG_{19}$ (OSP) are provided in Figure 5.3a (as all PEG-*b*-PBLG copolymers show similar SAXS results). Below the melting temperature of PEG, two Bragg reflections can be identified. The first intense peak, at q_1 = 0.54 nm^{-1} (with periodicity $d_1 = 2\pi/q$ = 11.6 nm), reveals the formation of a lamellar (LAM) structure, indicating nanophase separated PEG/PBLG domains. The second sharper peak, at q_2 = 1.1 nm^{-1} (d_2 = 5.7 nm), reflects the domain spacing of semicrystalline PEG (Figure 5.3b). At temperatures above PEG melting, the copolymer exhibits a single broad peak, at q_3 ~ 0.6 nm^{-1} (with a periodicity of ~ 10.5 nm), indicative of correlation hole scattering.[34] At T ~ 378 ± 5 K, there is a discontinuous change of the peak intensity, in line with the T_{ODT} obtained by DSC. The SAXS patterns exhibit some additional features at intermediate and higher q with a distinct minimum at $q \sim 2\ nm^{-1}$. They reflect the form factor of PBLG cylinders. In this case, the total scattered intensity is given by the product[35,36]

$$I(q) \sim K \cdot P(q) \cdot S(q) \tag{5.1}$$

where, $P(q)$, is the form factor and, $S(q)$, is the structure factor. The structure factor of the low-q interference peak associated with the inter-sphere correlations can be described by the Percus – Yevick approximation for cylindrically shaped objects, assuming that the interaction between two "particles" does not depend on particle size or orientation (monodisperse approximation) and is given by a hard-sphere potential as:

$$S(q, R_{\mathrm{h}}, f_{\mathrm{h}}) = \frac{1}{1 + \frac{24 f_{\mathrm{h}} G(A)}{A}} \tag{5.2}$$

where $A = 2qR_{\mathrm{h}}$, R_{h} and f_{h} are the effective interaction hard-sphere radius and volume fraction parameters describing the interference effects between the PBLG cylinders (i.e., the "particles"), and

$$G(A) = \frac{\alpha}{A^2}(sinA - AcosA) + \frac{\beta}{A^3}(2AsinA + (2 - A^2)cosA - 2) + \frac{\gamma}{A^5}[-A^4cosA + 4(3A^2 - 6)cosA + (A^3 - 6A)sinA + 6] \tag{5.3}$$

Where,

$$\alpha = (1 + 2f_{\mathrm{h}})^2/(1 - f_{\mathrm{h}})^4$$
$$\beta = -6f_{\mathrm{h}}\,(1 + f_{\mathrm{h}}/2)^2/(1 - f_{\mathrm{h}})^4 \tag{5.4}$$
$$\gamma = {}^1\!/_2\, f_{\mathrm{h}}\,(1 + 2f_{\mathrm{h}})^2/(1 - f_{\mathrm{h}})^4$$

The form factor of monodisperse cylinders with a radius *R* and length *L* is defined as

$$P(q,R,L) = \int_0^1 \left(2\frac{J_1\left(qR\sqrt{1-x^2}\right)}{qR\sqrt{1-x^2}}\frac{\sin(qL\,x/2)}{qL\,x/2}\right)^2 dx \tag{5.5}$$

where J_1 is the first-order Bessel function. The simulation of the experimental scattering curve using the above theoretical model (Figure 5.3d) results in a set of four fitting parameters: $R = 2.15 \pm 0.02\ nm, L = 3.0 \pm 0.2\ nm, R_h = 0.87 \pm 0.05\ nm, f_h = 0.48$ (where R_h is the helix radius and *L* is the helix length). The value of the helix length, *L*, can be compared with the length of an ideal helix as $\xi_{\mathrm{helix}}^{\mathrm{ideal}} = 0.15\ \mathrm{nm} \cdot 19\ \mathrm{repeat\ units} = 2.85\ \mathrm{nm}$ (the length of an ideal helix is 0.15 nm per repeat unit).[13,14] This suggests that the persistence length of the helices in the polypeptide block increases in the presence of PEG, compared to that of the homopolymer ($\xi_{helix}^{PBLG_{19}} \sim 2\ nm$). The experimental value of *L* being even longer than that of an ideal α-helix can associate with the reported α-to-PPII helix conversion for PBLG prepared in THF/water solutions.[37] At temperatures $T > 378$ K, the broad peak continuously decreases in intensity, signaling the order-to-disorder (ODT) transition (Figure 5.3c), and the distinct minimum around

$q \sim 2\ nm^{-1}$ due to the form factor is lost (Figure 5.3c). This suggests that mixing of the different blocks at temperatures above the T_{ODT} eventually destabilizes the PBLG α-helices.

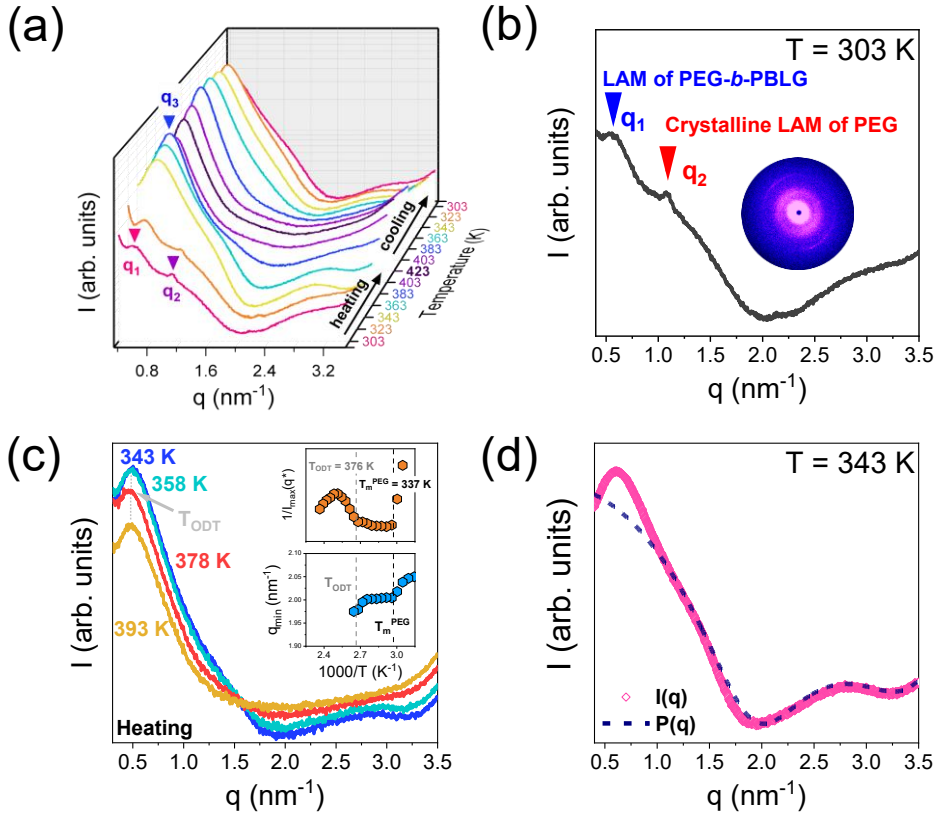

Figure 5.3. (a) SAXS patterns of PEG_{114}-*b*-$PBLG_{19}$ (OSP) block copolymer, during heating and subsequent cooling. The vertical arrows give the position of the Bragg reflections corresponding to the lamellar morphology of the copolymer (q_1), the crystalline lamellar of PEG (q_2) and the correlation hole scattering (q_3). (b) SAXS pattern of PEG_{114}-*b*-$PBLG_{19}$ recorded at 303 K. The corresponding 2D pattern from the extracted fiber is also shown. (c) SAXS patterns at 343 K, 358 K, 378 K and 393 K, indicating the characteristic order-to-disorder transition. The insets provide the inverse peak intensity, and the q_{min} (position of the first minima in the form factor) as a function of inverse temperature. The dashed lines indicate the melting and order-to-disorder transition temperatures. (d) SAXS pattern of PEG_{114}-*b*-$PBLG_{19}$ recorded at 343 K. The blue dashed-line represents the Percus-Yevick approximation for cylindrically shaped objects (eq 7).

The self-assembly in the second diblock system is very different. The SAXS data of PEG_{114}-*b*-$PLeu_{32}$ reveal mixing between the two blocks, even at lower temperatures. Within the disordered state, the structure factor can be described in the context of random phase approximation.[33] The resulting fits are presented in Figure 5.4a, with the theory effectively describing the experimental data. The extracted interaction parameter displays a weak *T*

dependence as $\chi = 0.07/T + 7 \cdot 10^{-6}$. An estimation of the order-to-disorder temperature can be provided from the representation in Figure 5.4b. Notice that the T_{ODT} (= 243 K) is significantly below the PEG block crystallization temperature (~ 300 K), indicating that PEG crystallization initiates from the disordered melt state.

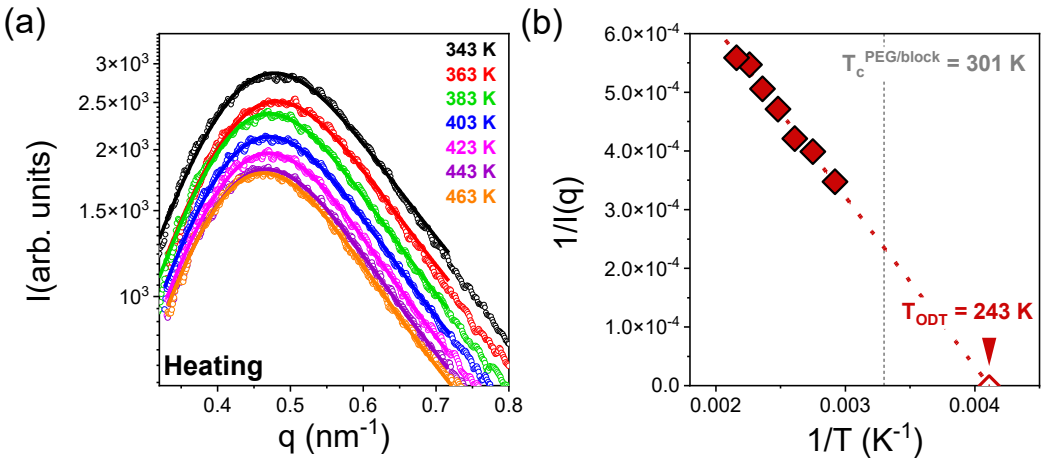

Figure 5.4. a) SAXS patterns of PEG_{114}-*b*-$PLeu_{32}$ (OSP) at different temperatures, ranging from 343 K to 463 K. A broad scattering maximum is evident, indicating scattering within the disordered state. The solid lines represent fits to the MFT. b) Inverse peak intensity plotted versus inverse temperature. Extrapolating provides an estimate of the hypothetical order-to-disorder transition temperature (243 K). The vertical line gives the crystallization temperature of PEG.

5.2.3 Secondary Structure

While scattering of X-rays at small angles (SAXS) can identify longer lengthscales, i.e., the nanodomain morphology of the copolymer and the crystalline lamellar of PEG, scattering at higher angles (WAXS) can provide the type and the organization of the peptide secondary structure, the PEG unit cell, and an independent measure of the PEG degree of crystallinity.

Figure 5.5 gives the WAXS patterns of two representative copolymers, PEG_{114}-*b*-$PBLG_{19}$ (FD) and PEG_{114}-*b*-$PLeu_{32}$ (FD), bearing different polypeptide blocks. Figure 5.6 presents the remaining investigated copolymers. Starting from intermediate to higher q, both curves display several Bragg reflections – (120), (032), (024), (131) main reflections – corresponding to the ordinary monoclinic unit cell of PEG (unit cell parameters a = 0.81 nm, b = 1.30 nm, c = 1.95 nm and β = 125.4 °),[38] while the amorphous halo reflect the semi-crystalline nature of the copolymers. The degree of crystallinity of all investigated copolymers can be calculated as $X_c^{XRD} = \frac{1}{f_{PEG}} \frac{I_c}{I_a + I_c}$,

where f_{PEG} is the volume fraction of PEG (Table 5.1), I_c is the intensity of all Bragg reflections associated with the monoclinic unit cell and I_a is the intensity of the amorphous halo (results from different methods are summarized in Table 5.2). The results show higher crystallinity in the OSP samples, as compared to the FD samples. This effect can be attributed to the synthesis protocol of the copolymers. In the FD copolymer following the ROPISA mechanism the chains grow and freeze in a less-optimum configuration as compared to the OSP copolymers. We will return to this point below with respect to the peptide secondary structure.

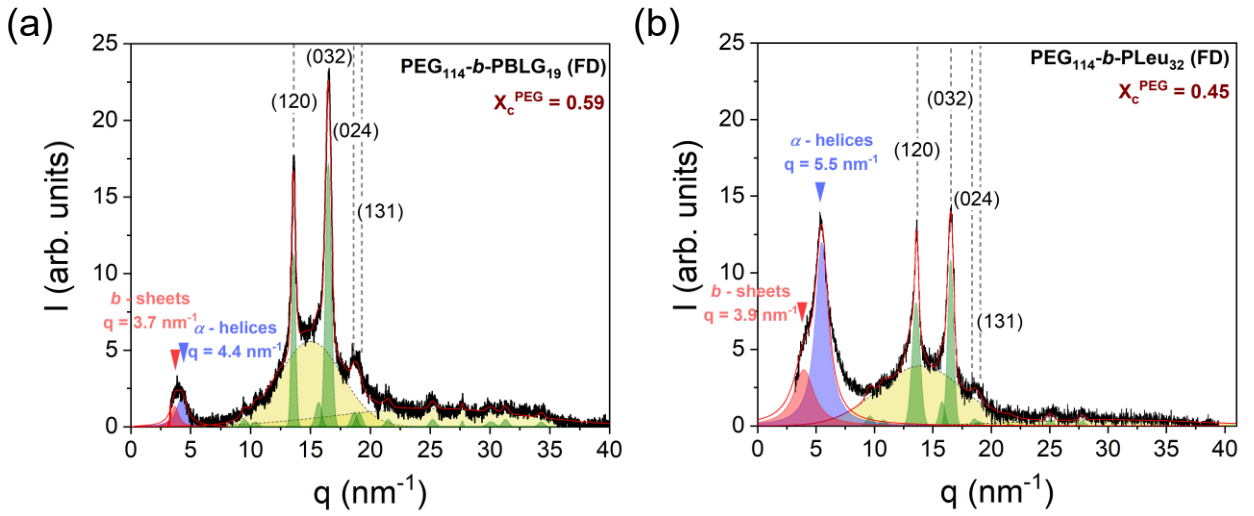

Figure 5.5. WAXS patterns of (a) PEG_{114}-*b*-$PBLG_{19}$ (FD) and (b) PEG_{114}-*b*-$PLeu_{32}$ (FD). At lower *q*, red arrows indicate the lamellar spacing of β-sheet secondary structure, while blue arrows give the position of the primary reflection from the weakly hexagonally packed cylinders composed from α-helical PBLG segments. At higher *q*, the short-dashed lines indicate the (*hkl*) indices of the Bragg reflections corresponding to the monoclinic unit cell of PEG, whereas the yellow areas give the contribution from the amorphous part.

Table 5.2. PEG degree of crystallinity as calculated from WAXS, ^{13}C NMR and DSC.

Samples	X_c^{WAXS}	X_c^{NMR}	X_c^{DSC}
PEG_{114}-*b*-$PLeu_{32}$ (FD)	0.45	0.27	0.46
PEG_{114}-*b*-$PLeu_{32}$ (OSP)	0.51	0.49	0.55
PEG_{114}-*b*-$PBLG_{19}$ (FD)	0.59	0.57	0.67
PEG_{114}-*b*-$PBLG_{19}$ (OSP)	0.67	0.66	0.71
PEG_{228}-*b*-$PBLG_{19}$ (FD)	0.68	0.69	0.82
PEG_{228}-*b*-$PBLG_{19}$ (OSP)	0.78	0.80	0.89

At lower q (q < 10 nm^{-1}), both copolymers reveal features associated with the peptide secondary structure. Literature data from well-oriented PBLG[13,14] reveal an α-helical secondary structure conformation with residues on a spiral pitch of 0.54 nm in a 18/5 helix (18 residues in 5 turns) with a repeat unit of c = 2.7 nm. The structure was ascribed to the paracrystalline form C; it consists of a periodic packing of α-helices in the direction lateral to the chain axis with a nematic-like paracrystalline order. The first strong equatorial reflection of PBLG at q = 4.4 nm^{-1} corresponds to the (10) reflection from a hexagonal unit cell of PBLG helices with a unit cell parameter of a = 1.65 nm. In the present copolymer PEG$_{114}$-*b*-PBLG$_{19}$ (Figure 5.5a), α-helices exist in the absence of long range order as revealed by the absence of higher order peaks. In addition, because of the low molar mass of PBLG, the presence of β-sheets at q ~ 3.7 nm^{-1} is also evident.[13] Respectively, for PEG$_{114}$-*b*-PLeu$_{32}$ (Figure 5.5b), the primary peak at q ~ 5.5 nm^{-1} for the PLeu peptide block indicates the presence of weakly hexagonally packed α-helices (intercylinder distance of ~ 1.32 nm), while β-sheets are shown from the weak Bragg peak at q ~ 3.9 nm^{-1}.[39]

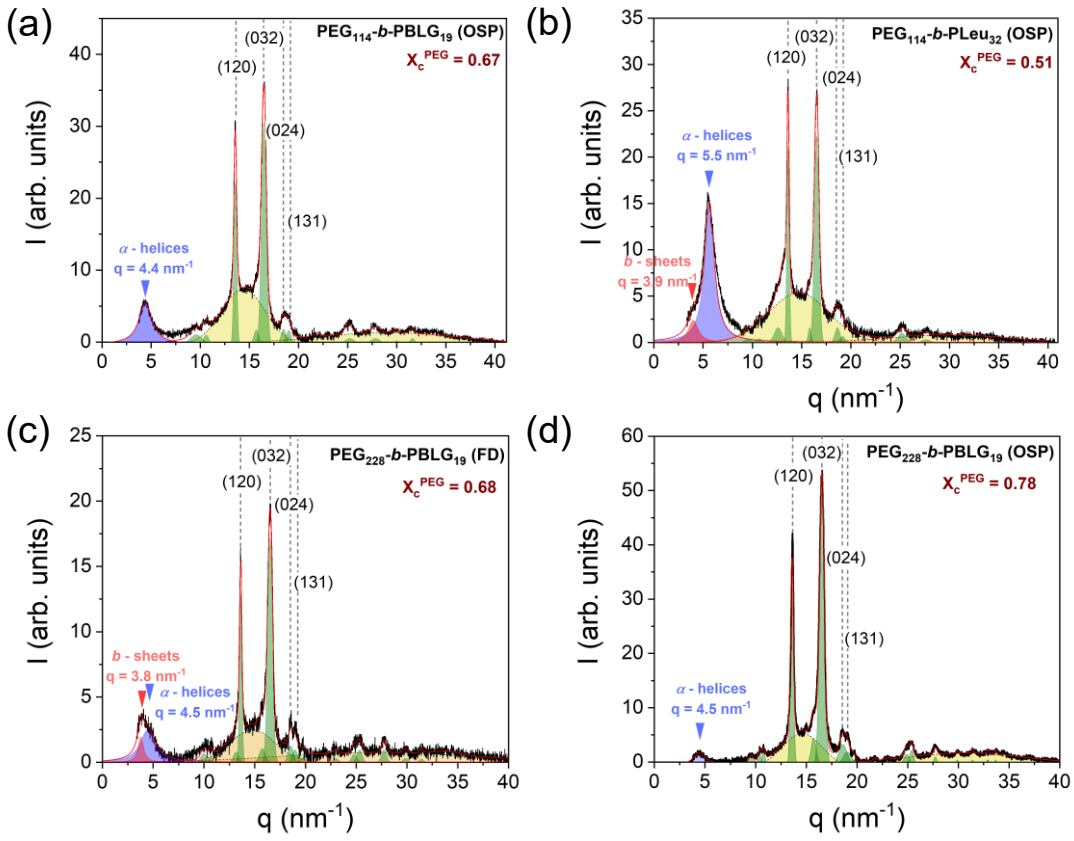

Figure 5.6. WAXS patterns of (a) PEG$_{114}$-*b*-PBLG$_{19}$ (OSP), (b) PEG$_{114}$-*b*-PLeu$_{32}$ (OSP), (c) PEG$_{228}$-*b*-PBLG$_{19}$ (FD) and (d) PEG$_{228}$-*b*-PBLG$_{19}$ (OSP).

As a next step, we investigate the effect of thermal annealing in Figure 5.7. Each secondary structure can be identified, as noted above, from its characteristic Bragg reflection, with the intensity of the peak corresponding to the relative β-sheet/α-helical fraction (in calculating fractions from WAXS assume only ordered secondary structures such α-helices and β-sheets) in the peptide block (as shown in Table 5.3). Both before and after annealing, α-helices are the dominant secondary structure in all copolymers.

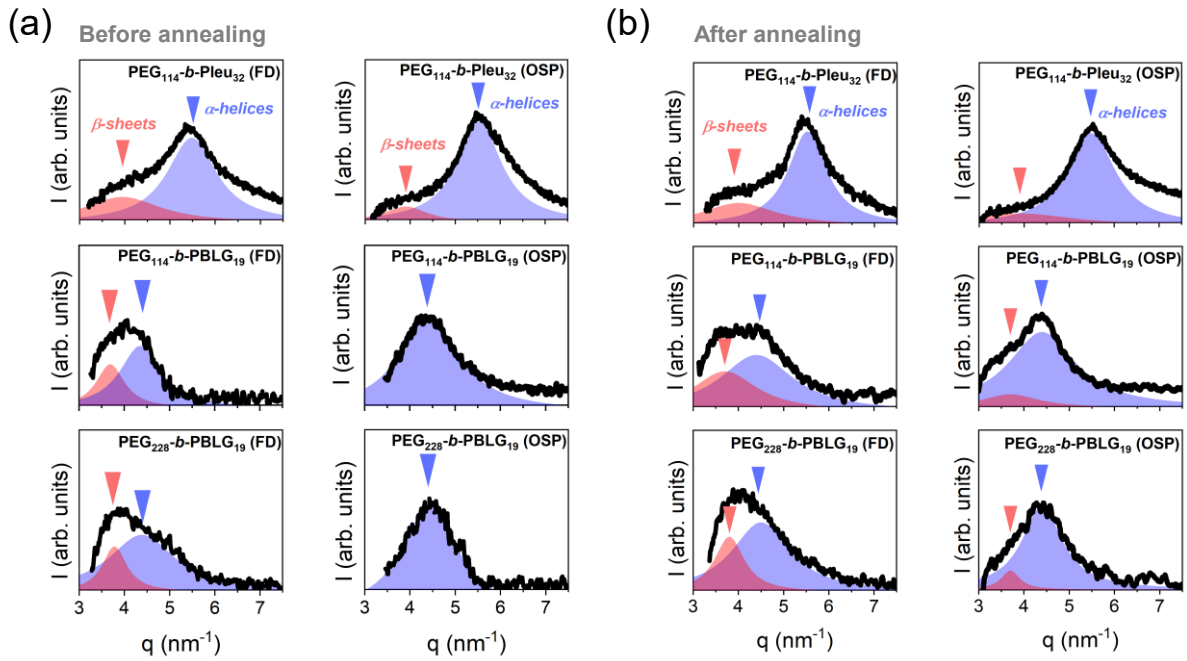

Figure 5.7. WAXS patterns of the copolymers (a) before and (b) after annealing for 1 day at 343 K. Red arrows identify the characteristic distance of β-sheets, while blue arrows indicate the position of the primary reflection associated with the α-helices.

Table 5.3. Relative fractions of α-helices and β-sheets in the peptide blocks of the investigated copolymers, as calculated from WAXS (before and after annealing) and absolute fractions of α-helices, β-sheets and random coil, as calculated from NMR (at 298 K and 343 K).

Samples	WAXS				NMR					
	β-sheets		α-helices		β-sheets		α-helices		random coil	
	b.a.*	a.a.*	b.a.*	a.a.*	298 K	343 K	298 K	343 K	298 K	343 K
PEG_{114}-*b*-$PLeu_{32}$ (FD)	0.33	0.34	0.67	0.66	0.35	0.38	0.45	0.41	0.20	0.21
PEG_{114}-*b*-$PLeu_{32}$ (OSP)	0.14	0.24	0.86	0.76	0.20	0.19	0.67	0.69	0.13	0.12
PEG_{114}-*b*-$PBLG_{19}$ (FD)	0.33	0.38	0.67	0.62	0.20	0.31	0.72	0.56	0.08	0.13
PEG_{114}-*b*-$PBLG_{19}$ (OSP)	0	0.13	1	0.87	0.02	0.13	0.93	0.73	0.05	0.14
PEG_{228}-*b*-$PBLG_{19}$ (FD)	0.22	0.31	0.78	0.69	0.19	0.32	0.81	0.57	-	0.11
PEG_{228}-*b*-$PBLG_{19}$ (OSP)	0	0.17	1	0.87	0.04	0.16	0.96	0.75	-	0.09

*b.a. = before annealing, a.a. = after annealing

One of the key probes for peptide secondary structure determination and PEG crystallinity determination is ^{13}C Solid State NMR.[40-42] The characteristic traces of the investigated copolymers are shown in Figure 5.8a at 298 K and in Figure 5.8b at 343 K. Starting from the PEG blocks, the intense resonances at $\delta \sim 73$ ppm and ~ 71 ppm are assigned to the crystalline and amorphous signals, respectively.[39] On the other hand, the resonances at $\delta \sim 176$ ppm (~ 172 ppm) and $\delta \sim 58$ ppm (~ 53 ppm), arising from the chemical shifts of the amide C=O and C_α carbon, respectively, reveal the formation of an α-helical (β-sheet) secondary structure in the peptide blocks. A distinct advantage of ^{13}C Solid State NMR is the additional identification of the random coil conformations, which can be detected from the resonances at $\delta \sim 53$ ppm of the C_α carbon. A quantitative analysis of the intensity of the resonances can determine the degree of crystallinity (Table 5.2) and the α-helical/β-sheet fractions (Table 5.3) in the copolymers. First, the α-helical content in the copolymers studied by slow water evaporation or freeze-drying is identical. Second, in all cases, the OSP samples exhibit higher relative α-helical fractions. For example, at 298 K, the α-helical fraction in the PEG_{114}-*b*-$PBLG_{19}$ copolymer is as high as 93%. This, at first sight, is surprising as DMF can solubilize both blocks and possibly weaken the propensity for PBLG α-helices. Nevertheless, the results (Table 5.3) clearly show an increasing α-helical content probably due to the slow precipitation process. The lower α-helical content in the copolymers prepared by aqueous ROPISA can reflect the α-to-PPII helix transition reported for PBLG prepared in

THF/water solutions.[37] PPII is an extended helical conformation for PBLG as a result of the weaker intramolecular hydrogen bonds in THF/water solutions high in water content. It was further suggested that this conformational change at the level of secondary structure could ignite a macroscopic change of the self-assembled morphologies from fibers to particles.[37]

In addition to the peptide secondary structure, ^{13}C NMR provides the PEG crystallinity. Overall, the degree of crystallinity calculated from NMR show excellent agreement with the WAXS results (Table 5.2). Potential discrepancies in the values, i.e., in the case of PEG_{114}-*b*-$PLeu_{32}$ (FD), arise from the restricted amorphous fractions in the PEG block and the size of its crystals. Concerning the secondary structure fractions, the comparison between the NMR results at 298 (343) K and the WAXS results before (after) annealing highlights the difference between the two probes. The ability to access the random coil fraction (*absolute fractions*) is now expressed as a "loss" in the α-helical content (Table 5.3). This underscores the complementary nature of NMR and WAXS results, in providing a comprehensive understanding (from the different chemical shifts) of the amorphous and crystalline PEG and the peptide secondary structure. The secondary structure investigation by a combination of WAXS and solid state NMR revealed a higher α-helical content in the copolymers following the slow precipitation in organic solvent as opposed to the freeze drying process, at the expense of the content of β-sheets and random coils. Furthermore, PEG-*b*-PLeu contains a high fraction of β-sheets when prepared via freeze drying.

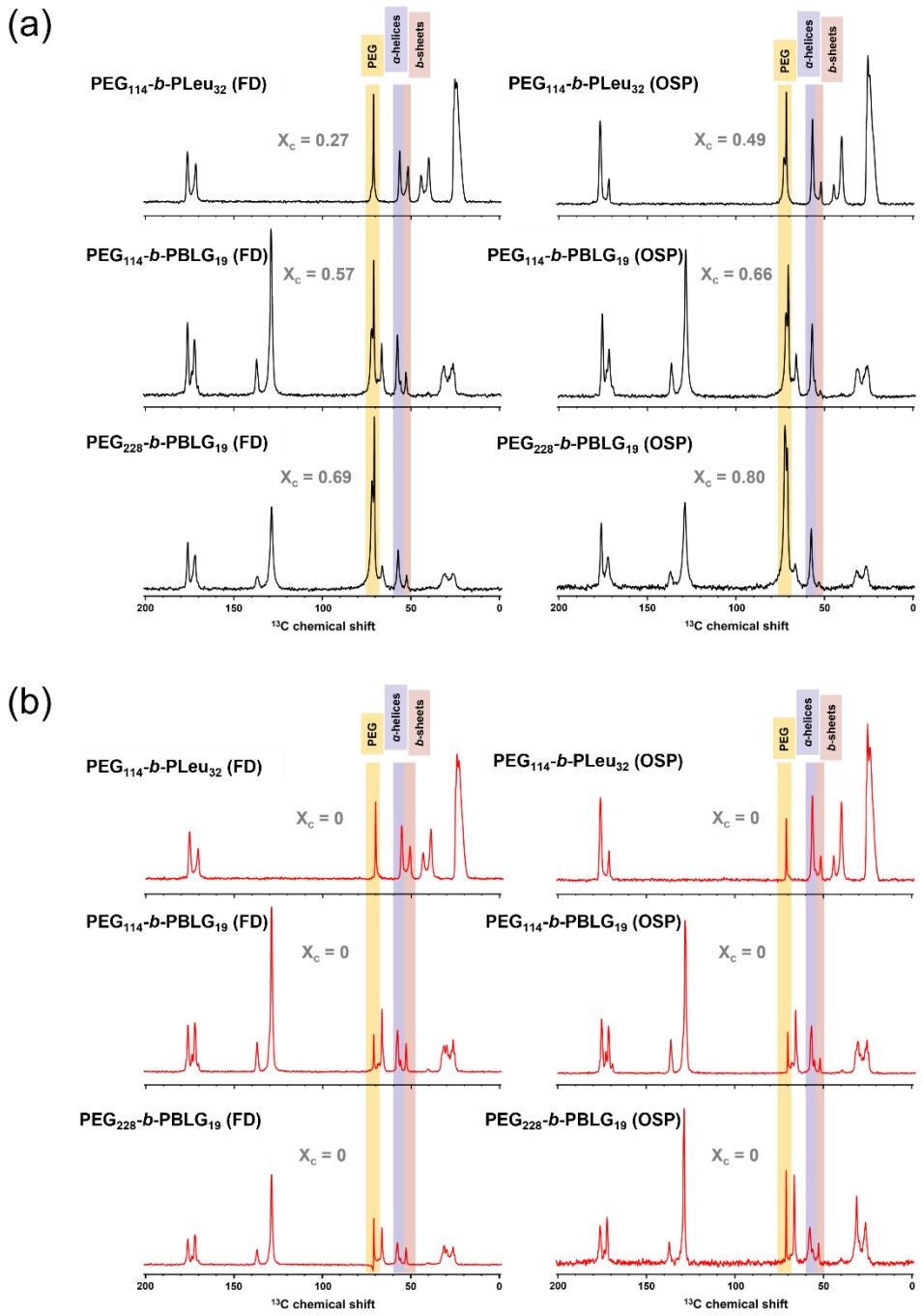

Figure 5.8. ^{13}C solid state NMR traces of the investigated copolymers at (a) 298 K and (b) 343 K. The highlighted areas refer to the chemical shifts used for the calculations of the degree of crystallinity (PEG) and the fraction of peptide (PBLG, PLeu) secondary structure (see text).

5.2.4 Superstructure Formation

The organization at a much higher lengthscale (superstructure) was studied by POM. Some representative POM images of PEG_{114}-*b*-$PBLG_{19}$ are shown in Figure 5.9. Interestingly, the superstructures deviate from the usual spherulitic-shape of PEG bulk. The copolymer forms an axialitic crystalline morphology, demonstrating a distorted Maltese cross pattern.

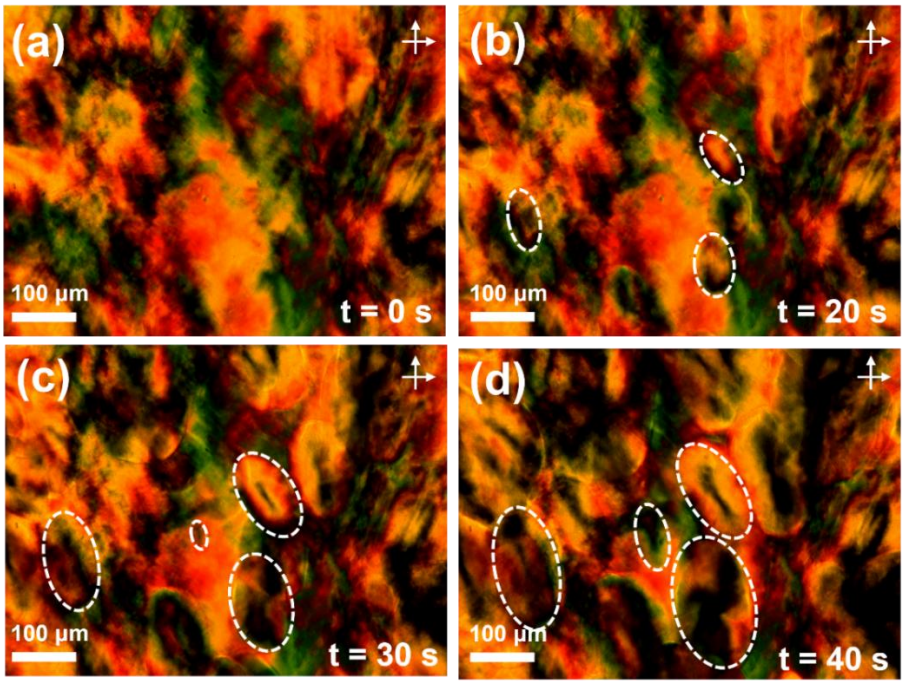

Figure 5.9. Representative POM images of the axialitic superstructures of PEG_{114}-*b*-$PBLG_{19}$ under isothermal conditions at $T = 286$ K, following jumps above the melting temperature, shown at different time intervals: (a) 0 s, (b) 20 s, (c) 30 s, and (d) 40 s. Dashed lines indicate the growing anisotropic superstructures.

Subsequently, the kinetics of the superstructure formation were investigated (Figure 5.10) and the different growth rates were obtained under isothermal conditions for different crystallization temperatures. Differences can be seen in both the temperature and the size of the axialites observed, in comparison to the spherulites found in the bulk PEG. The effect of thermodynamic confinement due to the presence of the PBLG block is threefold: First, the copolymers crystallize at lower temperatures (DSC results). Second, the inherent shape anisotropy of the PEG superstructures grows with time (Figure 5.10a). Third, the growth rates of the superstructures, when examined at a fixed temperature, are about 7 orders of magnitude slower than those of the PEG homopolymer (Figure 5.10b). Additionally, the Hoffman-Weeks plot shown in Figure 5.10d, reveals that the PEG

crystals in the copolymers exhibit lower equilibrium melting temperatures, in comparison to PEG_{114}, suggesting thermodynamic confinement and mixing. Concerning the PEG_{114}-*b*-$PLeu_{32}$ copolymer, formation of some anisotropic superstructures was also observed but the analysis of the growth rates was prohibited due to the extensive mixing between the two blocks (Figure 5.4).

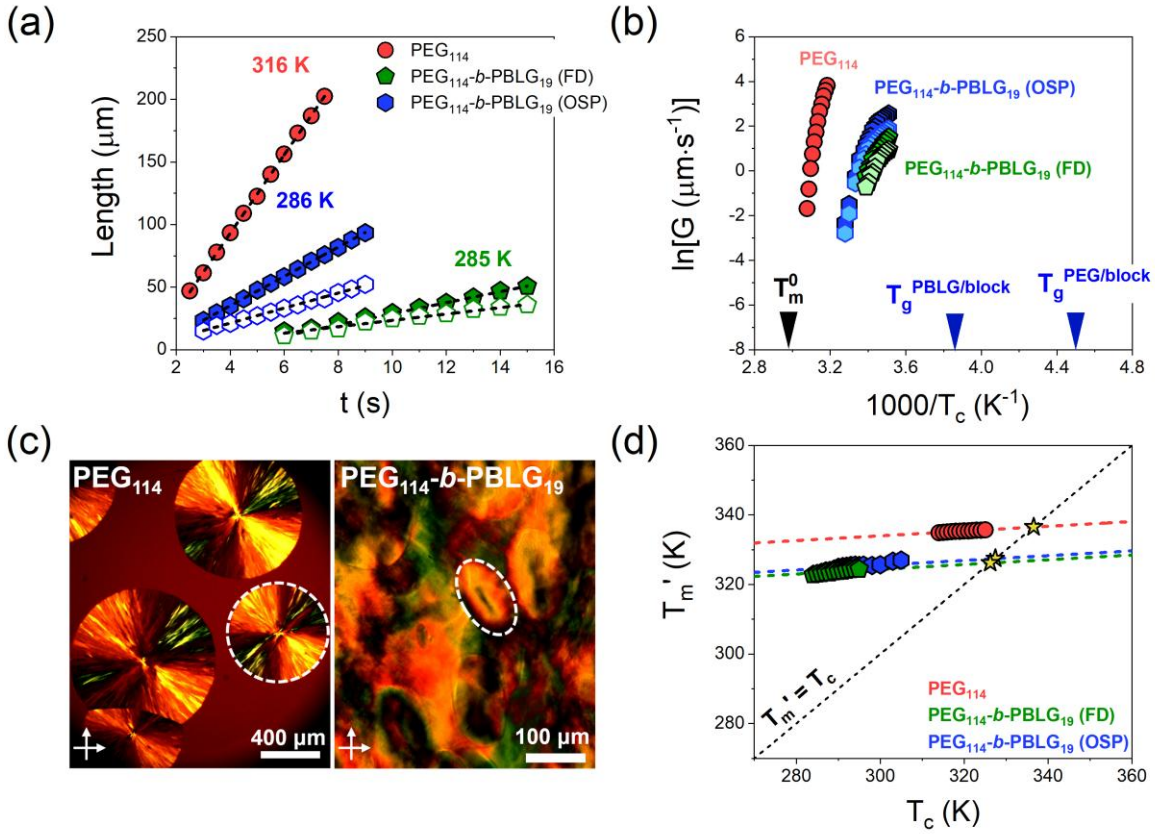

Figure 5.10. (a) Length of the long (filled symbols) and short (open symbols) axes (radius) of the PEG axialites (spherulites) as a function of time for PEG_{114}-*b*-$PBLG_{19}$ copolymers (bulk PEG_{114}). (b) Growth rates of the superstructures as a function of the inverse crystallization temperature. Green and blue symbols correspond to FD and OSP PEG_{114}-*b*-$PBLG_{19}$ copolymers; dark and light colors represent the long and short axes, respectively. Red symbols represent the bulk PEG. Arrows indicate the equilibrium melting temperature and the glass temperatures for the PEG and PBLG block in the OSP prepared copolymer. (c) POM image, obtained under isothermal conditions for bulk PEG_{114} at 311 K and the PEG_{114}-*b*-$PBLG_{19}$ copolymer at 286 K. (d) Apparent melting temperatures plotted against the crystallization temperature (Hoffman-Weeks plot). Green and blue correspond to the PEG_{114}-*b*-$PBLG_{19}$ (FD), and PEG_{114}-*b*-$PBLG_{19}$ (OSP) copolymers, respectively, while red represents the bulk PEG. The slope (dashed lines) of the two copolymers were held constant (from the bulk PEG). Star symbols indicate the extrapolated equilibrium melting temperatures.

5.2.5 Multiple Levels of Organization

The results from the structural investigation of the PEG-*b*-PBLG copolymers prepared by the ROPISA method can be summarized in a graphic plot, (Figure 5.11). It depicts the investigated lengthscales and the corresponding probes employed. Firstly, NMR identified the peptide secondary structures (α-helices, β-sheets as well as some random coil configurations). Secondly, WAXS provided the unit cell of the semicrystalline PEG block. Third, SAXS measurements revealed three ordered "objects": the form factor of PBLG α-helices, the domain spacing of the semicrystalline PEG, and the (lamellar) nanodomain morphology of the copolymer. Earlier TEM and AFM results in copolymers prepared by FP process provided some needle and wormlike intermediate structures.[22,23] The nanoparticle morphology was linked to the peptide secondary structure. For low molar mass PBLG a needle-like morphology appeared. Increasing the PBLG molar mass gave rise to wormlike morphologies as shown in Figure 5.11. At even longer lengthscales, POM documented the formation of some anisotropic superstructures. It was further shown that the growth of the latter superstructures was depended on the solvent treatment protocol. Overall, there exist six levels of organization in copolymers prepared by the ROPISA method imitating the multiple levels of organization found in natural materials.

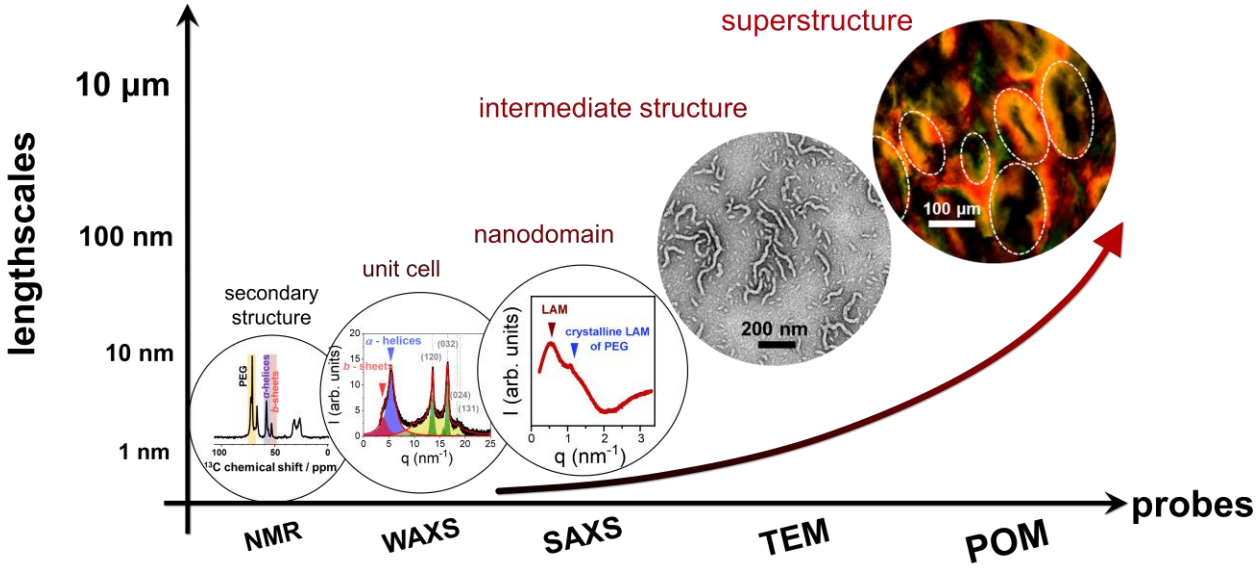

Figure 5.11. Schematic representation of the different lengthscales investigated for the PEG-*b*-PBLG copolymers prepared by ROPISA. Starting from smaller lengthscales they comprise; the secondary structures (α-helices and β-sheets), the PEG unit cell, the nanodomain morphology, an intermediate rod-like structure and the anisotropic superstructure can be identified, using a combination of probes (NMR, WAXS, SAXS, TEM/AFM and POM).

Earlier studies on PEO-*b*-PBLG diblock copolymers and PBLG-*b*-PEO-*b*-PBLG triblock copolymers, the latter as a function of composition, revealed different morphologies comprising rods, lamellae, and broken lamellae with increasing PBLG content. At a volume fraction of $0.34 < f_{PBLG} < 0.48$ the prevailing morphology was lamellar in agreement with the present investigation.[19] However, in both studies on PBLG-*b*-PEO-*b*-PBLG triblock copolymers[6,19] the SAXS contrast was low, and a definite assignment of the different structures was not possible only by X-rays. Contrast this with the present SAXS investigation of the PEG-*b*-PBLG copolymers (Figure 5.3) where not only the lamellar nanodomain morphology, but also, the form factor of PBLG helices can be clearly obtained. This is an advantage of the ROPISA method that eliminates interfacial mixing giving rise to purer nanophases and nanostructures.

5.2.6 Molecular Dynamics

Molecular dynamics provides a comprehensive understanding of the copolymers. While the static probes provided insights on the self-assembly of the copolymers over the several lengthscales, it is the molecular dynamic that can reveal the local and global peptide dynamics. The corresponding DS results for the PEG_{114}-*b*-$PBLG_{19}$ (OSP) can be discussed with the help of Figure 5.12. For clarity, the processes below glass temperature of PEG have been omitted. Two segmental processes can be identified at $T > T_g^{PEG}$. The faster one corresponds to the segmental dynamics of the PEG block, while the slower one is ascribed to the segmental relaxation of the PBLG block. The two processes approach each other in the copolymer, revealing some degree of molecular mixing at the interface between the blocks. At temperatures above 293 K, the motion of the ions trapped in the crystalline PEG block is also evident for both PEG_{114}-*b*-$PBLG_{19}$ (OSP) and PEG_{114}-*b*-$PBLG_{19}$ (FD) copolymers. It can be seen that ions move faster in the latter case. This can be explained through two competing factors in the PEG_{114}-*b*-$PBLG_{19}$ (FD): the mixing of the PEG block with the slower PBLG block, which decreases ion mobility, versus the reduced crystallinity of PEG, that increases ion mobility. The experimental data suggest the predominance of the second factor. At higher temperatures, electrode polarization and Maxwell- Wagner-Sillars interfacial polarization mask any molecular processes (e.g., the one associated with the relaxation of PBLG α-helices). Nevertheless, the DS results revealed two segmental processes in the PEG_{114}-*b*-$PBLG_{19}$ copolymers and molecular mixing at the interface.

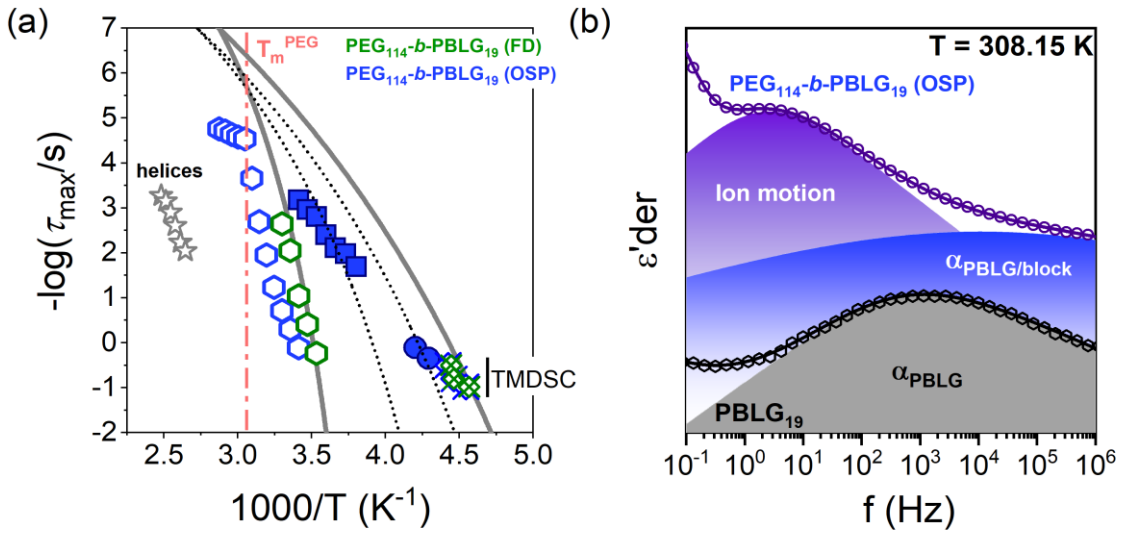

Figure 5.12. (a) Relaxation times as a function of the inverse temperature for the different processes of PEG$_{114}$-*b*-PBLG$_{19}$ (OSP) (blue) and PEG$_{114}$-*b*-PBLG$_{19}$ (FD) (green). Circles represent the segmental process of PEG, squares the segmental process of PBLG and hexagons the motion of ions. Doted black lines represent indicative fits to the PEG and PBLG segmental processes. Pink line indicates the melting temperature of the PEG block. Solid gray lines are simulation of the VFT function for the bulk PEG and PBLG homopolymers, while gray stars represent the slow helix process in bulk PBLG. TM-DSC data are also presented with crosses. (b) Derivative of dielectric permittivity as a function of frequency for PEG$_{114}$-*b*-PBLG$_{19}$ (OSP) (circles), and bulk PBLG$_{19}$ (hexagons). Blue and purple areas of the copolymer correspond to simulations of the segmental process and the ion motion, respectively. The grey area represents the *α* process in the PBLG$_{19}$ homopolymer.

5.3 Conclusion

Aqueous ring-opening polymerization-induced self-assembly of NCA monomers with the hydrophilic macromolecular initiator α-amino-poly(ethylene glycol) controls unwanted water-induced NCA ring-opening (by the formation of protective micelles) and gives rise to amphiphilic block copolymers with several levels of organization. Six levels of organization were found in the PEG-*b*-PBLG copolymers prepared by ROPISA imitating the multiple levels of organization found in natural materials. They comprise: the lamellar nanodomain morphology of unlike blocks, the domain spacing of semicrystalline PEG within its monoclinic unit cell, the peptide secondary structures (α-helices and β-sheets) within the PBLG nanodomain, and at longer lengthscales some rod-like structures (typically ~ 100 nm in size) and the strongly anisotropic superstructures of PEG crystals (typically ~ 100 μm in size). These levels of organization could not be obtained in earlier morphology investigations of copolymers based on PEG and PBLG. Evidently, the ROPISA method eliminates interfacial mixing giving rise to pure nanophases comprising PBLG domains with a high helical content. Subsequent, solvent annealing further gives rise to higher levels of organization within the nanodomains and to an α-helical content as high as 93%.

Furthermore, the type of NCA monomer (BLG-NCA vs Leu-NCA) had an influence on the degree of segregation and the order-to-disorder transition temperature in the PEG-*b*-PBLG and PEG-*b*-PLeu copolymers. The latter have shown mixing of the unlike blocks at a temperature above the melting of PEG. In contrast, the low-*q* scattering of PEG-*b*-PBLG revealed a lamellar nanodomain morphology that could be described by the Percus-Yevick approximation for cylindrical shaped objects with a helix length approaching an "ideal" helix. At temperatures above the ODT, mixing of the unlike blocks resulted in the destabilization of the PBLG α-helices.

Overall, the ROPISA method that combines one-pot synthesis and self-assembly from aqueous solutions minimizes interfacial mixing and gives rise to polypeptide copolymers with unprecedented levels of organization. The complementary static and dynamic characterization provides a complete picture of how hierarchical structure dictates material function across lengthscales.

5.4 References

1. Perly, B.; Douy, A.; Gallot, B. Block Copolymers Polybutadiene/Poly(benzyl-L-glutamate) and Polybutadiene/Poly(N^5-hydroxypropylglutamine) Preparation and Structural Study by X-Ray and Electron Microscopy. *Makromol. Chem.* **1976**, *177*, 2569-2589.
2. Douy, A.; Gallot, B. Block Copolymers with a Polyvinyl and a Polypeptide Block: Factors Governing the Folding of the Polypeptide Chains. *Polymer* **1982**, *23*, 1039.
3. Klok, H. A.; Langenwalter, J. F.; Lecommandoux, S. Self-Assembly of Peptide-Based Diblock Oligomers. *Macromolecules.* **2000**, *33*, 7819-7826.
4. Lecommandoux, S.; Achard, M.-F.; Langenwalter, J.F.; Klok, H.-A. Self-Assembly of Rod-Coil Diblock Oligomers Based on α-Helical Peptides. *Macromolecules* **2001**, *34*, 9100-9111.
5. Schlaad, H.; Kukula, H.; Smarsly, B.; Antonietti, M.; Pakula, T. Solid-State Morphologies of Linear and Bottlebrush-Shaped Polystyrene-Poly(Z-L-lysine) Block Copolymers. *Polymer* **2002**, 43, 5321-5328.
6. Floudas, G.; Papadopoulos, P.; Klok, H.A.; Vandermeulen, G.W.M.; Rodriguez-Hernandez, J. Hierarchical Self-Assembly of Poly(γ-benzyl-L-glutamate)-Poly(ethylene glycol)-Poly(γ-benzyl-L-glutamate) Rod-Coil-Rod Triblock Copolymers. *Macromolecules* **2003**, *36*, 3676-3683.
7. Schlaad, H.; Smarsly, B.; Losik, M. The Role of Chain-Length Distribution in the Formation of Solid-State Structures of Polypeptide-Based Rod-Coil Block Copolymers. *Macromolecules* **2004**, *37*, 2210-2214.
8. Tanaka, S.; Ogura, A.; Kaneko, T.; Murata, Y.; Akashi, M. Precise Synthesis of ABA Triblock Copolymers Comprised of Poly(ethylene oxide) and Poly(*β*-benzyl-L-aspartate): A Hierarchical Structure Inducing Excellent Elasticity. *Macromolecules* **2004**, *37*, 1370-1377.
9. Klok, H. A.; Lecommandoux, S. Solid-State Structure, Organization and Properties of Peptide-Synthetic Hybrid Block Copolymers. *Adv. Polym. Sci.* **2006**, *202*, 75-111.
10. Block, H. *Poly(γ-benzyl-L-glutamate) and Other Glutamic Acid Containing Polymers.* Gordon and Breach Science Publishers, **1983**, New York, NY 10016.
11. Muroga, Y.; Nagasawa, M. On the Flexibility of Poly(γ-Benzyl L-Glutamate) in Helicogenic Solvents. *Biopolymers* **1998**, *45*, 281-288.
12. Schlaad, H. Solution Properties of Polypeptide-based Copolymers. *Adv. Polym. Sci.* **2006**, *202*, 53-73.
13. Papadopoulos, P.; Floudas, G.; Klok, H.-A.; Schnell, I.; Pakula, T. Self-Assembly and Dynamics of Poly(γ-benzyl-L-glutamate) Peptides. *Biomacromolecules* **2004**, *5*, 81.
14. Floudas, G.; Spiess, H.W. Self-Assembly and Dynamics of Polypeptides. *Macromol. Rapid Commum.* **2009**, *30*, 278-298.
15. Duncan, R. The dawning era of polymer therapeutics. *Nature Reviews Drug Discovery* **2003**, *2*, 347-360.
16. Kugo, K.; Ohji, A.; Uno, T.; Nishino, J. Synthesis and Conformations of A-B-A Tri-Block Copolymers with Hydrophobic Poly(γ-benzyl-L-glutamate) and Hydrophilic Poly(ethylene oxide). *Polymer Journal* **1987**, *19*, 375-381.

17. Cho, C.-S.; Kim, S.-W.; Komoto, T. Synthesis and structural study of an ABA Block Copolymer Consisting of Poly(γ-benzyl-L-glutamate) as the A block and Poly(ethylene oxide) as the B block. *Die Makromolekulare Chemie* **1990**, *191*, 981-991.
18. Cho, C.-S.; Nah, J.-W.; Jeong, Y.-I.; Cheon, J.-B.; Asayama, S.; Ise, H.; Akaike, T; Conformational transition of nanoparticles composed of poly(γ-benzyl-L-glutamate) as the core and poly(ethylene oxide) as the shell. *Polymer* **1999**, *40*, 6769-6775.
19. Parras, P.; Castelletto, V.; Hamley, I. W.; Klok, H.-A. Nanostructure formation in poly(γ-benzyl-L-glutamate)–poly(ethylene glycol)–poly(γ-benzyl-L-glutamate) triblock copolymers in the solid state. *Soft Matter* **2005**, *1*, 284.
20. d'Agosto, F.; Rieger, J.; Lansalot, M. RAFT-mediated polymerization-induced self-assembly. *Angewandte Chemie International Edition* **2020**, *59*, 8368-8392.
21. Penfold, N. J. W.; Yeow, J.; Boyer, C.; Armes, S. P. Emerging Trends in Polymerization-Induced Self-Assembly. *ACS Macro Letters* **2019**, *8*, 1029-1054.
22. Grazon, C.; Salas-Ambrosio, P.; Ibarboure, E.; Buol, A.; Garanger, E.; Grinstaff, M. W.; Lecommandoux, S.; Bonduelle, C. Aqueous Ring-Opening Polymerization-Induced Self-Assembly (ROPISA) of N-carboxyanhydrides. *Angew. Chem. Int. Ed.* **2019**, *59*, 622-626.
23. Grazon, C.; Salas-Ambrosio, P.; Antoine, S.; Ibarboure, E.; Sandre, O.; Clulow, A. J.; Boyd, B. J.; Grinstaff, M. W.; Lecommandoux, S.; Bonduelle, C. Aqueous ROPISA of α-Amino Acid N-Carboxyanhydrides: Polypeptide Block Secondary Structure Controls Nanoparticle Shape Anisotropy. *Polym. Chem.* **2021**, *12*, 6242-6251.
24. Beauseroy, H.; Grazon, C.; Antoine, S.; Badreldin, M.; Salas-Ambrosio, P.; Harrisson, S.; Garanger, E.; Lecommandoux, S.; Bonduelle, C. Polypeptide- and Protein-Based Conjugate Nanoparticles via Aqueous Ring-Opening Polymerization-Induced Self-Assembly (ROPISA). *Macromol. Rapid Commun*. **2024**, *45*, 2400079
25. Meyers, M.A.; Chen, P.Y.; Lin, A.Y.M.; Seki, Y. Biological materials: Structure and Mechanical Properties. *Progress in Materials Science* **2008**, *53*, 1-206.
26. Fetters, L.J.; Lohse, D.J.; Richter, D.; Witten, T.A.; Zirkel, A. Connection Between Polymer Molecular Weight, Density, Chain Dimensions, and Melt Viscoelastic Properties. *Macromolecules* **1994**, *27*, 4639-4647.
27. Papadopoulos, P.; Floudas, G.; Schnell, I.; Aliferis, T.; Iatrou, H.; Hadjichristidis, N. Nanodomain-Induced Chain Folding in Poly(γ-benzyl-L-glutamate)-*b*-polyglycine Diblock Copolymers. *Biomacromolecules* **2005**, *6*, 2352-2361.
28. Poly-L-leucine, Chemsrc.com. Available at: https://www.chemsrc.com/en/cas/25322-63-8_1375819.html.
29. Zardalidis, G.; Mars, J.; Allgaier, J.; Mezger, M.; Richter, D.; Floudas, G. Influence of Chain Topology on Polymer Crystallization: Poly(ethylene oxide) (PEO) Rings vs. Linear Chains. *Soft Matter* **2016**, *12*, 8124-8134.
30. Kasten, H.; Stühn, B. Density Discontinuity at the Microphase Separation Transition of a Symmetric Diblock Copolymer. *Macromolecules* **1995**, *28*, 4777-4778.

31. Hajduk, D.A.; Gruner, S.M.; Erramilli, S.; Register, R.A; Fetters, L.J. High-Pressure Effects on the Order− Disorder Transition in Block Copolymer Melts. *Macromolecules* **1996**, *29*, 1473-1481.
32. Floudas, G.; Vazaiou, B.; Schipper, F.; Ulrich, R.; Wiesner, U.; Iatrou, H.; Hadjichristidis, N. Poly (ethylene oxide-*b*-isoprene) Diblock Copolymer Phase Diagram. *Macromolecules* **2001**, *34*, 2947-2957.
33. Leibler, L. *Theory of Microphase Separation in Block Copolymers*. *Macromolecules* **1980**, *13*, 1602-1617.
34. de Gennes, P.G. in *Scaling Concepts in Polymer Physics*. Cornell University Press (**1979**).
35. Kinning, D. J.; Thomas, E. L. Hard-Sphere Interactions Between Spherical Domains in Diblock Copolymers. *Macromolecules* **1984**, *17*, 1712-1718.
36. Pedersen, J. S. Determination of Size Distributions from Small-Angle Scattering Data for Systems with Effective Hard-Sphere Interactions. *J. Appl. Cryst.* **1994**, *27*, 595-608.
37. Liu, Z.; Shi, X.; Shu, W.; Qi, S.; Wang, X.; He, X. The effect of Hydration and Dehydration on the Conformation, Assembling Behavior and Photoluminescence of PBLG. *Soft Matter*, **2022**, *18*, 4396-4401.
38. Takahashi, Y.; Tadokoro, H. Structural Studies of Polyethers, (–(CH2)m–O–)n. X. Crystal Structure of Poly(ethyleneoxide). *Macromolecules* **1973**, *6*, 672-675.
39. Mondeshki, M.; Spiess, H. W.; Aliferis, T.; Iatrou, H.; Hadjichristidis, N.; Floudas, G. Hierarchical Self-assembly in Diblock Copolypeptides of Poly(*γ*-benzyl-L-glutamate) with Poly(L-leucine) and Poly(O-benzyl-L-tyrosine). *European Polymer Journal* **2011**, *47*, 668-674.
40. van Beek, J.D.; Beaulieu, L.; Schafer, H.; Demura, M.; Asakura, T.; Meier, B.H. Solid-state NMR Determination of the Secondary Structure of Samia Cynthia Ricini Silk. *Nature* **2000**, *405*, 1077.
41. Tycko, R. Biomolecular Solid-State NMR: Advances in Structural Methodology and Applications to Peptide and Protein Fibrils. *Ann. Rev. Phys. Chem.* **2001**, *52*, 575.
42. Wang, S.; Kang, J.; Jain, D.; Miyoshi, T. Application of NMR in Polymer Characterization. In Nuclear Magnetic Resonance; The Royal Society of Chemistry: Cambridge, UK **2016**, *45*, 79-82.

Chapter 6. Conclusions

Proteins achieve their functional diversity through hierarchical organization - from local secondary structures to complex tertiary folds. This thesis examines how synthetic polypeptides can mimic this architectural control by addressing two interconnected questions: first, how do secondary structures (α-helices and β-sheets) govern the dynamic and viscoelastic behavior of polypeptides in non-hydrated systems; and second, how can we control the higher-order assembly of these building blocks to create biomimetic materials with protein-like complexity? By investigating poly(γ-benzyl-L-glutamate) (PBLG) peptides - both as homopolymers and in block copolymers with poly(ethylene glycol) (PEG) - we demonstrate how molecular topology influences the self-assembly and the associated dynamics across length- and timescales.

In PBLG homopolypeptides, both α-helices and β-sheets exhibit distinct local and global dynamics. Two glass temperatures (T_gs) were identified by DSC and DS in polypeptides that stabilize both secondary structures: a lower T_g associated with amorphous α-helical segments and a higher T_g associated with amorphous β-sheet segments. The latter indicates significantly more restricted motions. This is the first report for β-sheet-associated T_g in a completely non-hydrated polypeptide. The relaxation of the α-helical and β-sheet macrodipoles was also evident at longer timescales. Again, it is the first time that β-sheets are shown to have chain dynamics associated with dipoles perpendicular to the chain. The differences between the two secondary structures were also evident in fragility and pressure dependence. β-sheets, stabilized by intermolecular hydrogen bonds, exhibit slower dynamics, lower fragility, and weak pressure response. In contrast, α-helices, organized through intramolecular hydrogen bonds, show more mobile and fragile dynamics that are highly sensitive to pressure. Evidently, it is the type of the hydrogen bond that determines the dynamic behavior.

The viscoelastic results revealed that both α-helices and β-sheets form distinct superstructures, as evidenced by their different viscoelastic signatures. Expectedly, due to their self-organization, an elastic response ($G' > G''$) was observed across all samples. Importantly, van Gurp-Palmen (vGP) plots analysis revealed correlations between the elastic modulus and the dominant secondary structure. Two minima in the phase angle, δ, were identified: one at the plateau modulus G_N^0 reflecting the elastic properties of the entanglement "network" ($\sim 10^5$ Pa) and another

in the vicinity of the T_g (~ 10^9 Pa). In low-molar-mass α-helix-rich peptides, we observed molar-mass-dependent mesh sizes, yielding compliant matrices with moduli spanning the range of soft biological tissues (1-20 kPa for epithelial tissues, 4-10 kPa for basement membranes). These properties make α-helical meshes particularly suitable for soft biomedical interfaces, membranes, and stimuli-responsive systems. Conversely, β-sheet-rich peptides displayed compact, network structures with significantly higher moduli (G_N^0 ~ 10^7 Pa). Their mechanical properties approach those of load-bearing biological tissues (e.g., tendon at ~ 1 GPa) and synthetic bone substitutes (15-20 GPa range), making them ideal for implant applications requiring structural integrity. This tertiary level of organization emerges through the percolation and aggregation of secondary structural motifs.

In copolypeptides, the study of new amphiphilic PEG-*b*-PBLG diblock copolymers broadened the scope to the mesoscopic and macroscopic levels. The samples were synthesized via aqueous ring-opening polymerization-induced self-assembly of NCA monomers with the hydrophilic macromolecular initiator α-amino-poly(ethylene glycol). Six levels of organization were observed, similar to those of natural proteins, such as tendons. These levels include: (1) the lamellar nanodomain morphology of unlike blocks, (2) the domain spacing of semicrystalline PEG within (3) its monoclinic unit cell, (4) the peptide secondary structures (α-helices and β-sheets) within the PBLG nanodomain, and (5) at longer lengthscales some rod-like structures (typically ~ 100 nm in size) and (6) the strongly anisotropic superstructures of PEG crystals (typically ~ 100 μm in size). This type of hierarchical organization could not be achieved in earlier morphology studies of PEG-PBLG copolymers prepared with other methods. The ROPISA method eliminates interfacial mixing, resulting in pure nanophases that comprise PBLG domains with helical content as high as 93%. Furthermore, the type of NCA monomer (BLG-NCA vs Leu-NCA) influenced the degree of segregation and the order-to-disorder transition temperature in the PEG-*b*-PBLG and PEG-*b*-PLeu copolymers. The latter showed mixing of the unlike blocks, whereas PEG-*b*-PBLG revealed a lamellar nanodomain morphology with mixing of the unlike blocks and destabilization of the PBLG α-helices only at temperatures above the ODT.

This work establishes that the hydrogen-bonding patterns of the polypeptide secondary structures dictate material function across different length- and timescales. In homopolypeptides, β-sheets yield bone-like rigidity, while α-helices provide tissue-matched elasticity – enabling

precise mechanical tailoring. For copolypeptides, ROPISA translates this molecular control into natural protein-like hierarchies, achieving structural precision unattainable through traditional synthesis. Together, these advances provide a design framework for biomaterials that bridges the gap between fundamental polymer physics and biomedical applications, from load-bearing implants to adaptive tissue interfaces, through controlled polypeptide self-assembly from angstroms to micrometers.